Polarization reversal dynamics in polycrystalline ferroelectric/ferroelastic ceramic materials

Polarisationsumschaltdynamik in polykristallinen ferroelektrischen/ferroelastischen keramischen Materialien
Zur Erlangung des akademischen Grades Doktor-Ingenieur (Dr.-Ing.)
genehmigte Dissertation von Jan Erich Schultheiß aus Coburg
Tag der Einreichung: 24.Mai 2018, Tag der Prüfung: 9.August 2018
Darmstadt — D 17

1. Gutachten: J. Koruza
2. Gutachten: W. Donner

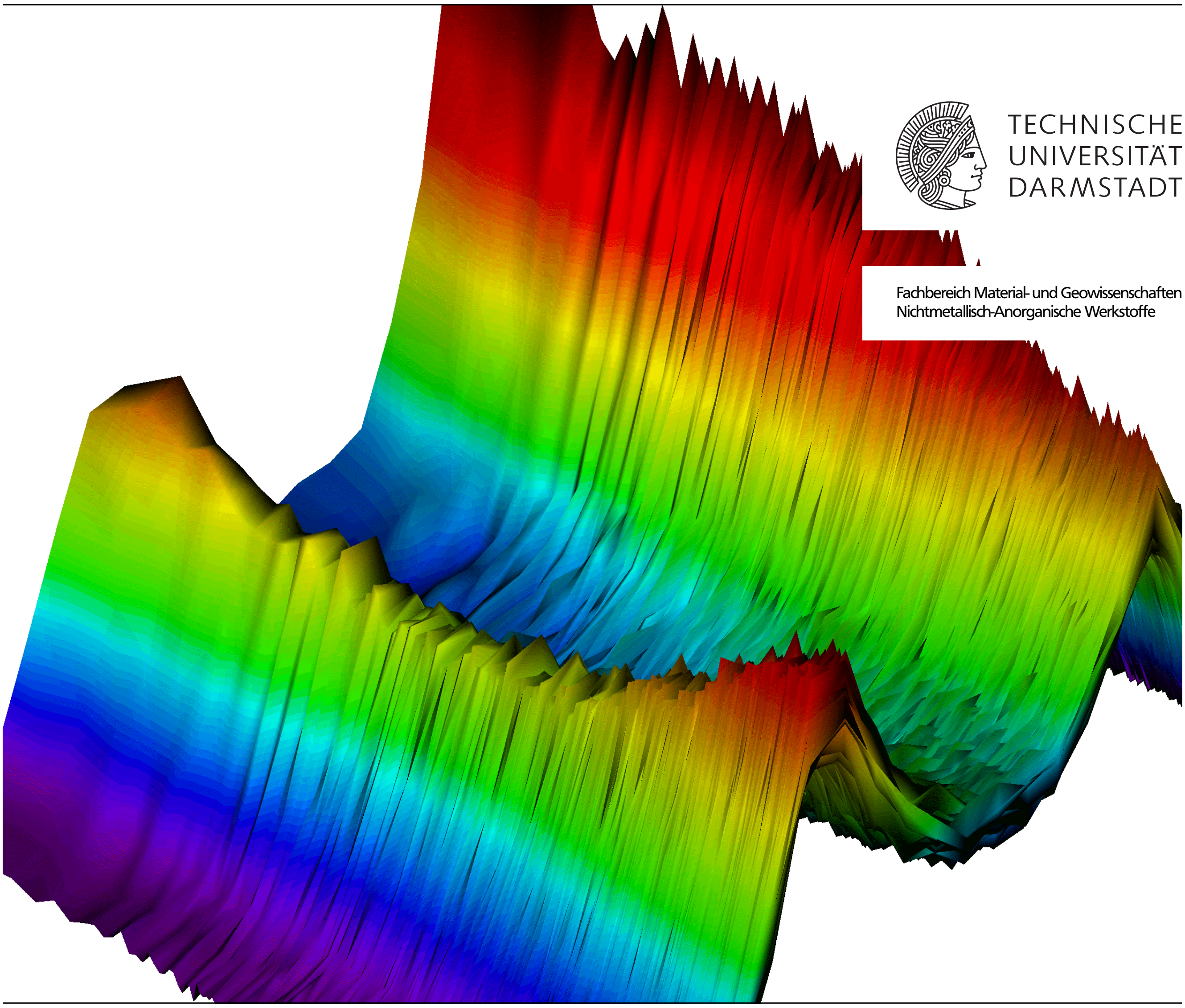

TECHNISCHE
UNIVERSITÄT
DARMSTADT

Fachbereich Material- und Geowissenschaften
Nichtmetallisch-Anorganische Werkstoffe

Polarization reversal dynamics in polycrystalline ferroelectric/ferroelastic ceramic materials
Polarisationsumschaltdynamik in polykristallinen ferroelektrischen/ferroelastischen keramischen Materialien

Genehmigte Dissertation von Jan Erich Schultheiß aus Coburg

1. Gutachten: J. Koruza
2. Gutachten: W. Donner

Tag der Einreichung: 24.Mai 2018
Tag der Prüfung: 9.August 2018

Darmstadt — D 17

Bitte zitieren Sie dieses Dokument als:
URN: urn:nbn:de:tuda-tuprints-77527
URL: http://tuprints.ulb.tu-darmstadt.de/7752

Erklärung zur Dissertation

Hiermit versichere ich, die vorliegende Dissertation ohne Hilfe Dritter nur mit den angegebenen Quellen und Hilfsmitteln angefertigt zu haben. Alle Stellen, die aus Quellen entnommen wurden, sind als solche kenntlich gemacht. Diese Arbeit hat in gleicher oder ähnlicher Form noch keiner Prüfungsbehörde vorgelegen.

Darmstadt, den 24.Mai 2018

(J. Schultheiß)

Acknowledgement

This project has been both enjoyable and challenging, and I am very grateful to everyone who has supported me on this journey.

First, I thank my supervisor Dr. Jurij Koruza. Thank you for always being available with excellent advice, for sharing your knowledge and excitement in ferroelectrics and processing with me, for providing experimental support whenever necessary, for your continuous deep interest in the project, for your open-door policy, for the cooperative attitude, for the nice working atmosphere, and for reading my manuscripts and my thesis over and over again and providing fast and constructive feedback.

Furthermore, my sincere gratitude goes to Prof. Dr. J. Rödel for the opportunity to be part of his research group. I appreciate his steady guidance and support, his careful and devoted organization of the research group and his appropriation of international contacts without which this work would not have been possible.

I would like to thank Prof. W. Donner for accepting to be the second reviewer of this work.

I would like to thank my collaborators with whom I was privileged to work with during the past years: Yuri Genenko, Ruben Khachaturyan, Dragan Damjanovic, John Daniels, Denis Alikin, Vladimir Shur, Hans Kungl, Lisha Liu, Barbara Malic, Sergey Zhukov, Emre Erdem, Oliver Clemens, Shuai Wang, Yangbin Ma and Wen Dong. I am very grateful to Vladimir Shur and Denis Alkin for welcoming me as a visiting scientist to join their group at the Ural State University in Ekaterinburg. Thank you for the interest in my work, your ongoing experimental work and the warm and friendly support of your entire research group. Dragan Damjanovic hosted me at EPFL Lausanne, where I shared his deep knowledge and enthusiasm of the field of ferroelectric materials. I am also indebted to Yuri Genenko and Ruben Khachatruyan, who provided theoretical simulations of the experimental data. Many thanks go to John Daniels and Lisha Liu for opening us the door to ESRF, for the time we spend in Grenoble together and for their guidance of the subsequent data analysis. Oliver Clemens is acknowledged for providing his expertise in refinement of diffraction data.

The excellent samples investigated in this thesis were manufactured by skilled collaborators. I would like to thank Hans Kungl for providing samples he manufactured during his time in Karlsruhe, Silvo Drnovšek from JSI Ljubljana and the group of Prof. Sakamoto from Nagoya university.

A fundamental part of this work wouldn't have been possible without the contributions of our skilled technicians. In particular, I would like to thank Michael Weber for his continuous motivated support in the construction of the electrical equipment and his curiosity about its functionality. Also, I highly acknowledge the help of Daniel Isaia, Patrick Breckner, Michael Heiße and Gundel Fließ. Many thanks also goes to our excellent secretary Gila Völzke and to the guys of our workshop.

I have also had the pleasure to supervise several students: Christian Weinkauf, Leif Carstensen and Tim Hundhausen. I have learned a tremendous amount from our collaboration and their contribution to this work are highly valued.

The German Research Foundation (DFG) is highly acknowledged for funding the work under grant No. KO 5100/1-1.

I want to thank Urs Gonzenbach and Gary Messing who sparked my passion for ceramics during my studies at ETH Zurich and Pennylvania State University.

I would like to thank everybody who volunteered to proof read this thesis and provided valuable input: Mihail Slabki, Marion Höfling, Lukas Porz, Florian Weyland, Sebastian Steiner, Satyanarayan Patel and Lalitha Kodumudi Venkataraman.

Working hours would have been much less fun and less enjoyable without my colleges. In particular, special thanks to Florian and Peter for felicitous deflections, innovative bets and some essential after work drinks. Also, to Matias and Martin, who shared an office with me during my early time at NAW.

The whole NAW group provided a great working environment. I would like to thank all my colleagues and former colleagues for various group excursions, our hiking trips in Kleinwalsertal, barbecues and conference trips. I also enjoyed a lot our privately organized ski trips, board game nights, soccer games, beer meetings and running challenges.

Finally, I would like to thank my family for their love and support. In particular I thank my parents Karin and Manfred for always being there for me. Also, to my aunt Ingrid for being the best godparent one could imagine. My sister Ina for the time we spent together in Darmstadt. I have also been very lucky that I met Yolita during my studies in Erlangen.

Jan Schultheiß
Darmstadt, Mai 2018

Contents

List of Figures

List of Tables

List of Abbreviations

BT Barium titanate, $BaTiO_3$

BNC Bayonet Neill–Concelman

CT Calcium titanate, $CaTiO_3$

CSL Coincidence site lattice

Cb Cubic

DFT Density functional theory

EBSD Electron backscatter diffraction

ESRF European Synchrotron Radiation Facility

GMO Gadolinium molybdate, $Gd_2(MoO_4)_3$

GLSL Gradient lattice strain layer

HV High voltage

HE Homogenized energy

IFM Inhomogeneous field mechanism

KAI Kolmogorov-Avrami-Ishibashi

KTP Potassium titanyl phosphate, $KTiOPO_4$

PZT Lead zirconate titanate

MD March-Dollase

m monoclinic

MPB Morphotropic phase boundary

NLS Nucleation limited switching

O Orthorhombic

PFM Piezoresponse force microscopy

pc pseudocubic

PZN-PT $0.955\,Pb(Zn_{1/3}Nb_{2/3})O_3 - 0.045\,PbTiO_3$

R Rhombohedral

SEM Scanning electron microscopy

SC Single crystal

T Tetragonal

TSDC Thermally-stimulated depolarization current

TEM Transmission electron microscope

TGS Triglycine sulfate, $C_6H_{17}N_3O_{10}S$

XRD X-ray diffraction

List of Symbols

E_a	Activation field
ι	Amplitude in PFM signal
V_{app}	Applied voltage
A	Area
Λ	Avrami coefficient
Ψ	Azimuthal angle
S_{bip}	Bipolar Strain
C	Capacity
E_C	Coercive field
k	Constant
Π	Correction factor in MD equation
ϑ_{Cur}	Curie temperature
β	Depinning exponent
ϑ_D	Depolarization temperature
D	Dielectric displacement
θ	Diffraction angle
ζ	Deviation angle
l	Dimension of the sample
α	Dielectric stiffness coefficients
$\triangle$	Dimensionality of the domain wall
δ_{dim}	Dimensionality of the domains
δ	Domain size
η	Domain switching fraction
ξ	Domain wall roughening coefficient
μ	Dynamic exponent
E	Electric field
R	Electric resistance
Q	Electrostrictive constant
U	Energy barrier
Γ	Eshelby transformation strain tensor

ν Frequency

ΔG Gibbs free energy

g Grain size

I Intensity

ω Intersection angle of lattice planes

d_{lat} Lattice spacing

ε Lattice strain

F Lotgering factor

$\phi(u)$ Master curve in IFM

σ Mechanical Stress

s Mechanical compliance

S_{neg} Negative strain

p Normalized intensity fraction of XRD peaks

κ Permittivity

κ_0 Permittivity of vacuum

Ψ Phase shift in PFM measurements

d Piezoelectric coefficient

P Polarization

P_r Remanent polarization

S Strain

χ Susceptibility

ΔP Switched polarization

E_{sw} Height of switching field pulse

ϑ Temperature

t Time

τ Time constant

v Velocity of domain walls

V Voltage

f Volume fraction of textured material

Ξ Volume fraction of domains

Abstract

Ferroelectric materials find application in numerous electronic devices and are continuously enabling the development of new technologies. Their versatility is intimately related to the unique property to switch the polarization with electric fields. However, the switching mechanisms in polycrystalline ferroelectric materials remain insufficiently understood.

Several questions regarding the mechanisms of the polarization reversal process in polycrystalline ceramic materials have been addressed in this work. The dynamics of the process was measured by a self-constructed high voltage switch, which provides high voltage pulses to the sample and measures its macroscopic polarization and strain response over several decades. Moreover, this macroscopic technique was supplemented by *in situ* synchrotron diffraction experiments using a high speed detector at the European Synchrotron Radiation Facility. This unique combination of macroscopic and microscopic time-resolved experimental data allowed to reveal the sequence of events during polarization switching in polycrystalline ferroelectric materials. The process is illustrated by a sequence of well-defined 180° and non-180° domain switching events, which can be separated into three regimes. Field-dependent measurements allow to determine activation fields for the individual regimes, which are a crucial input parameter for micromechanical models.

The domain structure in a poled polycrystalline ferroelectric/ferroelastic material mainly consists of non-180° domain walls. Several of them are misaligned to the poling field direction and polarization reversal can start from these misaligned domains. In the first switching regime, the non-180° domain walls are moving, driven by an external applied electric field and supported by internal mechanical fields. Auxiliary mechanical forces and the fact that nuclei are already available result in a low activation field and consequently a fast movement of the domain walls. The transition between the first and the second regime is governed by the interplay between electric and mechanical fields, which can be displayed by Landau energy landscapes. The polarization reversal in the second regime occurs by 180° or synchronized non-180° domain wall movement. Hereby, more than 60% of the total polarization was found to be switched in a model $Pb(Zr,Ti)O_3$ material. With the experimental methods available today, it is not possible to distinguish between pure 180° or synchronized non-180° domain wall movement. However, a more than three times lower Peierls barrier for non-180° compared to 180° domain wall movement and crystallographic arguments suggest that switching in the main switching phase occurs essentially by synchronized non-180° events. In any case, the mechanical stress in this regime is acting against the moving domain walls, which is expressed by a 35% higher activation field, as compared to the first regime. In the third regime the majority of domains are reversed and the electric field is parallel to the polarization vector. Here, creep-like movement of non-180° domain walls occurs.

The dynamic response of polycrystalline ceramic materials is strongly influenced by their microstructure, affecting the polarization and strain response in the individual regimes. In this context, the velocity of domain walls is set by the local electric field. The distribution of the latter in a polycrystalline ceramic material is inhomogeneous, since it represents a projection of the external electric field to the direction of the spontaneous polarization of a grain. In addition, other factors influence the dynamic response. A 47% higher activation field was found for $Pb(Zr,Ti)O_3$ materials with a tetragonal compared to a material with a rhombohedral crystallographic structure. This partially reflects the influence of the lattice distortion and the resulting internal stresses at the domain junctions, which have to be overcome when the domain walls are moving. In addition, mechanical and electrical interaction between grains play a significant role. In this context, internal mechanical stresses may enhance or suppress domain wall movement. This is for example expressed in a broader distribution of switching times for a polycrystalline ceramic with smaller grain sizes compared to a ceramic material with larger grain sizes. On the other hand, a 20% reduction in the activation field for polarization reversal was found for $BaTiO_3$-based materials which are highly crystallographically textured compared to untextured materials. Tailoring the microstructure accordingly may impede or facilitate the dynamic response of the polycrystalline ceramic material. In addition, a relation between microstructural parameters and the dynamic polarization response of polycrystalline ferroelectric ceramic materials is an important input parameter for theoretical models.

Zusammenfassung

Ferroelektrische Materialien werden in zahlreichen elektronischen Geräten angewendet und treiben die kontinuierliche Entwicklung neuer Technologien voran. Sie unterscheiden sich von anderen polaren Materialien dadurch, dass der Polarisationsvektor mit einem elektrischen Feld umgeschaltet werden kann. Die Mechanismen während dieses Umschaltvorgangs in polykristallinen ferroelektrischen Materialien sind jedoch nur unzureichend verstanden.

Um die Sequenz des Umschaltprozesses zu entschlüsseln wurde die Dynamik des Umschaltprozesses mit einem selbstgebauten Hochspannungsschalter gemessen. Die damit erzeugten Hochspannungspulse schalten den Polarisationsvektor um, während die makroskopische Polarisations- und Dehnungsantwort der Probe zeitaufgelöst gemessen wird. Diese makroskopischen Messungen wurden mit zeitaufgelösten Beugungsexperimenten ergänzt. Hierzu wurde ein Detektor mit hoher Messgeschwindigkeit der European Synchrotron Radiation Facility verwendet. Mit Hilfe der Kombination aus zeitaufgelösten makroskopischen und mikroskopischen Daten konnte die Sequenz des Polarisationsumschaltens in polykristallinen ferroelektrischen Materialien dargestellt werden. Der Prozess wird in drei Abschnitte unterteilt, wobei das Umschalten in jedem Abschnitt durch die Bewegung von 180° oder nicht-180° Domänenwänden stattfindet. Mit Hilfe von feldabhängigen Messungen können Aktivierungsfelder für das Umschalten der Polarisation in den jeweiligen Abschnitten bestimmt werden, die eine wichtige Eingangsgröße für mikromechanische Modelle sind.

Die Domänenstruktur in gepolten polykristallinen ferroelektrischen/ferroelastischen Materialien besteht zu einem Großteil aus nicht-180° Domänenwänden, von denen viele im remanenten Zustand nicht in die Richtung des Polungsfeldes ausgerichtet sind. Im ersten Abschnitt beginnt der Umschaltprozess durch die Bewegung dieser Domänenwände, stimuliert durch das externe elektrische Feld. Diese Domänenwandbewegung wird von internen mechanischen Spannungen unterstützt und ist durch eine hohe Geschwindigkeit und niedrige Aktivierungsfelder gekennzeichnet. Der Übergang vom ersten zum zweiten Abschnitt geschieht durch ein komplexes Zwischenspiel zwischen elektrischen und mechanischen Feldern, welches durch zweidimensionale Landau freie Energielandschaften beschrieben wird. Polarisationsumschalten im zweiten Abschnitt findet durch 180° oder synchronisierte nicht-180° Domänenwandbewegung statt, wobei die heute verfügbaren experimentellen Methoden keinen finalen Schluss zulassen, welche Domänenwandbewegung dominant ist. Die Tatsache, dass die Peierls Gitterenergie für nicht-180° Domänenwände dreimal geringer ist als für 180° Domänenwände und kristallographische Argumente deuten jedoch darauf hin, dass das Umschalten der Polarisation im zweiten Abschnitt hauptsächlich durch nicht-180° Domänenwandbewegung stattfindet. Der Beitrag der im zweiten Abschnitt umgeschalteten Polarisation zur gesamten umgeschalteten Polarisation wurde zu 60% in einem $Pb(Zr,Ti)O_3$ Modellmaterial quantifiziert. Hierbei wirkt die mechanische Spannung nun entgegen der Domänenwandbewegung. Dies hat ein um 35% höheres Aktivierungsfeld für die Domänenwandbewegung verglichen mit dem ersten Abschnitt zur Folge. Im dritten Abschnitt ist der Polarisationsvektor der Domänen parallel zum elektrischen Feld ausgerichtet. Der dritte Bereich zeichnet sich durch eine langsame nicht-180° Domänenwandbewegung aus und die makroskopische Antwort ähnelt elektrischem Kriechen.

Die dynamische Antwort eines polykristallinen ferroelektrischen Materials ist stark von dessen Mikrostruktur abhängig. Hierbei wird die Geschwindigkeit der Domänenwände von dem lokal wirkenden elektrischen Feld bestimmt. Dieses ist in einer polykristallinen Keramik inhomogen verteilt, da das externe elektrische Feld auf die Richtung der spontanen Polarisation eines einzelnen Korns projiziert wird. Neben der inhomogenen Feldverteilung wird das Schaltverhalten durch weitere Parameter beeinflusst. Zum Beispiel wurde für ein $Pb(Zr,Ti)O_3$ mit tetragonaler Kristallstruktur ein um 47% höheres Aktivierungsfeld verglichen mit einem Material mit einer rhombohedrischen Kristallstruktur gefunden. Dies spiegelt den Einfluss der Gitterverzerrung und die daraus resultierenden internen Spannungen an Domänentripelpunkten wieder, welche bei der Bewegung dieser Domänen überwunden werden müssen. Beim Umschalten von polykristallinen ferroelektrischen Materialien spielt außerdem die Wechselwirkung zwischen den einzelnen Körnern eine wichtige Rolle und interne mechanische Spannungen können das Umschalten verlangsamen oder beschleunigen. Zum Beispiel wird eine breitere Verteilung von Umschaltzeiten in Keramiken mit kleinerer Korngröße gefunden, während das Umschalten einfacher und die Verteilung der Umschaltzeiten mit steigender Korngröße schärfer wird. Auf der anderen Seite zeigen $BaTiO_3$ basierte Materialien mit kristallographisch texturierten Körnern ein um 20% verringertes Aktivierungsfeld für das Umschalten der Polarisation im zweiten Abschnitt, verglichen mit Materialien, die keine Vorzugsrichtung aufweisen. Durch gezieltes Einstellen der Mikrostruktur kann das Umschalten des Polarisationsvektors zweckmäßig beeinflusst werden. Der Zusammenhang zwischen Mikrostrukturparametern und Polarisation ist außerdem für die Berechnung der dynamischen Umschaltprozesse die Basis für eine Verbesserung von theoretischen Modellen.

1 Introduction

Ferroelectrics are arguably among the most versatile functional materials exhibiting numerous useful physical phenomena, such as piezoelectricity, pyroelectricity, switchable polarization, high permittivity, electrocaloric and electroopitic effects. These properties have made them indispensable in sensors, actuators, capacitors, and transducers, which represent enabling components for many of today's cutting-edge technologies in medicine, consumer electronics, robotics, communication, or space industries. [1; 2] Furthermore, ferroelectrics represent the backbone of emerging new fields, including high-performance sensors for the Internet of Things [3], nanoelectronics [4], renewable energy collection [5; 6], environmental-friendly electrocaloric cooling-technologies [7], nanogenerators [8], and ferroelectric-based photovoltaics [9].

From the discovery in 1921 until 1943, ferroelectricity has been an academic curiosity with little application or interest. The hydrogen bonds, which were thought to be necessarily related to the ferroelectric properties, made ferroelectric materials water soluble and fragile. The discovery of polycrystalline $BaTiO_3$ with its surprising structural simplicity, during the war years, triggered pioneering theoretical works and stimulated engineering devices. In 2017, electroceramics covered 6.0% of the total ceramic and glass industry market share by product type and piezoceramics are predicted to become the major industry within the electroceramics market by 2021. [10] Already today, the piezoelectric ceramics market is about \$1 billion per year worldwide and it enables a \$17 billion market of sensors and actuators for the health, consumer electronics, automotive, automation, military, and aerospace industries. [11]

More than 700 ferroelectric materials are known, among which perovskite oxides are technically most relevant. [12] Below the Curie temperature, ferroelectrics exhibit a spontaneous polarization, induced by a small displacement of individual ions from their centrosymmetric position. Polarization switching, *i.e.*, the reorientation of the polarization vector by an external electric field, is the main property that distinguishes ferroelectric materials from other polar materials and the mechanistic description of this process is crucial for their technical application.

In the 1960s, initial understanding of the polarization switching process was provided by seminal studies on ferroelectric single crystals [13–15], which initiated the development of theoretical models [16–19]. More recently, the interest in non-volatile memories [20; 21] has triggered intensive research into switching dynamics in ferroelectric thin films [19; 22–24]. These studies, however, cannot be directly utilized to explain the mechanism of polarization reversal of polycrystalline bulk ceramics, which are the most widely-used group of ferroelectrics [1]. The latter are characterized by a complex 3D electromechanical coupling among randomly-oriented grains, strongly influenced by the ferroelectric/ferroelastic nature of the domain walls, presence of grain boundaries, and the inhomogeneous distribution of the applied electric field.

The best evidence for this complexity is the absence of a general theoretical model for the description of the polarization dynamics of polycrystalline ferroelectric materials. Theoretical and experimental reports are inconsistent with respect to the kind and the sequence of events occurring during polarization reversal. Moreover, the influence of individual microstructral parameters, such as grain size or grain orientation, on the switching dynamics remains unclear. The objective of the present work is to discuss and clarify fundamental questions related to the polarization reversal in polycrystalline ferroelectric/ferroelastic ceramic materials. For this purpose, a model system will be investigated with respect to its electric, electromechanical, and structural dynamic response, supplemented by free energy calculations. This systematic and broad methodological approach gives deep insight into the mechanisms of the polarization reversal process. Moreover, the response of materials with different microstructures will be investigated and compared. The qualitative and quantitative description of the processes is expected to aid the development of ferroelectric applications and represents a basis for further advancement of theoretical models. The best evidence for this complexity is the absence of a general theoretical model for the description of the polarization dynamics of polycrystalline ferroelectric materials. Theoretical and experimental reports are inconsistent with respect to the kind and the sequence of events occurring during polarization reversal. Moreover, the influence of individual microstructral parameters, such as grain size or grain orientation, on the switching dynamics remains unclear. The objective of the present work is to discuss and clarify fundamental questions related to the polarization reversal in polycrystalline ferroelectric/ferroelastic ceramic materials. For this purpose, a model system will be investigated with respect to its electric, electromechanical, and structural dynamic response, supplemented by free energy calculations. This systematic and broad methodological approach gives deep insight into the mechanisms of the polarization reversal process. Moreover, the response of materials with different microstructures will be investigated

and compared. The qualitative and quantitative description of the processes is expected to aid the development of ferroelectric applications and represents a basis for further advancement of theoretical models.

2 Theoretical background

2.1 Material classifications

This section introduces the material classes of dielectrics, with a special focus on one of their subgroups, the ferroelectric materials. In this context a theoretical description of ferroelectric materials will be introduced, which allows to discuss stable states in terms of the free energy.

2.1.1 From dielectrics to ferroelectrics[1]

Dielectric materials are isolators and can be polarized with an applied voltage. The macroscopic polarization, P_i, is the sum of all dipole moments. It originates from the application of an external electric field, E_j, and is coupled by the dielectric susceptibility, χ_{ij}, according to the following equation.

$$P_i = \kappa_0 \cdot \chi_{ij} \cdot E_j \tag{2.1}$$

The permittivity of vacuum is termed κ_0=8.854·10^{-12} F/m. The polarization and dielectric displacement, D_i, are interrelated as follows:

$$D_i = \kappa_0 \cdot E_i + P_i \tag{2.2}$$

The polarization may have electronic, ionic, dipole, and space charge contributions. Fig. 2.1 highlights how the individual contributions originate due to an applied electric field. Electronic contribution refers to the displacement of the negatively charged electron shell with respect to the positively charged core. The ionic contribution is caused by the electric field driven displacement of positively charged cations against negatively charged anions. Dipolar materials, such as water, can be additionally polarized by alignment of the molecules in the electric field direction. Space charge polarization can be observed in dielectrics with inhomogeneously distributed charge carrier densities. Charge carriers are transported until they stop at a potential barrier, which can be a grain or a phase boundary.

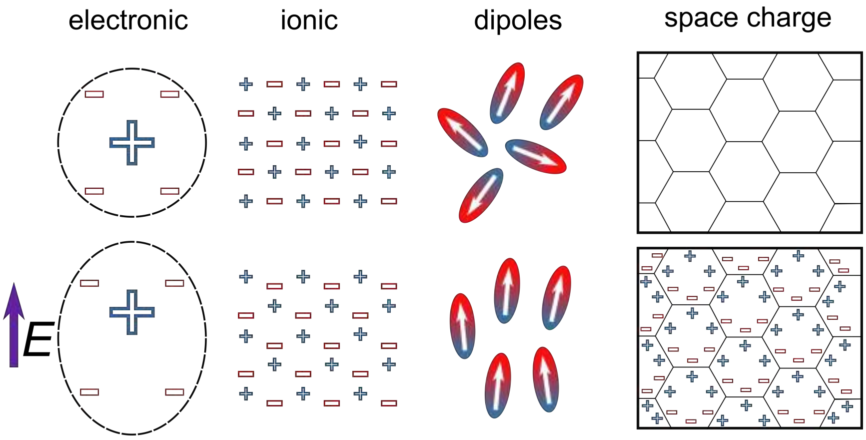

Figure 2.1.: Microscopic polarization mechanisms induced by an applied electric field [Redrawn after Ref. [25]].

Piezoelectric materials are a subgroup of dielectrics (Fig. 2.2). According to their crystallographic structure, materials can be classified into 32 crystallographic point groups (Tab. 2.1). Out of these, 21 are non-centrosymmetric, which is a necessary condition for piezoelectricity. Piezoelectricity can be observed in all 21 point groups, except in the point group 432. Piezoelectric materials are characterized by a linear coupling between electric and mechanical field. Application of a mechanical stress to a piezoelectric material results in the creation of an additional polarization. For this direct

---

[1] This section is based on the books by Waser *et al.* [25], Moulson and Herbert [26], and Setter and Colla [27].

piezoelectric effect, the dielectric displacement is coupled to the stress, σ_{jk}, via the piezoelectric tensor, d_{ijk},[1] and to the electric field via the permittivity κ_{ik}^{σ}[2]:

$$D_i = d_{ijk}^{E} \cdot \sigma_{jk} + \kappa_{ik}^{\sigma} \cdot E_k \tag{2.3}$$

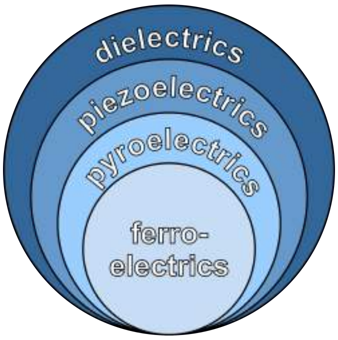

Figure 2.2.: Classification of dielectrics with their subgroups of piezoelectrics, pyroelectrics, and ferroelectrics.

For the converse piezoelectric effect, the strain, S_{ij}, is coupled to the electric field via the piezoelectric coefficient, while the first term in Eqn. 2.4 describes the coupling of stress and strain through the elastic compliance, s_{ijkl}^{E} (Hooke's law).

$$S_{ij} = s_{ijkl}^{E} \cdot \sigma_{kl} + d_{ijk}^{\sigma} \cdot E_i \tag{2.4}$$

Unlike in non-polar piezoelectric materials, which produce a polarization under stress, 10 out of the 21 point groups display a spontaneous polarization, P_S, below a characteristic temperature even without an external mechanical stress. These materials are termed pyroelectric, since the spontaneous polarization changes with temperature.

Table 2.1.: Crystallographic point groups. Overview of crystallographic point groups in short Hermann-Mauguin nomenclature [after Ref. [1]].

centrosymmetry		centrosymmetric	non-centrosymmetric	
polarity		non-polar	non-polar	polar
number of point groups		11	11	10
crystal class	cubic	m$\bar{3}$m, m$\bar{3}$	432, $\bar{4}$4m, 23	
	hexagonal	6/mmm, 6/m	622, $\bar{6}$m2, $\bar{6}$	6mm, 6
	tetragonal	4/mmm, 4/m	422, $\bar{4}$2m, $\bar{4}$	4mm, 4
	rhombohedral	$\bar{3}$m, $\bar{3}$	32	3m, 3
	orthorhombic	mmm	222	mm2
	monoclinic	2/m		2, m
	triclinic	$\bar{1}$		1

Ferroelectric materials are the last subgroup (Fig. 2.2). These are pyroelectrics that are characterized by the possibility to switch the direction of the spontaneous polarization with an applied external field. This group is described in more detail below.

---

[1] The piezoelectric tensor d_{ijk} is a third rank tensor, since the piezoelectric response is anisotropic. In general there are 27 tensor components, which reduce to 18 due to the symmetry of the stress tensor $\sigma_{jk}=\sigma_{kj}$. The piezoelectric effect can therefore be described by a 6x3 matrix: d_{ijk}. Crystal symmetry will further reduce the components in the piezoelectric tensor (Neumann's principle [28]), as discussed by Newnham [29].

[2] The superscripts indicate the quantity held constant. In the case of κ_{ik}^{σ} the stress is held constant, which means that the piezoelectric element is unconstrained, while in the case of s_{ijkl}^{E} the electric field is held constant.

2.1.2 Ferroelectric materials[1]

The history of ferroelectric materials goes back until the middle of the 16th century, when Rochelle salt was first prepared by Eli Seignette in La Rochelle, France, for medicinal purposes. At the end of the 19th century it was already known, that dielectrics are heated up when exposed to an AC electric field, which was related to the dielectric hysteresis. [33; 34] The birth of ferroelectricity is usually related to Joseph Valasek, who discovered ferroelectricity in Rochelle salt in 1921. [35] In 1946 van Hippel discovered ferroelectricity in $BaTiO_3$ (BT) [36], the prototype ferroelectric material. The following definition of ferroelectricity was suggested by Jaffe [37] in 1956:

> *"The ability of certain crystals of electrically polar structure to switch the direction of polarity under the influence of a strong electric field*[2] *between several crystallographically equivalent directions and to retain their new orientation after removal of the field."*

Ferroelectric materials need to possess at least two energetically equivalent directions of spontaneous polarization. An electric field can be applied to switch between these two directions. Many ferroelectric materials are also ferroelastic[3], which means that mechanical fields can be used to switch the spontaneous polarization.

In most practical cases, the polar structure of a ferroelectric material is a cubically distorted ABO_3 perovskite. In the following, the most prominent effects of ferroelectric materials are discussed taken the perovskite BT as a model material. The high-temperature polymorph is cubic with the large barium cation Ba^{2+} on the A-site, Ti^{4+} on the B-site, and oxygen anions O^{2-} on the centers of the faces. BT is paraelectric at temperatures beyond the transition Curie temperature $\vartheta_{Cur}=128\,°C$. Upon cooling, a phase transition from a cubic paraelectric phase to a tetragonal ferroelectric phase is observed (Fig. 2.3), which is associated with a discontinuous jump of the spontaneous polarization from zero to a finite value at the Curie temperature. The tetragonal distortion, arising from the relative displacement of B-site cations from the center of the unit cell, is associated with the creation of a spontaneous polarization. The associated strain is called the spontaneous strain.

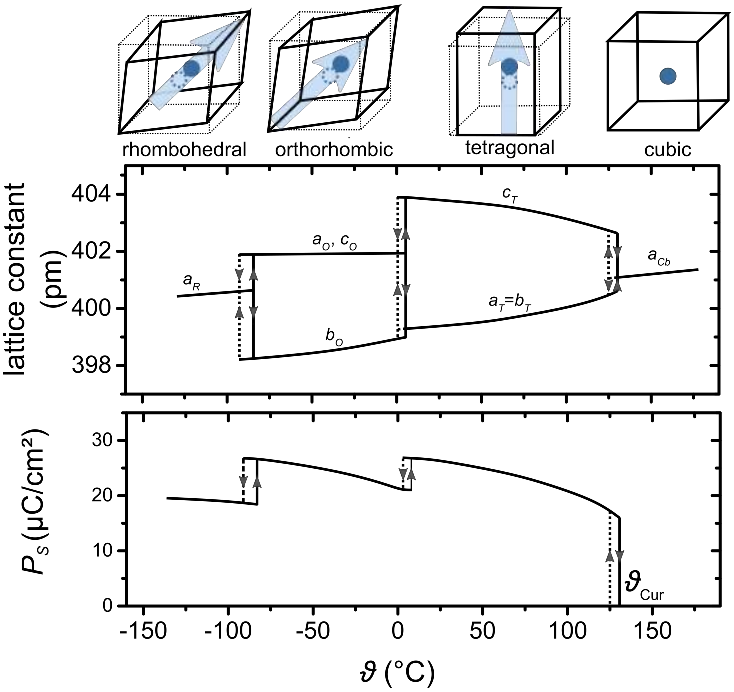

Figure 2.3.: Phase transitions in BT. Schematic evolution of unit cell, lattice parameters, *a*, *b*, and *c*, and spontaneous polarization of BT [Redrawn after Ref. [25]] for the four crystallographic structures: cubic (Cb), tetragonal (T), orthorhombic (O), and rhombohedral (R).

---

[1] This section is based on the books by Waser *et al.* [25], Lines and Glass [30], Uchino [1], and on the review articles by Haertling [31] and Damjanovic [32].

[2] The required electric field should not exceed the breakdown limit of the material. An experimental evidence of polarization reversal is required in order to term a pyroelectric material ferroelectric. [1]

[3] Aizu provides a tabulated summary stating the symmetry constraints that determine the ferroelectric/ferroelastic character of the material. [38]

A thermodynamic description of the transitions in ferroelectric materials is given by means of the Landau-Ginzburg-Devonshire theory. [39] In the framework of this phenomenological theory, an order parameter is introduced, which is homogeneous within pure phases and changes rapidly at the phase transitions. The Gibbs free energy ΔG of a single ferroelectric domain without external load or any mechanical pressure can be expressed in terms of the polarizations P_1, P_2, and P_3: [40]

$$\begin{aligned}\Delta G\left(P_1, P_2, P_3\right) = \alpha_1\left(P_1^2+P_2^2+P_3^2\right)+\alpha_{11}\left(P_1^4+P_2^4+P_3^4\right)+\alpha_{12}\left(P_1^2P_2^2+P_2^2P_3^2+P_1^2P_3^2\right)+\\ +\alpha_{111}\left(P_1^6+P_2^6+P_3^6\right)+\alpha_{112}\left[P_1^2\left(P_2^4+P_3^4\right)+P_2^2\left(P_1^4+P_3^4\right)+P_3^2\left(P_1^4+P_2^4\right)\right]+\\ +\alpha_{123}\left(P_1^2P_2^2P_3^2\right)\end{aligned} \tag{2.5}$$

where α_i, α_{ij}, and α_{ijk} are the dielectric stiffness coefficients at constant stress, also referred to as Landau coefficients. The symmetry of the energy landscape thereby matches the symmetry of the ferroelectric phase. The coefficients do not correspond to a physical property of the material and are determined by fitting of experimental data or by ab-initio calculations. The principle of minimum energy predicts a stable system polarization as a minimum in the free energy landscape. A two dimensional representation of the energy landscape for a tetragonal material is shown in Fig. 2.4. The tetragonal energy minima are directly visible along the direction of the axis of the coordinate system. Without any applied electric or mechanical field all four minima are energetically equivalent due to the symmetry of the system.

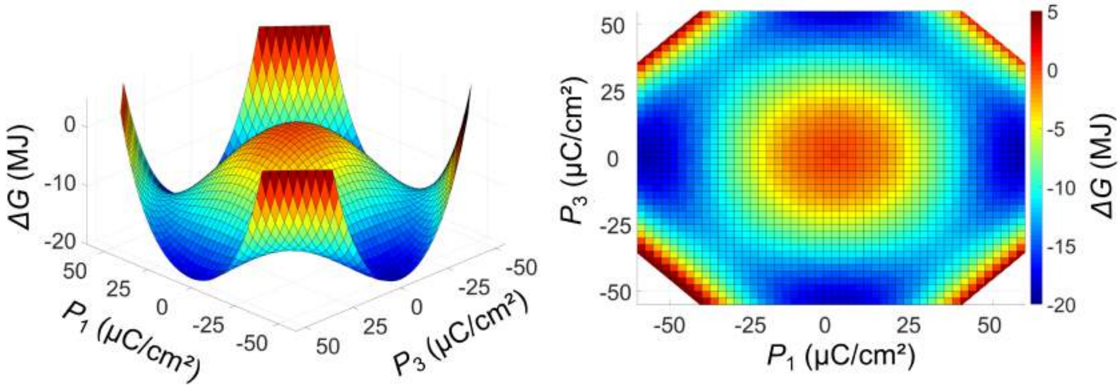

Figure 2.4.: Landau energy landscapes. Two dimensional representation of the Landau energy landscape for a tetragonal $Pb(Zr_{0.4}Ti_{0.6})O_3$ material. Dark blue color regions indicate regions of polarization orientations with a lower free energy, dark red color regions with higher free energy. Landau coefficients are taken from Ref. [41].

2.2 Domain walls

In the first part, this section discusses the formation of different types of domains in polycrystalline ferroelectric materials. In the second part, the literature about the properties of static domain walls in BT single crystals is briefly summarized, focusing on the Peierls potential of the lattice. The third part concentrates on the dynamics of domain walls. Experimental results on the interaction between electric field and domain walls are summarized, the mechanism of the movement of domain walls is explained, and the Merz equation is derived for the fundamental situation of a moving object in a random environment.

2.2.1 Formation of domains[1]

The spontaneous polarization vector in a ferroelectric material can be oriented along a family of crystallographic directions with the lowest free energy. For example, the spontaneous polarization vector of BT in the tetragonal phase will be parallel to any of the six equivalent <100> directions. Unit cells with uniform polarization direction form coherent regions, refered to as ferroelectric domains, separated by domain walls. 180° domain walls separate regions where the polarization vectors are parallel but of opposite direction, while 90° domain walls separate regions with perpendicularly-oriented polarization vectors. Both types of domains are ferroelectric (can be moved by an external electric field), while only non-180° domain walls are in addition also ferroelastic (can be moved by an external mechanical field). In general, the configuration of the domains will follow the head-to-tail configuration in order to avoid discontinuity in the polarization at the domain boundary.

---

[1] This section is based upon the review articles by Damjanovic [32] and Arlt [42].

When a ferroelectric material is cooled below its phase transition temperature, the cooperative alignment of polarization vectors in adjacent unit cells to a monodomain state is accompanied by an apparent surface charge, which gives rise to a depolarization field, E_D. These depolarization fields can be minimized by the formation of ferroelectric domains, as shown for 180° domains in Fig. 2.5a. It should be noted that other screening mechanisms, such as electrode screening, electric conduction through the material, and polarization gradients can also compensate for the depolarization field. [43]

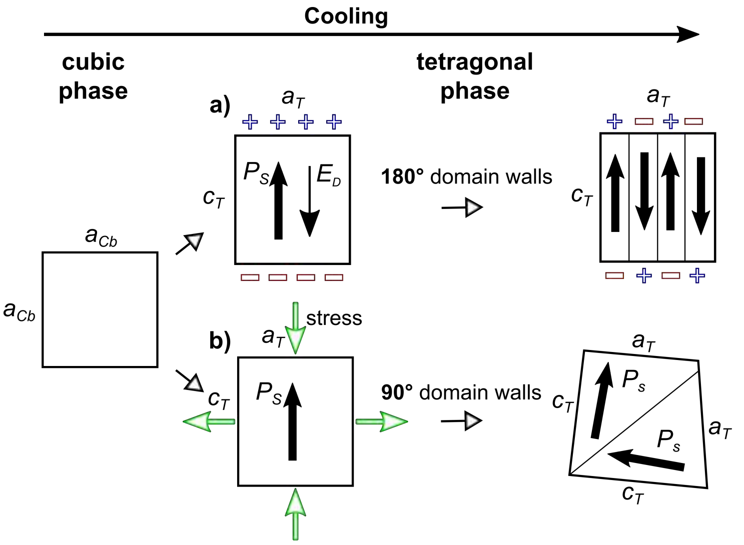

Figure 2.5.: Formation of a) 180° and b) 90° domains as a consequence of depolarization fields and internal stresses, which arise when the material is cooled below the phase transition temperature. [Redrawn after Ref. [32]].

In addition to the spontaneous polarization, also a spontaneous strain forms at the phase transition temperature in a single crystalline material upon cooling the material below its Curie temperature. The surfaces of a perfect single crystal are not constrained and the full strain can be released and the crystal remains unstrained when cooled. Cooling of a ferroelectric polycrystalline instead, results in internal mechanical stresses. These can be released by non-180° domains (Fig. 2.5b). In polycrystalline BT the mechanical stresses due to the spontaneous strain were quantified in the range of 62–78 MPa [44; 45][1] and are of a shear and longitudinal type according to the axes of the respective cubical grain. The formation of a 90° lamellar domain structure can release mechanical stresses in two dimensions, while three dimensional stresses can be released by a banded domain structure. A lamellar and a banded domain structure are schematically displayed in Fig. 2.6a and Fig. 2.6b, respectively. The type of domain structure is largely influenced by the grain size. The critical grain sizes above which the respective domain configuration can form are g_1 and g_2, as displayed Fig 2.6. The critical grain size g_2 is about 4.7 µm and 1–2 µm for BT and lead zirconate titanate (PZT), respectively. A fictional grain size of about $g_1 = 40$ nm was reported for BT, below which the grains are single domain. [42]

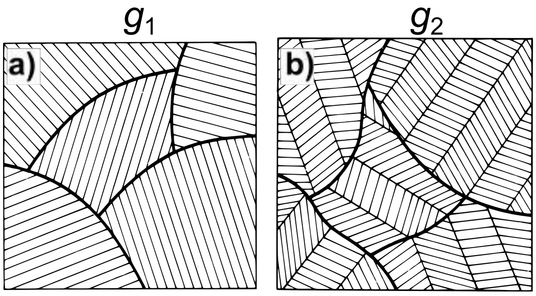

Figure 2.6.: Non-180° domain structures in polycrystalline ceramic materials. a) Lamellar twinning and b) banded domain structure in polycrystalline materials [Reprinted by permission from Springer Nature: J. Mater. Sci. [42], Copyright 1990]. The critical grain sizes above which the respective domain configuration can form are g_1 and g_2, as displayed in the figure, while $g_1 < g_2$. Grain boundaries are indicated by the solid lines.

---

[1] Even higher mechanical stresses of up to 355 MPa were reported in core-shell modified BT ceramics. [46]

2.2.2 Static domain wall properties

The thickness of a domain wall is defined as the width of a region where significant changes of the order parameter from its value deep inside the domains occur. [47] Experimental observation of the thickness of domain walls are important. For example, the interaction of a domain wall with the intrinsic lattice potential, the Peierls barrier, during its movement will depend on the thickness of the wall. The domain wall will only be influenced by the lattice potential, if the thickness of the domain wall is comparable to the lattice spacing. [48] Experimental measurements of the thickness of domain walls for multiaxial ferroelectric single crystals are however rare and strongly dependent on the experimental approach. For a 180° domain wall in BT single crystals, the measured thickness ranges from 0.05 µm [49] to 2–3 µm [50]. For a 90° domain wall in BT thicknesses in the range of 0.002–0.025 µm [51; 52] to 0.2 µm [49] were measured. More recent results displayed that the width of a 90° domain wall in BT can extend over several micrometers. [53] This effect is also described by other authors. A gradient lattice strain layer (GLSL) was found to compensate for the strain mismatch between the domain wall and the material deep inside the grain. [54; 55]

A domain wall has a higher energy compared to the domains which it separates. Considering a domain wall as a two-dimensional object, this energy is usually represented in J/m^2 and describes the surface energy density of the domain wall [47]. Well studied domain walls are the 180° and 90° domain walls in BT. All results in Tab. 2.2 assume, that domain walls have a thickness of zero and consequently their energy must be evaluated with respect to its orientation with respect to the ions in the lattice. The important finding is that the energy for a (100) 180° domain wall in a BT material is a factor of five lower, if it is centered around a Ba atom, compared to the case when it is centered around a Ti atom [56].

Table 2.2.: Domain wall energies. Domain wall energies (mJ/m^2) in BT (A and B indicate the planes passing through A and B perovskite sites; M indicates a plane passing through the ions of metals; O indicates a plane passing through the oxygen ions only. A schematic drawing of the different orientations can be found in Ref. [56]) [After Ref. [47]].

Type of domain wall	(100)-A	(100)-B	(110)-M	(110)-O	Peierls Barrier	Reference
180°	1.4 1.5 16	47.9	45.3	10.3	46	[57] [56] [58]
90°			22.5	36.4	14	[59]

Recent publications use more advanced ab-initio calculations to study the domain wall properties. In this case the energy of the system containing the wall is minimized and the energy of the wall is compared to the energy of the system. The $PbTiO_3$ system has been studied and results agree to the BT system. It has been found that A-centered 180° walls have the lowest energy among 180° domain walls. [60; 61] Meyer and Vanderbilt compared the energy of a 90° domain wall to a 180° domain wall in $PbTiO_3$ and the wall energy of a 90° domain wall has been found to be four times smaller compared to a 180° domain wall. The Peierls barrier in a defect free lattice in $PbTiO_3$ is $1.6\,mJ/m^2$ for a 90° domain wall, while it is $37\,mJ/m^2$ for a 180° domain wall, indicating that movement of the 90° domain wall will occur much more likely. [61; 62]

2.2.3 Dynamics of domain walls

Experimental observations

In their pioneering work in 1958 Miller and Savage investigated the dynamic response of 180° domain walls to an external electric field. They observed the expansion of a sidewise moving 180° domain wall in the tetragonal phase of a BT single crystal, etched down to 50 µm. The electric field was applied using liquid electrodes and the domains were made visible by partially etching the sample. [63] The velocity of the domain wall was found to increase when the electric field was applied and it saturated after moving a distance of 100 nm, as displayed in Fig. 2.7a. [64] This phenomenon was later interpreted as an interplay between the quickly moving domain wall and screening charges. [65] Fig. 2.7c displays a collection of data by various researchers [63; 66–71] on the field dependence of sidewise domain wall velocity of a 180° domain wall in BT. Two regimes are apparent in the graph. For low fields, Miller and Savage suggested an exponential relationship [63], while a power law was proposed for higher electric fields [69].

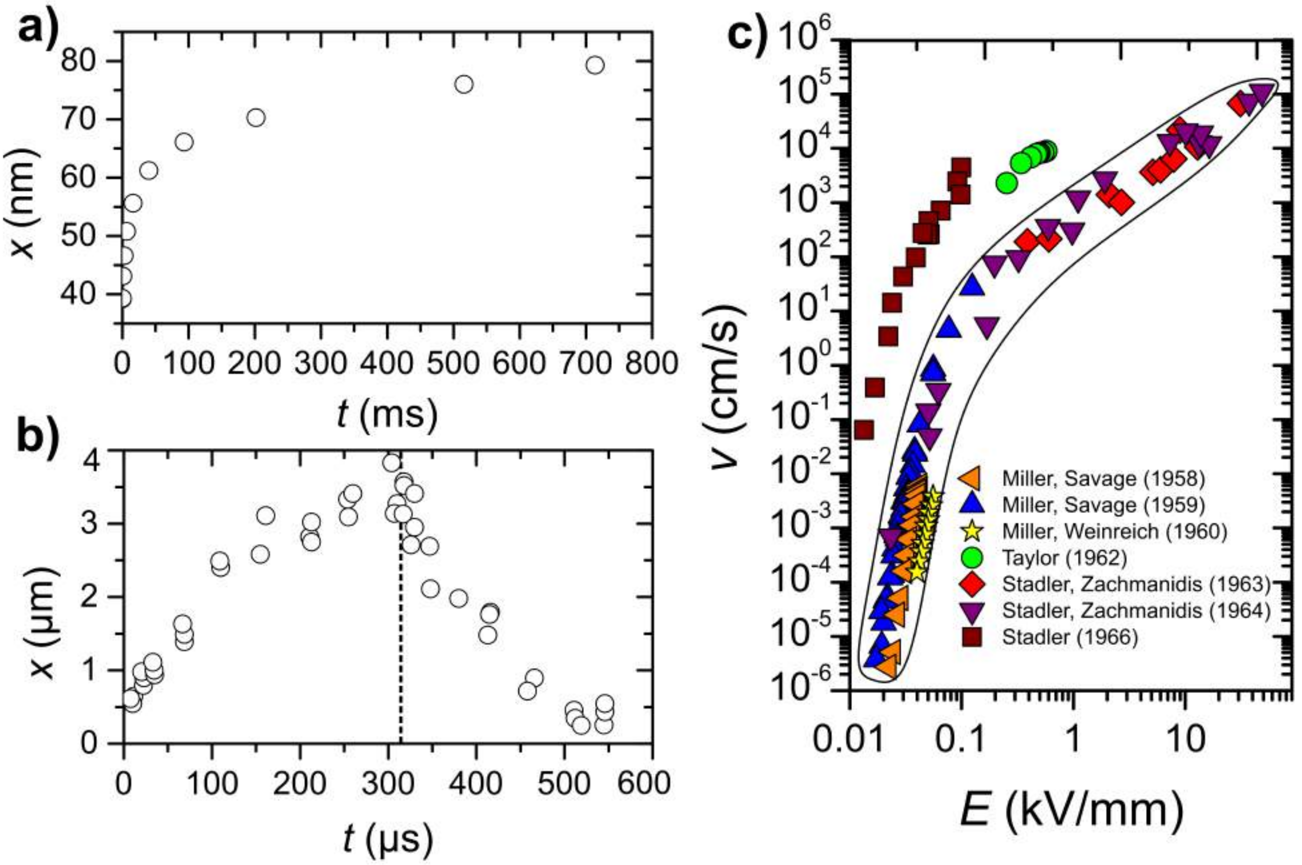

Figure 2.7.: Domain wall dynamics. Time-dependent domain wall position, *x*, for a) a 180° domain in BT [Redrawn after Ref. [64]] and b) a ferroelastic domain in Rochelle salt [Redrawn after Ref. [72]]. The dashed vertical line in b) indicates the time at which the electric field was switched off. c) Field-dependent domain wall velocity, *v*, of 180° domain walls in BT [Data taken from Ref. [63; 66–71]].

Unlike nonferroelastic domain walls, the movement of ferroelastic domain walls involves mechanical stresses which influence their dynamics. If a constant stimulus is applied to a ferroelastic domain wall, it should move with a constant velocity. [73; 74] However, in real materials the velocity decreases due to various damping effects. The velocity of a moving ferroelastic domain wall after the application of a square-like electric field was first measured in Rochelle salt. A threshold field was required in order to move the domain wall and the domain wall slowed down after departing by more than 1 μm from its original position, indicating the existence of a built-in restoring force. [75] Time-dependent domain positions are shown in Fig. 2.7b. Ferroelastic domains clearly slow down and switch back after the electric field is switched off, indicated by the vertical dashed line. [72] Similar results were observed for other materials, such as $Gd_2(MoO_4)_3$ (GMO) [65] and KH_2PO_4 [76] single crystals. In the later case, it was reported that when two ferroelastic domain walls approach each other a strong repulsive interaction takes place.

Mechanism of domain wall motion

By definition, a domain wall is moving if an interplay of thermal fluctuations and external fields helps to overcome the potential barrier on its way. In a defect free ferroelectric material the depth of the potential barrier is defined by the Peierls potential of the lattice. The domain wall may either jump over the Peierls barrier as a whole or, alternatively, move forward by jumps of small pieces of the wall. In 1960 Miller and Weinreich suggested that a 180° domain wall does not move sidewise in a continuous manner. Instead, the sidewise motion occurs by a continuous nucleation and growth of domains at the domain wall. These have a triangular shape with a large aspect ratio, expanding laterally on the same atomic plane [77], as schematically depicted in Fig. 2.8a. A very similar picture was already suggested before by Drougard [78] and Abe [79].

On the one hand the suggested mechanism reduces the Peierls energy that has to be overcome. On the other hand the entire energy of the wall gets increased, because the total area of the wall increases. This interplay is reflected by a strong electric field dependency. While for low fields the layers grow virtually flat, for high fields the nuclei pile up on the surface of the domain wall and the surface of the moving wall appears rough. [80] The latter situation is displayed in Fig. 2.8b.

The suggested geometry from the original Miller and Weinreich model leads to unrealistically large nucleation energies and depolarization fields. [81] Burtsev and Chervonobrodov optimized the model by considering an oval shape of nuclei instead of a triangular one, which decreases the value of the activation field by two orders of magnitude. [62] Recently, square nuclei with a diffuse interface were suggested based on atomistic Monte Carlo simulations. [82] Experimentally, these steps were observed on (110) planes in a $Pb(Zr_{0.2}Ti_{0.8})O_3$ thin film using negative sperical-aberration imaging technique in transmission electron microscopy (TEM). [83] Computation results give insight to the atomic nature of the defects. It was found that the transition from one plane to the next plane occurs gradually and a large polarization rotation was found around the steps. [84]

In contrast to ferroelectric domains, it was claimed that ferroelastic domain walls are not influenced by the Peierls potential. [74] Instead the pinning of the ferroelastic domain wall occurs mostly by extrinsic defects. [48] A single domain wall in $LaAlO_3$, exposed to a small external stress, was found to move by a superposition of a smooth front and a stop-and-go propagation of the needle tip, sometimes classified as an avalanche. This type of movement was related to the pinning/depinning of the domain wall by defects: when a defect is hit, the field strength increases and the pinned wall ruptures and progresses further. [85; 86] In time-resolved experiments, these events can be observed as discrete jumps. The dynamics of ferroelastic domains is strongly temperature-dependent with the Vogel-Fulcher temperate (ϑ_{VF}) as a transition temperature (Fig. 2.8c and d). At higher temperatures jerky domain wall movement occurs by horizontal and vertical needle domains, while at very low temperatures, the lateral movement of the ferroelastic domain wall is operated by kinks that propagate along the twin wall. [87] It was recently shown that these kinks inside the wall are highly mobile and can travel with the speed of sound. [88]

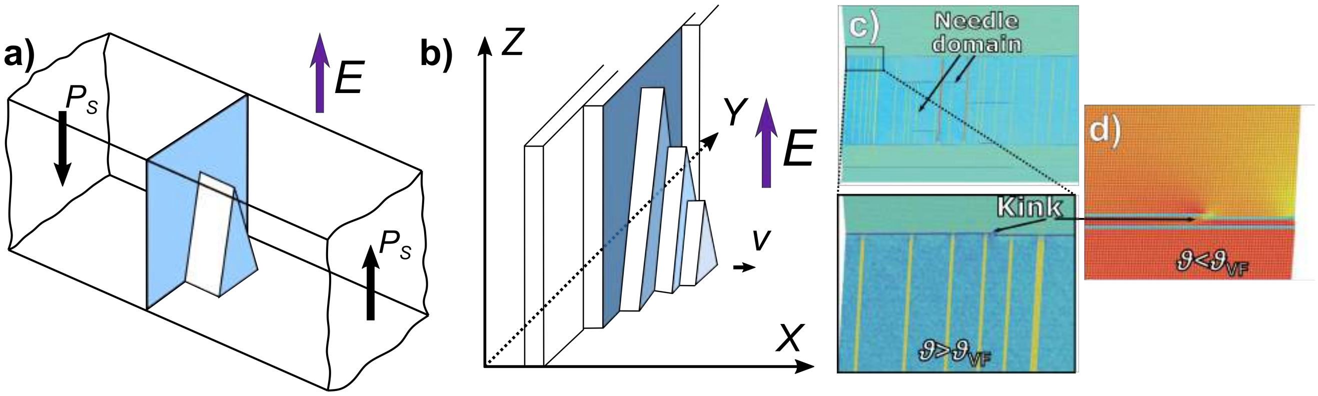

Figure 2.8.: Mechanisms of domain wall motion. a) Schematic drawing of a triangular step on a 180° domain wall, following the model of Miller and Weinreich [Redrawn after Ref [77]]. The nucleation occurs at the bottom face, which represents the electrode. b) Schematic drawing of nucleation and expansion of nucleation-controlled domain wall motion. A 180° domain wall moves in X-direction. The polarization and applied field are parallel to the Z direction. The nucleation of the reverse domain takes place at the XY-plane [Redrawn after Ref. [80]]. c) and d) Influence of temperature on the dynamics of ferroelastic domain walls, revealed by simulations of a model ferroelastic material. c) Needle domains and kinks can be observed above ϑ_{VF}, while needle domains are absent below ϑ_{VF}, displayed in d) [Reprinted with permission from [87]. Copyright (2011) by the American Physical Society].

Creep theory[1]

The motion of a domain wall can be described by the dynamics of an elastic object in a random environment with pinning centers, induced by an external electric field, as schematically displayed in Fig. 2.9a. The pinning potential with a barrier height U, shown in Fig. 2.9b, is thereby a superposition of the intrinsic Peierls potential and the extrinsic contribution due to defects.

---

[1] This section is based upon the book by Tagantsev *et al.* [47] and the review articles by Chave *et al.* [89] and Pramanick *et al.* [90].

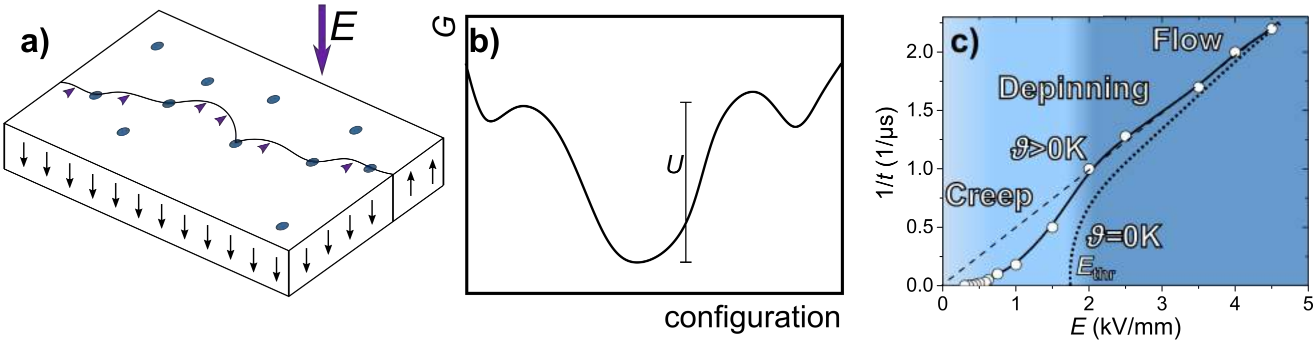

Figure 2.9.: Creep theory of domain wall movement. a) Domain wall bowing between pinning centers (displayed as blue dots) during the application of an electric field. b) Energy landscape with many metastable states in the valleys with barriers U between them [Redrawn after Ref. [89]]. c) Typical dependence of the velocity (expressed as $1/t$) of a moving elastic wall on the applied electric field without (ϑ=0 K, dotted line) and with temperature activation (ϑ>0 K, solid line) exhibiting creep, depinning, and flow scenario [Redrawn after Ref [89]]. The points represent the inverse switching times in a $C_6H_{17}N_3O_{10}S$ (TGS) single crystal measured at room temperature [data points were taken from Fatuzzo and Merz [91]].

A general relationship between the external driving field and the velocity of a domain wall is shown in Fig. 2.9c. Depending on the temperature, three characteristic scenarios can be distinguished: creep, depinning and flow. The electric field-dependent domain wall velocity of a TGS single crystal, measured at room temperature [91], is plotted for comparison in Fig. 2.9c and follows the theoretical prediction, displayed as a solid line. More recent measurements of field and temperature-dependent domain wall velocities of PZT thin films can be found elsewhere [92].

If thermal activation is absent ($\vartheta = 0\,\mathrm{K}$), a domain wall does not necessarily move under the action of a driving force, resulting in the existence of a threshold field, E_{thr}. For an applied field larger than the threshold field, $E > E_{\mathrm{thr}}$, depinning occurs and the domain wall moves with a small velocity

$$v = k_1 \cdot (E - E_{\mathrm{thr}})^{\beta}\,. \tag{2.6}$$

Here, β is the depinning exponent and k_1 is a proportionality constant. At finite temperatures ($\vartheta > 0\,\mathrm{K}$) the motion is governed by periodic and disordered pinning potentials (Fig. 2.9b). The velocity

$$v\,(E) = k_2 \cdot \exp\left[-\frac{U}{k_B \vartheta}\left(\frac{E_c}{E}\right)^{\mu}\right] \tag{2.7}$$

depends on the competition between the pinning potential and the surface energy of the wall (creep scenario). The latter thereby tends to keep the wall flat, while the former prevents sliding of the wall under external excitation. The exponent in Eqn. 2.7 is

$$\mu = \frac{\Delta - 2 + 2\xi_{\mathrm{eq}}}{2 - \xi_{\mathrm{eq}}}, \tag{2.8}$$

where ξ_{eq} is the roughening exponent of the domain wall with a dimensionality Δ. U is a characteristic energy barrier, E_c is the coercive field, k_2 is a proportionality constant, and k_B is the Boltzmann constant. The value of μ represents the nature of the pinning potential in the material.

Disorder, such as defects or vacancies, can modify the periodical pinning potential and the exponent μ offers an experimental access to the underlying physical mechanisms. A short range pinning potential (random bond) modifies the depth of the ferroelectric potential and one- and two-dimensional domains should have a value of μ=0.25 and μ=0.5–0.6, respectively. A long range pinning potential (random field) breaks the symmetry of the potential and a dynamic exponent of 1 always holds, independently of the dimensionality of the domains [93].

The exponent μ is poorly studied in ferroelectric materials and experimental information on the movement of 180° domain walls were obtained exclusively by piezoresponse force microscopy (PFM). Several researchers reported a value of the critical exponent close to 1 [81; 92; 94] for the dynamics of the domain walls in a PZT thin film, indicating that the ferroelectric domains move in a weak-pinning regime with random field defects. In a $\mathrm{Pb(Zr_{0.2}Ti_{0.8})O_3}$ thin film the dynamic exponent was found to be 0.26, the roughening exponent of the domain wall was 0.26 and the effective domain wall dimensionality was 2.5 [95]. In an epitaxial BT thin film a μ value of 0.5 was reported. [96] In this set of experiments it was assumed that the wall moves in the weak-pinning regime with random bond defects. Interestingly, a decrease of μ has been reported when artificial defects were introduced into the material. [93] While nominally defect-free systems show μ values of 0.62–0.69, the values were reduced to 0.38–0.50 after introduction of defects.

In this context, the Merz [13] equation, which can be applied for the region of relatively low fields and high temperatures [97], describes the movement of a ferroelectric domain wall in a random field potential. It is obtained by reformulating Eqn. 2.7, considering a dynamic exponent μ=1 and $E_a = \frac{UE_c}{k_B\vartheta}$. Eqn. 2.9 relates the velocity of a domain wall to the electric field by an exponential equation, where v_0 is the domain wall velocity for an infinite field and E_a is the activation field. It should be noted, that activation fields found in this model are orders of magnitude greater than experimental observations [81], which is related to implausibly large nuclei of switched domains [98].

$$v\left(E\right) = v_0 \exp\left[-\left(E_a/E\right)\right] \tag{2.9}$$

2.3 Mechanisms of polarization reversal[1]

The polarization vector in ferroelectric ceramic materials can be reoriented by an external electric field, a process which is called ferroelectric switching. This is usually achieved by the movement of domain walls, macroscopically changing the polarization and the dimension of the sample (strain). Field-dependent macroscopic measurements of these parameters give the polarization and strain hysteresis loops, schematically displayed in Fig. 2.10. These loops are often considered as the "fingerprint" of a ferroelctric material.

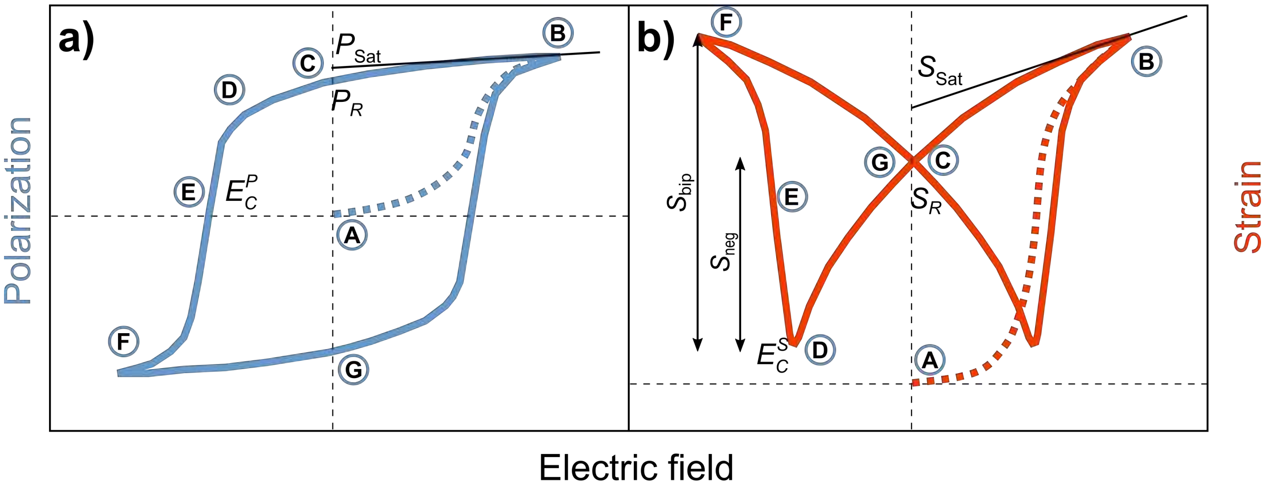

Figure 2.10.: Polarization and strain hysteresis loops. Schematic field-dependent a) polarization and b) strain of a ferroelectric polycrystalline ceramic material. The dashed lines represent the curves from the virgin state measurements. All terms are explained in the text.

In the virgin state (A), the domains' polarization directions are statistically distributed, thus the macroscopic polarization is zero. When an electric field is applied, polarization and strain slightly increase, which is related to intrinsic material responses, such as dielectric and electronic polarization contributions. At higher fields this is accompanied by the reorientation of the domain walls until a saturated state is reached (B). Here, domain wall reorientation is completed and further increase of polarization and strain is related to intrinsic material responses. The saturation polarization and strain (P_{Sat} and S_{Sat}) can be obtained by linear extrapolation to zero field, as highlighted by the black solid lines. These values represent an ideal material state in which all domain polarization directions remain aligned in the electric field direction after turning it off. In reality, a certain amount of domains will switch back, when the field is decreased to zero (C) and a stable remanent state (P_r, S_r) is established. To reverse the polarization an electric field $E > E_C$ is required,[2] where E_C is

---

[1] This section is based on the book by Waser *et al.* [25].

[2] The intrinsic (thermodynamic) coercive field corresponds to a field strength, at which the polarization is switched completely without the movement of domain walls [99], as predicted by the Landau-Ginzburg-Devonshire mean-field theory [39]. The electric field E_C required to reverse polarization in practice, however, is several orders of magnitude lower than the theoretical value, due to domain nucleation and growth.

the coercive field.[1] It should be noted that the coercive field can either be determined from the minimum of the strain curve (E_C^S, (D) in Fig. 2.10b) or zero polarization (E_C^P, (E) in Fig. 2.10a). The former is usually related to the electric field, at which the switching process starts, while the latter is correlated to the field at which domain wall movement is maximized [1]. At high electric fields, after the reversal process is completed, the polarization increases again linearly (F). Turning off the electric field returns the material in the remanent state, now with opposite polarization direction (G). The difference in strain between (G) and (D) is defined as the negative strain, S_{neg}, while the difference between (D) and (F) is called bipolar strain, S_{bip}.

2.3.1 Switching mechanisms in single crystals

In order to describe the mechanisms of the polarization reversal process, early research focused on the optical and transient current investigation of ferroelectric single crystals.[2] Based on optical microscopy and electric pulse experiments, the switching process in 50 µm thin BT single crystals [13; 102] was described by the following sequence (Fig. 2.11): nucleation of new domains, growth of those domains through the crystal, sidewise expansion, and domain coalescence until the reversal of the entire polarization. Two examples, where complete polarization reversal occured by the nucleation of a single domain followed by sidewise motion of the 180° domain wall across the entire crystal, were reported for BT [103] and GMO [104]. More recently, the domain reversal process in $Sr_{0.61}Ba_{0.39}Nb_2O_6$ was visualized using 3D Čerenkov-type second-harmonic generation. [105]

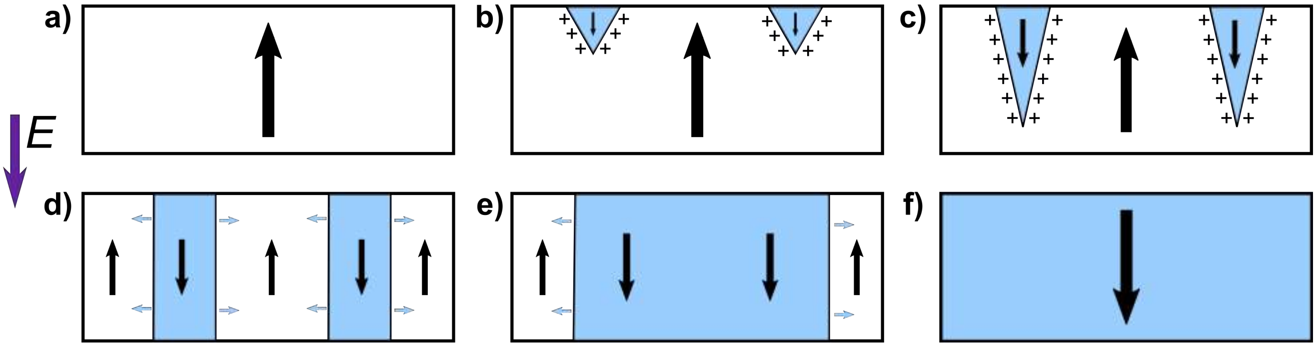

Figure 2.11.: The process of polarization reversal in a monodomain single crystal: a) monodomain state with polarization oriented upwards, b) nucleation of new domains, c) forward growth of nuclei, d) sideways growth, e) coalescence of domains, and f) the final monodomain state with polarization oriented downwards [Redrawn after Ref. [106]].

While this phenomenological description holds for an uniaxial single crystal, where other processes than 180° are forbidden, single crystals of multiaxial ferroelectrics exhibit a more complex switching behavior. For example, Pan *et al.* characterized BT single crystals by field-induced strain loops and found that some switching occurred by 90° domain wall movement [107]. Jiang *et al.* reported similiar behavior using optical microscopy on a BT single crystal (Fig. 2.12a). Starting from a monodomain state, (a^+ domain), they found an intermediate step (b^+ domain) with a polarization vector perpendicular to the applied electric field, before the final monodomain state was achieved (a^- domain). [108] Yin *et al.* investigated polarization reversal in a $0.955\,Pb(Zn_{1/3}Nb_{2/3})O_3-0.045\,PbTiO_3$ (PZN-PT) single crystal by attenuation-field curves using acoustic measurements. Since the ultrasonic velocity is a function of the anisotropic elastic stiffness, the reorientation of the domains can be illustrated using this method. Two peaks were found in the attenuation versus electric field response (indicated by the blue arrows in Fig. 2.12b). This demonstrates that switching occurs by 0°→ 71°→ 180° rather than 0°→ 180°. [109; 110] This observation was later confirmed by Zhu and Cross by simultaneous polarization and longitudinal and transverse strain measurements [111], by Zhang *et al.* using TEM, [112] and by neutron diffraction studies by Daniels *et al.* [113].

Li and Li recently suggested an approach to close the gap between early and recent experimental results on the switching mechanism of multiaxial ferroelectric single crystals. [114] Using polarized light microscopy, they compared the switching behavior of a perfectly poled BT specimen to that of a specimen, which was previously partially depolarized by mechanical stresses. While the former switched by a 180° process involving nucleation and growth, as shown in Fig. 2.11, the latter

---

[1] Time-dependent measurements have shown that also an electric field half of E_C can reorient the polarization vector, if it is applied for a sufficiently long time [100].

[2] Early research on the polarization reversal in single crystals is summarized in the books of Fatuzzo and Merz [101], Lines and Glass [30], and in a book section by Shur [65].

switched by two successive non-180° processes. The influence of the switching process on the shape of the polarization loop is depicted in Fig. 2.12c for the two scenarios: while the 180° switching process results in a step-like polarization behavior, the non-180° process results in a slanted polarization loop. This demonstrates the important role of the initial domain pattern: in the case of partial mechanical depoling, some a-a domain patterns were generated, while the perfectly in-plane poled BT single crystal exhibits a monodomain state.

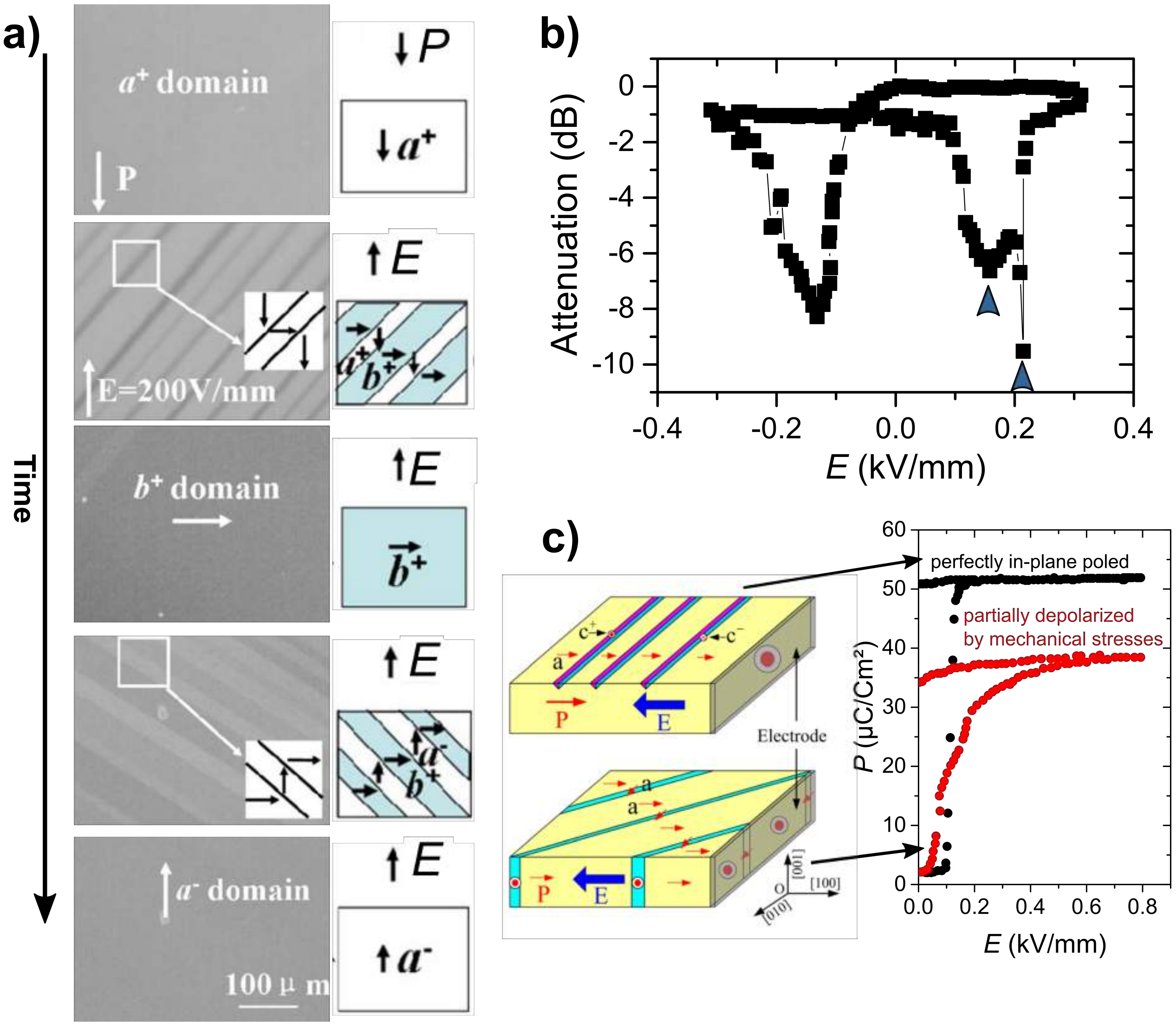

Figure 2.12.: Recent experimental results for the switching behavior in single crystalline multiaxial ferroelectrics. a) *In situ* optical observations on a BT single crystal investigated by polarized light microscopy, indicating polarization reversal by two successive 90° switching steps [Reprinted from [108], with the permission of AIP Publishing]. b) Ultrasonic attenuation showing polarization reversal in a PZN-PT single crystal. The two peaks in the positive field range marked by the arrows indicate switching over non-180°steps. [109] c) Comparison of the switching behavior of a perfectly in-plane poled BT single crystal to a single crystal, which was previously partially depolarized by mechanical stresses [Reprinted from [114], with the permission of AIP Publishing].

2.3.2 Switching mechanisms in polycrystals

As compared to the model laboratory experiments described above, the switching behavior of polycrystalline ferroelectric materials is more complex, related to their complicated multidomain states and to grain interactions.[1] These strongly

---

[1] This accounts for bulk polycrystalline ceramic materials, as well as for thin films. The switching behavior in polycrystalline thin films, however, is even more complicated, due to the mechanical boundary conditions introduced by the substrate. This will not be further discussed in this work.

influence the switching mechanisms, requiring a discussion of the different domain reorientation processes involved.

Switching mechanisms

Pioneering measurements by Berlincourt and Kruger in 1959 on domain processes in PZT and BT polycrystalline ceramics suggested that non-180° domain processes contribute to the reversal of polarization in polycrystalline ferroelectric materials [115], which is in agreement to later measurements by Uchida *et al.* [116; 117] and Tsurumi *et al.* [118]. In contrary to single crystals, the effect of internal stresses in polycrystalline ceramic materials largely determines the polarization reversal process. [119] Therefore, many authors find two successive 90° processes (in general non-180° processes) in order to achieve an overall 180° polarization reversal. Li *et al.* performed *in situ* X-ray diffraction (XRD) measurements on a polycrystalline PZT ceramic, which was located at the morphotropic phase boundary. They observed that polarization reversal occurs by two successive 90° domain reorientation processes instead of a 180° domain reversal process. [120] Jing *et al.* investigated switching in individual grains of a 100 nm thick polycrystalline tetragonal PZT thin films by 3D-PFM. They found that almost half of the domains switched by 90° and some 180° reversal clearly went through two successive 90° switching steps. [121] Hsieh *et al.* performed PFM investigations on a substrate-free polycrystalline PMN-PT film (Fig. 2.13a) indicating that polarization first switched in-plane by a 90° reversal step, followed by a second 90° reversal step to switch to the opposite polarization direction at a higher applied field. [122] Switching current measurements during polarization reversal of a polycrystalline tetragonal PZT ceramic (the two arrows in Fig. 2.13b represent the successive non-180° switching events) confirm this finding. [123] Daniels *et al.* recently determined the time constants for the individual non-180° switching steps by dynamic time-resolved *in situ* diffraction experiments of a commercial tetragonal PZT ceramic (Fig. 2.13c). They found a rapid first non-180° reversal step with a time constant $\tau_{\rightarrow}$, which is much lower than the second time constant $\tau_{\uparrow}$. The difference was related to a residual tensile strain in the ceramic after poling, acting as an auxiliary force for polarization reversal. [124]

Contrary to the findings described above, recent diffraction measurements by Fancher *et al.* quantified the contribution of 180° domain wall movement to the measured macroscopic polarization to more than 80% for BT and PZT. [125] Measurement data for a PZT sample are displayed in Fig. 2.13d. The black solid line indicates the measured polarization, while the blue dots highlight the contributions from 180° switching events. Similar results were obtained by Gorfman *et al.* for a $BaTiO_3$-$Bi(Zn_{0.5}Ti_{0.5})O_3$. [126] They applied a resonant XRD method, which allows to observe 180° domain reorientation processes. They concluded that polarization reversal occurs by 180° domain reversal or, if non-180° processes are involved, those are faster than 2 μs, which was the time resolution of the experimental setup. On the other hand, other experiments completely excluded the contributions from non-180° switching events. For example, investigations using 3D-PFM in a polycrystalline $PbTiO_3$ thin films indicated that switching exclusively occurs by 180° reversal processes. [127]

Arlt suggested an alternative polarization reversal mechanism, which does not require two successive 90° processes to reorient the polarization by 180°. [18; 128][1] A new transient 90° domain wall (blue line in Fig. 2.13e) is generated in each grain with a lamellar 90° domain structure. This new wall is highly mobile, because it is macroscopically not ferroelastic and no elastic forces hinder its motion. By this mechanism switching is considered locally as a 90° process, although for the whole grain it appears as a 180° process, inverting the polarization of the grain. Experimentally this mechanism was never systematically investigated and confirmed. Some evidence was given by Keve and Bye who observed individual 90° domain switching events, reversing the polarization of the grain in a polycrystalline ceramic material by 180°. [129]

Only a few studies tried to combine complementary measurements of respective physical parameters in order to account for ferroelectric 180° and ferroelectric/ferroelastic non-180° events simultaneously. Based on field-depended XRD peak intensities, coupling coefficient, and normalized polarization, Yamada *et al.* suggested a sequence of switching steps for a tetragonal PZT polycrystalline material. In this sequence, 90° reorientation occurred at $E = 1.0$ kV/mm and $E = 3.0$ kV/mm, while 180° switching events appeared at $E = 2.0$ kV/mm. [130; 131]

In a series of publications, Krüger, Gerthsen, and Schmidt investigated the polarization reversal process utilizing simultaneous polarization and strain measurements in polycrystalline PZT ceramics. [132–134] Starting from the remanent state, they found that the strain markedly decreased when an electric field was applied anti parallel to the poling direction, while the polarization did not change significantly. However, no complete sequence of the switching process could be revealed in this work. It was suggested that the switching process in polycrystalline ceramics is different to the switching

---

[1] Being discovered in 1996, this idea was not followed in the following years. Interestingly, a recent publication by Scott *et al.* [24] suggested a similar switching mechanism for thin films. They find that in many ferroelectric-ferroelastic materials, "superdomains" will form in which the strain and polarization average to zero over mesoscopic distances to minimize the depolarization and strain energies. They claim that these superdomains switch as a block, resulting in a hysteresis loop with a large step. Unfortunately no experimental proof was provided.

process in a single crystal, because in the former small misaligned nuclei are already present and no energy for nucleation is required. They demonstrated that these nuclei are of non-180° type, because they can be grown by either electric or mechanical fields.

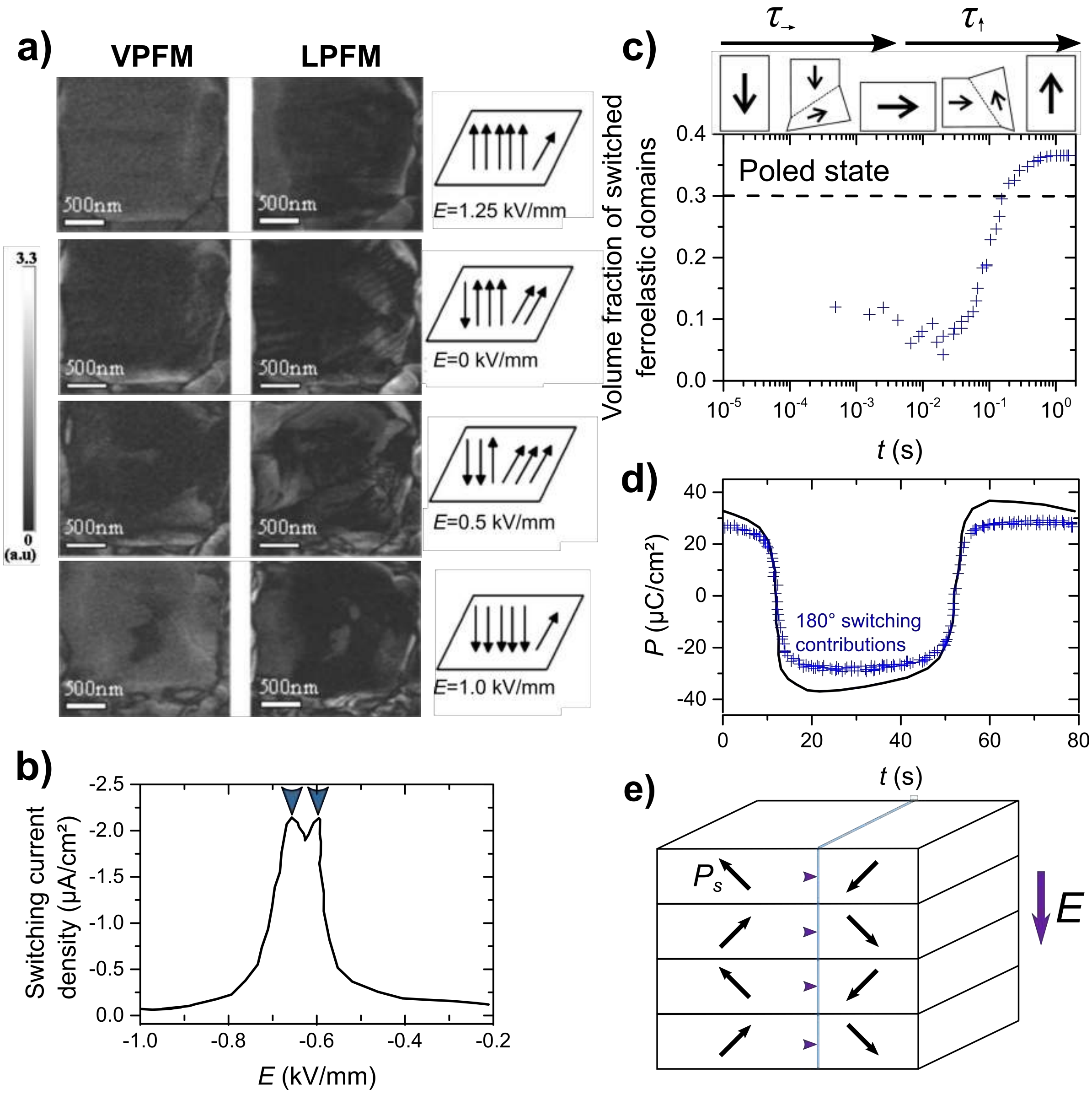

Figure 2.13.: Experimental results on polarization reversal in polycrystalline ceramic materials. a) Vertical PFM (VPFM) and lateral PFM (LPFM) of the same region at different applied electric fields in a polycrystalline PMN-PT thin film. The domain switching sequence is shown schematically [Reprinted from [122], with the permission of AIP Publishing]. b) Switching current density during polarization reversal for a polycrystalline PZT sample indicating two sequential non-180° switching events, as shown by the arrows [After Ref. [123]]. c) Volume fraction of switched ferroelastic domains as a function of time in a polycrystalline PZT material with a schematic domain switching sequence [After Ref. [124]]. d) Comparison of the measured macroscopic polarization (solid line) and polarization contribution from 180° switching events (blue dots). Data measured on PZT [After Ref. [125]]. e) Scheme of a transient non-180° domain wall moving in a lamellar twinned domain structure under an applied electric field. The polarization of the grain is reversed by 180°, while local switching occurs by 90° [Redrawn after Ref. [128]].

Electric and mechanical grain interactions

The interactions between grains in a polycrystalline ceramic body are of both electric and mechanical nature. Electric interactions occur by depolarization fields, when a region within a material reverses its polarization. If unscreened, the depolarization field acts as an additional barrier to nucleation, which tends to backswitch the nucleated region. In single crystalline model systems with a monodomain state, individual regions cannot be screened because of the nonconducting nature of the material. Calculations suggest that isolated nuclei generate an insurmountable energy barrier, making independent nucleation very unlikely. [135] In single crystalline materials this barrier can be overcome if switching events occur highly correlated with long spatial correlation lengths [136], if switching happens next to defects stabilizing the nuclei [137], or if the nuclei are stabilized by thermal activation [138; 139].

Theoretical calculations in polycrystalline materials suggest independent region-by-region switching with very short correlation lengths [140], based on the assumption that non-mobile local bound charges are randomly distributed over the grain boundaries, which change in time in order to screen the depolarization field [141; 142]. In contrast, Arlt *et al.* suggested that internal electric fields in one grain support switching in the neighboring grains. [143–146] Micromechanical modelling, which includes multigrain analysis, also indicate electromechanical interactions between grains during the polarization reversal process. [147; 148]

Experimental evidence indeed supports the predictions that grains in polycrystalline materials are correlated electrically. Domains in one grain of a polycrystalline ferroelectric material may continue in the adjacent grain over the grain boundary, experimentally observed in various materials, such as BT [149; 150] and PZT [151–153] polycrystalline bulk ceramics and thin films (Fig. 2.14a and b). For a set of grain misorientations, possible grain boundary planes, which allow domain matching, were identified recently. [154] An interesting result is that although the grain orientation in a material is random, the grain boundaries are not random and experimental data proove that the $\Sigma 3$ orientation relationship[1] is preferred over other relationships in BT, PZT, and $SrTiO_3$ polycrystalline ceramics. [156] One of the grain boundaries that allows domain continuity is the {111} boundary, which shows {110} plane matching [157; 158] and allows domain continuity [154].

Independent of the feature of the grain boundary to allow domain continuity, the domain structure in adjacent grains in polycrystalline materials is found to be mechanically correlated. Ivry *et al.* found a correlation length, which is larger than the grain size [159], indicating that the domains in neighboring grains influence each other both electrically and mechanically [160]. The domain structure in PZT ceramics in one grain was strongly influenced by the domain structure in the neighboring grain upon electric poling, indicating that polarization reversal involves both intergranular and transgranular cooperation. [161] A combined PFM and electron backscatter diffraction (EBSD) study suggested interaction between grains with different crystallographic orientations, which will enhance or suppress the switching behavior [162], due to a spatial coupling of mechanical fields [163]. Tip-induced switching in PFM in one grain leads to grain deformation, which promotes switching of adjacent grains. [164] Ferroelastic switching in a part of a grain was found to trigger switching in the adjacent part. [165] The motion of a domain wall with an external electric field in a single grain forces a mechanical pressure on a domain wall in the same grain due to the elastic deformation, hence increases the probability of their simultaneous displacement. [166] Localized Rayleigh measurements indicate collective domain wall dynamic behavior in regions spanning over several grain boundaries with correlation lengths of several microns. [167] PFM studies suggest that stress concentrations are maximized at grain corners and boundaries, which enhances or suppresses switching locally due to favored nucleation and domain pinning at the grain boundary, respectively. [162] This was confirmed by phase field simulations (Fig. 2.14c). Switching in one grain promotes the nucleation of new domains in the neighboring grains. [138; 168; 169] For highly misaligned grains, it was found that grain boundaries can promote 90° switching in neighboring grains due to stress concentrations induced by ferroelastic domain wall movement. [170]

Internal residual stresses, originating from mechanical grain-to-grain interaction, were quantified by Hall *et al.* using the method of Eshelby. [171] The Eshelby inclusion problem for switching in polycrystalline ceramic materials is presented in Fig. 2.14d–f. The lattice strains accommodate the electric-field-induced movement of non-180° domain walls. [172] The shape change of a non-constrained grain under the application of an electric field can be described with an Eshelby transformation strain tensor, $\varepsilon^{\mathrm{Trs}}$. The deformation process is schematically displayed for a stack of 90° domains in a grain of a ceramic with a tetragonal crystal structure. During the application of an electric field, the dimensions of the grains increase in direction 3 and decrease in directions 1 and 2 (Fig. 2.14e). This results in a misfit between the unstrained

---

[1] 5 parameters are required to macroscopically characterize the boundary between two grains, which is usually represented as *[axis](grain boundary plane)angle*. The Σ notation describes the grain boundary in the concept of the coincidence site lattice (CSL). In this context, the quantity Σ (always integer and odd) defines the ratio between the volume of the standard unit cell and the volume enclosed by a unit cell of the coincidence sites of the two lattices. Thereby a smaller value of Σ describes a highly ordered grain boundary. For example, in a $\Sigma 1$ small angle grain boundary nearly all lattice points are part of the CSL. [155]

matrix and the strained grain. If this deformation occurs constrained, the matrix and the grain will deform simultaneously (Fig. 2.14f). According to Eshelby, the constrained strain ε^{Cst} for an equivalent homogeneous inclusion can be calculated by $\varepsilon^{Cst}=\Gamma\varepsilon^{Trs}$, where Γ is the Eshelby tensor. [173] The constraint of the matrix induces a strain of ε^{Cst}-ε^{Trs} inside the grain.

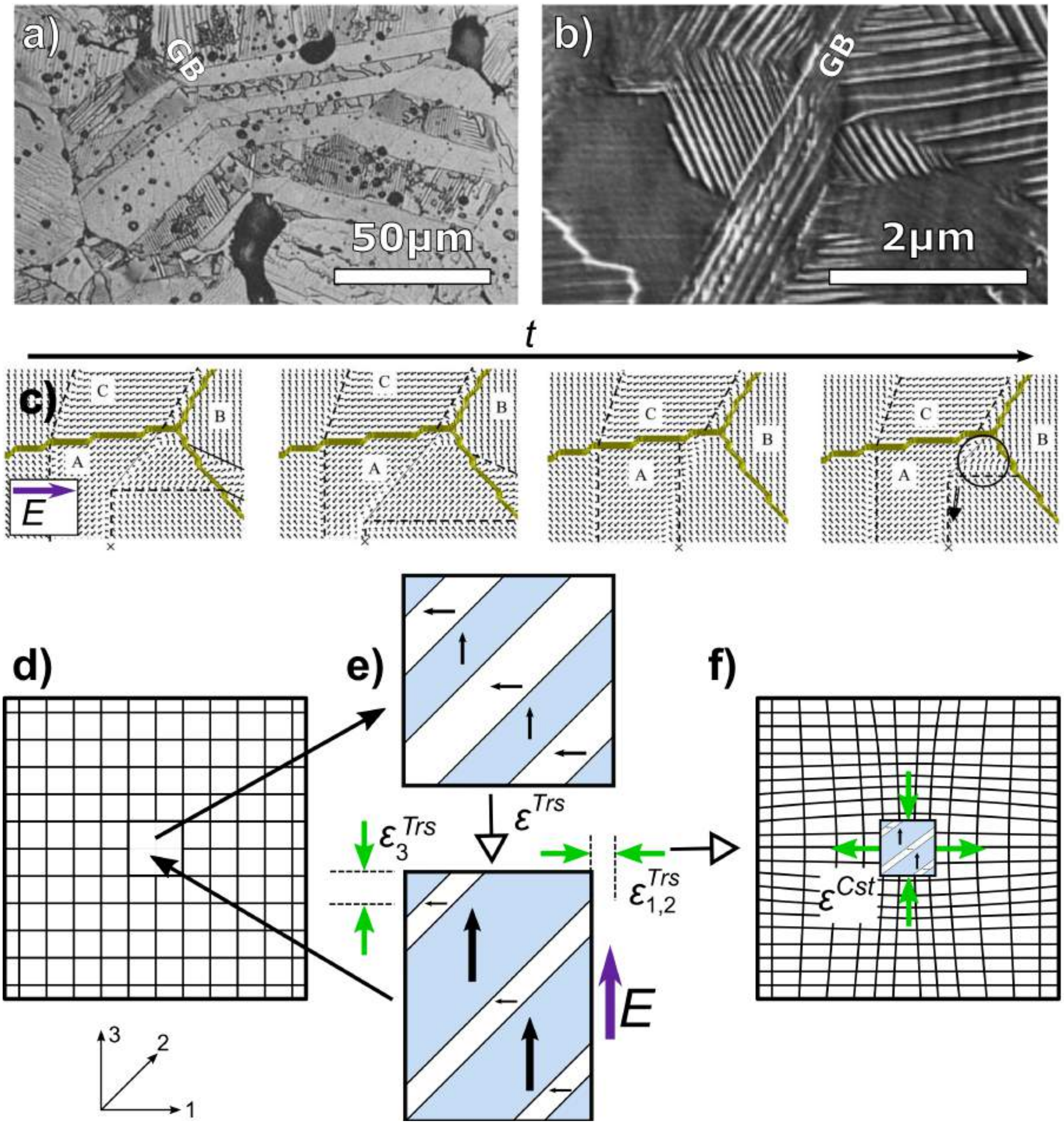

Figure 2.14.: Electric and mechanical grain interactions. Depending on the nature of the boundaries, domains may continue over several grains, as shown for a) BT [Reprinted from [149], with permission of John Wiley & Sons, Inc.] or stop, as displayed for b) PZT polycrystalline ceramic materials [Reprinted from [151], with permission from Elsevier]. c) Domain structure during polarization reversal in a polycrystalline ceramic material. The yellow lines represent the grain boundaries. The dashed and thin lines denote 90° and 180° domain walls, respectively. The arrow indicates the direction of growth of the 90° domain wall [Reprinted from [168], with permission from Elsevier]. d–f) Eshelby inclusion problem on the strain fields in a linear elastic body (represents the polycrystalline material) containing an inclusion (represents a single grain): d) unconstrained matrix without the inclusion, e) the inclusion undergoes a free transformation through motion of 90° domain walls by an applied electric field. The dimensions of the inclusion change by ε^{Trs}. f) The deformation of the inclusion is restricted because of the surrounding material, resulting in a stress state in the inclusion and the surrounding matrix [Redrawn after Ref. [172]].

The stresses are highly heterogeneous within a bulk material, depending on the orientation of the grains with respect to the electric field. The interacting length scale of the stresses was recently quantified by Daniels *et al.*. They suggested that the local strains average out over clusters of 10 and 20 grains [174; 175] using a variant of three-dimensional XRD measurements [176].

2.4 Influence of parameters on polarization reversal

Compared to a single crystal, the polarization loop of a polycrystalline material is considerably different. While the loop is typically rectangular for a perfect single crystal, it gets slanted for a polycrystalline material. Polarization switching gets more difficult as manifested by an increase in the coercive field, usually accompanied by a decrease of the switchable polarization. The goal of this section is to discuss the influence of various parameters on the domain wall movement in polycrystalline ceramic materials, and thus the shape of the polarization loop.

2.4.1 Local electric field

The velocity of a domain wall within a grain of a polycrystalline ceramic material is influenced by the locally-acting electric field. In a first approximation, the local electric field is a projection of the external macroscopic field onto the spontaneous polarization vector. [177; 178] Several secondary effects were reported to further influence the local electric field, such as stress concentrations near grain boundaries [179], porosity [180], crystallographic structure [181], and degree of crystallographic texture [182]. In polycrystalline PZT materials, for example, a broader distribution of switching times and a higher coercive field were found for a tetragonal PZT material, compared to a rhombohedral one. This was related to a higher anisotropy in the dielectric tensor κ_{11}/κ_{33} [183].

In the context of inhomogeneous electric fields, the idea of a propagating switching front in a polycrystalline ceramic material was first developed by Arlt, Hwang, and Waser [143–146] and later reconsidered by Lupascu *et al.* [177]. Arlt found for the case of a nonconducting polycrystalline ceramic material that the fluctuating fields at the grain boundary are much larger than the coercive field. He concluded that adjacent grains interact with the strongly fluctuating electric fields, resulting in a propagating switching region. [144] Qualitative predictions of the shape of the region were done by Hwang *et al.*. [145; 146] They represented each grain by a cubic element in a mesh. Their model predicts, that once a grain has reversed its polarization, the switching probability of the neighboring grains will be increased. Thereby, the probability of switching of the nearest top and bottom elements is two times higher compared to the six elements at the side. The propagating switching region can be described by an ellipsoid with its long axis in the direction of the applied electric field (Fig. 2.15).

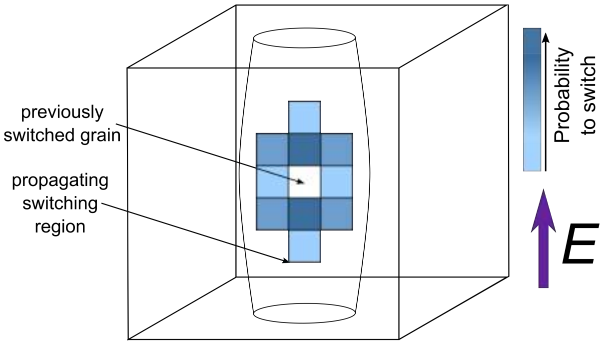

Figure 2.15.: Propagating switching front. Individual elements represent grains of a polycrystalline ceramic material, while the color scheme gives the probability to switch [Redrawn after Ref. [145; 146]].

2.4.2 Lattice distortion

The influence of lattice distortion on switching will be discussed for tetragonal samples, since the effects in these materials are well investigated. In other crystal structures the effects are expected to be similar, but less pronounced due to a smaller distortion of the lattice.

The angle between the two polarization axes of ferroelectric domains in tetragonal materials usually deviates from the 90° configuration. Stemmer *et al.* show examples of domain wall deviations for highly tetragonal $PbTiO_3$ thin films. [184] The deviation angle ζ can be calculated as

$$90^\circ - \zeta = \arctan((c/a)^{-1}), \tag{2.10}$$

where c/a is the lattice distortion of the tetragonal material. Calculations for different material systems are in good agreement with experimental results. For example, a BT single crystal with a lattice distortion of $c/a=1.01$ exhibits a value of $\zeta=0.5°$. [185–187] For a $PbTiO_3$ crystal with a c/a ratio of 1.063, higher deviation angles of up to 3.6° were found. [188; 189] The dependence of the angle ζ on the lattice distortion (Eqn. 2.10) is plotted as a blue solid line in Fig. 2.16a, where the blue squares represent experimental values.

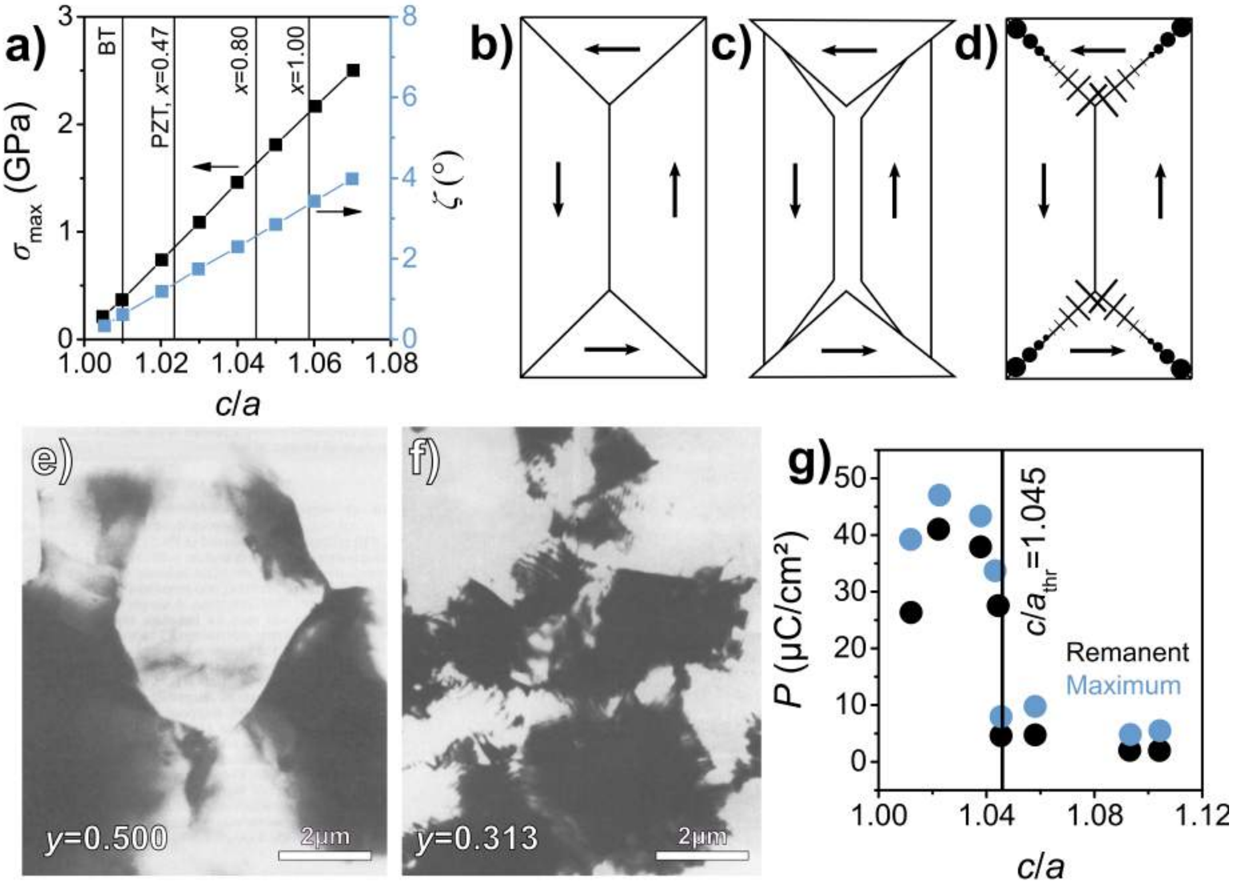

Figure 2.16.: Correlation between the lattice distortion, internal compatibility stresses, domain structure, and switching behavior. a) The influence of increasing lattice distortion on the maximum stresses at a band junction between two domains and deviation angle ζ. The blue solid line represents the calculation based on Eqn. 2.10. [190] The c/a ratios of BT and $Pb(Zr_{1-x}Ti_x)O_3$ with different titanium contents x are plotted for comparison as vertical lines [Redrawn after Ref.[190]]. The influence of the c/a lattice distortion on a simple 2D domain structure is shown in b–d): b) Customary drawing, c) separated domains showing the mismatch due to the lattice distortion, and d) dashed and dotted zones show the tensile and compressive strains in the joint domain pattern [Redrawn after Ref. [191]]. The influence of c/a ratio on the domain structure is depicted in TEM images in e) and f) for $(Pb_{1-y}Ca_y)TiO_3$ polycrystalline ceramic materials. e) For y=0.500 (c/a close to 1.00) strain-induced domains are absent, while they can be clearly observed for f) y=0.313 (c/a close to 1.04) [Reprinted from [192], with permission of John Wiley & Sons, Inc.]. The influence of c/a ratio on the remanent and maximum switchable polarization for a La modified $BiFeO_3$-$PbTiO_3$ is highlighted in g). A threshold value c/a_{thr}=1.045 was identified, beyond which polarization reversal was completely suppressed [Redrawn after Ref. [193]].

The correlation between the deviation angle and internal compatibility stresses is explained in Fig. 2.16b-d. A stress-free domain structure is schematically depicted in Fig. 2.16b. This domain structure can be separated into four pieces, displayed in Fig. 2.16c.[1] Mechanical stresses arise, which will peak at the junction points, where the domain structure is forced back to be exactly 90° (Fig. 2.16d). [191] Calculations by Pertsev and Arlt showed that a large amount of strain energy is stored in such junctions between different lamellar regions. [194] This strain mismatch has to be accommodated in the crystal or can be partially released by edge dislocations at the boundaries. Significant stress levels, which exceed 1.03 GPa for a c/a ratio of 1.03 at the junction of 90° domains, were calculated based on TEM and EBSD results, while no dislocation patterns where found. [190; 195] It is well known that these stresses can be large enough to destroy the polycrystalline ceramic material. [196]

The maximum stress is plotted as a function of the c/a ratio in Fig. 2.16a. In order to accommodate high elastic strains, the domain structure will become smaller with increasing c/a ratio. [42] A good example is the $(Pb_{1\text{-}y}Ca_y)TiO_3$ system. Increasing the Ca content will decrease the c/a ratio. TEM images, which display the influence of c/a ratio on the domain structure in this system, are displayed in Fig. 2.16e and f. While strain-induced domains are absent for a c/a ratio of 1.00, they can be clearly observed if the c/a ratio increases to 1.04. [192].

A direct influence on macroscopic switching properties is depicted in Fig. 2.16g. For a $BiFeO_3$-$PbTiO_3$ model system with different La contents [193], a decrease in remanent and maximum polarization was found with increasing c/a ratios. In this context, switching was easiest for small c/a ratios, while it got more difficult if the c/a ratio increases. Moreover, a threshold value of $c/a_{\mathrm{thr}}=1.045$ was identified, beyond which ferroelectric/ferroelastic switching was completely suppressed under the applied electric field. In agreement to this work, an increase of the coercive field with the c/a ratio for other PZT-based systems is usually found [197; 198].

2.4.3 Crystallographic structure

In several polycrystalline material systems, such as PZT [181; 199–201], $(1\text{-}x)Ba(Zr_{0.2}Ti_{0.8})\text{-}x(Ba_{0.7}Ca_{0.3})TiO_3$ [202; 203], and BT [204], easier switching of the rhombohedral phase compared to the tetragonal phase was observed. In particular, a higher activation energy for polarization reversal, a broader distribution of switching times [202], a higher coercive field [205], and a reduced switchable polarization were found for tetragonal PZT compared to the rhombohedral one.

The influence of crystallographic structure on polarization reversal can be rationalized by the amount of equivalent polarization directions, which is 6, 12, and 8 for a tetragonal, orthorhombic, and rhombohedral state, respectively. Under an applied electric field the polarization vector of a domain in a polycrystalline material will tend to orient as close as possible to one of the favorable polarization axes. The fraction of the single crystalline polarization value, which can be ideally realized in a random polycrystalline ceramic material, was calculated by Baerwald assuming the absence of any correlations between polarization vectors in different grains [206] and is summarized in Tab. 2.3.

Table 2.3.: Crystal structures, the number of equivalent directions and its influence on the maximum possible fraction of single crystal polarization value, which can be achieved in a random polycrystalline state [After Ref. [196]].

Crystal symmetry	Polar axis	Number of equivalent polarization directions	Fraction of single crystal polarization obtainable in a polycrystal [206]
Tetragonal	<001>	6	0.831
Orthorhombic	<110>	12	0.912
Rhombohedral	<111>	8	0.866

Li *et al.* investigated the influence of crystal structure on non-180° switching and the corresponding strain. They claimed that non-180° switching is forbidden in tetragonal materials due to constraints by differently oriented neighboring grains. For a rhombohedral material, it was found that polarization reversal through 71° and 109° domain switching is possible, although no macroscopic strain from these processes can be observed. [207] This is in disagreement to findings by Hall *et al.*, who clearly proved that lattice strains were induced in tetragonal and rhombohedral materials by non-180° domain switching. [172; 208–210]

With the crystal structure also the lattice distortion changes. While a value of lattice distortion of 2.4% was reported for a tetragonal $(Pb_{0.965}La_{0.01}Sr_{0.02}(Zr_{0.51}Ti_{0.49})O_3)$ PZT ceramic material, a lower value of only 0.7% was reported for

---

[1] It was specifically noted that the reported effects will only occur above a critical grain size, where a banded domain structure can be formed. [190] This critical grain size is about 4.7 µm and 1–2 µm for BT and PZT, respectively [42].

its rhombohedral ($Pb_{0.965}La_{0.01}Sr_{0.02}(Zr_{0.56}Ti_{0.44})O_3$) counterpart. [211] This has two consequent effects. Firstly, higher stresses and therefore a finer domain structure to compensate these stresses are expected for the tetragonal composition. Indeed, a finer domain structure for tetragonal compared to rhombohedral polycrystalline ceramic materials was reported for a PZT system. [212] Secondly, polarization reversal in a tetragonal material involves larger stresses compared to a rhombohedral counterpart. This can be manifested by diffraction measurements. The contribution of non-180° switching to the volume fraction of domain switching has been quantified to 20–25% for a rhombohedral material, while a lower value of 7–8% was found for a tetragonal material. [213]

2.4.4 Grain size and grain boundaries

Grain boundaries are 2D defects, classified according to their tilt or twist nature and the misorientation angle between the grains. The influence of grain boundaries on macroscopic polarization reversal was studied intensively in various polycrystalline ferroelectric materials by changing their concentration, which was realized by synthesizing samples with various grain sizes. It is generally accepted that the switchable polarization decreases with decreasing grain size and the polarization hysteresis loop gets more slim. Moreover, ferroelectricity was found to vanish, if a critical grain size is achieved. [214–223] Characteristic polarization loops for a BT ceramic with different grain sizes are revealed in Fig. 2.17a. Other effects originating from grain boundaries, such as the influence of the type of a grain boundary or the misorientation angle on macroscopic properties, are usually neglected. These can be studied, by the comparison of textured to randomly oriented material. A characteristic polarization loop of a polycrystalline BT material, displaying the influence of crystallographic texture is given in Fig. 2.17b.

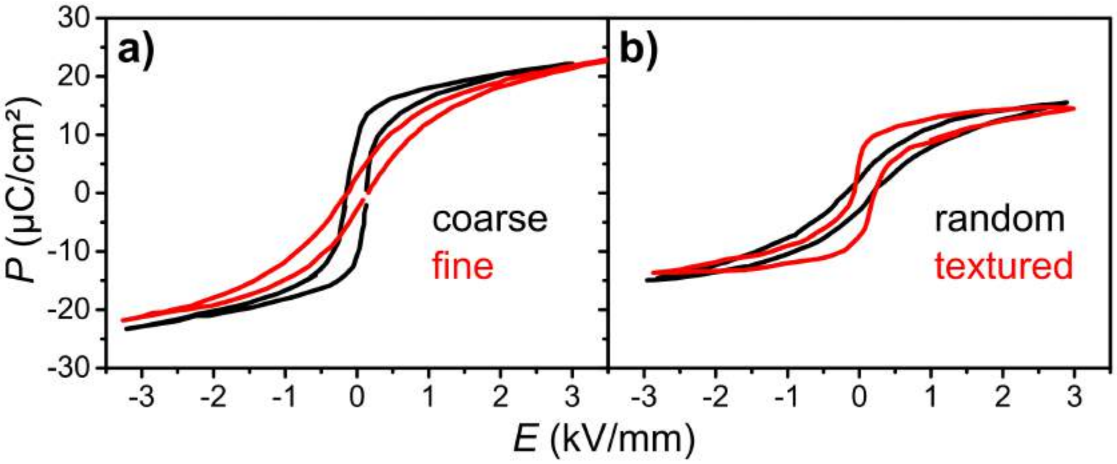

Figure 2.17.: Influence of grain size and boundaries on polarization loops. a) Polarization loops for polycrystalline BT ceramics with different grain size [Redrawn after Ref. [214]]. b) Polarization loops for random and crystallographically textured polycrystalline BT ceramics [Redrawn after Ref. [224]].

Upon cooling a ferroelectric/ferroelastic material from a high-temperature stress-free cubic state below its phase transition temperature, internal stresses arise due to anisotropic thermal extension coefficients and the formation of the spontaneous strain. For polycrystalline non-ferroelectric Al_2O_3 it was demonstrated that internal residual stresses, which mainly develop due to anisotropic thermal expansion coefficients in this system, decrease slightly with decreasing grain size, due to enhanced stress relaxation mechanisms along the grain boundaries. [225; 226] Therefore, as suggested by Bussem *et al.* [44], internal stresses in ferroelectric/ferroelastic materials mainly develop as a result of the formation of the spontaneous strain and are tensile in *a* and compressive in *c* direction in a tetragonal unit cell, since the grain is clamped by its neighbors. This effect gets more pronounced when the grain size of the piezoceramic material decreases. Arlt calculated a dependence of the inhomogeneous stress state on the grain size. The volume of material influenced by the inhomogeneous stress state in BT accounts to 7%, 22%, and 70% for a grain size of 10 μm, 1 μm, and 0.1 μm, respectively [214], indicating moderate mechanical fields inside the grain and extremely high fields at and near the grain boundary [227; 228]. Also other observations, without giving a more detailed explanation, suggest that internal stresses should decrease with decreasing grain size. [229; 230]

The weakening of the grain boundary by internal stress concentration influences the mechanical properties of the material. With a weakened grain boundary, predominantly intergranular crack propagation was observed for PZT samples with a small grain size, while in samples with larger grains mainly transgranular fracture occurred. [231]

In a more recent work, Ghosh *et al.* quantified the influence of grain size on the internal stresses in BT polycrystalline ceramics using high-energy synchrotron radiation. They found that for tetragonal BT samples with grain sizes in the range of 0.21–3.52 µm, neither the internal residual stresses nor the microstresses vary significantly. [232] The former were quantified according to the position, while the latter by the broadness of the (111) Bragg reflection peaks, respectively. The (111) Bragg peaks for BT samples with different grain sizes are displayed in Fig. 2.18a. Kungl and Hoffmann investigated PZT materials with a grain size ranging from 1–3.5 µm. [200] Similar to Ghosh *et al.*, they observed no or little changes in the dependence of internal stresses on the grain size in polycrystalline ceramic materials. This indicates that the residual mechanical stresses are almost completely released by the formation of twinned non-180° domain walls, as mechanistically described in section 2.2.1.

The domain size of a grain scales with the grain size; a correlation described by the Kittel's law. [233] Above a critical grain size of about 1 µm, the domain size, δ, was found to increase with grain size, g, exhibiting a square-root dependence [42], similar to the findings in magnetic materials [234].

$$\delta \propto \sqrt{g} \tag{2.11}$$

A typical domain structure of a BT ceramic material with a fine grain size is compared to the domain structure of a coarse-grained material in Fig. 2.18d and e, respectively. [235] The dependence of domain size on grain size is displayed in Fig. 2.18f. As verified by the dashed line, Eqn. 2.11 can be roughly confirmed for a grain size range $1<g<10$ µm for a BT polycrystalline material. [236]

The increase in non-180° domain wall density in the lamellar domain structure is also manifested by an increase in diffuse scattering between the (002) and (200) diffraction peaks displayed in Fig. 2.18b. [232] This diffuse scattering was related to an enhanced strain distribution around the non-180° domain walls [237; 238], which could be derived mathematically [239]. This feature was later on investigated in more details by Choi *et al.*. They described a 90° domain wall in a tetragonal BT as a complex structure, which is tetragonal deep inside the grain, while they assume that the domain wall is cubic. In between, GLSL form in order to compensate for the strain mismatch [54], as schematically displayed in Fig. 2.18h. The mass fractions of the individual layers for a BT polycrystalline material could be determined by Rietveld analysis of XRD profiles and are plotted in Fig. 2.18i. While for a grain size of 2.5 µm the cubic and the GLSL mass fractions account to approximately 20 wt.% of the material, it decreases to approximately 10 wt.% for a grain size of 20 µm. [55]

The domain size is directly related to the mobility of the non-180° domain walls. In an early model by Arlt *et al.* [236], a force constant for the movement of non-180° domain walls was introduced, which was independent of the domain size. In follow up publications, Arlt and Pertsev [166; 227] suggested a dependence of the force constant on the width of the domain structure, related to electric and mechanical field concentrations at and near the grain boundary. According to their calculation, fine-grained materials have a higher force constant than coarse-grained materials. This directly indicates that non-180° domain walls in finer domain structures are more difficult to move than domain walls in coarser domain structures. This finding was also supported experimentally for small ac excitation signals by Wu and Schulze. [240] They reported, that fine-grained BT ceramics do not exhibit nonlinear dielectric effects and have a lower dielectric loss. This is an indication that domain walls are more clamped in fine grain materials. Also, Demartin and Damjanovic [241] found a weaker domain wall activity in fine-grained BT (0.7 µm) than in course-grained materials (26 µm).

Building up on a conventional nucleation and growth model [16; 242; 243], which is applied to describe the polarization reversal of single crystalline materials, Duiker *et al.* discussed the influence of grain boundaries on the polarization reversal process [244; 245]. As schematically depicted in Fig. 2.18g they found an increase of the switchable polarization and a sharpening of the distribution of switching times, when increasing the grain size.

While until now all studies focused on the influence of grain size on internal stresses and domain wall activity, this paragraph will discuss the influence of the type of the grain boundary. In this context, internal stresses were found to be strongly dependent on the degree of crystallographic texture. Vedula *et al.* found lower residual stresses and narrower stress distributions in textured Al_2O_3 ceramic materials, compared to untextured samples (Fig. 2.18c). [246] This is in agreement with other studies on Al_2O_3, which found a significant reduction of residual stresses to one third of the value measured in samples without crystallographic texture. [247] Even though no experimental study is available on the effect of crystallographic texture on the internal stress state in ferroelectric materials, it can be assumed that the effect is even more pronounced due to the possibility of a cooperative alignment of the grains and reduced clamping during the formation of the spontaneous strain.

As a direct result of the stress state, domain switching in the core of a grain might be fundamentally different from domain switching in the vicinity of the grain boundary, as suggested by Anton *et al.* [179]. The effect could be made visible by PFM measurements.[1] Polarization loops measured at the grain boundary between grains with dissimilar crystallographic orientation in a PZT thin films were strongly shifted along the voltage axis, *i.e.*, they showed a strong imprint [163] and coercive fields measured locally at the grain boundary were considerably larger compared to measurements at the center of the grain [165]. It was found that the grain boundary impedes ferroelastic switching, while ferroelectric switching is facilitated at one side of the grain boundary and restrained at the other side. [248]

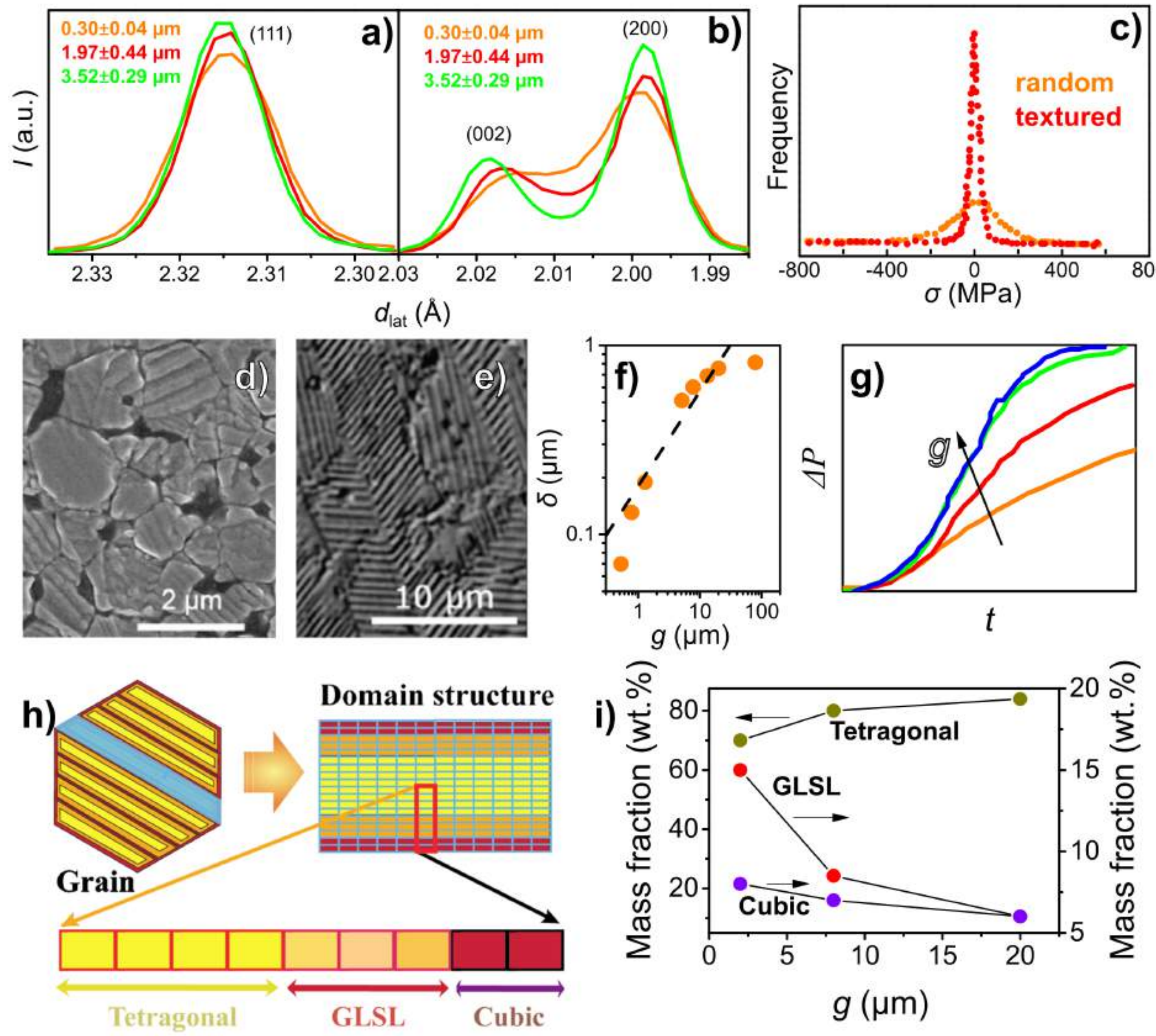

Figure 2.18.: Influence of grain size on internal stresses, domains, and the switching behavior of polycrystalline ceramic materials. High-energy XRD patterns of a) (111) and b) (200) Bragg reflections of BT samples with different grain sizes in the range of 0.30–3.52 µm [Redrawn after Ref. [232]]. c) Residual stress distribution in textured and random Al_2O_3 [Redrawn after Ref. [246]]. A domain structure of tetragonal BT is shown for a d) fine grain structure (g=0.74±0.07 µm) and a e) coarse grain size (g=74.3±5.1 µm), respectively [Reprinted from [235], with permission from Elsevier]. The dependence of domain size on grain size for tetragonal BT is shown in f) [Data were taken from [236]]. The dashed lines represents the expected square-root dependence, Eqn. 2.11, in the range of 1<g<10 µm. g) The switched polarization for samples with different grain sizes according to a model based on nucleation and growth of domains [Redrawn after Ref. [244]]. h) Model describing a 90° domain wall in a lamellar domain structure. The GLSL is required to compensate the strain mismatch between the cubic grain boundary and the tetragonal material phase. i) The mass fraction of the cubic, tetragonal and GLSL phase are displayed as a function of the grain size for a BT material [Reprinted from [55], with the permission of AIP Publishing].

---

[1] The general limitation of this experimental approach is that the stress state of the material changes, because the surface needs to be removed. This might influence the results obtained from localized PFM measurements.

Pinning of domain walls at grain boundaries is another frequently observed phenomenon. For example, density functional theory (DFT) calculations suggest that 180° domain walls get pinned at $\Sigma5$ grain boundaries. [249] Pinning of domain walls at a grain boundary was also observed experimentally and depinning only occurred when the applied voltage was sufficiently increased. [250] In a bicrystal, it was found that a domain wall was attracted and pinned by a 24°(100) grain boundary. [251]

A detailed study of the interaction between moving domain walls and grain boundaries was carried out in a recent series of publications by Marincel *et al.* using a bicrystal thin film model system and PFM. [252–254] A region of 720–820 nm in the vicinity of the grain boundary was identified, where the domain wall mobility was influenced by the grain boundary. TEM images indicate that static type domain walls are present near the grain boundary, while mobile domain walls are observed far from this region. [252] The influence of crystallographic structure on local pinning was investigated on a series of PZT thin films. It was found that the grain boundary influences domain wall motion in a range of 800 ± 79 nm and 450 ± 30 nm for a tetragonal and rhombohedral thin film, respectively, which was attributed to a higher domain wall density in case of the rhombohedral thin film. [253] The influence of the type of grain boundary was also studied. It was found that tilted grain boundaries with angles 15° or less have similar energy to other pinning centers in the film, while 24° tilt angle grain boundaries pinned the domain wall much stronger. For twist grain boundaries, the grain boundaries with a 30° misorientation showed significant pinning, while a misorientation angle of 10° was comparable to other pinning sites. [254] This value is in good agreement with phase field simulations. It was found that the switching behavior in a bicrystal with a misorientation less than 15° was similar to the switching behavior of a single crystal. [169] This indicates that the nature of the grain boundary, or its respective energy [255], play a significant role for the description of the switching behavior in polycrystalline ferroelectric materials.

Grain boundaries are typically paraelectric and distort ferroelectric switching. This was manifested by phase field simulations, in which grain boundaries with a thickness of 0.8 nm were used and the grain size decreased from 80 nm to 10 nm. It was found, that the switchable ferroelectric phase and the mobility of domains were influenced by the grain boundary volume concentration. Macroscopically, tilted hysteresis loops, substantially lower remanent polarization and coercive fields were suggested, if the grain size gets reduced. [256] The influence of the thickness of the grain boundary was also studied. Thereby, it was found that both the coercive field and the remanent polarization decrease with increasing thickness of the grain boundary, indicating easier domain wall movement. [257; 258]

2.4.5 Other effects influencing the movement of domain walls

Various other effects influence the domain dynamics in polycrystalline ferroelectric materials. The following list gives a brief summary:

- **Domain interactions:** It is clear that domain wall processes cannot occur independently, as proven in various experimental and theoretical works. It was for example found that ferroelectric domains can pin other ferroelectric domains [259] and the presence of 90° domain walls inhibits the motion of 180° domain walls [260].
- **Chemical doping:** Doping can have a large influence on the domain wall movement. Lanthanum doping in PZT ceramics, for example, is known to enhance the domain wall mobility. [261] This effect was explained by immobile La-defect dipoles, which create random destabilizing fields that make the domain structure less stable and domain wall movement easier. [262] On the other hand, acceptor doping can lead to presence of defect complexes that pin the domain walls [263], which is the common approach to obtain hard-type piezoelectrics.
- **Electrode defects:** For a GMO single crystalline model system, it was found that a single moving domain wall stops due to extended electrode defects and larger electric fields are required in order to move the domain wall away of the defect. [264; 265]
- **Composites:** The coercive field was reported to increase when ZnO was added as a secondary phase at the grain boundaries of $0.94(Na_{1/2}Bi_{1/2})TiO_3$-$0.06BaTiO_3$ polycrystalline ceramic materials. [266; 267]
- **Dislocations:** Dislocations can act as pinning sites for domains. [259; 268]

2.5 Theoretical models

Theoretical models to describe the polarization reversal in ferroelectric materials can be in general classified into the following groups: statistical, micromechanical, phenomenological, and homogenized energy models. The goal of this section is to introduce the models conceptually and comment on their suitability for polycrystalline ceramic materials. Thereby, the focus is on the statistical models, since they aim to describe the macroscopic dynamics of the polarization reversal process.

2.5.1 Statistical models

Statistical models are based on the theories developed by Johnson and Mehl [269], and independently by Avrami [243] in the 1940s. Ishibashi and Takagi [16] systematically applied their method to ferroelectric switching using the mathematical method of Kolmogorov [270], which is commonly used to describe the crystallization kinetics in metals. The driving force for the classical Avrami approach is the difference in free energies between the starting and the new phase. In the framework of the Kolmogorov-Avrami-Ishibashi (KAI) model, it is assumed that the mean size of individually-transformed regions is small compared to the sample size, the nucleation probability is spatially uniform, and the value of growth velocity is the same for all transforming regions. Additionally, following the theory developed by Fatuzzo [242], the domain wall movement is considered as the time-dependent step. In the KAI model, a temporal dependence of the reversed polarization is presented as

$$\Delta P\left(t, \tau_{E_{\mathrm{Sw}}}\right) = \Delta P_{\mathrm{max}} \left\{ 1 - \exp\left[-\left(\frac{t}{\tau_{E_{\mathrm{Sw}}}} \right)^{\Lambda} \right] \right\}, \tag{2.12}$$

where $\tau_{E_{\mathrm{Sw}}}$ is a unique time constant, related to the movement of a domain wall after nucleation in an infinite sample. ΔP_{max} is the amount of the reversed polarization reached at saturation and Λ is the Avrami exponent. The latter depends on the dimensionality of the domain nucleus and on the nucleation rate and is expected to take only integer values from 1 to 4. The KAI model distinguishes between one-step-nucleation (no additional nuclei form and domain walls move with a constant velocity, $\Lambda = \delta_{\mathrm{dim}}$) and continuous nucleation (additional nuclei form during the switching process with a constant rate and domain walls move with a constant velocity, $\Lambda = \delta_{\mathrm{dim}} + 1$), where δ_{dim} is the dimensionality of the domain. Stripe domains ($\delta_{\mathrm{dim}} = 1$), circular domains ($\delta_{\mathrm{dim}} = 2$), and spherical domains ($\delta_{\mathrm{dim}} = 3$) are distinguished, as displayed in Fig. 2.19a. Even though the relationship between Λ and the dimensionality of domains has never been proven by experimental methods, the KAI model is commonly used to describe the time-dependent polarization or current of many single crystals, such as BT [182; 271], $(CH_3NH_3)_5Bi_2Br_{11}$ [272; 273], TGS [274; 275], and $KTiOPO_4$ (KTP) [276]. A typical example of the time-dependent switched polarization of a [111] oriented BT single crystal is provided in Fig. 2.19b. Thereby, solid lines reveal fits according to Eqn. 2.12. Field-dependent and non integer Avrami exponents are found. [271]

The KAI model provides a good description of the polarization for short and medium times, while deviations from the experiment occur mainly in the late switching stage. [277] Therefore, the model was later on modified to take finite samples into account [278; 279] and a new mathematical treatment of experimental data was proposed by the group of Shur. When the growing domain touches any boundary it stops growing in that direction, resulting in a change of the Avrami exponent; a phenomenon called "geometrical catastrophe". [15; 280] Non-integer and field-dependent Λ values were also explained by a mixing of one-step-nucleation and continuous nucleation. [276]

The KAI model was also applied to describe switching in more complex systems, which are characterized by a higher degree of disorder than single-crystalline materials. For example, Furukawa *et al.* applied the KAI model to describe switching in certain copolymers [281] and found Λ values as large as 5. While the switching dynamics of some polycrystalline [282–284] and epitaxial [285; 286] thin films could be described by a KAI behavior, Lohse *et al.* [22] compared the switching behavior of thin films to single crystalline materials and found that thin films exhibit a broadened distribution of switching times and suggested that the KAI model cannot be applied in its current form. Their findings triggered the extension of the KAI model by Tagantsev *et al.*. [19] They suggested that in a thin film the polarization reversal process is controlled by an aggregation of regions with different switching dynamics, while the switched polarization of the bulk material is a superposition of all switching regions. In their nucleation limited switching (NLS) model, switching of a region is limited by the nucleation of new domains rather than by domain wall movement, and a smooth and exponentially broad distribution of nucleation waiting times was suggested to describe the switching process in a thin film. Individual regions thereby correspond to single grains or clusters of grains and grain boundaries act as frontiers to limit the propagation of the switched region. [287] While polarization reversal in thin films could be described by a distribution of nucleation waiting times in the frame of the NLS model [288; 289], the physical origin of the time-distribution remained unclear.

Based on the relation between electric field and switching time, Genenko *et al.* suggested to described switching by the inhomogeneous field mechanism (IFM) model. In their model, the switching time distribution is related to the inhomogeneous field distribution in the polycrystalline material, without implying a certain mechanism of domain nucleation and subsequent growth. [100; 290] Instead, it is assumed that each grain has a homogeneous polarization in the direction of its pseudocubic axis most close to the direction of the applied field, and the externally applied field gets locally distributed, as shown in Fig. 2.19c. In this context, the time-dependent switched polarization

$$\Delta P\left(E_{\mathrm{Sw}}, t\right) = \Delta P_{\max} \int_{0}^{E_{\mathrm{Sw}}/E_{\max}(t)} \frac{du}{u} \phi\left(u\right) \tag{2.13}$$

can be calculated for any high voltage (HV) field pulse E_{Sw}, if the functions $E_{max}(t)$ and $\phi(u)$, which represent fingerprints of the ferroelectric material, are determined experimentally. An inhomogeneous distribution of the electric field for a polycrystalline PZT sample is displayed in Fig. 2.19d. In Fig. 2.19e, this distribution of the electric field is applied and $\Delta P(t)$ curves for different switching fields are constructed according to Eqn. 2.13.

Even though the model in its final form [290] can describe the polarization dynamics of polycrystalline ceramic materials [180–182; 202; 203; 291], and even ferroelectric polymers [292; 293], the influence of domain walls and mechanical and electric correlations between grains is neglected. In addition the model cannot describe the macroscopic strain response.

2.5.2 Micromechanical models[1]

The first micromechanical models to describe polarization reversal were suggested by Chan and Hagood [298] and Hwang *et al.* in 1994 [17]. In the latter approach, the polycrystalline material is made up of many randomly-oriented tetragonal and single-domain grains and the switching behavior of each individual grain is described by an idealized rectangular hysteresis behavior. Each grain is subjected to the same externally-applied electric field and stress. The applied field is increased stepwise and for each step the change in energy, related to a possible 180° or 90° switching event, is calculated. It is important to note that the critical switching energies for the respective events usually cannot be determied experimentally. When the sum of the electric and the mechanical work exceeds a critical value (Eqn. 2.14), the direction of the spontaneous polarization switches.

$$E_i \Delta P_i + \sigma_{jk} \Delta S_{jk} \geq 2 P_S E_C \tag{2.14}$$

Here, ΔP_i is the change in remanent polarization and ΔS_{jk} is the change in remanent strain of the switching domain. Experimental results and the description by the model of Hwang *et al.* are provided in Fig. 2.19f. The first set of models described a very simplified behavior. Individual grains were described as monodomain single crystal regions and domain walls were neglected. [17; 299; 300] Also, inhomogeneities in the electric field and stresses, and consequently grain interactions, were ignored (Reuss-type approximation). [301] Later on, interactions between grains were implemented by the Eshelby approach [302; 303] or finite element methods [304]. The models were extended and domain configurations [305; 306] and interaction between domains [307] were taken into account. Extensions to other crystallographic systems, such as rhombohedral materials [303], or a phase coexistence [308] are also available.

2.5.3 Phenomenological models[2]

By introducing internal variables, complex constitutive equations for structural mechanics problems, such as elasticity and plasticity, can be reformulated as differential equations. [309] This approach was first applied to the modeling of the hysteresis in ferroelectric materials by Chen *et al.* in the 1980s. [310; 311] The internal variables, which represent the remanent states of polarization and strain, were supposed to characterize the degree of alignment of microscopic dipoles with a certain directions in space. Even though the model is relatively complex and limited to electric hysteresis, the polarization and strain response of a rhombohedral PZT material could be described well, as demonstrated in Fig. 2.19g.

The model was implemented into a thermodynamic framework and the polarization and strain were decomposed into reversible and irreversible parts. [312; 313] A yield surface similar to metal plasticity was introduced, which defined the switching criteria. Reversible behavior was assumed to occur within the yield surface and irreversible remanent strain and polarization were allowed to develop for loading states on the surface. [314] On this basis, the first complete phenomenological multiaxial description of the ferroelectric and ferroelastic hysteresis under nonlinear, coupled mechanical and electric loads was developed by Landis. [315] A correlation between the internal variables and the domain and microstructure of the material was later provided by Kamlah and Wang [316] and Mehling *et al.* [317].

---

[1] This section is based on the review articles by Kamlah [294], Huber [295], Landis [296], and on the recent dissertation by Stark [297].

[2] This section is based on the review articles by Kamlah [294] and Landis [296].

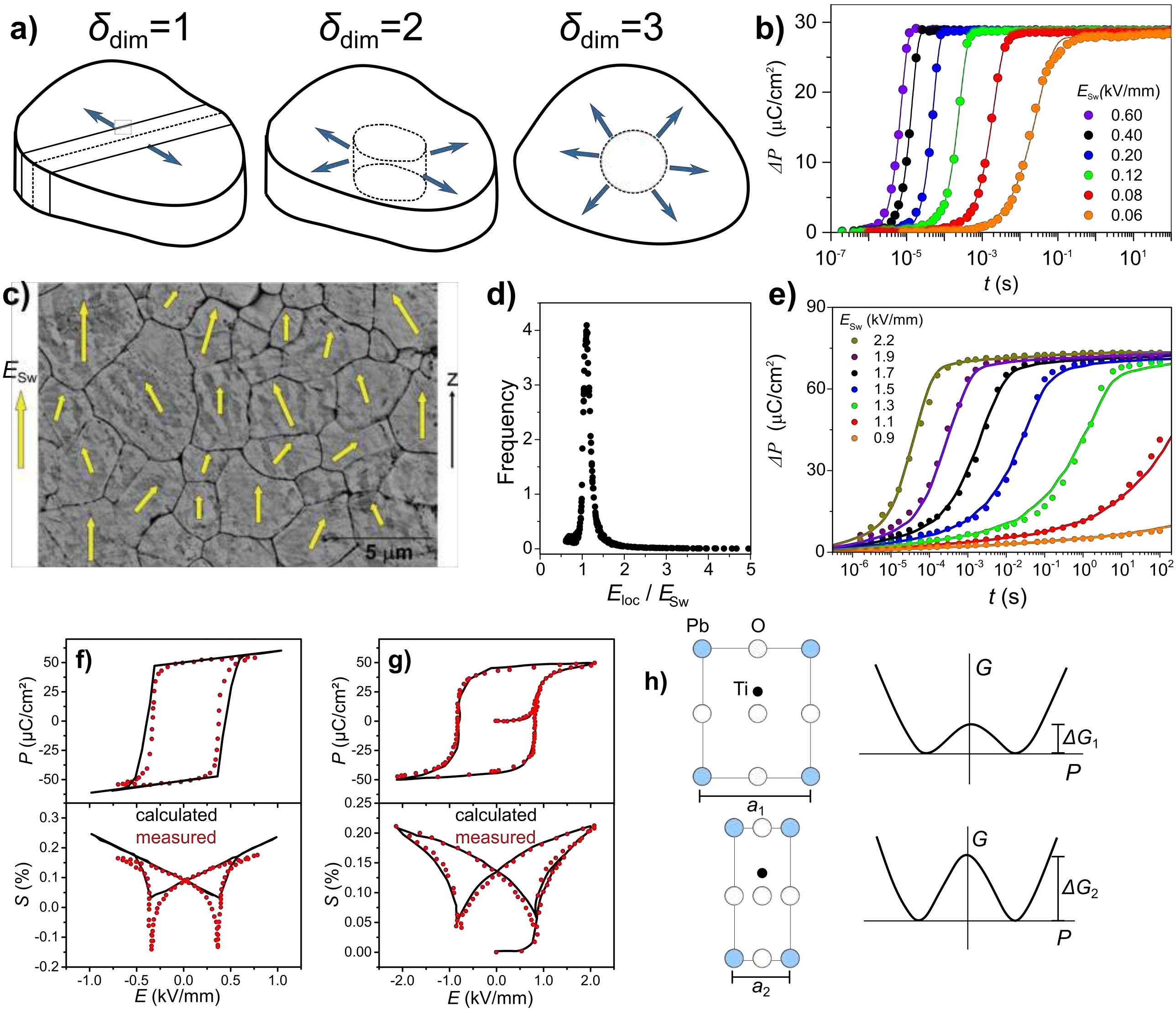

Figure 2.19.: Theoretical models describing the switching process. The shape of domains with different dimensionality according to the KAI approach are revealed in a) [Redrawn after Ref. [16]]. The blue arrows indicate the direction of growth. b) Switched polarization as a function of time for a [111] oriented BT single crystal. The symbols correspond to the experimental results obtained at a constant switching field as indicated, while the solid lines represent fits according to Eqn. 2.12 [Redrawn after Ref. [271]]. Scheme of the inhomogeneous distribution of the externally-applied electric field for a polycrystalline ferroelectric material, with a scanning electron microscopy (SEM) image of a polycrystalline PZT sample as a background [Reprinted from [290], with permission of John Wiley & Sons, Inc.]. The weighted statistical distribution of the local electric field value extracted from experimental data, displayed in d), can be used to describe the experimental results for a polycrystalline PZT sample highlighted in e) using the IFM model. In e), the symbols correspond to experimentally-measured data points, while the solid lines are constructed according to Eqn. 2.13 [Redrawn after Ref. [290]]. Comparison of measured and calculated field-dependent polarization and strain of a PZT material for the early f) micromechanical [Redrawn after Ref. [17]] and g) phenomenological model [Redrawn after Ref. [311]], respectively. h) The influence of non-uniform lattice spacing, $a_1 > a_2$, of a PZT unit cell on the free energy landscapes [Redrawn after Ref. [318]] creating different activation barriers, $\Delta G_1 < \Delta G_2$.

2.5.4 Homogenized energy models

Homogenized energy (HE) models were developed in a series of publications by Smith *et al.*. [318–322] Initially proposed for 180° polarization reversal [318; 320] they were extended to account for 90° polarization reversal later on [321; 322]. In the framework of these models, constitutive relations are constructed on the unit cell level. While these can be directly applied to describe the polarization reversal in homogeneous single crystalline materials, in polycrystalline materials properties such as the coercive field, the critical driving forces, and the interaction fields are assumed to be homogeneously distributed. An example is outlined in Fig. 2.19h. Here, it is displayed that nonuniformities in the lattice, as expressed by different lattice constants, $a_1 > a_2$, produce a variation in the Gibbs free energy profiles, $\Delta G_1 < \Delta G_2$, resulting in a variation in the local coercive field and remanent polarization.

3 Objective of the work

The possibility to switch the polarization vector is the main property distinguishing ferroelectrics from other polar materials. The understanding of this process represents a challenging scientific problem and is crucial for technical applications. Despite this, some fundamental questions have not yet been answered sufficiently:

1. What is the sequence of 180° and non-180° switching events in polycrystalline ferroelectric materials?
2. How does the microstructure of a polycrystalline material influence the activation barrier for switching and the distribution of switching times?
3. What is the correlation between mechanical stresses, domain structure or other microstructural parameters, and the macroscopically observable dynamic switching response?

Although different experimental techniques shed light on various aspects of the switching process and a broad range of models were provided, the first question was not sufficiently answered. Even more, different experiments report contradicting results. Some researchers claim that polarization reversal happens by two successive non-180° switching events [120; 124], others predominantly observe 180° processes [125; 126], while again others propose only a single 180° event [127]. A similar discrepancy is found when comparing the theoretical switching models. The state of the art statistical models assume only one single 180° event [290], while non-180° events were already included in other models more than a decade ago [17; 321].

The first aim of this work is to develop a combined approach to tackle the first question. A device was constructed which allows to apply sharp HV pulses to the material and measure its dynamic response over several decades, ranging from 1 μs to several s. A detailed description of the construction of this device will be given in Sec. 4.2.1. Thereby, the macroscopic polarization and strain response are measured simultaneously. This allows to separate between purely ferroelectric, and ferroelectric/ferroelastic domain contributions. Both contribute to polarization, while only the latter contributes to the strain response of the sample. Combining the setup with high-energy synchrotron diffraction allows to simultaneously track the structural changes of the material, giving additional information about ferroelastic domain switching and internal mechanical stresses. The latter can be incorporated into a Landau energy landscape and the influence of combined electric and mechanical loads on the stable states of a domain can be revealed. The obtained results will be presented in detail in Sec. 5.1.

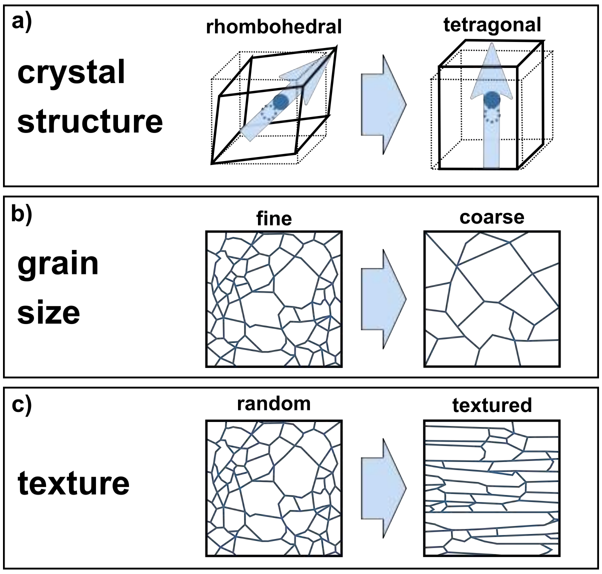

Figure 3.1.: Schematic representation of the different parameters to be investigated in this work. a) Crystallographic structure, b) grain size, and c) crystallographic texture. The blue solid lines in b) and c) represent grain boundaries.

The literature related to the second and third question was reviewed in Sec. 2.4. While easier and faster switching has been observed for polycrystalline BT samples with larger grain sizes [214], or a higher degree of crystallographic texture [224], little is known about the influence of microstructural parameters on the dynamics of the polarization reversal process. In particular, the origin of the broad distribution of switching times in polycrystalline ceramics remains unclear. The specific objective of the second part of this study is to investigate the effect of the different microstructural boundary conditions and degree of disorder on the polarization reversal process. In this context, a set of three series of parameters, as summarized in Fig. 3.1, is investigated.

The influence of the crystal structure was studied on a PZT series with different Zr/Ti ratios and thus different crystallographic structures, including pure tetragonal, morphotropic phase boundary, and rhombohedral compositions. The influence of the grain size was studied for rhombohedral PZT materials with a grain size ranging from 4.1 to 11.3 μm. The influence of the degree of crystallographic texture was studied for polycrystalline materials on $Ba_{0.85}Ca_{0.15}TiO_3$ samples with microstructures ranging from a random orientation to a high degree of crystallographic texture. The synthesis procedures for the different series of samples will be summarized in Sec. 4.1, while the obtained experimental results will be presented in Sec. 5.2. Thereby, the distribution of switching times is discussed with respect to internal stresses, mechanical boundary conditions, the domain configuration, and the inhomogeneous field distribution. State of the art statistical models claim that the broad distribution of the switching times is solely a result of the inhomogeneous distribution of the applied electric field [290], while the chemistry and the microstructure of the material are completely neglected. Therefore, the systematic correlation between the microstructure and the switching dynamics of polycrystalline materials, presented in this work, represents the basis for future improvement of theoretical models.

4 Materials and methods

4.1 Materials

Different ferroelectric ceramics were investigated as model materials. The mechanism of polarization reversal was investigated on a commercial PZT material, while the influence of crystal structure was revealed on PZT materials with different Zr/Ti ratios. Various grain sizes were realized by changing the sintering conditions for a PZT materials with a rhombohedral composition. Materials on the basis of BT were used as model materials to investigate the influence of the degree of crystallographic texturing.

4.1.1 Mechanism of polarization reversal

A commercial soft polycrystalline $Pb_{0.99}[Zr_{0.45}Ti_{0.47}(Ni_{0.33}Sb_{0.67})_{0.08}]O_3$ (PIC 151, PI Ceramic, Lederhose, Germany) with a tetragonal structure was investigated as a model material.[1] Bar-shaped samples ($1x1x10mm^3$) were cut and sputtered with platinum. Prior to the measurement, all samples were annealed at 500° and cycled 20 times at 0.5 Hz and 3 kV/mm to remove any unstable electric contributions. Bipolar polarization and strain loops were measured at 3 kV/mm and 0.1 Hz before and after each switching experiment, to ensure that the pulse experiment did not irreversibly influence the properties.

4.1.2 Influence of crystal structure on polarization reversal

$Pb_{0.985}La_{0.01}(Zr_{1-x}Ti_x)O_3$ ceramics were prepared by the mixed-oxide route [323] with different compositions x=0.5, 0.475, 0.46, 0.44, and 0.40 to obtain samples with different crystal structures.[2] Donor doping with 1 mol.% La^{3+} was performed on the A-site. Powders were pressed into cylindrical pellets of 12 mm in diameter using uniaxal pressure of 17.7 MPa, followed by cold isostatic pressing at 400 MPa. The pellets were sintered at 1050° C for 6 h with a heating rate of 2 °C/min. The samples were ground to a thickness of 0.7 mm and sputtered with platinum electrodes. Prior to the measurements, all samples were annelaed at 500° and cycled 20 times at 0.5 Hz and 3 kV/mm to remove any unstable electric contributions. Bipolar polarization and strain loops were measured at 3 kV/mm and 0.1 Hz before and after each switching experiment, to ensure that the pulse experiment did not irreversibly influence the properties.

4.1.3 Influence of grain size on polarization reversal

Rhombohedral $Pb(Zr_{0.7}Ti_{0.3})O_3$ ceramics with different grain sizes were prepared[3] by varying the sintering conditions. Cylindrical pellets with a diameter of 8 mm were pressed uniaxialy at 50 MPa, followed by cold isostatic pressing at 300 MPa. The samples were sintered at a sintering temperature ranging from 1150°–1250° C, while the sintering time varied from 2–8 h. The heating and cooling rate was 5°C/min. The density of the samples was measured using the Archimedes method. The grain size of the samples was measured using SEM (Jeol JSM-7600F, Tokyo, Japan) images. Therefore, the samples were polished to 0.25 µm (DP-Paste M, Struers, Ballerup, Denmark) and chemically etched. For the grain size analysis 100–500 grains were analyzed in each sample.

For electric characterization, the samples were ground to a thickness of 1.2 mm, followed by 500° C stress-free annealing and sputtering with platinum electrodes. Prior to the measurement the samples were annealed at a hot plate at 500°C to remove possible aging effects. All samples were cycled 20 times at 0.5 Hz and 3 kV/mm to remove any unstable electric contributions. Bipolar polarization and strain loops were measured at 3 kV/mm and 0.1 Hz before and after each switching experiment to ensure that the pulse experiment did not irreversibly influence the properties.

---

[1] Please note that among several self-made lead-containing and lead-free ferroelectric materials, the commercial PIC151 material was the only material which could be investigated under synchrotron radiation. All other materials showed irradiation damage under combined synchrotron radiation and pulse or bipolar electric fields with a low frequency of <0.1Hz. This was manifested by changed strain and polarization response. Locally, at the position where the beam hits the sample, a black dot appears. The effect is reversible and disappears after thermal annealing.

[2] Dr. Hans Kungl from KIT Karlsruhe is acknowledged for the preparation of the samples.

[3] Silvo Drnovšek from JSI Ljubljana is acknowledged for the preparation and initial characterization of the samples.

4.1.4 Influence of crystallographic texture on polariaztion reversal

Polycrystalline ceramics with the chemical composition $Ba_{0.85}Ca_{0.15}TiO_3$ with different degrees of crystallographic texture were produced.[1] The samples with a high degree of texture were fabricated by the reactive templated grain growth process using a mixture of BT and $CaTiO_3$ (CT) template particles as crystal seeds, while samples with a low degree of texture were prepared by a solid state reaction without templates. The composition of the starting materials for all samples was $0.85BaTiO_3$-$0.15CaTiO_3$ with 1 mol.% Ba excess. In addition, 1 mol.% $MnCO_3$ and 1 wt.% B_2O_3-ZnO-SiO_2 glass powder were added to reduce the leakage current and to improve the density, respectively. Tape casted and laminated samples with a thickness of approximately 0.4 to 0.6 mm were prepared and sintered at a temperature of 1350° C for 5 h in Ar flow containing 0.3 % H_2. Detailed processing conditions can be found elsewhere. [324]

The density of the sintered samples was measured using the Archimedes method. XRD patterns of the samples were determined using K_α/K_β radiation (Rigaku Smart Lab DPK, Tokyo, Japan). The degree of crystallographic texture was described using the Lotgering factor [325]

$$F = \frac{p - p_0}{1 - p_0} \cdot 100\% \tag{4.1}$$

with

$$p_0 = \frac{\sum I_{00l}}{\sum I_{hkl}}. \tag{4.2}$$

Here, p measures the normalized intensity fraction of the diffraction planes contributing to the crystallographic texture of the sample and the parameter p_0 is the normalized intensity fraction of diffraction planes contribution to the crystallographic texture of a nontextured sample. Since a perfectly random sample was not available, the intensities for a nontextured sample were simulated using the same chemical composition and instrumental parameters.

In addition, the recorded patterns were fitted by the Rietveld method using the March-Dollase (MD) equation [326]. In this model, the intensities of each *hkl* reflection are corrected by a factor $\Pi_{hkl}(f,r,\omega)$, in relation to two predefined crystallographic lattice planes $(h_1k_1l_1)$ and $(h_2k_2l_2)$:

$$\Pi_{hkl}(f,r,\omega) = f \cdot \left(r_1^2 \cdot \cos^2 \omega_{(h_1k_1l_1)} + \frac{1}{r_1} \sin^2 \omega_{(h_1k_1l_1)}\right)^{-\frac{3}{2}} + (1-f)\left(r_2^2 \cdot \cos^2 \omega_{(h_2k_2l_2)} + \frac{1}{r_2} \sin^2 \omega_{(h_2k_2l_2)}\right)^{-\frac{3}{2}} \tag{4.3}$$

In this equation, f indicates the textured volume fraction, r is the degree of texture, and ω is the intersection angle of the lattice planes *hkl* with the lattice planes $(h_ik_il_i)$ $(i{=}1{,}2)$. The software Topas 5 was used for the refinement[2]. Pseudo-Voigt functions and asymmetry correction were used to describe the shape and width of the reflections. The positions of the reflections were determined from refining lattice parameters together with a correction for sample height displacement. Positional parameters were fixed according to the positions reported by Tiwari *et al.* [327]. The model of MD was used to describe the intensity change of reflections resulting from crystallographic texturing. In this respect, a model with two lattice planes, (001) and (100) of preferred orientation was used, where the same MD-parameter was used for both types of lattice planes with additionally fixing their fractional appearance to a ratio of 1:2 according to the theoretical reflection multiplicities.

For microstructural investigations, cross sections of the samples were ground, polished to 0.25 µm, and thermally-etched at 1250° C for 10 min. Thermally-etched surfaces were investigated in a SEM (XL 30 FEG, Philips Corporation, Netherland). The grain size analysis was performed using the linear intercept method (Lince software Version 2.4.2e, Nichtmetallisch Anorganische Werkstoffe, TU Darmstadt, Germany).

Electric characterization of the samples was carried out with a triangular wave signal with a frequency of 0.1 Hz and an amplitude of 3 kV/mm. Characterization of the polarization dynamics was carried our using the setup from Dr. S. Zhukov[3] and is published in details elsewhere [182].

Temperature- and frequency-dependent relative permittivity values were measured on poled samples at frequencies from 1 kHz to 1 MHz with a measurement voltage of 1 V between room temperature and 200 °C at a heating rate of 2 °C/min. An impedance analyzer 4192A (Hewlett Packard Corporation, CA, USA) was used for the measurement. The

---

[1] The group of Prof. Sakamoto from Nagoya University is acknowledged for the preparation of the samples.

[2] Ass. Prof. Dr. O. Clemens is acknowledged for helping with refinement of the diffraction data.

[3] Dr. S. Zhukov is acknowledged for providing the measurement data.

Curie temperature was taken as the temperature of the maximum of the loss factor. To investigate the thermally-stimulated depolarization current (TSDC), measurements in short-circuit mode have been performed. The samples were heated with a constant rate of 3 °C/min, while the discharge currents were monitored by a Keithley electrometer (Keithley, Model 617, OH, USA). Before TSDC measurements, the samples were poled by a positive electric field of 2 kV/mm applied for 10 min at ambient temperature and short circuited for 30 min to remove any unstable contributions of polarization.

4.2 Electric measurements

4.2.1 Pulse large signal measurements

The dynamics of the polarization reversal can be characterized if the response of a poled material to a pulse electric field is measured on the logarithmic time scale. [13] An experimental setup and measurement technique was described by von Seggern and Fedosov [328] for ferroelectric polymers, which was later transferred to polycrystalline ferroelectric ceramic materials by Zhukov *et al.* [100]. The aim of this section is to describe the electric circuit and remote control of the experimental setup and the treatment of the raw data.

Experimental approach

The electric field sequence displayed in Fig. 4.1 is applied to the polycrystalline material in order to measure its polarization reversal dynamics. Thereby, the material is poled with an electric field E_P for a time t_P. After poling, the sample was allowed to relax for a waiting time of t_w. The actual **switching** was performed with a HV pulse of height E_{Sw} for a time t_{Sw}. Then the material was poled again with the parameters E_P and t_P. A **reference** measurement was performed with a HV pulse of height E_{Sw} for a time t_{Sw}.

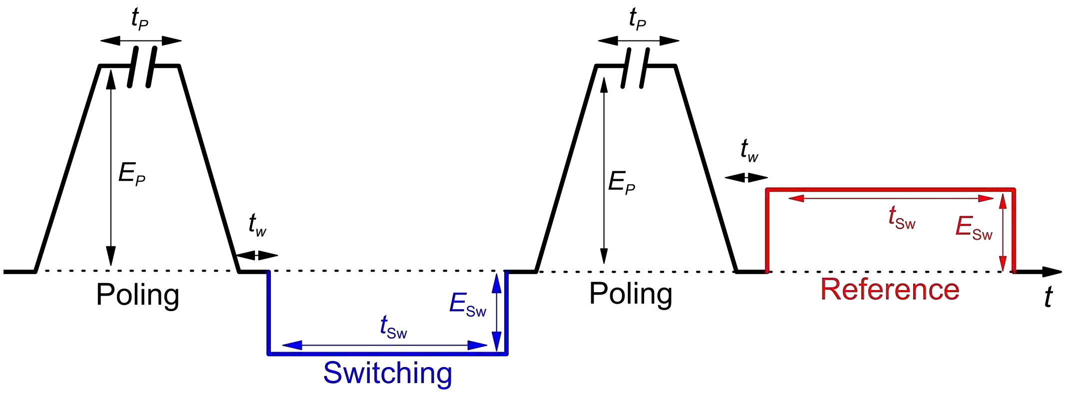

Figure 4.1.: Electric field sequence to measure the polarization reversal dynamics in ferroelectric materials. The symbols are explained in the text. The switching measurement is marked in blue, while the reference measurement is marked in red [After Ref. [100]].

Experimental setup

Experimentally, the polarization switching method is challenging because a setup is required, which provides a sharp HV pulse with a sufficiently small rise time and no overshoot. Also, data acquisition on a logarithmic time scale over several orders of magnitude, usually spanning from 1 µs to 10 s, needs to be realized.

The setup was constructed by combining commercially available equipment and a self-built HV Fast Switch, schematically shown in Fig. 4.2a. The control element of the setup was a USB measurement card (USB-6211, National instruments, Austin, TX, USA), which allowed to control the setup by analog and digital output channel and data acquisition. The control of the setup was in particular realized by HV relays[1] (H Serie, Meder electronic, Großbreitenbach, Germany) in the HV Fast Switch. They can be switched by 5 V signals, provided by the analog output channels of the measurement card. In the following terminology, a HV relay is activated and the original state is switched, if a 5 V pulse is provided.

---

[1] The maximum voltage of the HV relays is 10 kV [329].

The HV pulses were realized by a commercial HV transistor switch (HTS 41-06-GSM, Behlke GmbH, Kronberg, Germany)[1], which can switch between HV and ground. A schematic electric circuit of the HV Fast Switch showing all important elements is displayed in Fig. 4.2b. The HV is provided by a buffer capacitor with a capacity of C_B=2 µF, which is charged by a HV source (Trek Model 20/20C, Lockport, NY, USA), and allows to provide a voltage V_0. A voltmeter connected in parallel to the buffer capacitor is used to monitor the charge on the capacitor. The charging of the capacitor can be controlled by two HV relays K1/1 and K1/2. If activated, the buffer capacitor can be charged, if not activated, the buffer capacitor is ground.

The HV transistor switch is triggered by a 5 V[2] pulse, provided by a function generator (Agilent 33220A, Santa Clara, CA, USA). The HV transistor switch is protected by two current limiting resistances R_S.[3] A tradeoff between speed and protection has to be found and for all experiments in this work a protection resistance of R_S=100 Ω was used. In case of a breakdown of the sample the voltage drop will occur at these resistances. The shape of the HV pulse provided by the HV Fast Switch is shown in Fig. 4.3. 75 % of the maximum voltage is reached after 115 ns, while 100 % is reached after 250 ns.

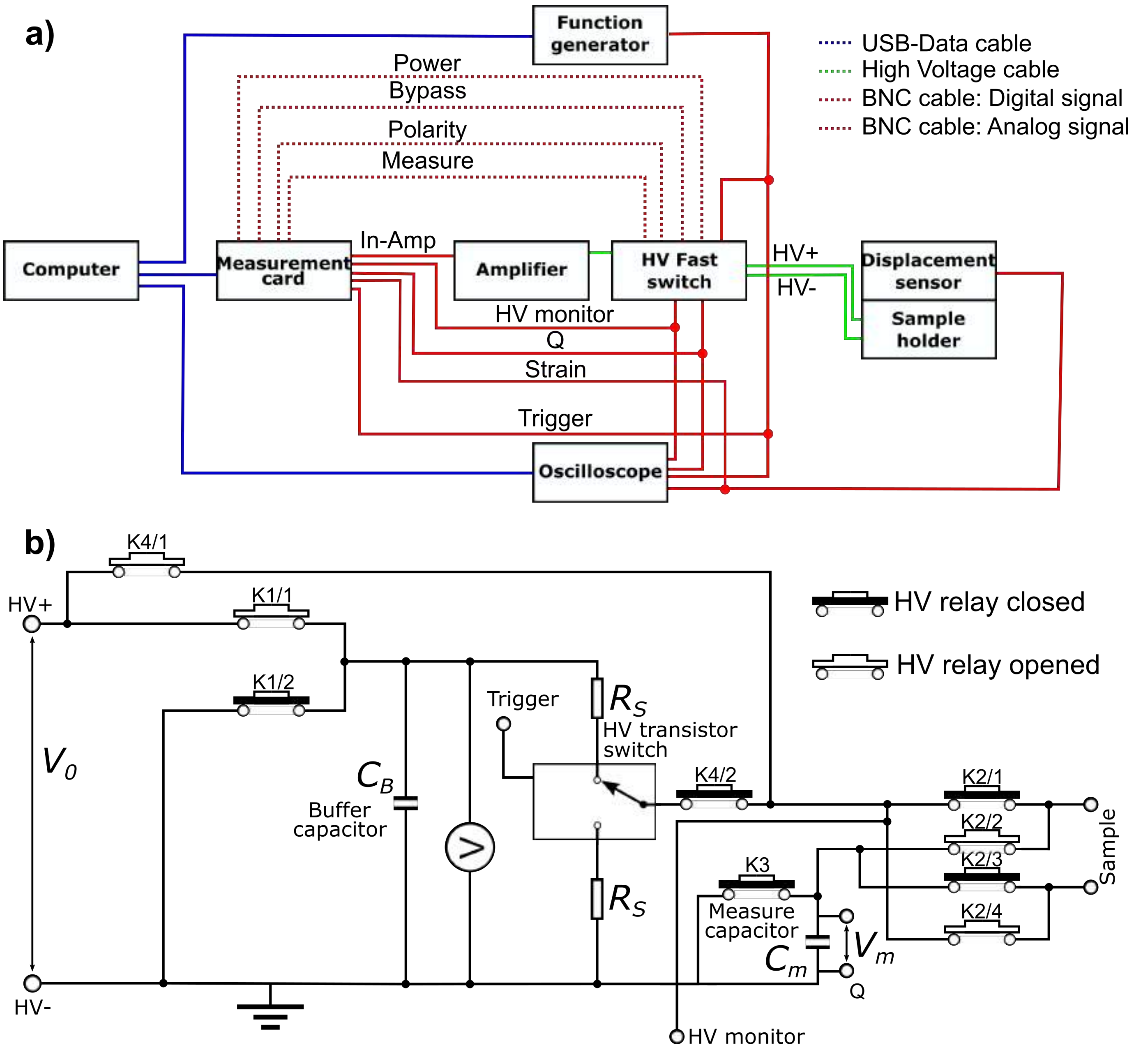

Figure 4.2.: Experimental setup to measure switching dynamics using HV pulses. a) Schematic integration of the HV Fast Switch and combination with other electric equipment to realize simultaneous measurement of polarization and strain. b) Schematic electric circuit of the HV Fast Switch showing the most important elements. The HV relays are shown in the non-activated state. All terms are explained in the text.

---

[1] The maximum operating voltage and peak current capability of this model is $V_{0_{\max}}$=4 kV and $I_{P_{\max}}$=60 A, respectively [330].

[2] Please note that any trigger voltage above 5 V will destroy the HV transistor switch irreparable.

[3] The resistance R_S will determine the rising time of the HV pulse at the sample. A higher resistance value will decrease the rising time dramatically. On the other hand, the resistance R_S will determine the maximum applicable voltage $V_0=R_S I_{P_{\max}}$.

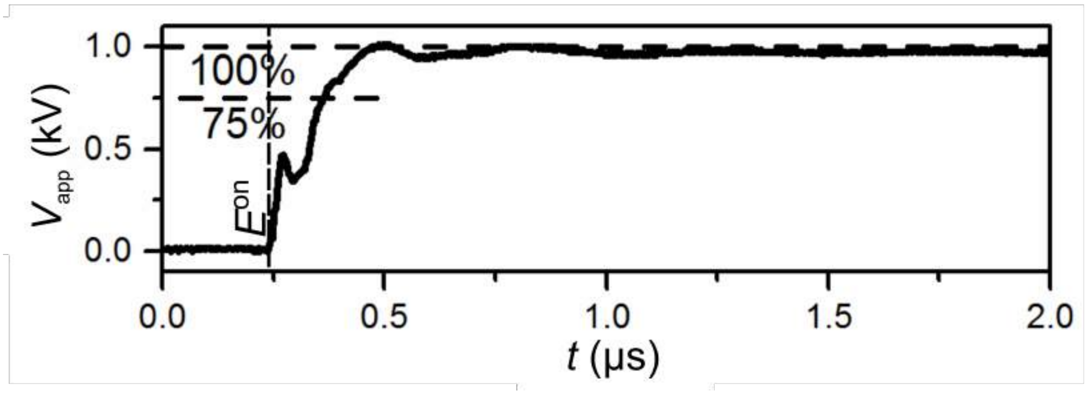

Figure 4.3.: HV pulse provided by the HV Fast Switch. HV pulse provided by the HV Fast Switch setup of height V_{app} during polarization reversal for a commercial PZT sample. A protection resistance of R_s=100 Ω was used. The time when the electric field is switched on is marked by a vertical dashed line.

The poling of the sample does not require a sharp HV pulse. In order to apply the HV from the amplifier directly to the sample, a bypass was realized by a combination of two HV relays K4/1 and K4/2. If activated, the bypass-path is active, if not activated, the switching/reference-path is active.

The poling/reference measurement requires a change of polarity of the sample, which was realized by four HV relays, K2/1, K2/2, K2/3, and K2/4. If they are activated, the polarity of the sample changes and the reference measurement is realized. If they are not activated, the switching measurement is realized.

A modified Sawyer-Tower-circuit [331] was used in order to measure the electric displacement of the sample. Therefore a measurement capacitor C_m[1] (WIMA MKS4, Wima, Mannheim Germany) was connected in series to the sample and the voltage drop V_m across the capacitor was read by a high input impedance operational amplifier (LF356, Texas Instruments, Dallas, TX, USA). The electric displacement was calculated as

$$D = \frac{V_m \cdot C_m}{A}, \tag{4.4}$$

where A is the area of the sample. The measurement capacitor can be short circuited by a HV relay K3. If activated, the measurement is possible, if not activated, the measurement capacitor is short-circuited and the charge on the capacitor is deleted. The HV signal was read directly at the sample. The HV monitor signal has a ratio of 500 V:1 V.

The simultaneous measurement of the macroscopic strain of the sample was realized by an optical displacement sensor (LF356, Texas Instrument, Dallas, TX, USA) with a time resolution of 0.1 ms[2]. The setup for time-dependent displacement measurements is schematically shown in Fig. 4.4. The change of the macroscopic dimensions of the sample in the direction of the applied electric field, $l(t)$, allowed to calculate the sample's strain dynamics

$$S(t) = \frac{l(t) - l_{\text{init}}}{l_{\text{init}}}, \tag{4.5}$$

where l_{init} is the dimension of the sample after electric poling.

Data recording on the logarithmic time scale was realized by two simultaneous data acquisition techniques. The sample's response on the fast time domain (10^{-6} s–$5 \cdot 10^{-4}$ s) was measured by an oscilloscope (Agilent MSO7014B, Santa Clara, CA, USA), while the slow time domain ($>10^{-4}$ s) was recorded by a measurement card (USB-6211, National instruments, Austin, TX, USA).

---

[1] The size of the capacitor will depend on the area of the sample, as well as on the electric displacement of the sample and needs to be optimized in order to reduce the noise of the measurement signal. For all experiments in this work a measurement capacitor in a range between C_m=2.2 μF to C_m=9.8 μF was used.

[2] Please note that the displacement sensor has a 3 dB cutoff frequency at 200 kHz [332]. The low time resolution of 0.1 ms is a result of the setup used (Fig. 4.4), which transfers the displacement of the sample via a mechanical spring and a mirror to the glass fiber and the optical displacement sensor.

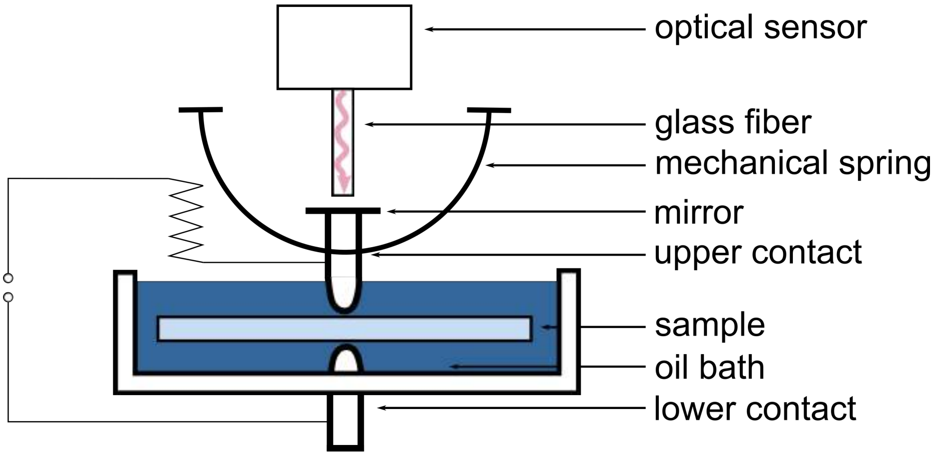

Figure 4.4.: Scheme of the setup for time-dependent displacement measurements.

Remote control

The experimental setup is remote controlled by a LabView program with a front panel shown in Fig. 4.5.

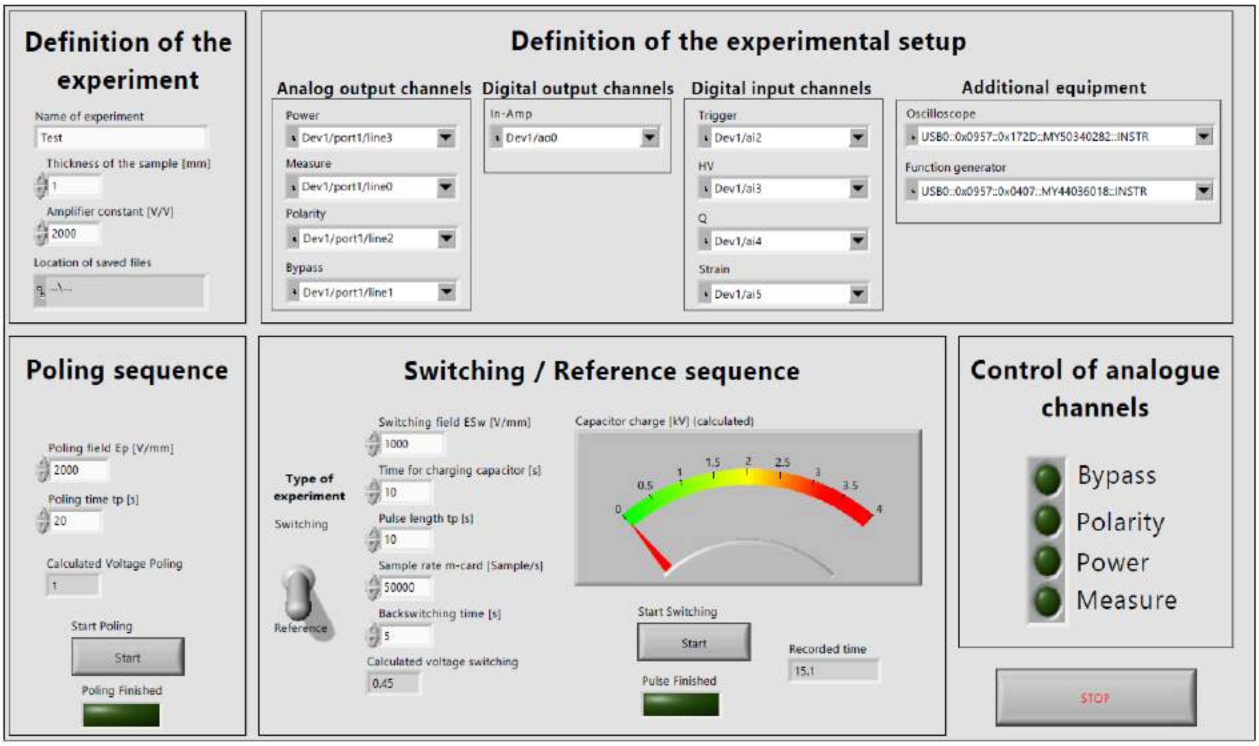

Definition of the experiment

Name of experiment: Test
Thickness of the sample [mm]: 1
Amplifier constant [V/V]: 2000
Location of saved files: ...\...

Definition of the experimental setup

Analog output channels
Power: Dev1/port1/line3
Measure: Dev1/port1/line0
Polarity: Dev1/port1/line2
Bypass: Dev1/port1/line1

Digital output channels
In-Amp: Dev1/ao0

Digital input channels
Trigger: Dev1/ai2
HV: Dev1/ai3
Q: Dev1/ai4
Strain: Dev1/ai5

Additional equipment
Oscilloscope: USB0::0x0957::0x172D::MY50340282::INSTR
Function generator: USB0::0x0957::0x0407::MY44036018::INSTR

Poling sequence

Poling field Ep [V/mm]: 2000
Poling time tp [s]: 20
Calculated Voltage Poling: 1

Switching / Reference sequence

Type of experiment: Switching / Reference
Switching field ESw [V/mm]: 1000
Time for charging capacitor [s]: 10
Pulse length tp [s]: 10
Sample rate m-card [Sample/s]: 50000
Backswitching time [s]: 5
Calculated voltage switching: 0.45
Recorded time: 15.1

Control of analogue channels

Figure 4.5.: Front panel of the LabView program used to remote control the Fast Switch. In the first row the experiment and the experimental setup are defined. The second row allows to run a poling or switching/reference sequence. On the right, the status of the analog channels is monitored.

Before an experiment can be started, the respective connections for the input and output channels at the measurement card have to be defined and the required equipment has to be added. Also the following parameters have to be defined:

- **Name of experiment:** Name of the current experiment.[1]
- **Thickness of the sample [mm]:** Required to calculate the input voltage for the amplifier.

---

[1] The applied electric field during switching as well as the measurement type (switching/reference) will be automatically added to the sample name when the file is created.

- **Amplifier constant [V/V]:** The amplification constant is a characteristic device value of the amplifier used. It is required to calculate the input voltage for the amplifier.

- **Poling field [V/mm]:** Defines the maximum field applied during poling.

- **Poling time [s]:** Defines the time during which the poling field is applied.

- **Type of experiment:** The switch allows to change between different types of experiments: switching and reference.

- **Switching field [V/mm]:** Defines the height of the field applied during the switching/reference sequence.

- **Time for charging capacitor [s]:** Defines the time, during which the capacitor is charged.

- **Pulse length [s]:** Defines the time during which the HV pulse is applied.

- **Sample rate m-card [Sample/s]:** Defines the amount of data points per second which are read by the measurement card.[1]

- **Backswitching time [s]:** Defines the additional time which is read out after the electric field is switched off.

The second row of the program allows to run the poling and switching/reference sequence. The respective flow charts are displayed in Fig. 4.6a and b. They will be explained in detail in the following section. After pressing the start button the respective sequence will run automatically.

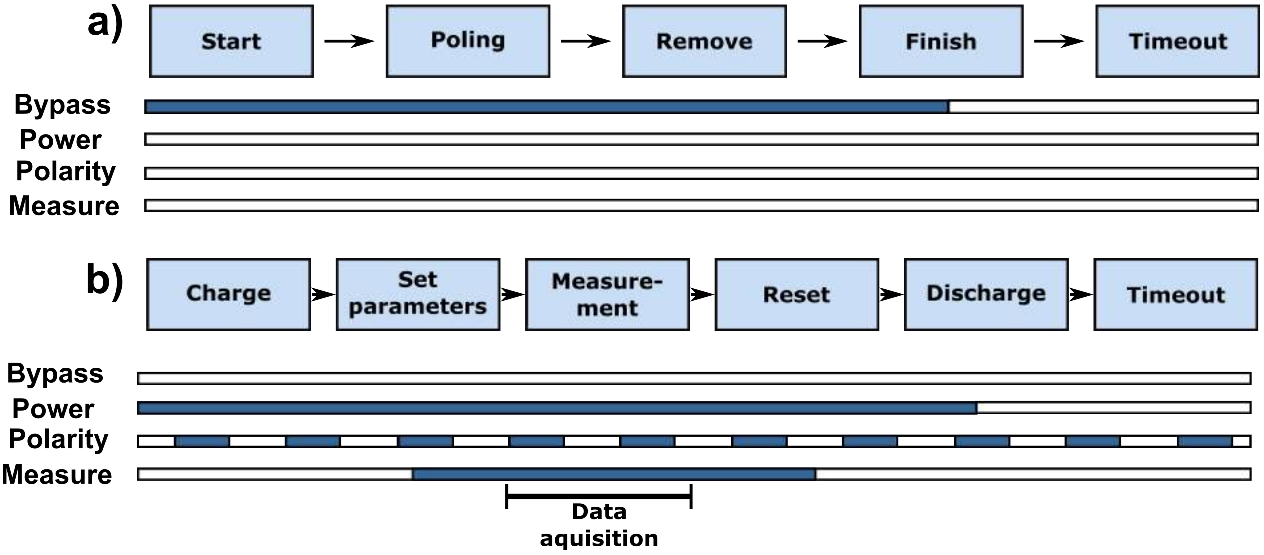

Figure 4.6.: Steps of the LabView program during the a) poling and b) switching/reference sequence. The lines show the analog output signal channels, which control the HV relays. The color blue indicates that the respective channel is activated. Please note that the polarity channel in b) is either switched on or off, depending on the type of experiment (switching/reference).

The poling sequence (Fig. 4.6a) **start**s with activating the bypass. In the **poling** step the voltage is increased with 0.1 Hz up to the set poling field. After the field is applied for a defined poling time, it is **remove**d with 0.1 Hz. The sequence **finish**es with deactivating the bypass and tagging the label 'Poling Finished' on the front panel of the LabView program (Fig. 4.5). Then the program goes back to **timeout** where it waits for the next command.

For the switching/reference sequence (Fig. 4.6b) the bypass channel is always deactivated and depending on the type of measurement (switching/ reference), the polarity channel is either activated or deactivated. In the first step, the buffer capacitor is **charge**d with a voltage that corresponds to the switching field. Therefore, the power channel is activated.

---

[1] The maximum amount of data points that can be read out depends on the total amount of time for which the data is recorded. For example, a measurement of 10 s allows a sample rate of 50000 samples/s, while a measurement of 1000 s is limited to 5000 samples/s. A recording on the logarithmic time scale is not possible due to software issues.

In the second step, the LabView program **set**s the **parameters** for the function generator[1] and the oscilloscope[2]. The measure channel is activated. When the **measurement** is started, the program continuously reads out the signals from the measurement card and saves the data in a TDMS file, using the continuous sample mode. After a waiting time of 1 s, the function generator sends a trigger pulse of 10 V[3] for the switching time. This pulse simultaneously triggers the HV transistor switch and the oscilloscope. The former provides the HV pulse to the sample, while the later starts data aquisition with a very high time resolution. The data from the oscilloscope are read out after the measurement is finished and are saved to the same TDMS file. In the next step, the oscilloscope is **reset** and the measurement channel is deactivated, which short-circuits the measurement capacitor of the Sawyer-Tower circuit. The buffer capacitor is **discharge**d by deactivating the measure channel, which grounds the buffer capacitor. The program is waiting in the **timeout** for the next command.

Data analysis

A representative measurement for the switching and reference cycle is shown in Fig. 4.7a for the switching sequence and Fig. 4.7b for the reference sequence. The blue datapoints represent the measurement on the fast time domain, while the black data points represent the measurement on the slow time domain.

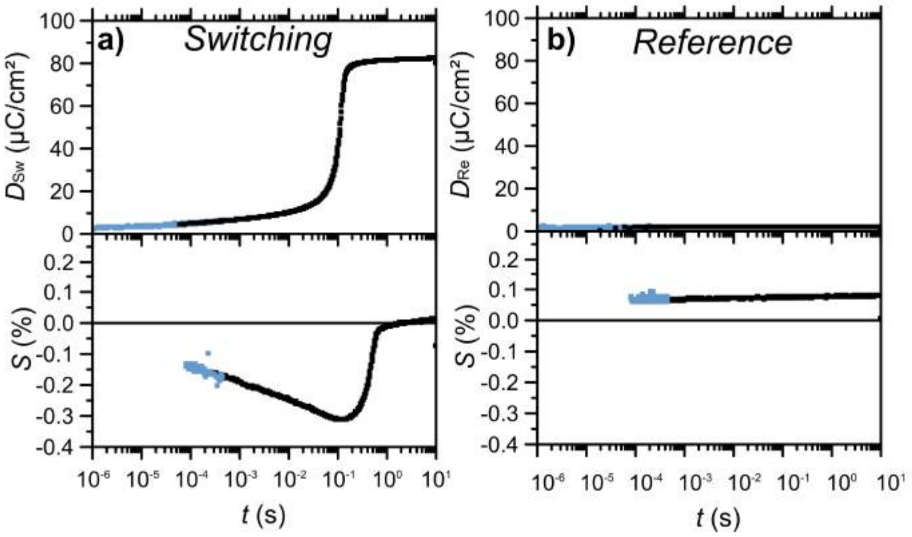

Figure 4.7.: Representative measurements of the electrical displacement and strain of a PZT sample during the a) switching and b) reference sequence. The data points in blue represent the measurement done by the oscilloscope on the fast time domain, while the datapoints in black represent the slow time domain measured by the measurement card.

The electric response during the switching sequence (D_{Sw}, electric field applied *opposite* to the poling direction) contains contributions from the switched polarization ΔP, the sample's dielectric displacement D_{di}, and the integrated leakage current D_{lkg} [328]:

$$D_{\mathrm{Sw}} = \Delta P + D_{\mathrm{di}} + D_{\mathrm{lkg}} \tag{4.6}$$

On the other hand, the reference sequence (D_{Re}, electric field applied *in* the poling direction) only contains contributions from the dielectric displacement and the integrated leakage current.

$$D_{\mathrm{Re}} = D_{\mathrm{di}} + D_{\mathrm{lkg}} \tag{4.7}$$

---

[1] A pulse function with a DC offset of 2.5 V and an amplitude of 5 V is used. The burst mode is enabled and the burst count is set to 1. The trigger source is 'software' and the pulse width and period is set according to the pulse length. The output is switched on and the function generator is waiting for the trigger from the LabView program in order to send the pulse.

[2] The acquisition mode of the oscilloscope is 'continuous'. Each channel is set to 'DC' and the measurement range for each channel is set according to the expected voltage. All channels are calibrated to zero, except the strain channel, which is calibrated according to the recent voltage value, which is read out from the displacement sensor. The record length was set to 'MAX' and the time base and start time were set to t_b and a value smaller than $t_b/2$, respectively. In most experiments a value of t_b=0.0005 s was used. A positive 'edge' trigger with a trigger level of 1 V was used and the trigger channel is the channel coming from the function generator. Then the waveform acquisition is initialized and the oscilloscope is waiting for the trigger input from the function generator.

[3] Please note that due to the internal impedance of the HV Push Pull switch, the pulse is reduced to 5 V.

If the time dependence of both contributions is known, the time-dependent switched polarization can be calculated by subtracting both values for any time:

$$\Delta P(t) = D_{\mathrm{Sw}}(t) - D_{\mathrm{Re}}(t) \tag{4.8}$$

4.2.2 Bipolar measurements

For bipolar polarization and strain measurements using a triangular field, the same optical displacement sensor and a measurement capacitor, as previously described, was used. The additional setup described here was used for simultaneous measurement of small signal properties.

A commercial piezoelectric evaluation system (aix-ACCT Systems, Aachen, Germany) was used for the bipolar electromechanical measurements. Large signal measurements were performed with a bipolar triangular signal of 2 kV at a frequency of 0.05 Hz. For the small signal permittivity, κ_{33}, and piezoelectric coefficient, d_{33}, measurements, a waveform of 1 kHz and 10 V/mm was modulated on top of a base waveform of 2 kV/mm and 0.05 Hz.

4.3 *In situ* diffraction experiments

The experimental setup to simultaneously measure dynamic polarization, strain, and high-energy diffraction using HV pulses is shown in Fig. 4.8.

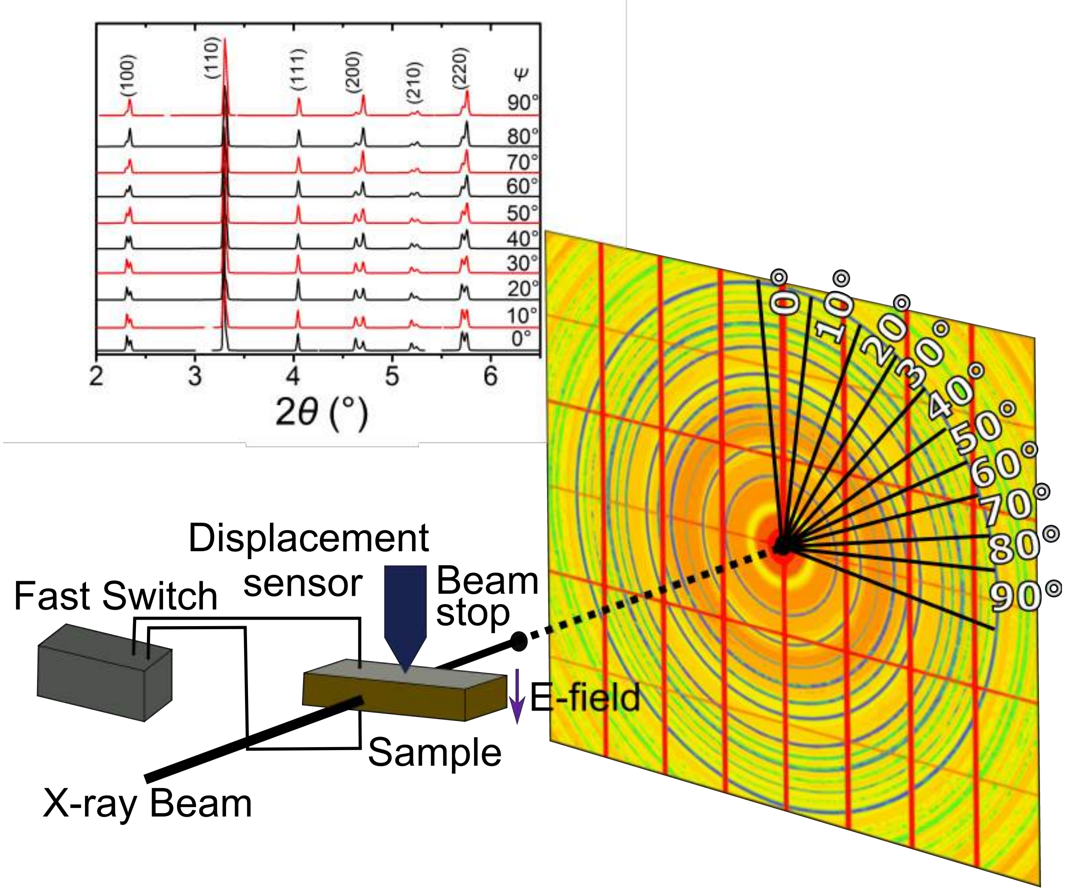

Figure 4.8.: ***In situ* diffraction experiments.** Schematic representation of the setup to measure dynamic polarization, strain, and structural changes simultaneously. Different azimuthal section with the azimuthal angle Ψ are shown at the detector image. Radially integrated diffraction intensities of a poled PZT sample at different azimuthal angles are shown in the upper left.

In situ diffraction experiments were carried out at beamline ID15a of the European Synchrotron Radiation Facility (ESRF) using a beam energy of 75 keV (16.5 pm wavelength) in transmission geometry. Further information about the diffraction geometry can be found elsewhere. [333; 334] Diffraction intensities were collected using a Pilatus CdTe 2M area detector with a time resolution of 4 ms. The 5 V signal provided by the function generator (Fig. 4.2a) was split and was used to trigger the detector. 3500 images were recorded for a pulse length of $t_{\mathrm{SW}}=10$ s in order to realize simultaneous measurement of polarization, strain, and structure.

The diffraction image from the detector (Fig. 4.8) was corrected for dead pixels, beam stop shadow and image distortion. For the latter a reference measurement was carried out using a CeO_2 sample. The white areas in Fig. 4.8 are a result of this correction and represent areas of zero intensity. The 36 azimuthal cakes were radially integrated in the 2θ range from 2–9 °. The 36 azimuthal cakes are shown as a function of 2θ in Fig. 4.9a. The different azimuthal cakes contain information of domains oriented with their polar axis at an angle Ψ to the electric field. The material investigated by high-energy diffraction was a tetragonal PIC151. Therefore, the (111) peak contains information on the lattice strain, ε_{111}, while the (200) peak contains information on the domain switching fraction, η_{200}. In a tetragonal material the (111) peak is a singlet, while the (200) peak is a doublet.

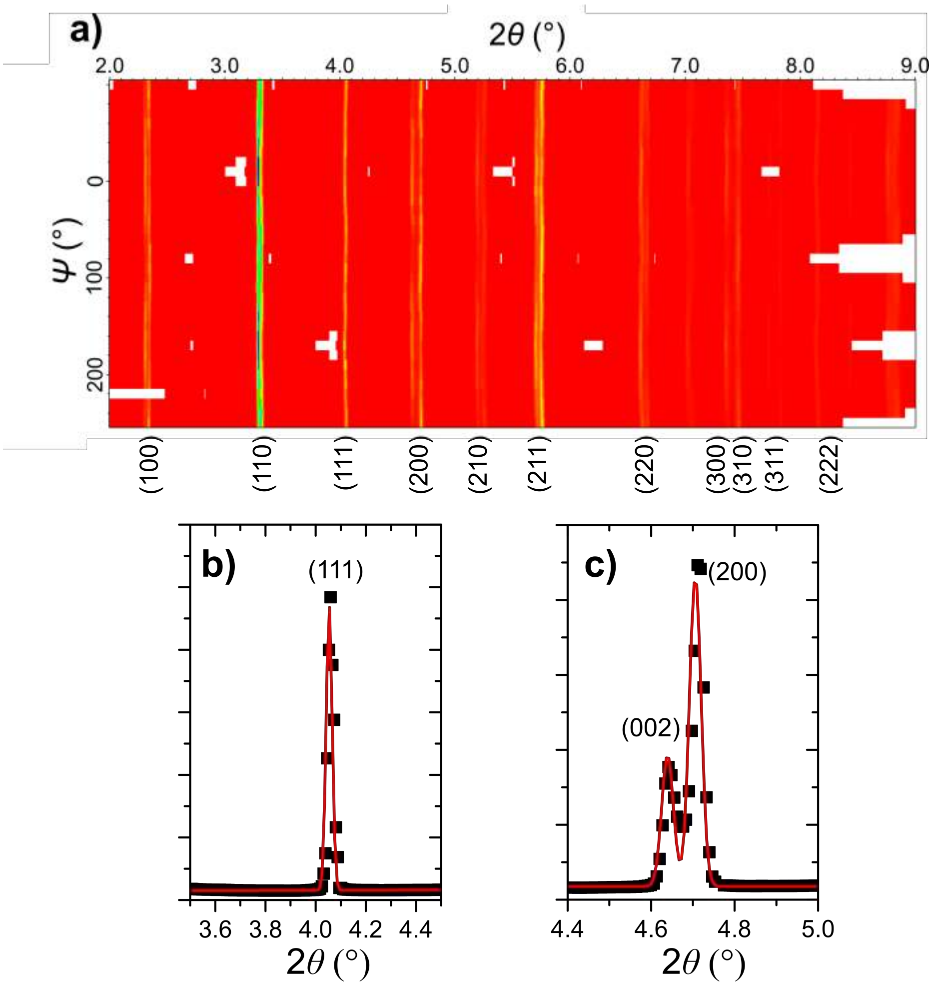

Figure 4.9.: Diffraction data analysis. a) Radially integrated diffraction data for the 36 different azimuthal angles Ψ of a poled PIC151 material. The schematic fitting is shown for a b) (111) and a c) (200) peak using Gaussian functions.

In the next step, the intensity profiles of the (111) and (200) peak were fitted using Gaussian functions. For the intensity of the (111) peak a single Gaussian function was used.

$$\begin{gathered} I(x) = d + e \cdot x + a \cdot (g_1/c) \exp\left(\left(-g_2 \cdot \left((x-b)^2/c^2\right)\right)\right) \\ x = 2\theta \end{gathered} \tag{4.9}$$

For the intensity of the (200) peak a double Gaußian function was used.

$$\begin{gathered} I(x) = d + e \cdot x + a \cdot (g_1/c) \exp\left(\left(-g_2 \cdot \left((x-b)^2/c^2\right)\right)\right) + f \cdot (g_1/c) \exp\left(\left(-g_2 \cdot \left((x-(b+g))^2/c^2\right)\right)\right) \\ x = 2\theta \end{gathered} \tag{4.10}$$

The parameters a, b, c, d, e, f, and g are fitting parameters, while g_1 and g_2 are defined as follows.

$$g_1 = 2\sqrt{\frac{\ln 2}{\pi}} \qquad g_2 = 4\ln 2 \tag{4.11}$$

The fitting procedure is schematically shown in Fig. 4.9b and c for a (111) and a (200) peak, respectively. The position of the (111) peak and the intensity of the (200) peaks are important for further analysis. In this context, the fitting parameter $b = \theta_{111}$ (Eqn. 4.9) represents the position of the (111) peak, while the fitting parameters $a = I_{002}$ and $f = I_{200}$ (Eqn. 4.10) correspond to the intensity of the (002) and (200) peaks, respectively. The volume fraction of domains with their polar axis for any azimuthal angle is given by:

$$\Xi_{002}(\Psi) = \frac{\frac{I_{002}}{I'_{200}}}{\frac{I_{002}}{I'_{002}} + 2\left(\frac{I_{200}}{I'_{002}}\right)} \tag{4.12}$$

Here, I_{hkl} represents the intensity of the respective hkl peak, while I'_{hkl} represents the intensity in a virgin unpoled sample. The domain switching fraction with respect to a virgin sample can be calculated as [335]

$$\eta_{002}(\Psi) = \Xi_{002}(\Psi) - \frac{1}{3}. \tag{4.13}$$

The lattice strain was calculated with respect to a virgin sample as [336][1]

$$\varepsilon_{111} = -\left(\theta_{111} - \theta'_{111}\right) \cdot \cot(\theta_{111}). \tag{4.14}$$

Here, ε_{111} represents the 2θ position of the (111) peak, while θ'_{111} represents the peak position in a virgin sample.

4.4 Piezoresponse Force Microscopy

PFM was used to study the domain structure of a poled sample. In addition, PFM was applied in order to investigate the influence of grain size on domain configuration and size.

4.4.1 Poled samples

Sample preparation

Platinum electrodes were sputtered on round PIC151 samples. A diamond saw was used to cut a $1 \text{x} 1 \text{x} 10 \text{mm}^3$ bar-shaped sample. The surface perpendicular to the electrodes was prepared for PFM measurements. After grinding, they were polished to 0.25 µm (DP-Paste M, Struers, Ballerup, Denmark) and subsequently colloidal silica with particle sizes below 50 nm (Master Prep, Buehler, Lake Bluff, IL, USA) for 5 seconds was used to ensure slight etching of the grain boundaries. The sample was annealed to release any mechanical stresses at 500 °C for one hour with a cooling rate of 0.5 °C/min. In the next step, the sample was cycled 20 times at a frequency of 0.5 Hz at 3 kV/mm, followed by poling with 3 kV/mm at a frequency of 0.1 Hz.

Prior to measurement in the PFM the surface of the sample was cleaned by acetone at room temperature to remove the dust on the surface of the sample.

PFM measurements

The domain structure was studied by the Scanning Probe Microscope MFP-3D$^{\text{TM}}$ (Oxford Instruments, Abingdon, United Kingdom)[2]. The surface of the sample was scanned with a sharp tip, coated with W_2C (HA_NC/W2C+, NT-MDT Spectrum Instruments, Moscow, Russia), acting as a top electrode. The sample was grounded via the bottom electrode. An AC wave

---

[1] Please note that the angles θ_{111} and θ'_{111} are inserted with the unit *rad* into the equation.

[2] The equipment of the Ural Center for Shared Use of Nanotechnology, Ural Federal University was used.

of 7 V amplitude was applied with a frequency of 21 kHz (single frequency mode) and an area of 30x30 µm^2 was scanned. The application of an electric signal causes a local oscillation of the sample due to the converse piezoelectric effect, which can be detected as amplitude ι and phase shift Φ. The vertical displacement of the material is referred to as out-of-plane PFM signal, while the shear deformation contributes to the in-plane signal. The results of the measurement are displayed as

$$x = \iota \cdot \cos(\Phi) \tag{4.15}$$

and

$$y = \iota \cdot \sin(\Phi), \tag{4.16}$$

shown in Fig. 4.10a. Background-free data would solely lie on the y axis, while the x-part can be considered as mainly originating from background and noise. [337] The PFM data is corrected by mathematical translation and rotation of the data, as indicated by the arrows in Fig. 4.10a, and the corrected data is presented in Fig. 4.10b. The $\iota\sin(\Phi)$ image after correction is shown in Fig. 4.10c, while the $\iota\cos(\Phi)$ image, which contains almost no image information, is displayed in Fig. 4.10d.

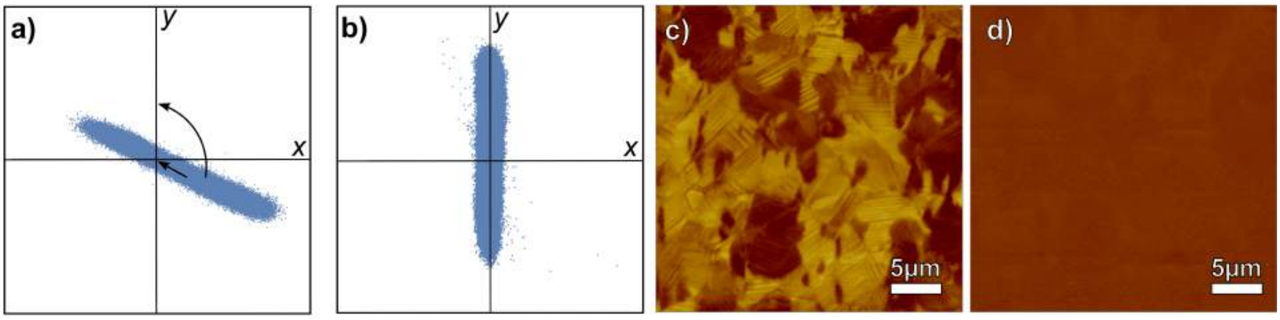

Figure 4.10.: PFM data analysis. The PFM data represented in a *xy* graph a) before and b) after offset and background correction. The arrows indicate the mathematical translation and rotation of the data. c) $\iota\sin(\Phi)$ image after subtraction and alignment of the data. d) $\iota\cos(\Phi)$ image after correction, which mainly contains noise and almost no image information.

4.4.2 Domain size

Sample preparation

After grinding, the samples for the domain size investigations were polished with diamond abrasive from to 0.25 µm (DP-Paste M, Struers, Ballerup, Denmark) surface finish. Fine polishing was done by colloidal silica with particle sizes below 50 nm (Master Prep, Buehler, Lake Bluff, IL, USA) for 1.5 h. Before the image collections the samples were cleaned in distilled water.

PFM measurements

The topography and the PFM images were recorded with an atomic force microscope (Asylum Research, Molecular Force Probe 3D, Santa Barbara, CA, USA)[1]. Electric field was applied between a conductive PFM tip and the bottom electrode, which was electroded with conductive silver paste. Ti/Ir-coated Si tips (Asyelec-01, AtomicForce F&E GmbH, Mannheim, Germany) with a radius of curvature ≈28 nm were used. The PFM out-of-plane amplitude images were scanned in a PFM Dual AC Resonance Tracking mode at 4–8 V and a frequency of ≈300 kHz.

In all samples the scanned AC amplitude was 2/3 of the voltage required for local domain switching, determined from local hysteresis loops measured in the switching spectroscopy mode. The waveform parameters were: increasing step signal (maximum amplitude of 35 V and frequency of 0.2 Hz) with an overlapping sinusoidal signal (4 V and 20 Hz).

---

[1] Ass. Prof. Dr. Hana Uršič is acknowledged for providing the PFM images.

The Gibbs free energy ΔG of a single ferroelectric domain can be expressed as an expansion in terms of the polarization components P_1, P_2, and P_3 [40] (extending Eqn. 2.5):

$$\begin{aligned}\Delta G\left(P_1,P_2,P_3\right) = \alpha_1\left(P_1^2+P_2^2+P_3^2\right)+\alpha_{11}\left(P_1^4+P_2^4+P_3^4\right)+\alpha_{12}\left(P_1^2P_2^2+P_2^2P_3^2+P_1^2P_3^2\right)+\\ +\alpha_{111}\left(P_1^6+P_2^6+P_3^6\right)+\alpha_{112}\left[P_1^2\left(P_2^4+P_3^4\right)+P_2^2\left(P_1^4+P_3^4\right)+P_3^2\left(P_1^4+P_2^4\right)\right]+\\ +\alpha_{123}\left(P_1^2P_2^2P_3^2\right)-0.5s_{11}\left(\sigma_1^2+\sigma_2^2+\sigma_3^2\right)-\\ -s_{12}\left(\sigma_1\sigma_2+\sigma_1\sigma_3+\sigma_2\sigma_3\right)-0.5s_{44}\left(\sigma_4^2+\sigma_5^2+\sigma_6^2\right)-\\ -Q_{11}\left(\sigma_1P_1^2+\sigma_2P_2^2+\sigma_3P_3^2\right)-\\ -Q_{12}\left[\sigma_1\left(P_2^2+P_3^2\right)+\sigma_2\left(P_1^2+P_3^2\right)+\sigma_3\left(P_2^2+P_1^2\right)\right]-\\ -Q_{44}\left(\sigma_4P_2P_3+\sigma_5P_1P_3+\sigma_6P_2P_1\right)+EP_3\end{aligned} \tag{4.17}$$

Here α_i, α_{ij}, and α_{ijk} are the dielectric stiffness coefficients at constant stress, s_{ij} are the elastic compliances, Q_{ij} are the electrostrictive constants, and σ_i are the stress components in Voigt notation. In this notation, the components of the symmetric stress tensor can be expressed as

$$\sigma = \begin{bmatrix}\sigma_1 & \sigma_6 & \sigma_5\\ & \sigma_2 & \sigma_4\\ \mathrm{sym} & & \sigma_3\end{bmatrix}. \tag{4.18}$$

The electric field E is applied parallel to direction 3.

In this work, two dimensional representations of Eqn. 4.17 were used in order to reduce the number of necessary parameters and to limit the complexity. Therefore, the allowable polarization directions were limited to one representative plane. For the tetragonal case $P_2 = 0$, while for the rhombohedral case $P_1 = P_2 \neq 0$ was used. [338] The representative plane of interest for the two dimensional Landau representations are displayed in Fig. 4.11a and Fig. 4.11b for a tetragonal and rhombohedral crystal structure, respectively. Within this plane both 180° and non-180° switching processes can be described.

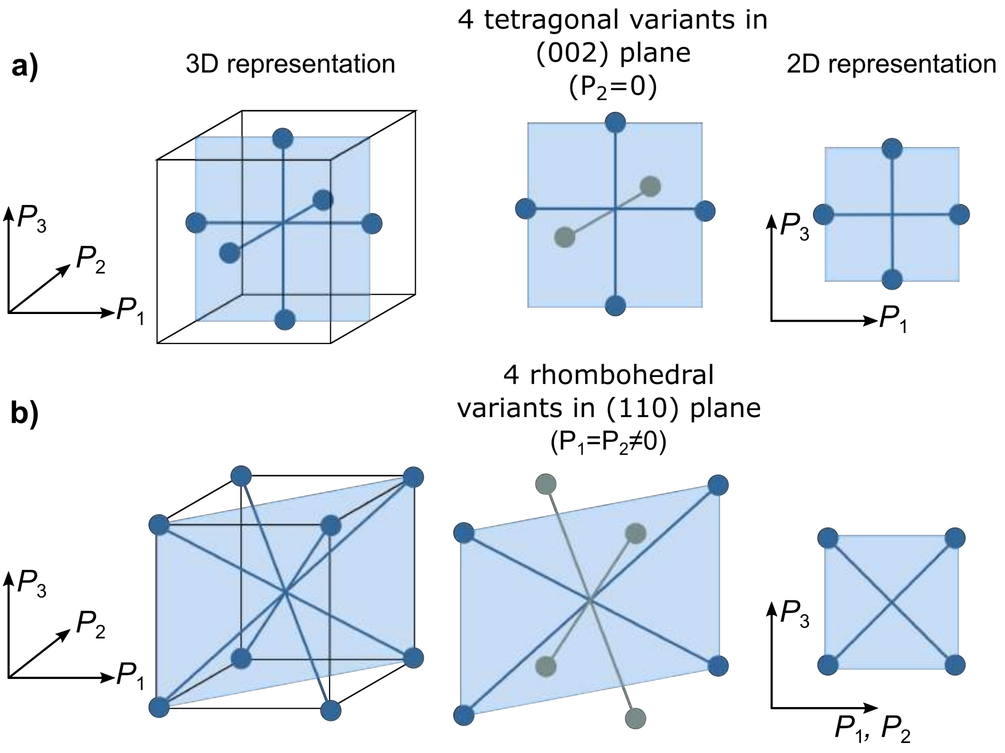

Figure 4.11.: Two dimensional pseudocubic Landau representations for a a) tetragonal and b) rhombohedral crystal structure. The blue dots represent the stable variants of the tetragonal and rhombohedral phases, while the plane of interest for the two dimensional Landau representation is highlighted.

Dielectric stiffness coefficients, elastic compliance, and electrostrictive constants given in Ref. [41], which are based on reports by Haun *et al.* [40], were used. The values for rhombohedral Pb($Zr_{0.7}Ti_{0.3}$)O_3 and tetragonal Pb($Zr_{0.4}Ti_{0.6}$)O_3 at room temperature are summarized in Tab. 4.1.

Table 4.1.: Landau coefficients for a rhombohedral ($Pb(Zr_{0.7}Ti_{0.3})O_3$) and tetragonal ($Pb(Zr_{0.4}Ti_{0.6})O_3$) crystal structure. Calculated from Ref. [41].

Coefficient	Tetragonal	Rhombohedral	Units
α_1	-8.87	-8.78	$10^7\ m^2N/C^2$
α_{11}	3.61	2.23	$10^7\ m^6N/C^4$
α_{12}	3.23	1.69	$10^8\ m^6N/C^4$
α_{111}	1.86	3.56	$10^8\ m^{10}N/C^6$
α_{112}	8.50	15.27	$10^8\ m^{10}N/C^6$
α_{113}	-4.06	-7.05	$10^9\ m^9N/C^6$
s_{11}	8.6	8.8	$10^{-12}\ m^2/N$
s_{12}	-2.8	-2.9	$10^{-12}\ m^2/N$
s_{44}	21.2	24.6	$10^{-12}\ m^2/N$
Q_{11}	8.12	6.17	$10^{-2}\ m^4/C^2$
Q_{12}	0.27	-0.68	$10^{-2}\ m^4/C^2$
Q_{44}	3.36	2.76	$10^{-2}\ m^4/C^2$

5 Results and discussion

5.1 Sequence of polarization reversal mechanisms in polycrystalline ferroelectric/ferroelastic materials[1]

Perhaps the best evidence for the complexity of the polarization reversal process in polycrystalline materials is the absence of a complete sequential mechanistic description of the process on the domain level. As outlined in detail in Sec. 2.3.2, previous experimental reports shed light on different parts of the sequence; however, they fail to capture the process as a whole. In addition, different experimental reports disagree on important aspects of the process. Some publications suggest that polarization reversal occurs by two successive non-180° events [120; 122; 124], other experiments predominantly find 180° events [125; 126] or even exclusively one single 180° event [127; 290]. While all the works focus on the measurement of the time/field dependence of a single parameter, typically polarization, a deeper understanding of the process can be achieved if the time/field dependence of various parameters, *i.e.*, polarization and strain, is measured simultaneously.

In this section a mechanistic understanding of the polarization reversal process is derived. Novel simultaneous time-dependent measurements of macroscopic polarization and strain dynamics, as well as microscopic domain switching fraction and lattice strain, are presented and analyzed for a commercial PZT material with a tetragonal crystal structure. The complex interplay between electric and mechanical fields is revealed by Landau energy calculations. In the end, a schematic sequence of the polarization reversal process is presented.

5.1.1 Bipolar hysteresis measurements

Polarization reversal is often investigated by analyzing the electric field dependence of various parameters. Representative large signal polarization and strain of a bipolar hysteresis loop are depicted in Fig. 5.1a, while changes in small-signal dielectric permittivity and piezoelectric coefficient are displayed in Fig. 5.1b. Fig. 5.1c magnifies part of the positive branches and characteristic properties are highlighted as vertical lines.

The coercive field, obtained from polarization loops, represents a field at which the polarization is zero. [25] Here, the piezoelectric response is absent. This is manifested by the coincidence of the coercive field obtained from polarization loops and the coercive field obtained from small signal d_{33} loops (for these the coercive field is the field at which $d_{33}=0$, $E_C^P = E_C^{d_{33}} = 1.07\,\mathrm{kV/mm}$). The coercive field is also defined as the field, at which the negative strain is maximized. [1] The coercive field obtained from the bipolar strain loops ($E_C^S = 0.99\,\mathrm{kV/mm}$), however, is lower compared to the coercive field obtained from the polarization loops. E_C^S is sometimes considered as to the start of the switching process. [1] However, as evidenced by the maximum of negative strain, a considerable amount of non-180° domain wall motion must already be in progress at E_C^S. None of these characteristic fields coincides with the maximum of the dielectric permittivity, which peaks at a lower field, $E^{\kappa_{33}^{\max}} = 0.84\,\mathrm{kV/mm}$. These differences between the different characteristic fields cannot be described by the existing knowledge on switching mechanics.

In the following, time-dependent dynamic measurements will be utilized to reveal the mechanisms of the polarization reversal process. Compared to field-dependent loops, measurements with a constant electric field allow to reveal individual events on a broad time scale. Additionally, activation fields can be determined, if measurements are carried out for a broad range of fields.

5.1.2 Dynamic measurements

The time dependences of the following parameters, characterizing the switching process on a macroscopic and microscopic level, are measured simultaneously: switched macroscopic polarization (Fig. 5.1d), macroscopic strain (Fig. 5.1e), domain switching fraction (Fig. 5.1f), and lattice strain (Fig. 5.1g). Measurements were performed at various electric field pulses of height E_{Sw}.

---

[1] Part of this section was published previously in [339].

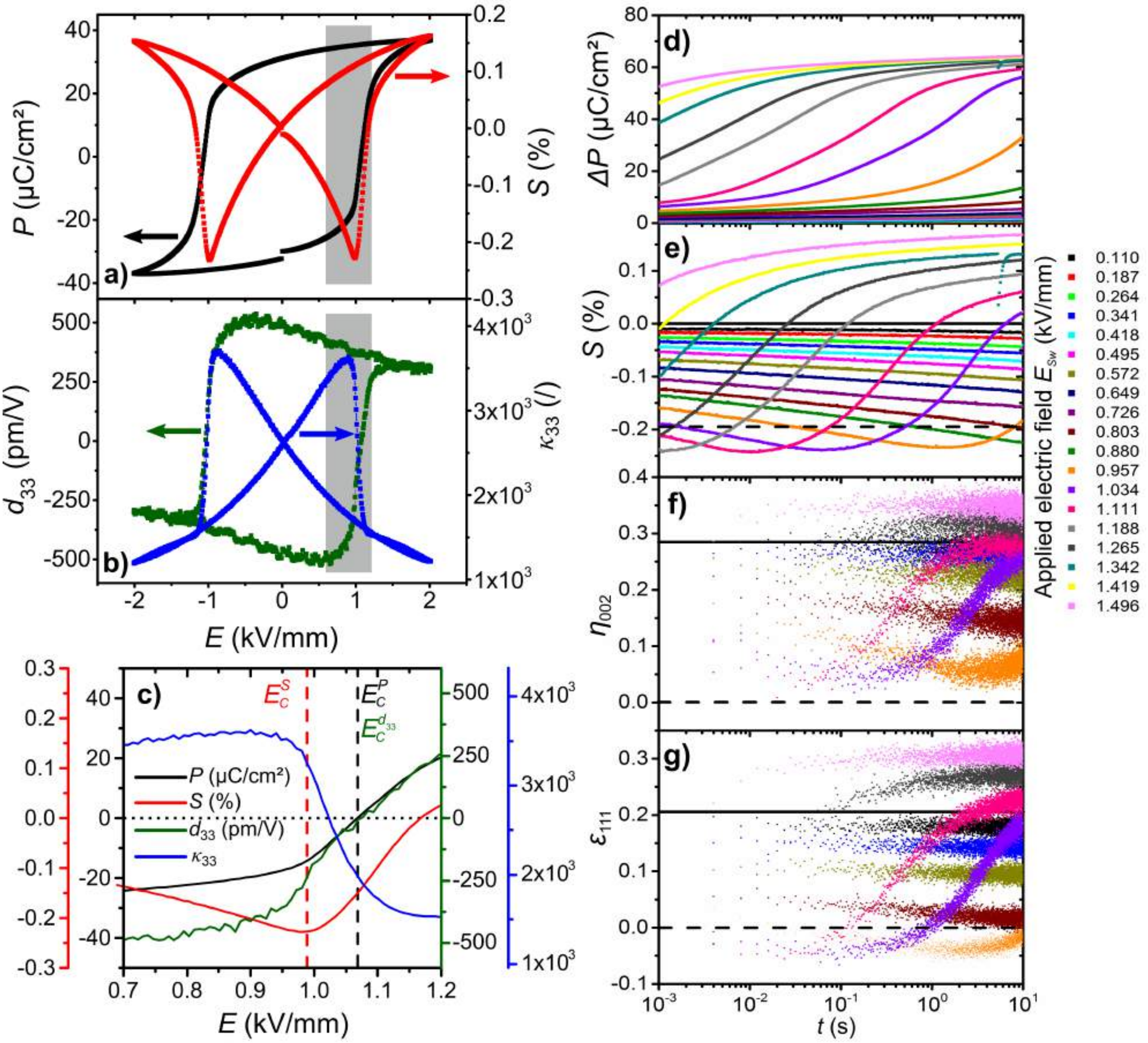

Figure 5.1.: Electromechanical and structural data. a–c) Bipolar large signal polarization, strain, small signal piezoelectric coefficient, and small signal dielectric permittivity measured as a function of the electric field. The frequency of the large signal wave form was 0.05 Hz. The shaded area in a) and b) for the positive branch of the electric field signal is highlighted in c). The dashed vertical lines in c) mark the characteristic coercive field values for the respective curves. d–g) Simultaneous dynamic measurements under HV pulses with different amplitudes: d) switched polarization, e) the macroscopic strain of the sample, f) the domain switching fraction, and g) lattice strain. The data for f) and g) were taken from an azimuthal section, which represents grains with their polarization vector parallel to the applied electric field. The dashed line in d–g) indicates the value of a virgin material, while the solid line that of a material after poling.

The time-dependent polarization curves contain information from all switching events, *i.e.*, ferroelectric 180° and ferroelectric/ferroelastic non-180° processes. As shown in Fig. 5.1d, the $\Delta P(t)$ curves exhibit the expected broad step-like behavior on the logarithmic time scale. On the contrary, the strain curves (Fig. 5.1e), the lattice strain (Fig. 5.1f), and the non-180° domain switching fraction (Fig. 5.1g),[1] mainly contain contributions from ferroelectric/ferroelastic non-180° events. Besides non-180° events, the piezoelectric effect contributes to the former two.

---

[1] As the investigated material is tetragonal, the (200) intensity ratio allows to determine the ferroelectric/ferroelastic domain switching, while the lattice strain is most pronounced in the (111) peak position. [172]

As displayed in Fig. 5.1e, the negative strain is first linearly increasing on the logarithmic time scale. It can be observed that the slope increases with applied electric field. The initial increase of negative strain is accompanied by a rather small increase in polarization (Fig. 5.1d). This initial step ends after a field-dependent critical time is reached (time at which the negative strain of the sample is maximized, Fig. 5.1e). In the following, the negative strain decreases, which is accompanied by a large increase in polarization (Fig. 5.1d), before both curves saturate. Note that for the measurements with lower electric fields in Fig. 5.1d–g the two latter stages are only partially visible or completely absent within the investigated time period of 10 s, but would appear at longer measurement times.

5.1.3 Mechanisms of polarization reversal

Based on the time-dependent measurements in Fig. 5.1d–g, a sequence of switching events can be established. This is featured schematically in Fig. 5.2. Three different regimes can be distinguished: 1) Non-180° domain wall movement, 2) main switching phase, and 3) creep-like domain wall movement. Individual regimes will be described in detail below.

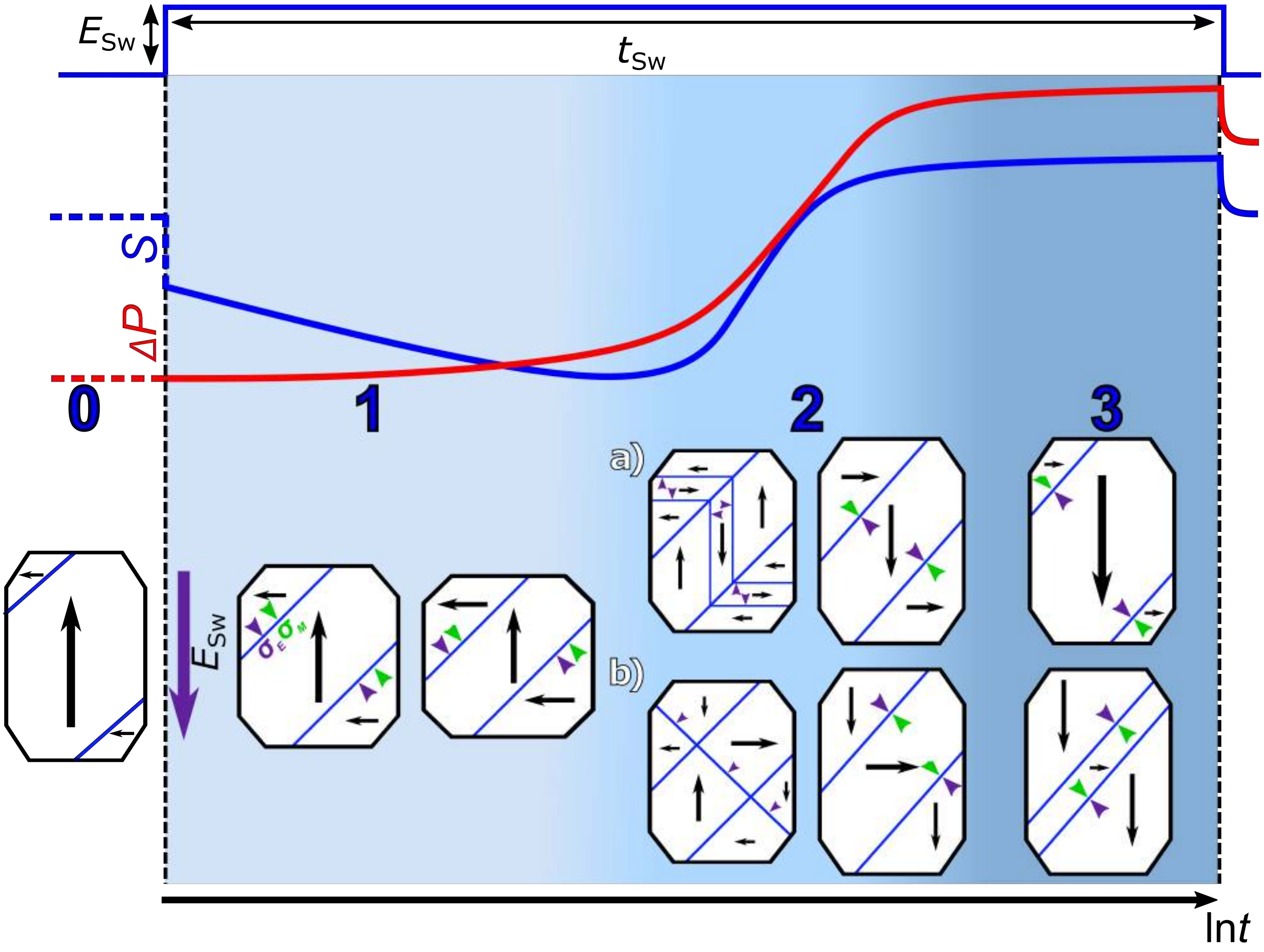

Figure 5.2.: Mechanisms of polarization reversal in polycrystalline ceramic materials. Schematic material's switched polarization and strain response to a HV pulse. The schematic domain images display the sequence of the polarization reversal mechanisms for a grain with a polarization vector oriented antiparallel to the applied electric field. The starting poled state (0) and the three distinguishable regimes of the dynamic response are highlighted: 1) initial non-180° domain wall movement, 2) main switching phase by a) nucleation and sidewise growth of 180° domain walls and b) strain-free 180° polariaztion reversal by a nucleated non-180° domain wall, which is moving through the grain, and 3) creep-like domain wall movement. The small triangular arrows mark the stress exerted on domain walls, which arise by electric (σ_E) and mechanical (σ_M) fields.

Poled state

Since ferroelectric switching is strongly linked to the response of the material's domain structure to an electric field, it is mandatory to know the domain structure in the starting state of the measurement, *i.e.*, the poled state (0 in Fig. 5.2), before the electric field is switched on. PFM images of a poled PIC151 sample are presented in Fig. 5.3. Different types of domain boundaries can be identified in the PFM images according to the shape of their walls. As recently demonstrated by 3D vector PFM, 180° domain walls mostly appear as curvy lines [340], also known as watermarks. This indicates that the straight lines, which represent the major part of the observable domain wall features in Fig. 5.3, can mainly be identified as non-180° domain walls.

The large amount of non-180° domain walls is formed to compensate the high lattice strains after electric poling (Fig. 5.1g) and is a direct consequence of a four times lower domain wall energy of non-180° domain walls, as compared to 180° domain walls [61]. In accordance, mainly non-180° domain walls in a tetragonal PZT-based material were identified after poling using optical microscopy [129], in agreement to various other reports [341–344]. In comparison, in a unpoled virgin sample, the domain structure mainly consists of 180° domain walls. [345]

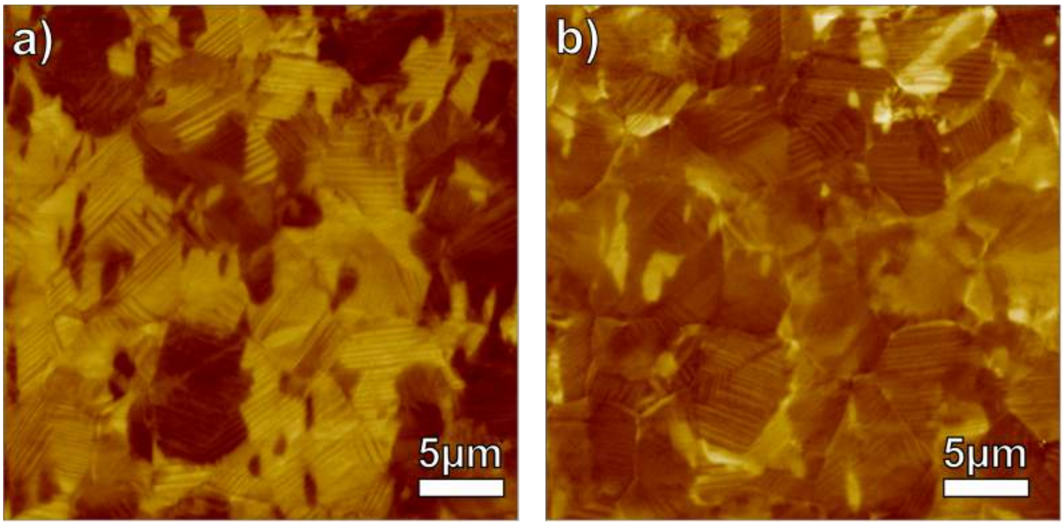

Figure 5.3.: Characterization of the poled state by PFM. a) In-plane and b) out-of-plane PFM image ($\iota \sin \phi$ representation) of a PIC151 sample after electric poling, representing the poled state (0 in Fig. 5.2). As recently investigated by 3D vector PFM on the same material system, the straight domain walls are non-180° domain walls, while the curvy domain walls are 180° domain walls. [340]

Regime 1: Initial non-180° domain wall movement

The electric field in Fig. 5.2 is applied anti-parallel to the polarization direction. This results in an initial rapid shrinkage of the poled sample due to the converse piezoelectric effect, which cannot be resolved in our measurements due to the limited time resolution of the measurement system. The observed linear increase of negative strain (Fig. 5.1e) is a result of non-180° domain wall movement [335] and lattice strains, which originate from grain-to-grain coupling. [172] In the initial regime, the electric field generates a constant stress on the non-180° domain walls (σ_E in regime 1 in Fig. 5.2), which initiates their movement. [134] As suggested by Krüger, Gerthsen, and Schmidt [132–134], no nucleation step is required for this process, because small misaligned nuclei are already present after poling and polarization reversal can start from here.

High lattice strain and high domain switching fraction after electric poling can be explained adopting the approach of Hall *et al.* [172], which is based on the Eshelby method [171]. This approach is described in detail in Fig. 2.14d–f. Poling a grain of a polycrystalline ceramic induces a high domain switching fraction. Consequently, the elastic matrix, which is compensating the shape change, gets strained as well. The corresponding stresses act as an auxiliary mechanical force (σ_{M} in Fig. 5.2) for non-180° domain wall movement and tend to bring the non-180° domain walls back to a more stable position. Here, the approach of Daniels *et al.* is followed, who related the rapid first non-180° switching step in their model to large internal residual strains inside the material. [124] Non-180° domain wall movement and decreasing lattice strains macroscopically result in a linear increase of the negative strain (Fig. 5.1e) on the logarithmic time scale. Physically, a linear-log(t) behavior is an interesting phenomenon. In the context of ferroelectric materials, a linear-log(t) relaxation of the dielectric permittivity was reported, which was related to the movement of domain walls to more stable positions without external stimulation [346; 347], a phenomenon known as aging [348]. In a purely ferroelastic $LaAlO_3$ model system, a linear-log(t) was rationalized by a Gaussian distribution of activation energies for motion of ferroelastic domain walls. [349]

The interaction between electric and mechanical fields in the initial non-180° domain wall movement (regime 1 in Fig. 5.2) is revealed in more details by Landau energy landscapes, displayed in Fig. 5.4. The energy landscape for a tetragonal PZT material without electric or mechanical fields is displayed in Fig. 5.4a. The stable position of the tetragonal states, which are energetically equal for this configuration due to fourfold symmetry reasons, are highlighted by white dots. A significant internal mechanical stress σ_{M_1} (Fig. 2.14f), which is present right after the poling process (Fig. 5.1f), energetically favors a stable position of the tetragonal state T_2. The polarization reversal process to achieve state T_2 occurs over the path $T_1 \rightarrow T_2$ (Fig. 5.4d), which is realized by non-180° domain wall movement on the domain level (regime 1 in Fig. 5.2). This consequently reduces the grain-to-grain clamping [172], which again decreases the internal strains (Fig. 5.1f and g). With the resulting reduced auxiliary forces, also the driving force for the movement of the non-180° domain walls decreases, slowing down the movement of the non-180° domain walls throughout regime 1. Reduced mechanical constraints on the vibration of the domain walls is also manifested by the linear increase of the dielectric permittivity with electric field in the electric field range of 0–0.84 kV/mm (Fig. 5.1b).

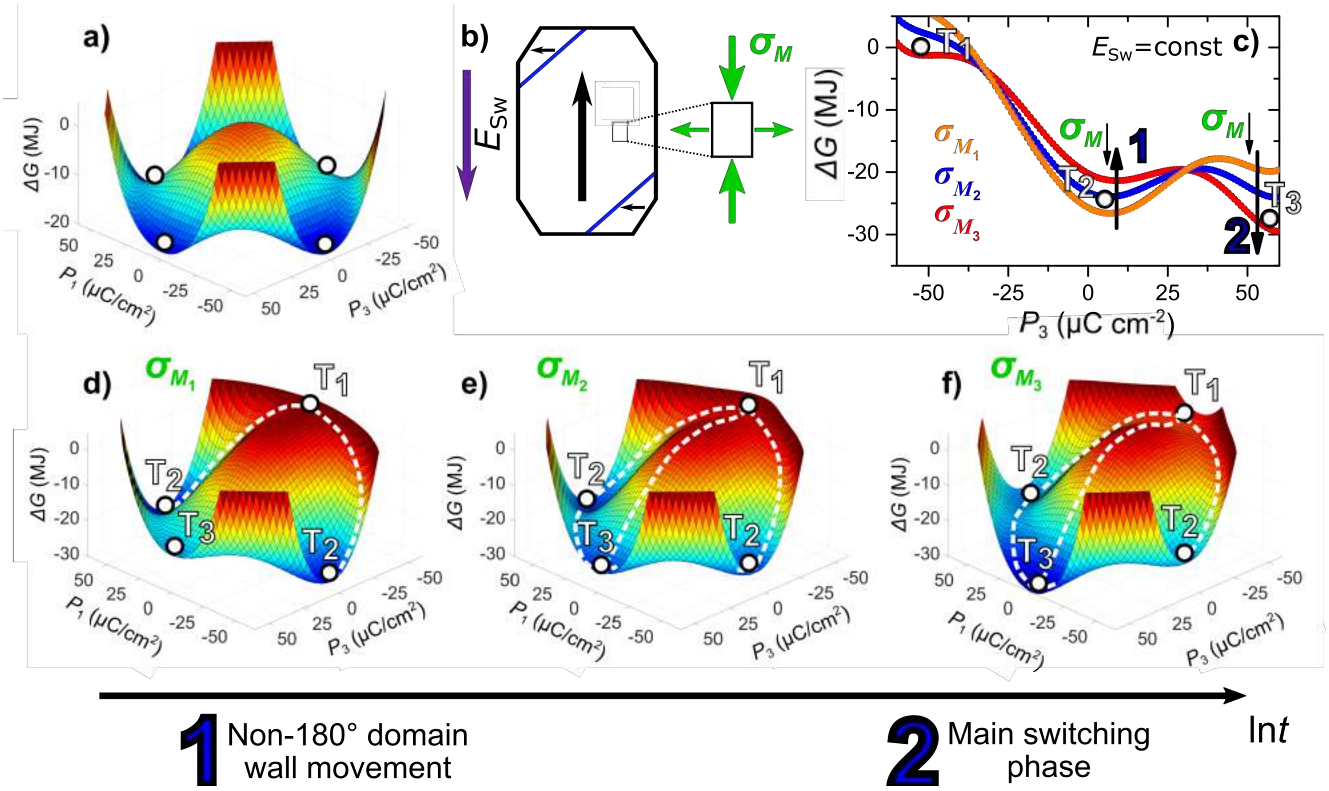

Figure 5.4.: Landau energy landscapes displaying, that the transition from regime 1 (non-180° domain wall movement) to regime 2 (main switching phase) is governed by a complex interplay of electric and mechanical fields. a) Landau energy landscape for a tetragonal PZT without applied electric or mechanical fields. The stable positions of tetragonal states are highlighted by the white dots. b) Schematically explains the action of an electric field pulse and mechanical stress (Fig. 2.14f) on a poled ferroelectric domain during the initial non-180° domain wall movement (regime 1 in Fig. 5.2). In the following figures d), e), and f) the energy landscapes for different mechanical stress states $\sigma_{M_1} > \sigma_{M_2} > \sigma_{M_3}$ are revealed, while the electric field is kept constant for all energy landscapes. The influence of decreasing mechanical stress on the non-180° path $T_1 \rightarrow T_2 \rightarrow T_3$ is summarized in c) for a constant electric field. Here, the arrows ↑ and ↓ indicate the influence of decreasing mechanical stress $\sigma_M \downarrow$ on the position of the tetragonal states T_2 and T_3. The position of the tetragonal state T_2, shown in d), is energetically favored for the highest mechanical stress σ_{M_1}, while the position of the tetragonal state T_3, shown in f), is more stable for the smallest mechanical stress σ_{M_3}. The medium stress state σ_{M_2} represents the critical stress state for the transition from regime 1 (path $T_1 \rightarrow T_2$, non-180° domain wall movement) to regime 2 (path $T_1 \rightarrow T_2 \rightarrow T_3$ or path $T_1 \rightarrow T_3$, main switching phase): as shown in the energy landscape in e), at the stress state σ_{M_2}, the tetragonal states T_2 and T_3 are in equilibrium.

Regime 1 ends at a characteristic value of negative strain, S_{neg}=-0.24 %, and switched polarization, ΔP=16 µC/cm^2. The switched polarization in regime 1 accounts to 26 % of the total switched polarization during the entire process of polarization reversal.

The discrepancy between reported models, which consider solely non-180° events or a single 180° event, and experimental results is highlighted in Fig. 5.5. A schematic polarization and strain dynamic measurement for successive purely non-180° domain switching, where the two events are clearly separated, is displayed in Fig. 5.5a. The situation for a purely 180° event is revealed in Fig. 5.5b. None of these scenarios can conclusively explain the experimental observation shown in Fig. 5.1d and e and Fig. 5.2. For the schematic curves displayed in Fig. 5.5a the time required for reaching 50% of the switched polarization coincides with the time at which the maximum negative strain is obtained (dashed line). This is contradictory to our experimental findings, where only 26% of polarization reversal occurs by the time when the maximum negative strain is reached, *i.e.*, by the first non-180° event (regime 1 in Fig. 5.2). On the other hand, only the piezoelectric effect should contribute to the negative strain for the case of a single 180° event (Fig. 5.5b), which does not explain the substantial negative strain observed in our experiments. This indicates, that both 180° and non-180° events contribute to the polarization reversal process in polycrystalline ferroelectric materials.

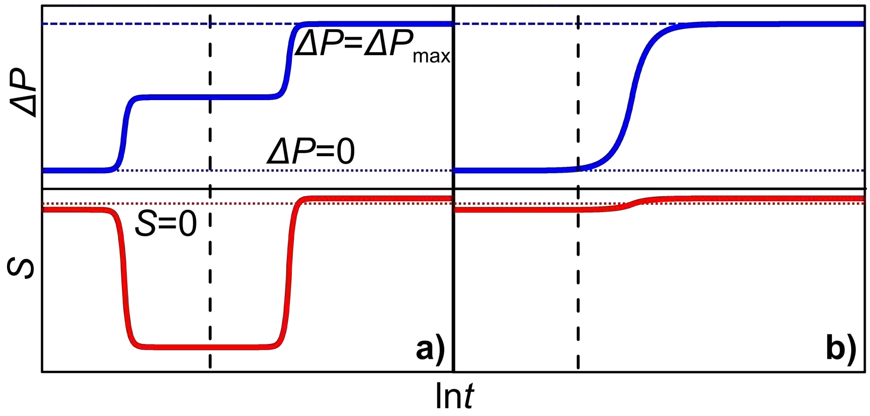

Figure 5.5.: Schematic curves of simultaneous polarization and strain dynamics for polarization reversal, which occurs solely by a) non-180° events or by b) a single 180° event. The vertical dashed line indicates the time when the maximum in negative strain is reached. The dotted horizontal lines indicate the zero value of polarization and strain, while the dashed horizontal line displays the maximum switchable polarization.

Regime 2: Main switching phase

At the end of regime 1, a critical state is reached within the grains, defined by the interplay between local mechanical and electric fields. This critical state triggers the main switching phase (regime 2 in Fig. 5.2). In the context of the bipolar measurements (Fig. 5.1a–c), the coercive field obtained from strain loops can be seen as the transition from regime 1 to regime 2, while the coercive field obtained from polarization loops defines the main switching phase. The transition from regime 1 to regime 2 can be explained if Landau energy landscapes for the respective regimes are considered (Fig. 5.4). For a certain mechanical stress state, σ_{M_2}, the position of tetragonal states T_2 and T_3 are in equilibrium and polarization reversal can occur over the following paths: $T_1 \rightarrow T_3$, $T_1 \rightarrow T_2$, or $T_1 \rightarrow T_2 \rightarrow T_3$. This situation is visualized in Fig. 5.4e. If the mechanical stress state is further decreased to σ_{M_3} (Fig. 5.4f), the position of the tetragonal state T_3 is energetically more favorable than any other tetragonal state and polarization reversal will most likely occur over the paths $T_1 \rightarrow T_3$ or $T_1 \rightarrow T_2 \rightarrow T_3$, whereby the material enters the main switching phase (regime 2 in Fig. 5.2). The influence of mechanical stress state σ_M on the path $T_1 \rightarrow T_2 \rightarrow T_3$ is depicted in Fig. 5.4c.

The main switching phase is characterized by a reversal of the polarization, which accounts for 64% (Fig. 5.1d) of the total switched polarization, accompanied by a decrease of the negative strain and extension of the sample in the direction of the electric field. Even higher values of switched polarization (>90%) in this regime have recently been reported for simultaneous measurement of displacement and charge in a PZT thin film. [350] The polarization reversal in the main switching phase can occur by two different scenarios, which are presented in Fig. 5.2a and b. In the first scenario, polarization reversal occurs by a nucleation and growth process of antiparallel 180° domains, followed by sidewise domain wall motion (Fig. 5.2a). [351] This scenario is based on the switching behavior commonly observed in single crystalline systems [106], schematically displayed in Fig. 2.11. In this scenario, the nucleation of the antiparallel 180° domains probably occurs correlated over the lamellar domain structure of a grain. According to the second scenario, polarization reversal can occur by synchronized non-180°domain switching (Fig. 5.2b). This process requires the nucleation of a non-180° domain wall, which moves through the lamellar domain structure of a grain. [18; 128] This scenario is schematically displayed in Fig. 2.13e. Since low elastic forces are involved in its motion, this non-180° domain wall type is highly mobile. Due to the synchronization of several non-180° events in a lamellar domain structure, this scenario appears as a 180° switching event, since it does not change the strain of a grain, but only its polarization. Locally, however, the polarization is reversed by non-180°. Based on the experimental results, however, it is not possible to distinguish if polarization reversal in the main switching phase happens by 180° (Fig. 5.2a) or by synchronized non-180° switching events (Fig. 5.2b).

Recent diffraction experiments indicate that polarization reversal mainly occurs by 180° switching events. For example, Fancher *et al.* found that 180° domain wall motion accounts for >80% of the polarization reversal in PZT and BT-based materials, and is thus the dominant mechanism. [125] In accordance, Gorfman *et al.* recently suggested that polarization reversal in BT-based material occurs most likely by 180° domain wall motion. [126]

However, microstructural arguments indicate that mainly non-180° domains should be involved in the polariaztion reversal process in the main switching phase. The Peierls barrier for the movement of non-180°domain walls is lower compared to 180° domain walls. [61; 62] A detailed discussion is given in Sec. 2.2.2 and values for the Peierls barrier of BT and PZT systems are provided. In addition, crystallographic arguments suggest polarization reversal by non-180° events. Kubel and Schmid calculated the movement of iron and oxygen for different switching angles in $BiFeO_3$. While the largest displacement value of 1.34 Å was found for 180°, smaller values of 0.87 Å and 1.12 Å could be identified for 60° and 120° switching, respectively. [352] Similar values were previously presented by Ng and McDonald for a PZT material. [353] Both authors concluded that due to larger atomic displacement values for 180° polarization reversal, switching by non-180° should be favorable based on crystallographic arguments. Tadmor *et al.* developed a continuum constitutive model for $PbTiO_3$. [354] Based on this, the activation fields for 180° and non-180° switching could be revealed. An activation field of 52 kV/mm was found for non-180° switching, which is by a factor of three smaller than the calculated activation field for 180° switching.

Even though the current measurement techniques are not adequate to give a final answer to the question about the exact mechanism of polarization reversal during the main switching phase, a combination of 180° and non-180° switching events seems likely for polycrystalline ferroelectric materials.

The macroscopically observed expansion of the sample in the direction of the electric field in regime 2 occurs due to the converse piezoelectric effect and the movement of ferroelastic domain walls, as indicated by the increased domain switching fraction (Fig. 5.1f). Towards the end of this regime, a saturated poled state is approached and mechanical stresses are building up. This is evidenced by the increase in lattice strain during the main switching phase, as displayed in Fig. 5.1g.

Regime 3: Creep-like domain wall movement

At the end of the main switching phase, the majority of domains has reversed and the material enters regime 3 (creep-like domain wall movement in Fig. 5.2). The electric field is here parallel to the polarization vector. In this regime about 10% (Fig. 5.1d) of the polarization reversal occurs and the polarization and strain values monotonically increase at a decreasing rate. The shape of the curves in regime 3 resembles time-dependent measurements of polarization [355] and strain [356] in poled polycrystalline ceramic materials with the electric field applied in the direction of poling, a phenomenon called electric creep. The strain and polarization rate decay during electric creep were related to polarization hardening, which was explained by increased internal depolarization fields and mechanical stresses. [357]

While a saturation of polarization and strain with time is usually observed for lead-containing ferroelectric/ferroelastic polycrystalline ceramic materials [100; 290], fatigued [358] and lead-free materials [182; 202; 203] do not exhibit a saturation in regime 3. For highly fatigued materials, the transition between regime 2 and regime 3 smears out and individual regimes cannot be separated any longer [291], which was related to mechanical degradation, domain wall pinning and the creation of a dead layer [359].

5.1.4 Activation fields

Activation fields for the individual regimes can be determined, if field-dependent characteristic parameters, describing the individual physical processes, are known. For non-180° domain wall movement (regime 1 in Fig. 5.2), this is the time at which 50% of the maximum negative strain is reached, while for the main switching phase (regime 2 in Fig. 5.2), this is taken as the time where 50% of the maximum switchable polarization is reversed. Finally, for the creep-like domain wall movement (regime 3 in Fig. 5.2), the time is plotted, at which 90% of the maximum switchable polarization is reversed. The dependence of these parameters on the inverse applied electric pulse field is plotted in Fig. 5.6.

In order to describe the field-dependent domain wall velocity, the Merz law, Eqn. 2.9 [13], can be applied. After rearrangement, the field-dependent switching time can be expressed as

$$\tau = \tau_0 \exp(E_a / E_{Sw}). \tag{5.1}$$

The fits according to the Merz law in Fig. 5.6 show an excellent agreement to the experimental data and allow to determine the activation fields for the individual regimes, which are summarized in Tab. 5.1. It has to be taken into account that Merz suggested the aforementioned equation for the field-induced movement of 180° domain walls in single crystalline materials, in which the local electric field distribution is homogeneous. Instead, in polycrystalline materials the local electric field distribution is inhomogeneous as a direct result of their polycrystalline nature. [177; 178] Therefore, the determined activation fields represent an averaged value over all crystallographic orientations.

According to Tab. 5.1 the activation field for the initial non-180° domain wall movement is 36% lower compared to the activation field for the main switching phase. This observation reflects the support of the mechanical auxiliary forces, as well as the presence of nuclei in the poled state. On the contrary, both scenarios during the main switching phase (regime 2 in Fig. 5.2) require a nucleation process and the mechanical stress is acting against the moving domain walls [360]. In addition, internal electric fields in regime 2 should be broader distributed as compared to regime 1. [140] The activation fields for the creep-like domain wall movement and for the main switching phase exhibit a similar value.

It is important to note that the activation fields should be considered as time averaged over the entire respective regime of Fig. 5.2. For example, the activation field for the non-180° domain wall movement will increase with progressive movement of the domain walls [361], since the mechanically auxiliary forces decrease continuously within this regime. At some point, the activation fields for the main switching phase and the initial non-180° domain wall movement will be similar and the main switching phase will be triggered.

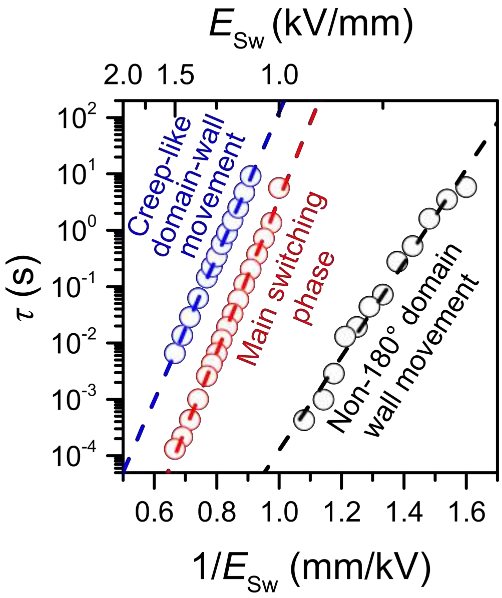

Figure 5.6.: Field-dependent switching times, plotted as a function of the inverse applied electric pulse fields, for the different regimes marked. 1) non-180° domain wall movement (determined from *S(t)* curves (Fig. 5.1e); time where 50 % of the maximum negative strain is reached), 2) main switching phase (determined from $\Delta P(t)$ curves (Fig. 5.1d); time where 50 % of the polarization is reversed), and 3) creep-like domain wall movement regime (determined from $\Delta P(t)$ curves (Fig. 5.1d); time where 90 % of the polarization is reversed). The dashed lines in the figure represent a fit to the data points according to the Merz law.

Table 5.1.: Activation fields for different regimes, revealed by fitting the Merz relation [13] to field-dependent switching times (Fig. 5.6). The arrow bars represent the standard deviation obtained from fitting by the least square method.

Regime	Name of regime	E_a (kV/mm)
1	Non-180° domain wall movement	**19.2**±0.8
2	Main switching phase	**29.8**±0.3
3	Creep-like domain wall movement	**29.4**±0.5

5.1.5 Mechanical grain interactions

While it is clear that the switching behavior of polycrystalline materials is strongly influenced by the coupling of individual grains, the state of the art description of these correlations is only given on a theoretical level [143–145] or by localized measurements [162–165; 167]. A detailed description of the literature can be found in Sec. 2.3.2. The drawback of theoretical calculations is that mostly only electric correlations, which arise due to depolarization fields, are considered, while the localized measurements are surface sensitive and thus do not represent the internal material's properties (different boundary conditions). Here, an experimental approach is presented which gives statistical information on grains with their polarization axis oriented within a certain azimuthal angular range (Fig. 4.8) with respect to the direction of the applied electric field. In Fig. 5.7a and b the time evolution of the (002) and (111) diffraction peaks upon the application of a step HV electric field is displayed for three different orientations: parallel (Ψ=0°), perpendicular (Ψ=90°), and at an intermediate angle (Ψ=50°) to the applied electric field. Clearly, a change in the (002) peak intensities and (111) peak positions can be observed with time for the former two, while the latter remains nearly unchanged.

In Fig. 5.7c and d, the time-dependent domain switching fraction, and lattice strain, at various angles to the direction of the applied electric field are revealed and compared to the poled state, which is represented by the respective solid lines.

Two important observations can be obtained from these results. Firstly, even though the grains have a different orientation with respect to the applied electric field, their shrinkage and expansion are strongly correlated in time. This is evidenced by the fact that all orientations have their minima/maxima in domain switching fraction, and lattice strain at the same characteristic time. This time represents the transition from regime 1 to regime 2 (Fig. 5.2), which thus occurs correlated in grains independent of their orientation to the applied electric field. This is an important finding, since all state of the art statistical models assume that switching in polycrystalline materials occurs uncorrelated in individual grains. [290]

Secondly, while only one grain was considered to describe the mechanism of polarization reversal in Fig. 5.2, real polycrystalline materials consist of many grains. The local electric field acting on a domain wall of a grain, σ_E, is a projection of the external electric field in the respective crystallographic direction of the domain. [177; 178] Therefore, the domain wall velocity is highest for favorably-oriented domains (Ψ=0°), while the velocity continuously decreases as the angle Ψ is decreasing. Finally, no change in domain wall velocity can be observed for an angle Ψ=50°. This is evidenced by the slope in the $\eta_{002}(t)$ curves in Fig. 5.7c, which has the highest value for favorably oriented grains (Ψ=0°), while it does not change for unfavorably oriented grains (Ψ=50°). Therefore, in agreement to previous suggestions about correlations between electric field and domain wall velocity [177; 178], the crystallographic orientation of a grain determines the domain wall stress, σ_E, which results in a movement of the domain wall with a constant velocity. It is important to note that prior theoretical models consider the interplay between local electric field and domain wall velocity as the sole reason for the broadening of the distribution of switching times in polycrystalline materials. [290] Instead, Fig. 5.7c proves that the velocity of the domain wall is set by the crystallographic orientation of a grain with respect to the electric field. It should be noted that the velocity will be additionally influenced by various defects (grain boundaries, pores, and dislocation), lattice distortion, crystallographic structure, and chemical composition. A detailed description of literature on parameters, which influence the domain wall velocity, is given in Sec. 2.4. The velocity of the domain in the polycrystalline material will finally be determined by a complicated interplay between these effects. This is important, because this interplay will determine the shape of the polarization loop, which is the fingerprint of the ferroelectric material.

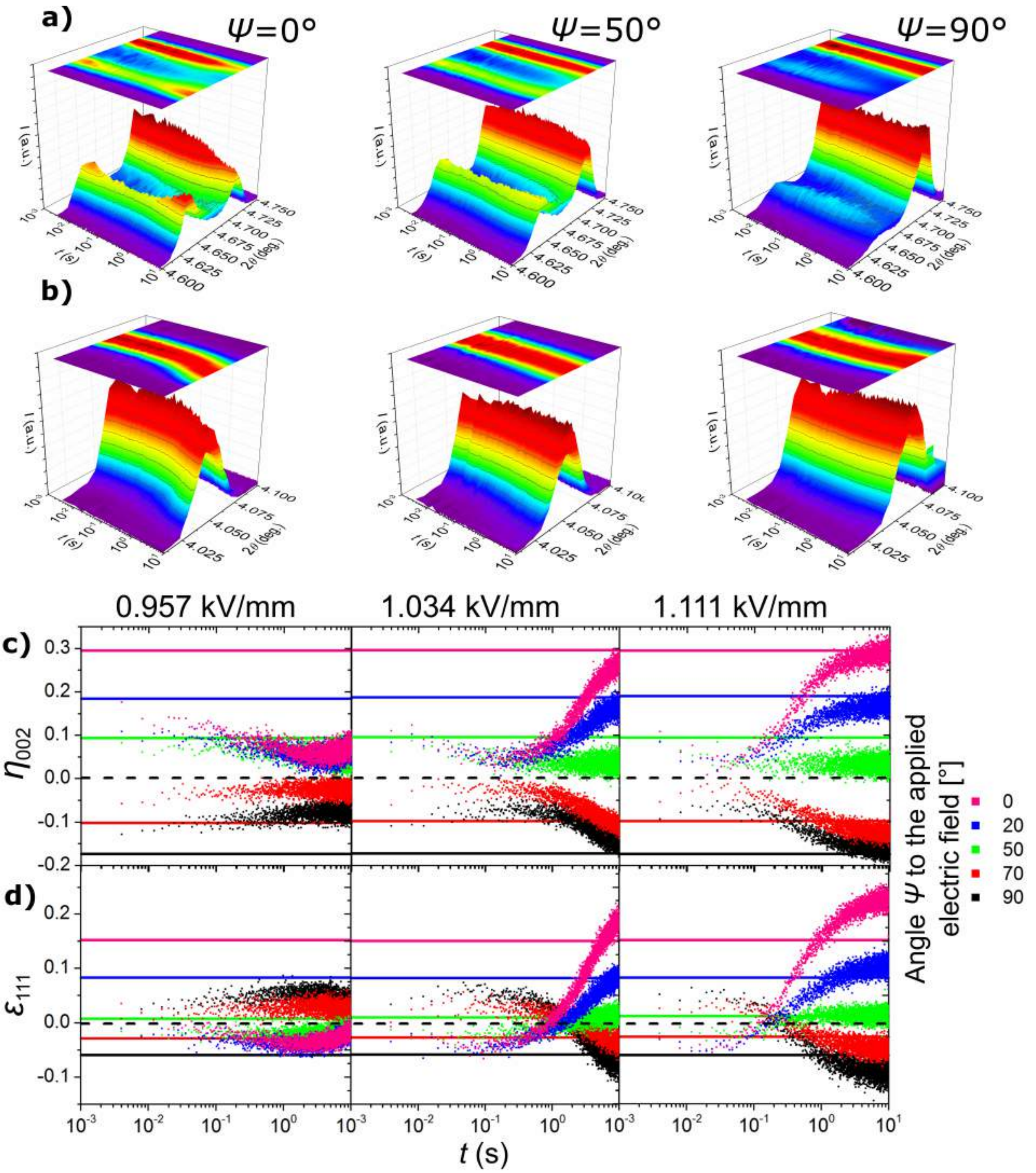

Figure 5.7.: Mechanical grain interactions. Time-dependent diffraction intensities of a) (200) and b) (111) diffraction profiles during a HV pulse switching experiment for an applied electric field of E_{SW}=1.034 kV/mm. The diffraction profiles contain information of grains with their polarization vector parallel (Ψ=0°), perpendicular (Ψ=90°), and at an intermediate angle (Ψ=50°) to the direction of the applied electric field. The calculated values of the domain switching fractions and the lattice strains of grains with their polarization vector at different azimuthal angles to the applied electric field, are displayed for different fields in c) and d), respectively. The solid lines indicate the respective values after poling, while the dashed lines mark the values of a virgin sample.

5.2 Influence of crystal- and microstructure on polarization reversal

Influence of the crystal structure on polarization reversal was studied in a series of La-modified PZT compositions, while the influence of the grain size was investigated in a series of rhombohedral PZT samples with a range of grain sizes. Influence of the crystallographic texturing on polarization reversal was studied on tetragonal $Ba_{0.85}Ca_{0.15}TiO_3$ (BCT15) samples with different degrees of crystallographic texture.

5.2.1 Influence of crystal structure

Crystallographic analysis

The investigated samples are polycrystalline $Pb_{0.985}La_{0.01}(Zr_{1\text{-}x}Ti_x)O_3$ ceramics with different Zr/Ti ratios. Respective XRD profiles for the compositions are shown in Fig. 5.8. The x=0.46 sample is located at the morphotropic phase boundary (MPB) and exhibits a coexistence of rhombohedral and tetragonal phases. The x=0.475 and x=0.5 samples are on the tetragonal (T) side , manifested by the split in the (200) peak, while the (111) peak is a singlet. The x=0.44 and x=0.4 samples are on the rhombohedral (R) side of the MPB. Here, the (111) peak exhibits a clear splitting, while the (200) peak is a singlet. A detailed microstructural and crystallographic analysis was reported elsewhere. [362] The c_m/a_{pc} ratio, obtained by Rietveld refinement of high resolution X-ray and neutron powder diffraction data [362] displayed in Tab. 5.2, increases with increasing titanium content. A value of c_m/a_{pc}=1.016 was reported for x=0.5(T), while a value of c_m/a_{pc}=1.002 was found for x=0.44(R).

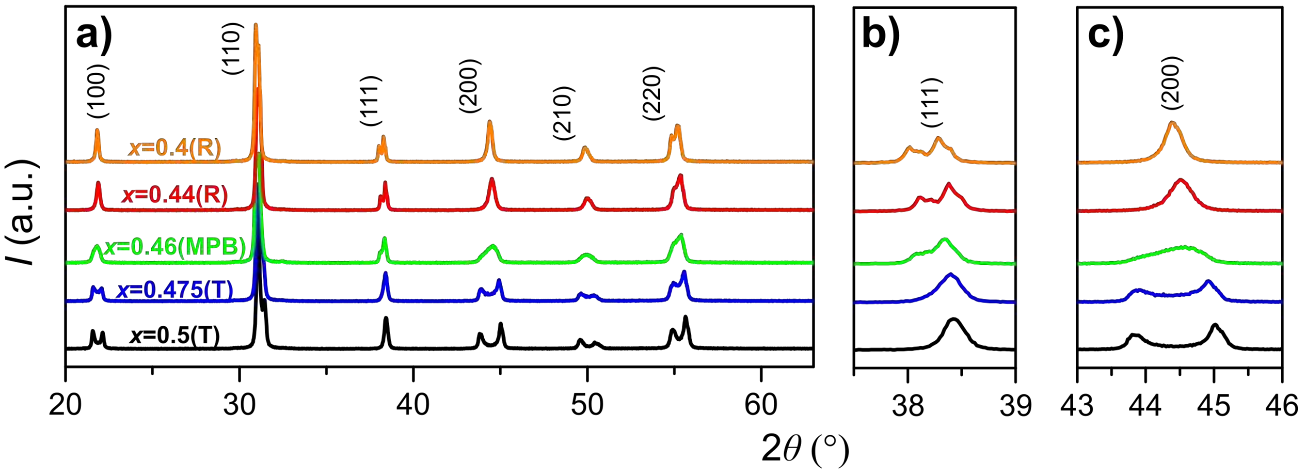

Figure 5.8.: XRD profiles of polycrystalline PZT ceramics with different titanium contents. The full pattern is shown in a), (111) and (200) peaks are highlighted in b) and c), respectively.

Bipolar measurements

Large signal polarization and strain loops of PZT with different Zr/Ti ratios are displayed in Fig. 5.9a and b with the characteristic properties summarized in Tab. 5.2. The highest electromechanical response and the highest switchable polarization were found for the x=0.46(MPB) sample. The remanent polarization of x=0.4(R) is 37.6 $\mu C/cm^2$, while a lower value of 32.2 $\mu C/cm^2$ was found for x=0.5(T). This is in agreement to the prediction of Baerwald [206], who calculated the fraction of switchable polarization obtainable in polycrystalline materials (Tab. 2.3) and found lower values for tetragonal compositions compared to the rhombohedral ones. The coercive fields are plotted in Fig. 5.9c as a function of the titanium content. The coercive fields increase with increasing the titanium content and the values for the tetragonal compositions are about twice as high as the values obtained for their rhombohedral counterparts. This is in good agreement to results obtained by Kungl and Hoffmann. [200] A coercive field of 0.6 kV/mm was reported for a rhombohedral PZT sample doped with niobium and strontium, while a value of 1.2 kV/mm was reported for a tetragonal composition. Also other authors found the coercive fields to be higher for the tetragonal phase in comparison to the rhombohedral phase. [201; 205] The negative strain and the bipolar strain are plotted as a function of the titanium content in Fig. 5.9d and e, respectively, and peak at the MPB. The sharpness of the curve at the maximum negative strain is broader in the case of the tetragonal compared to the rhombohedral materials; a feature, which was found to be even more pronounced for undoped PZT samples [363].

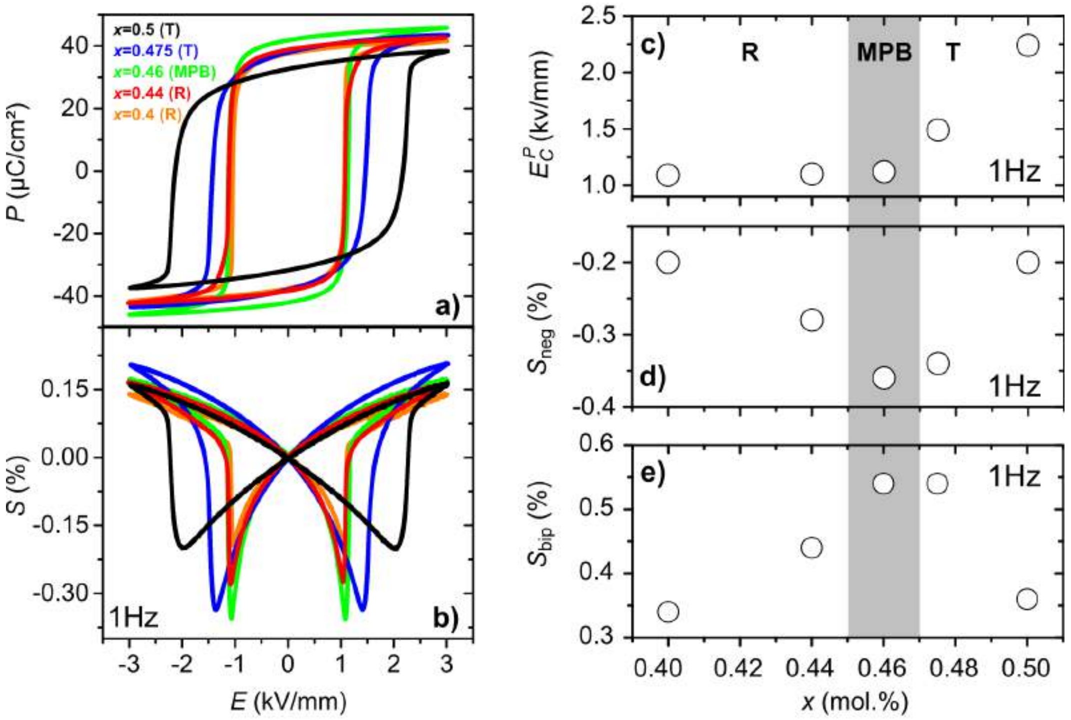

Figure 5.9.: a) Polarization and b) strain loops as a function of the electric field of polycrystalline La-doped PZT ceramics with different titanium contents measured at 1 Hz. The coercive field, the negative, and the bipolar strain as a function of the titanium content are plotted in c), d), and e), respectively.

Table 5.2.: Summary of large signal ferroelectric (measured at 1 Hz and 3 kV/mm) and crystallographic (from Ref. [362]) properties of polycrystalline PZT ceramics with different titanium contents.

x (mol.%)	E_C^P (kV/mm)	P_r (µC/cm^2)	S_{bip} (%)	S_{neg} (%)	c_m/a_{pc}
0.5(T)	2.24	32.2	0.36	-0.20	1.016
0.475(T)	1.49	36.5	0.54	-0.34	1.011
0.46(MPB)	1.12	42.6	0.54	-0.36	1.005
0.44(R)	1.10	40.2	0.44	-0.28	1.002
0.4(R)	1.09	37.6	0.34	-0.20	*n. a.*

Dynamic measurements

Time-dependent polarization and strain dynamic measurements for the investigated PZT compositions are displayed in Fig. 5.10 for various applied electric fields. The $\Delta P(t)$ curves, presented in the first row, show the expected step-like behavior on the logarithmic time scale. Compared to the dynamic polarization responses presented for PIC151 (Fig. 5.1d) or other studied polycrystalline ceramic materials [180–182; 202; 203; 291], switching in La-doped PZT happens faster and the distribution of switching times is narrower, which is related to the softening effect of lanthanum in these compositions.

The influence of crystal structure on the polarization switching dynamics of the investigated materials can be roughly estimated from the time dependence of the switched polarization. In order to completely switch the material in the investigated time interval of 10 s, electric fields of 0.833 kV/mm and 0.889 kV/mm are required for x=0.4(R) and x=0.46(MPB) compositions, respectively, while a much higher electric field of 1.818 kV/mm needs to be applied for the x=0.5(T) composition.

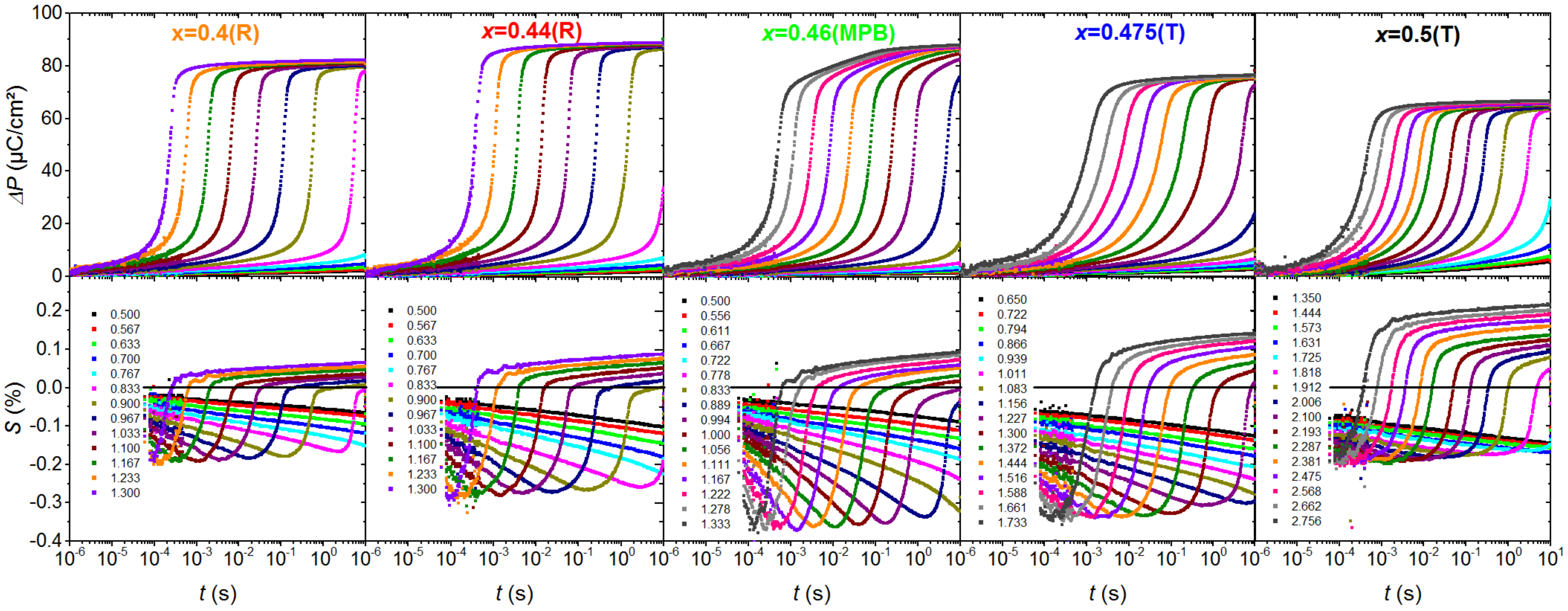

Figure 5.10.: Results of the simultaneous dynamic measurements of switched polarization, and strain of polycrystalline PZT ceramics with different titanium contents. The curves were measured at different applied electric field pulses, as indicated by the inset values in kV/mm. The solid line represents zero relative strain, obtained by normalizing with the poled state (Eqn. 4.5).

A more detailed investigation of the influence of crystal structure on the dynamics of the process can be revealed when time-dependent strain curves, *S(t)*, measured simultaneously with the polarization, are investigated. These are depicted in the second row of Fig. 5.10. Three regimes, which were described in detail in Sec. 5.1, are again identified for all investigated compositions. The activation fields for the three regimes can be determined if field-dependent characteristic parameters describing the individual physical processes are known. For the respective regimes, the field-dependency of the characteristic switching times is plotted in Fig. 5.11, whereby the error bars represent the standard deviations from three averaged measurements on different samples. The data can be well described by the Merz law (Eqn. 5.1), which allows to derive the activation fields for switching.

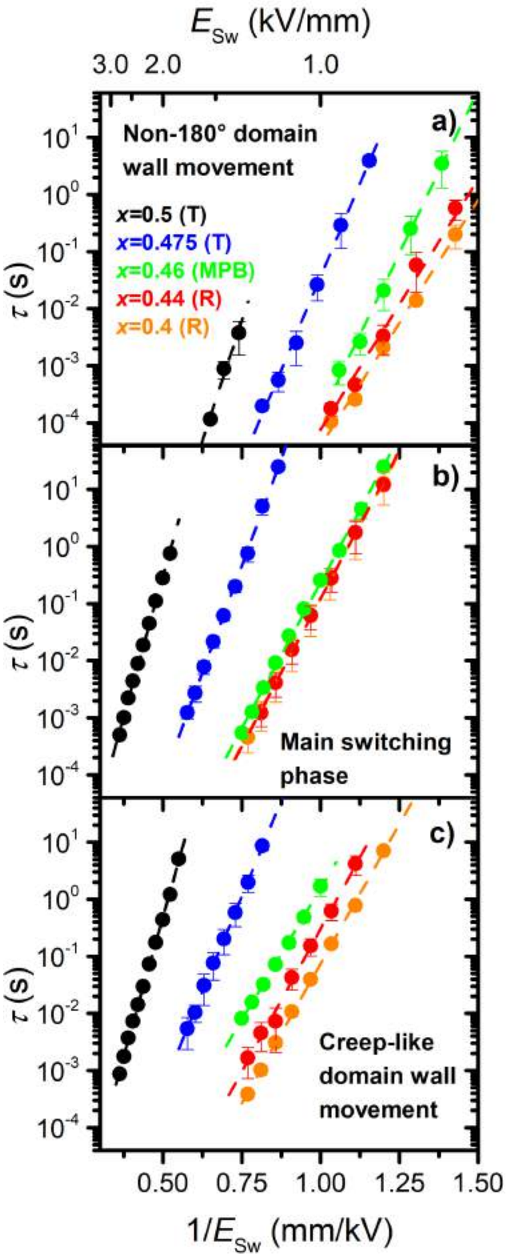

Figure 5.11.: Field-dependent switching times for different regimes, determined from dynamic measurements in Fig. 5.10: a) non-180° domain wall movement (determined from *S(t)* curves; time, where 50% of the maximum negative strain is reached), b) main switching phase (determined from $\Delta P(t)$ curves; time where 50% of the polarization is reversed) and c) creep-like domain wall movement (determined from $\Delta P(t)$ curves; time were 90% of the polarization is reversed). The dashed lines represent fits according to the Merz law (Eqn. 2.9).

The determined activation fields for all three regimes are summarized in Tab. 5.3. The activation field for the non-180° domain wall movement (regime 1) is lower compared to the main switching phase (regime 2) for all compositions, except for the MPB. The activation field for the creep-like domain wall movement is similar or slightly lower compared to the activation field of the main switching process. As discussed in Sec. 5.1.4, the low activation field of regime 1 is a consequence of the presence of nuclei in the poled state and internal mechanical stresses, which are acting as an auxiliary force for non-180° domain wall movement in regime 1.

Table 5.3.: Activation fields (in kV/mm) for non-180° domain wall movement (regime 1), the main switching phase (regime 2) and the creep-like domain wall movement (regime 3) of polycrystalline PZT ceramics with different titanium contents.

x (mol.%)	Non-180° domain wall movement	Main switching phase	Creep-like domain wall movement
0.5(T)	38.4±5.3	45.4±0.7	45.1±0.5
0.475(T)	30.0±1.0	34.4±0.4	30.8±0.4
0.46(MPB)	26.3±1.0	23.5±0.3	21.2±0.3
0.44(R)	20.2±0.9	23.6±0.3	23.1±0.7
0.4(R)	19.8±0.5	23.9±0.2	22.5±0.2

Fig. 5.12a–c show the dependence of the activation field on the titanium content for the three respective regimes. An activation field of 45.5±0.7 kV/mm was found for the main switching phase for a x=0.5(T) composition, which is about double the value of a x=0.4(R) composition (Tab. 5.3). A comparable tendency can be found in literature. Zhukov *et al.* measured the activation fields for the main switching phase of niobium and strontium doped PZT compositions. They reported an activation field of 25 kV/mm for a rhombohedral, while a value of 35 kV/mm was found for a tetragonal composition. [181]

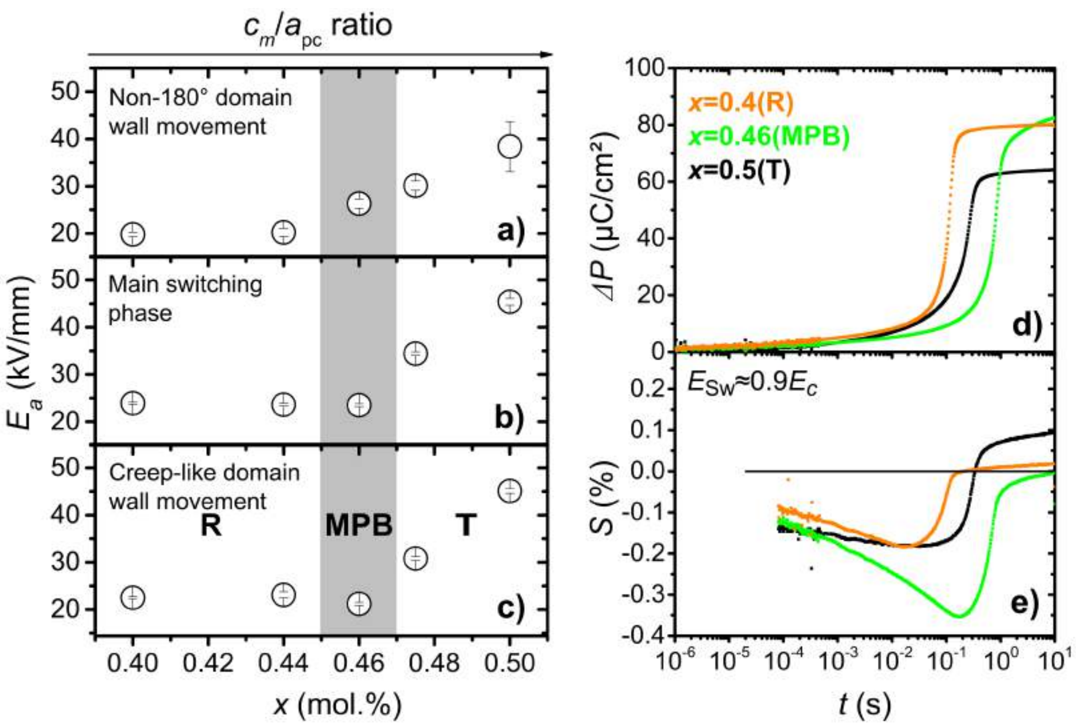

Figure 5.12.: Summary of switching dynamics for samples with different crystal structure. Activation fields for the a) non-180°domain wall movement (regime 1), b) main switching phase (regime 2), and c) creep-like domain wall movement (regime 3) as a function of titanium content. The error bars display the standard deviations according to the least square fit in Fig. 5.11. The arrow indicates the increasing c_m/a_{pc} ratio (Tab. 5.2). d) and e) display dynamic measurements of switched polarization and strain, respectively, highlighting the influence of crystal structure on the individual regimes of polarization reversal. Respective curves for a switching field E_{SW}≈$0.9E_C^P$ are displayed (E_{SW}=2.006 kV/mm for x=0.5(T), E_{SW}=0.994 kV/mm for x=0.46(MPB), and E_{SW}=0.967 kV/mm for x=0.4(R)). The solid line in e) represents zero relative strain, obtained by normalizing with the poled state (Eqn. 4.5).

The easier and faster switching behavior of the rhombohedral compared to the tetragonal composition can be explained by a higher number of equivalent polarization directions (Tab. 2.3). [178] In addition, the tetragonal phase has a higher anisotropy in the dielectric tensor κ_{11}/κ_{33} (2.5 for a tetragonal and 1.8 for a rhombohedral material [183]), which will result in a broader distribution of the local electric field for a tetragonal material, as calculated in Fig. 5.13.[1] Also, as indicated in Fig. 5.12a–c, the increase in activation parameters follows the c_m/a_{pc} ratio. A higher lattice distortion will influence the internal compatibility stresses between non-180° domains, the domain structure, and the switching behavior, as revealed in Sec. 2.4.2. In particular, large stresses of the order of GPa were measured at domain wall junctions for tetragonal PZT compositions. For a lattice distortion of c/a=1.02, which is close to the lattice distortion of the investigated tetragonal sample (c_m/a_{pc}=1.016, x=0.5(T)), a maximum stress of $\sigma_{\max}$=0.8 GPa was found at the junction between lamellar domain regions (Fig. 2.16a). It was also predicted that during the movement of the domain walls, these large internal mechanical stresses have to be overcome [190], impeding the switching process. This effect is expected to be much less pronounced for materials on the rhombohedral site of the MPB, where the lattice distortion is much smaller. The interplay between lattice distortion and domain structure was demonstrated for a Ca doped $PbTiO_3$ model system. In this system, the density of strain-induced non-180° domains was found to increase with the lattice distortion (Fig. 2.16e and f). [192] In agreement to this prediction, a fine domain structure was observed for a tetragonal material, while the domain structure was much coarser in rhombohedral counterparts. [212] According to theoretical works, this should result in a reduced domain wall mobility for tetragonal materials, compared to rhombohedral counterparts [166; 227], as discussed in Sec. 2.4.4.

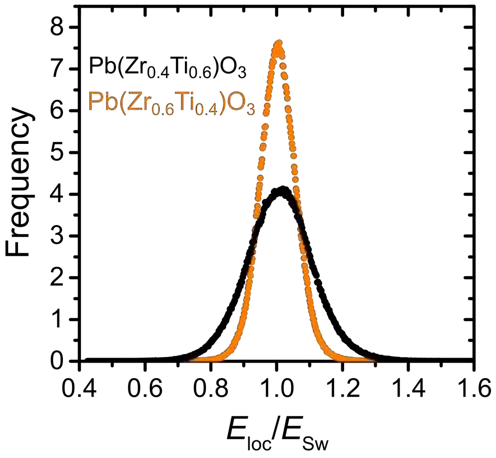

Figure 5.13.: Calculated local electric field distribution for a tetragonal ($Pb(Zr_{0.4}Ti_{0.6})O_3$) and rhombohedral ($Pb(Zr_{0.6}Ti_{0.4})O_3$) composition. For calculation the dielectric permittivity of a tetragonal (κ_{11}=499, κ_{33}=198), and a rhombohedral (κ_{11}=940, κ_{33}=530) material, as provided in Ref. [183], were used.

In the following, the influence of crystal structure on the shape of the dynamic polarization and strain curves, displayed for an exemplary switching field of $E_{\mathrm{Sw}}\approx0.9E_C^P$ (Fig. 5.12d and e) will be revealed.

The first regime is characterized by a linear increase of the negative strain on the logarithmic time scale with a field- and composition-dependent slope, which is accompanied by a small increase in polarization. The initial increase of the negative strain due to the converse piezoelectric effect at $6\cdot10^{-5}$ s (Fig. 5.12e) is highest for x=0.5(T), which is probably related to the height of the applied electric field pulse, being twice as high compared to x=0.4(R) and x=0.46(MPB). In addition, the slope $\Delta S/\Delta \ln(t)$ in the first regime is lowest for x=0.5(T), while it increases from x=0.4(R) to x=0.46(MPB). The slope in this regime can be related to the velocity of moving non-180° domain walls, which is highest for the MPB and lowest for the T composition. As displayed in Fig. 5.10, for electric fields above a certain field (0.700 kV/mm for x=0.4(R), 0.700 kV/mm for x=0.44(R), 0.667 kV/mm for x=0.46(MPB), and 1.011 kV/mm for x=0.475(T)) a change of the slope with time is visible, which is related to a change of the velocity of non-180° domain walls with time. This change of the slope cannot be observed for x=0.5(T).

The end of the first regime (Fig. 5.12d and e) is characterized by a material-specific maximum value of the negative strain and switched polariaztion, $\Delta P_{\mathrm{reg.\ 1}}$. The negative strain values are -0.18±0.01%, -0.35±0.01%, and -0.17±0.01% for x=0.4(R), x=0.46(MPB), and x=0.5(T), respectively. The errors represent the scattering between measurements with different electric field amplitudes. The amount of negative strain obtained from a sample is usually determined by the interplay between lattice distortion and domain wall mobility. With respect to the mechanical stresses involved in

---

[1] R. Khachaturyan is acknowledged for providing the calculated data.

the switching process [148; 172; 335] these parameters are however not independent [364] and the interplay provides maximum negative strain close to the tetragonal site of the MPB [211].

The corresponding switched polarizations at the end of the first regime (Fig. 5.12d and e) are 11.5±1.5 μC/cm^2, 12.6±0.5 μC/cm^2, and 11.9±3.0 μC/cm^2 for x=0.4(R), x=0.46(MPB), and x=0.5(T), respectively. These values account for 15±2%, 14±1% and 17±3% of the total switched polarization. For all the investigated compositions, the maximum negative strain value increases with increasing applied electric field pulse. This is accompanied by an increase in switched polarization. This is displayed in Fig. 5.14a for a PZT material with x=0.475(T). This is an interesting feature, which, however, is not completely understood. It should be noted that frequency-dependent measurements on the same material also indicate an increase in negative strain, when loops are measured under a higher frequency. The change of the shape of the loops with frequency is displayed in Fig. 5.14b, while the frequency dependence of the negative strain is plotted in Fig. 5.14c. An increase of negative strain with increasing frequency was previously also reported in literature. [365–367] Since the negative strain is mainly a result of non-180° domain wall contributions, the share of non-180° switching events is expected to be time- and frequency-dependent. The share of non-180° switching events thereby increases with increasing frequency or height of the applied electric field pulse, *i.e.*, the speed of polarization reversal. It is worth to mention that all state of the art models can solely describe the influence of frequency on the coercive field, but not on the strain. Typical examples are the models by Vopsaroiu *et al.* [368; 369], Orihara *et al.* [370] or Du and Chen [371]. However, all models neglect non-180° domain effects, even though the correlation between the frequency dependence of the negative strain and coercive field is apparent, as displayed in Fig. 5.14c.

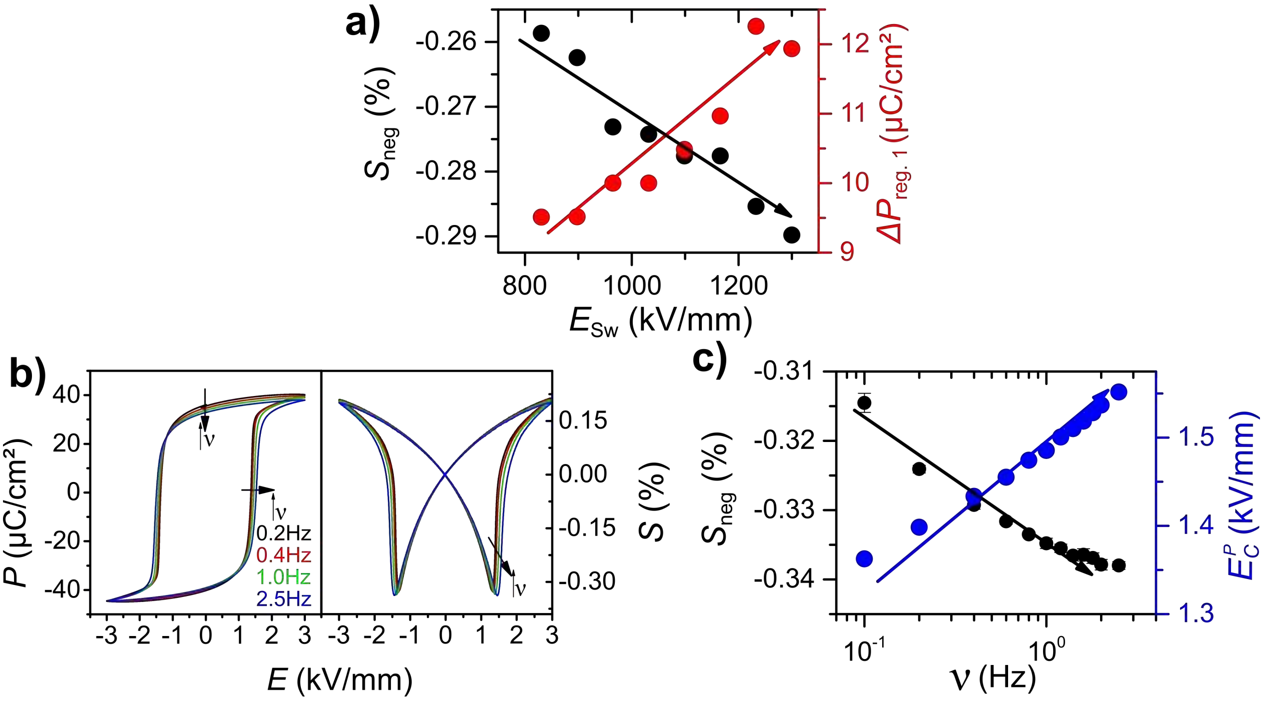

Figure 5.14.: Dependence of the negative strain on the speed of polarization reversal. All results are displayed for a PZT material with x=0.475(T). a) Dependence of negative strain and switched polarization in regime 1 on the height of the electric field pulse. The arrows represent a guide to the eye. b) Polarization and strain loops measured at different frequencies. The arrows indicate the influence of increasing frequency on the shape of the loops. c) Frequency dependence of the negative strain and the coercive field, obtained from the *P(E)* loops presented in b). The arrows represent a guide to the eye. Error bars represent values averaged from three measurements with different samples.

After the end of the first regime, the material enters the main switching phase (Fig. 5.12d and e). The change of the slope $\Delta S/\Delta\ln(t)$ at the maximum negative strain (Fig. 5.12e) is sharp for rhombohedral and MPB materials, whereas a broader plateau can be observed for tetragonal materials. This is in agreement to the strain loops (Fig. 5.9b) which also exhibit a broadening with increasing titanium content. Most of the polarization is switched in the main switching phase: 67.5 μC/cm^2 (84%), 64.5 μC/cm^2 (75%), and 51.0 μC/cm^2 (78%) for x=0.4(R), x=0.46(MPB), and x=0.5(T), respectively. This is accompanied by a large change in the macroscopic strain. The slope of the $\Delta\Delta P/\Delta\ln(t)$ at the inflection point of polarization vs. time curves on the logarithmic time scale in Fig. 5.12d can be used as an approximate estimation of the switching speed. While this slope is highest for x=0.4(R), it gradually decreases with increasing titanium content. This indicates that switching slows down with increasing titanium content.

The third regime is characterized by a small increase of the macroscopic strain on the logarithmic time scale, which is accompanied by a gradual saturation of the polarization. In this regime 4.4 μC/cm^2 (4%), 10.3 μC/cm^2 (10%), and 1.2 μC/cm^2 (1%) are switched for x=0.4(R), x=0.46(MPB), and x=0.5(T), respectively. The high fraction of switched polarization can also be manifested by the additional second slope appearing in the x=0.46(MPB) composition after the main rise of the switched polarization at 75 μC/cm^2 (Fig 5.10), which was not observed for other investigated compositions. This anomaly was previously observed in the $\Delta P(t)$ response in other polycrystalline ferroelectric samples [182; 202; 203] but could not be explained yet; however, it is not a characteristic of MPB compositions, as it was frequently reported for other samples.

5.2.2 Influence of grain size

Microstructure

The influence of grain size on switching dynamics was investigated on a series of rhombohedral samples with the composition $Pb(Zr_{0.7}Ti_{0.3})O_3$. The samples were sintered at different conditions. The sintering temperature ranged from 1100–1250 °C, while a dwell time in the range from 2–8 h was used. Higher sintering temperatures or longer dwell times resulted in considerable PbO volatilization and reduced properties. The obtained respective microstructures are shown in Fig. 5.15. A coarsening of the microstructure can be observed with increased sintering temperature and dwell time.

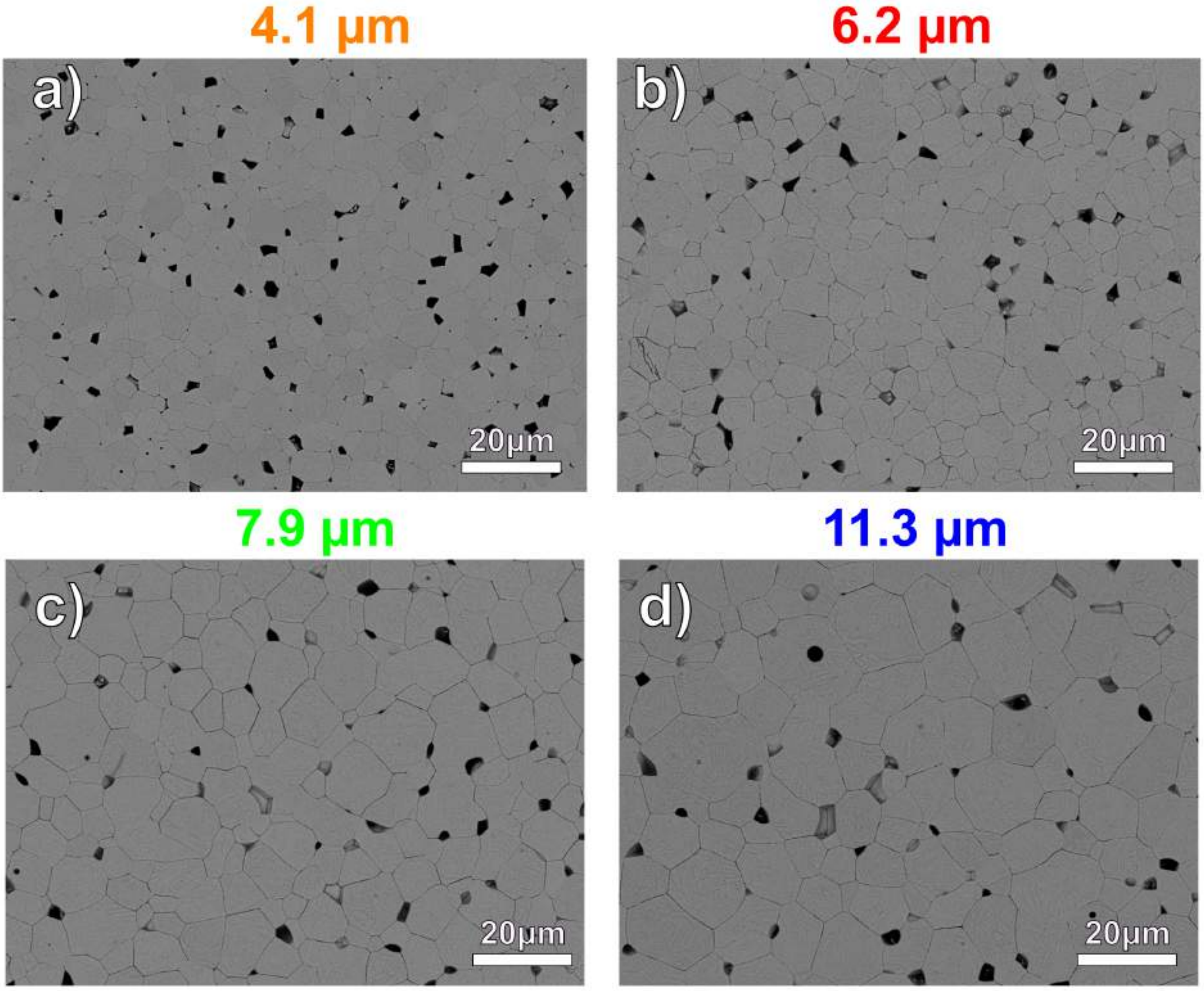

Figure 5.15.: Microstructural analysis for samples with increasing grain size from a) to d). The sintering conditions were: a) 1100 °C, 2 h, b) 1150 °C, 2 h; c)1150 °C, 8 h, and d) 1250 °C, 2 h.

The average grain size and the relative density of the samples are summarized in Tab. 5.4. It can be observed that the average grain size continuously increases from 4.1±0.3 μm to 11.3±3.8 μm, as the temperature or the dwell time increase, while the density, independently of the sintering conditions, reached a value of approximately 96–98% of the theoretical density. A theoretical density of 7.97 g/cm^3 was used for this calculation. [372] In addition, the grain size distribution broadened, as evidenced by the increased standard deviation. Similarly, a broadening of the distribution of grain sizes with increasing sintering temperature was observed for $Pb_{0.975}Sr_{0.02}[(Zr_{0.5275}Ti_{0.4725})Nb_{0.01}]O_3$ polycrystalline ceramics. [200]

Table 5.4.: Summary of microstructural parameters for samples with different grain sizes.

g (μm)	ρ (g/cm^3)	ρ_{rel} (%)	ϑ_{Sin} (°C)	t (h)
4.1±0.3	7.80	97.8%	1100	2
6.2±2.4	7.71	96.7%	1150	2
7.9±3.2	7.62	95.6%	1150	8
11.3±3.8	7.69	96.4%	1250	2

Domains in the unpoled samples with the smallest and the largest grains were visualized by PFM (amplitude images are displayed in Fig. 5.16, while phase images are displayed in Fig. A.1). Both samples exhibit a banded domain structure (Fig. 2.6b), which contains 180° as well as non-180° domain walls. This type of domain structure is expected for PZT samples above a critical grain size of about 1–2 μm. [42] As indicated in Fig. 5.16, the 180° domain walls appear as watermarks, while the non-180° domain walls exhibit a wedge-shaped domain morphology, which is typical for rhombohedral PZT ceramic materials [373]. The red lines indicate the position of the grain boundaries obtained from topography images. The green asterisks highlight grain boundaries that exhibit domain wall continuity. Domain walls that show continuity over grain boundaries can be found in all samples. Domain walls continue over grain boundaries, if the shape and the phase of the domain are not changed over the grain boundary. Therefore, PFM amplitude and phase images have to be investigated simultaneously. This was done for the domain wall marked by the blue square in Fig. 5.16b). Magnified PFM amplitude and phase images are displayed in Fig. A.2. Domain wall continuity over grain boundaries is a frequently observed feature in polycrystalline ferroelectric/ferroelastic materials [149–154], which is related to electric correlations across the grain boundary, as discussed in Sec. 2.3.2. A finer domain structure can be observed for the sample with a smaller grain size (g=4.1 μm),while the domain structure is broader for the sample with a larger grain size (g=11.3 μm). A decrease in grain size is accompanied by an increase in internal mechanical stresses [44; 229; 230]. In order to compensate for these stresses, the size of non-180° domains decreases [42], following Kittel's law [233]. Consequently, the domain structure gets finer when the grain size of the material is reduced. [235; 236] However, due to the wedge-shaped character of the domains it was not possible to quantify the domain size.

Bipolar measurements

Large signal polarization and strain loops of samples with different grain sizes are displayed in Fig. 5.17a and b, respectively, and characteristic properties are summarized in Tab. 5.5. The remanent polarization increases with increasing grain size (Fig. 5.17c). The sample with the grains size of 4.1 μm has a remanent polarization of 15.9 μC/cm^2, while the remanent polarization is almost doubled to 29.0 μC/cm^2 when the grain size of the samples is increased to 11.3 μm. Interestingly, the coercive field slightly increases with increasing grain size (Fig. 5.17d) from 0.70 kV/mm for the sample with the smallest grain size (g=4.1 μm) to 0.76 kV/mm for the sample with the largest grain size (g=11.3 μm).

The dependence of the coercive field on the grain size is provided in Fig. 5.18a and b. Here, literature results of various PZT-based compositions with different sintering conditions[1] and crystal structures are displayed. [212; 215; 216; 375–380] The results obtained from this study are highlighted as orange stars. The grain size dependence of the macroscopic properties can be separated into two ranges. The first range shows a rapid decrease of coercive field with increasing grain size, which is accompanied by an increase of polarization. The transition is clearly evident in the grain size dependence of the remanent polarization in the results by Randall *et al.* [215], Sakaki [379], and Yamamoto [378]. The transition occurs in the grain size range of 1–2 μm. This grain size correlates to the critical transition grain size at which the domain configuration changes between a lamellar and banded domain structure, reported previously. [42] The lamellar domain configuration (g<1–2 μm) can relax stresses in two dimensions. Therefore, the mechanical stresses developed at the phase transition temperature due to the spontaneous strain can be only partially released (Sec. 2.2.1) and significant internal

---

[1] Since hot pressing is known to have a significant influence on the internal stresses in polycrystalline ceramics [374], care must be taken when hot pressed and conventionally sintered samples are compared.

stresses remain in the polycrystalline materials, increasing the coercive field and significantly decreasing the remanent polarization. On the other hand, a banded domain structure ($g>1$–2 µm) can compensate for mechanical stresses in three directions. In addition, 180° domain walls can form. In this grain size range the coercive field decreases slightly with increasing grain size, accompanied by a small increase in remanent polarization. As confirmed by the PFM images, which show 180° and non-180° domain walls for both grain sizes (Fig. 5.16), all investigated materials are in the second range of grain sizes.

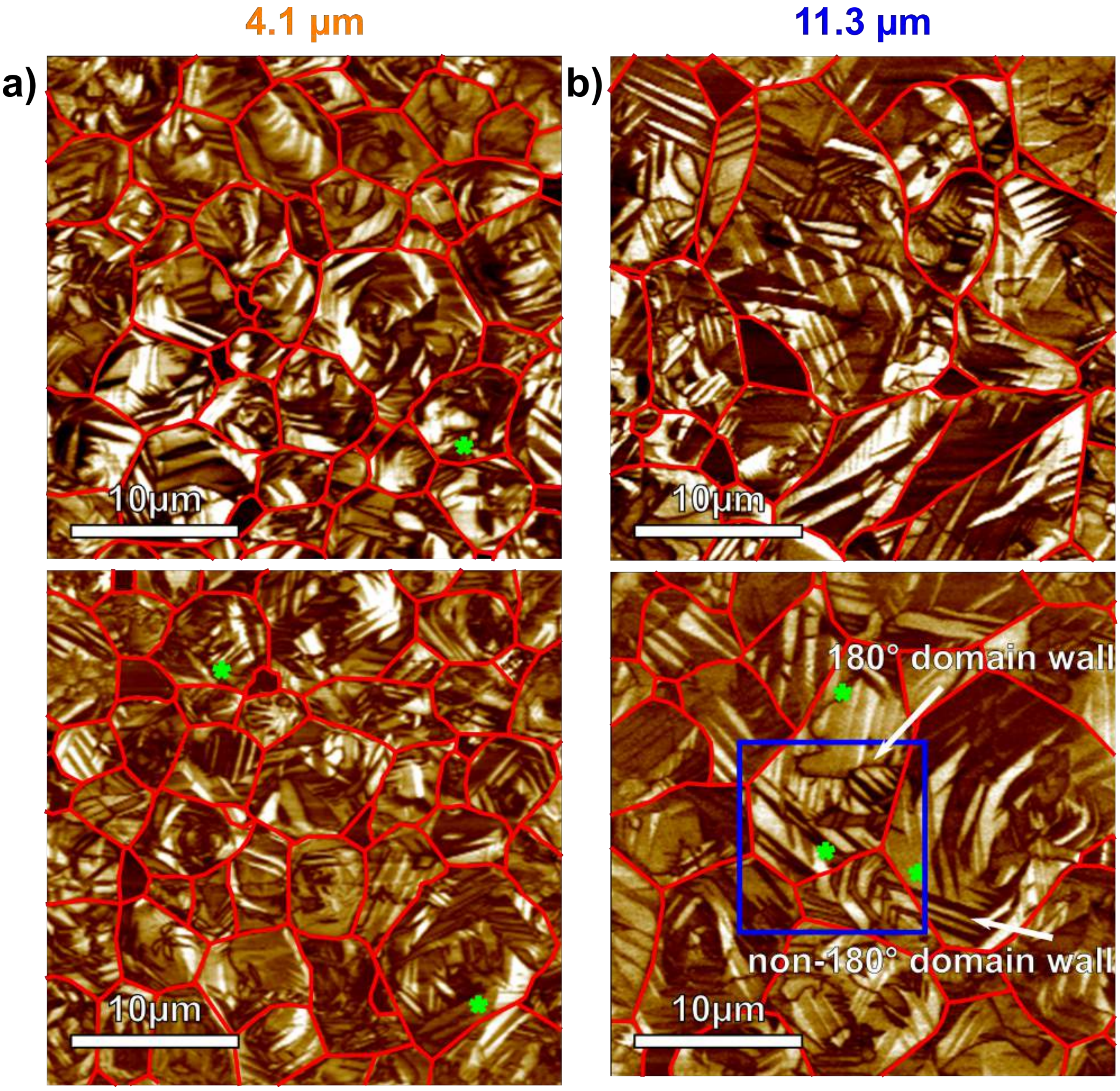

Figure 5.16.: Influence of grain size on the size and morphology of domains. PFM amplitude images of unpoled rhombohedral PZT samples with different grain sizes: a) 4.1 µm and b) 11.3 µm. For each sample representative images at two different positions are displayed. The red lines indicate the position of the grain boundaries according to topography images measured simultaneously. The green asterisks highlight grain boundaries that exhibit domain wall continuity. A 180° domain wall watermark structure is displayed, while non-180° domain walls usually exhibit a wedge shape [373]. Phase images are displayed in Fig. A.1. The blue marked area is magnified in Fig. A.2.

Both bipolar and negative strain increase with increasing grain size. While for the sample with the smallest grain size (g=4.1 µm) a bipolar strain of 0.10% and a negative strain of -0.03% were measured, the values increase to 0.16% and

-0.07% for a sample with a grain size of 11.3 μm. The shapes of the *P(E)* loops (Fig. 5.17a) were characterized by the squareness ratio R_{Sq} [201]

$$R_{\mathrm{Sq}} = \frac{P_r}{P_{\mathrm{Sat}}} + \frac{P_{1.1E_C}}{P_r}, \tag{5.2}$$

where $P_{1.1E_C}$ is the polarization at 1.1-times the coercive field. As revealed in Tab. 5.5 and displayed in Fig. 5.17e, the squarness ratio increases with increasing grain size. However, the values are well below the value of R_{Sq}=2, which is the theoretical value for a defect-free single crystalline material. This is also manifested by the change of slope $\Delta S/\Delta E$ at the maximum negative strain (Fig. 5.17b). While the change of slope at the maximum negative strain is sharp for a material with a large grain size (g=11.3 μm), it is more dispersive for a material with a small grain size (g=4.1 μm).

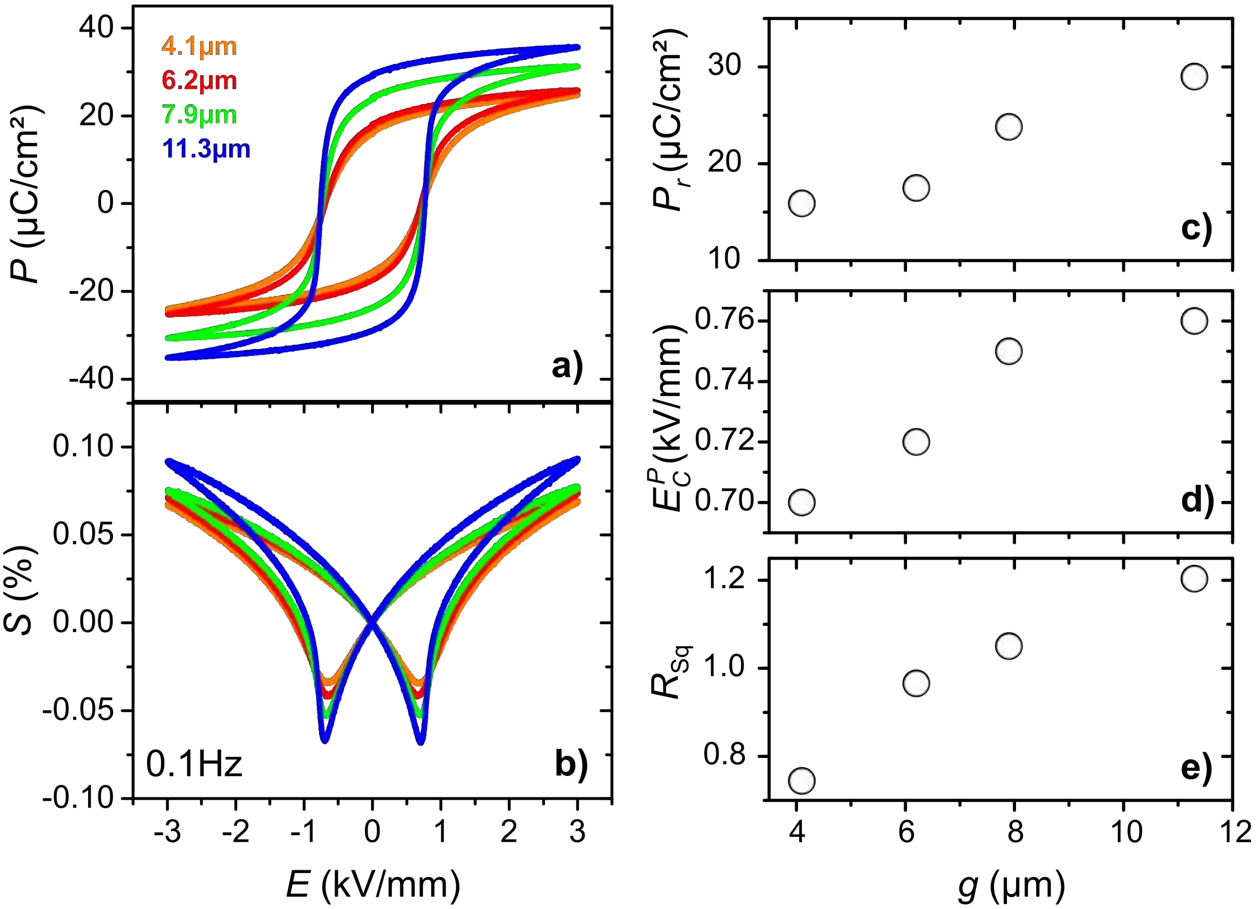

Figure 5.17.: a) Polarization and b) strain as a function of the electric field for samples with different grain sizes. The influence of grain size on the shape of the loop is characterized by the grain size dependence of c) the remanent polarization, d) the coercive field, and e) the squareness ratio of the polarization loops.

Table 5.5.: Summary of large signal ferroelectric properties of samples with different grain sizes.

g (μm)	E_C^P (kV/mm)	P_r (μC/cm^2)	R_{Sq}	S_{bip} (%)	S_{neg} (%)	E_a (kV/mm)
4.1±0.3	0.70	15.9	0.74	0.10	-0.03	26.5±1.2
6.2±2.4	0.72	17.5	0.96	0.11	-0.04	24.5±1.4
7.9±3.2	0.75	23.8	1.05	0.13	-0.05	24.6±1.6
11.3±3.8	0.76	29.0	1.20	0.16	-0.07	22.1±0.7

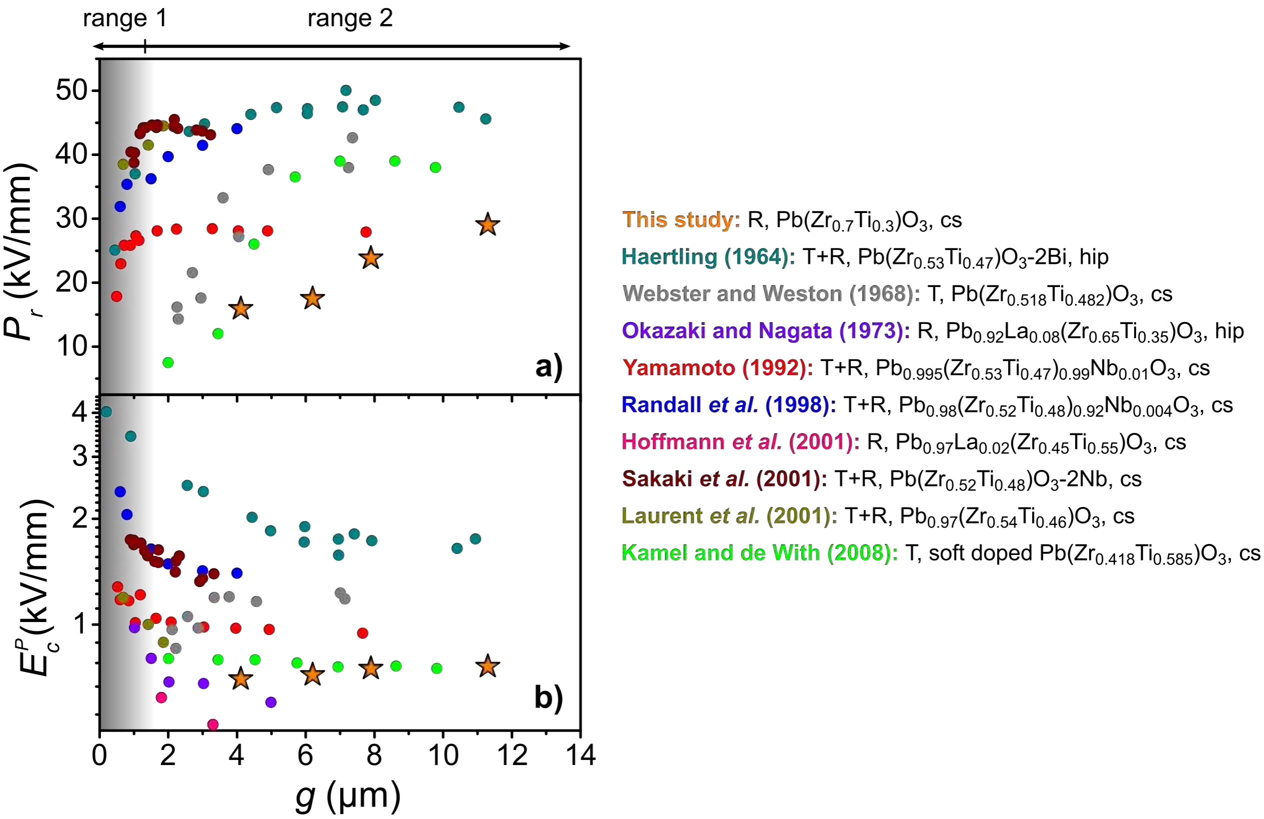

Figure 5.18.: Summary of the dependence of the average grain size on the a) remanent polarization and b) coercive field. The results from this study are plotted as orange stars. Values obtained from literature are plotted for comparison. [212; 215; 216; 375–380] (cs: conventional sintered, hip: hot isostatic pressed) The transition between range 1 (lamellar domain structure) and range 2 (bandend domain structure) at 1-2 µm is marked by the shaded area. [42]

Dynamic measurements

A more detailed analysis of the switching behavior is provided by time-dependent polarization and strain dynamics measurements, displayed in Fig. 5.19. The different regimes of polarization reversal, introduced and explained in Fig. 5.2, can be identified in the strain dynamic measurements.

The influence of grain size on the dynamic response in individual regimes is revealed in Fig. 5.20. Here, a comparison of characteristic curves is provided for a constant applied electric field. It should be noted that even though the external electric field is constant, local field distributions might be different in samples with different grain sizes. This is related to the anisotropy in the dielectric permittivity tensor and different domain configuration in the poled samples. For the first regime (Fig. 5.20a), the slope $\Delta S(t)/\Delta \ln(t)$ of the curves increases with increasing grain size. This indicates that the velocity of non-180° domain walls in the first regime increases with increasing grain size. According to theoretical calculations an increase of velocity of non-180°domain walls was predicted when the width of the domain structure increases. [166; 227] The time at which the transition from regime 1 to regime 2 occurs is independent of the grain size and occurs at approximately $4\cdot10^{-3}$ s for an applied electric field of $E_{\mathrm{Sw}}=0.840$ kV/mm. This indicates that the critical field required for this transition is independent of the grain size. The maximum negative strain at the transition from regime 1 to regime 2 (Fig. 5.20b) increases from -0.028% for the sample with a small grain size (g=4.1 µm) to to -0.048% for the sample with a large grain size (g=11.3 µm). The dependence of the negative strain is plotted as a function of grain size in Fig. 5.21a.

Hoffmann *et al.* investigated the origin of the macroscopic strain as a function of grain size in PZT materials using high resolution XRD. [212] In fine-grained materials, the intrinsic lattice strain of 0.11% was nearly the same as the macroscopically measured strain of 0.13%. In contrast in coarse-grained materials, the intrinsic lattice strain accounted to 0.08%, while the macroscopically measured strain was 0.13%. The difference of 0.05% between fine- and coarse-grained

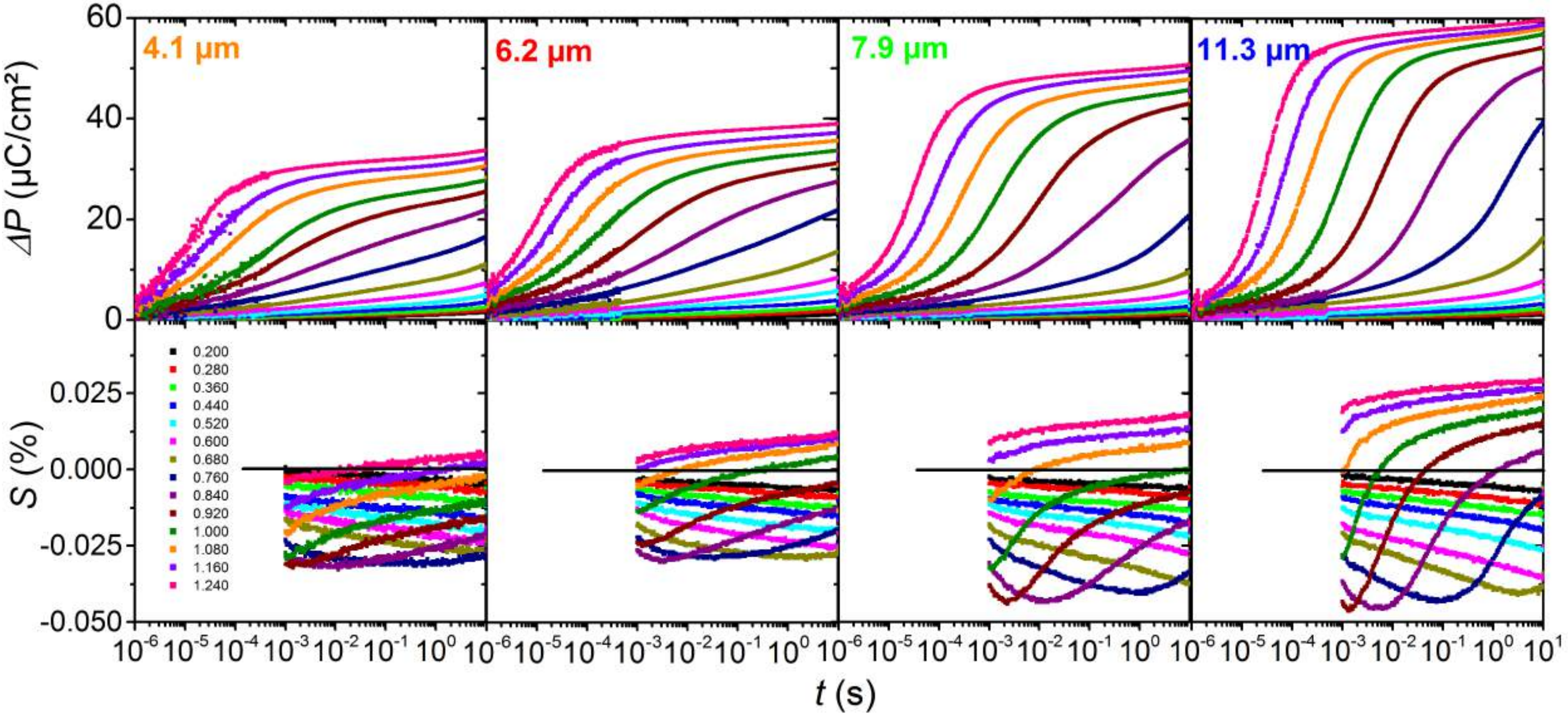

Figure 5.19.: Results of the simultaneous measurements of the switched polarization and strain of polycrystalline PZT ceramics with different grain sizes. The curves were measured at different applied electric field pulses, as indicated by the inset values. The solid line represents a poled material. The solid line represents zero relative strain, obtained by normalizing with the poled state (Eqn. 4.5).

samples was explained with an enhanced motion of non-180° domain walls, as the grain size increased.[1] This observation was related to reduced grain-to-grain clamping in coarse-grained materials compared to fine-grained materials. Since the switching process requires mechanical correlations over the grain boundaries [161–164], transgranular cooperation of domain walls will be involved. As schematically indicated in Fig. 5.2, the movement of ferroelastic domain walls causes a change of the shape of the grain. Since the grains are randomly oriented, the amount of ferroelastic domain switching fraction is different in individual grains, depending on their orientation to the applied electric field (Fig. 5.7c). This results in elastic stress fields between grains, which hinder the switching process. [148; 172; 335] These stresses should increase with decreasing grain size. In a recent diffraction study by Khatua *et al.*, the influence of grain size on the switching process in $(Na_{0.5}Bi_{0.5})TiO_3$ was investigated. In agreement with other studies, they found a dramatic reduction in switched polarization and a suppression of the ferroelectric behavior, when the grain size decreases to the submicron range, if a bulk ceramic material is investigated. However, when loosely-connected particles of the same material and size, embedded in an elastic polymer matrix (powder-poling technique [381]) were subjected to the same electric field, a distinct splitting of the Bragg peaks was observed. [382] While the clamped grains in the former case did not exhibit switching, the almost free particles in the later case clearly exhibited ferroelectric/ferroelastic switching.

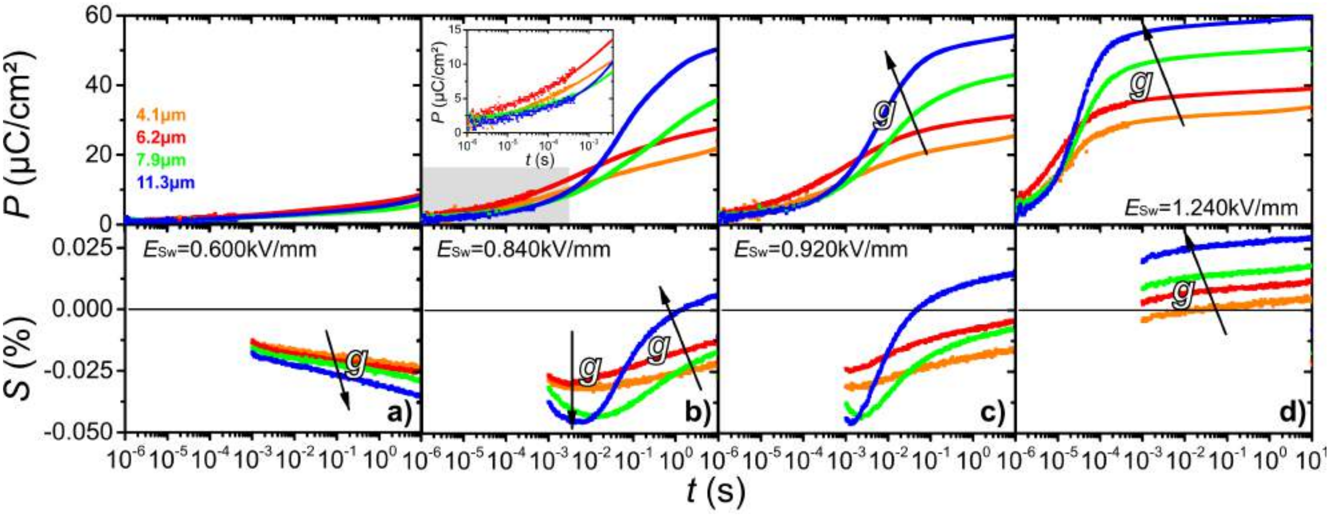

Figure 5.20.: Influence of grain size on the different regimes of polarization reversal. The measurements were performed at constant electric fields, as indicated. The influence of grain size on initial non-180° domain wall movement is displayed in a). The transition from regime 1 to regime 2 is shown in b). The gray shaded area, highlighting the time-dependent switched polarization at the transition from regime 1 to 2, is magnified in the inset. The influence of grain size on the main switching phase (regime 2) and creep-like domain wall movement (regime 3) is shown in c) and d), respectively.

Interestingly, for the grain sizes of 4.1 µm and 6.2 µm, ≈35% of the total reversed polarization occurs in regime 1, while this value reduces to ≈18% for larger grain sizes of 7.9 µm and 11.3 µm (inset in Fig. 5.20b). The dependence of the share of switched polarization in regime 1 to the totally switched polarization is displayed as a function of the grain size in Fig. 5.21a. The increase of the share of the switched polarization, in combination with a decrease in negative strain with decreasing grain size, indicates an enhanced contribution of strain-free 180° switching events to the totally switched polarization in regime 1, when the grain size gets reduced.

This observation can be explained by Landau free energy calculations. The influence of stress on the Landau free energy landscapes for a rhombohedral $Pb(Zr_{0.7}Ti_{0.3})O_3$ material is displayed in Fig. 5.21c–e. The applied stress is compressive in the direction of the spontaneous polarization. This mimics the suppression of the development of the spontaneous strain at the phase transition temperature in polycrystalline ferroelectrics. The 180° switching path is marked by the white line between the two stable rhombohedral states in Fig. 5.21c–e. The activation barrier for this path is plotted as a function of the magnitude of the applied stress in Fig. 5.21b. The stresses of two hypothetical polycrystalline ceramic materials with different grain sizes ($g_1 > g_2$) are highlighted in Fig. 5.21b. Thereby, the hypothetical material with a smaller grain size, g_2, has a broader stress gradient. The activation barriers for the two hypothetical materials can be calculated as ΔG_{g_1} and ΔG_{g_2}. It can be observed that the activation barriers for the material with the smaller grain size, g_2, are broader compared

---

[1] It should be noted, that recent results obtained by Ghosh *et al.* do not agree with the report by Hoffmann *et al.* [212]. They found a higher non-180° domain switching fraction of $\Delta\eta_{002}$=0.013±0.02 for a material with a grain size of 1.97±0.44 µm, while a domain switching fraction of $\Delta\eta_{002}$=0.007±0.02 was found for a material with a grain size of 3.52±0.29 µm. [232] Unfortunately, in both studies only two samples were measured.

to the material with the larger grain size, g_1. Smith *et al.* correlated the distribution in the lattice strains to the broad distribution of switching times [318], which can explain the observed switching behavior, characterized by enhanced 180° domain contribution in regime 1 when the domain size gets reduced (Fig. 5.21a).

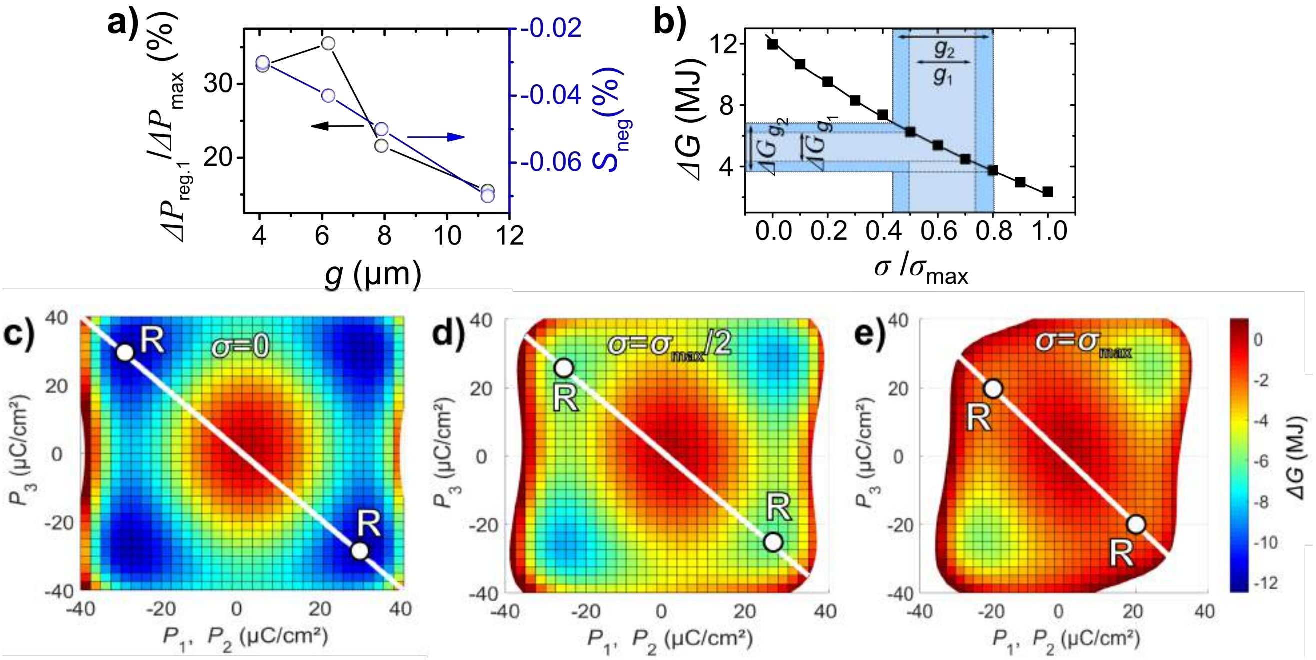

Figure 5.21.: Grain size effects on polarization reversal. a) Influence of grain size on the maximum negative strain and on the share of switched polarization in regime 1 to the total switched polarization. b) The influence of stress on the energy barrier of the 180° switching path obtained from Landau energy landscapes for a rhombohedral PZT ($Pb(Zr_{0.7}Ti_{0.3})O_3$). Landau energy landscapes for σ=0, σ=$\sigma_{max}/2$, and σ=σ_{max} are displayed in c), d), and e), respectively. The stress is compressive and is applied in the direction of the spontaneous strain. Two hypothetical materials, with different grain sizes, $g_1 > g_2$, are displayed and the respective energy barriers for the 180° switching path are highlighted.

In agreement with the strain loops presented in Fig. 5.17, the transition from regime 1 to regime 2 is broad for a small grain size of 4.1 µm, while it is sharp for larger grain sizes (Fig. 5.20b). This can also be observed from the $\Delta P(t)$ curves measured at an applied electric field of E_{Sw}=0.920 kV/mm, presented in Fig. 5.20c. While a rapid and sharp increase occurs for the material with the grain size of 11.3 µm, the polarization slowly rises for a material with the grain size of 4.1 µm, indicating a sharp and a broad distribution of switching times, respectively. In a region of 720–820 nm around the grain boundary, domains with a lower mobility were observed in a thin film model system, as compared to domains in the grain interior. [252] For this grain boundary region also a two times higher coercive field was reported [165], which indicates the influence of the grain boundary on the domain wall mobility. Assuming in this context grains as spherical particles, a 46 vol.% of the material will be influenced by the grain boundary in rhombohedral PZT materials for a grain size of 4.1 µm, while only a 20 vol.% will be influenced when the grain size is increased to 11.3 µm. In addition, it should be kept in mind, that grain boundaries act as pinning sites, adding an additional barrier for the movement of the domain walls. [249–251]

The characteristic times for the main switching phase, obtained from the $\Delta P(t)$ curves (Fig. 5.19), are plotted in Fig. 5.22a as a function of the inverse applied electric field amplitude. Please note that due to the broadness of the distribution of the switching response, only the field dependence of the characteristic switching times for the second regime could be extracted for this sample series. The solid lines in Fig. 5.22a represent the fits according to the Merz law (Eqn. 5.1). The determined activation fields for the main switching phase are summarized in Tab. 5.5. Activation fields of 26.5±1.2 kV/mm and 22.1±0.7 kV/mm were determined for the samples with a grain size of 4.1 µm and 11.3 µm, respectively. As indicated in figure 5.22b, the activation fields for the main switching phase decrease with increasing grain size. These results are in agreement to the activation fields reported by Zhukov *et al.*, who found a slight decrease in activation field for a tetragonal PZT material for grain sizes in the range of 1.12–2.65 µm [181]. Interestingly, the coercive fields of the samples exhibit an opposed trend (Fig. 5.17d). However, it should be noted that the activation fields were calculated from data measured over a broad time- and field-range, while the coercive field was measured at a single frequency. While an exact explanation of this discrepancy would require additional analysis, it is likely that the observed change is related to the frequency-dependence of the domain dynamics.

For high electric field pulses, the material is in the third regime ($E_{\mathrm{Sw}}=1.240\,\mathrm{kV/mm}$, Fig. 5.20d). In this regime, the slope $\Delta S(t)/\Delta \ln(t)$ of the curves is independent of the grain size or the deviations are small and not detectable by our methods.

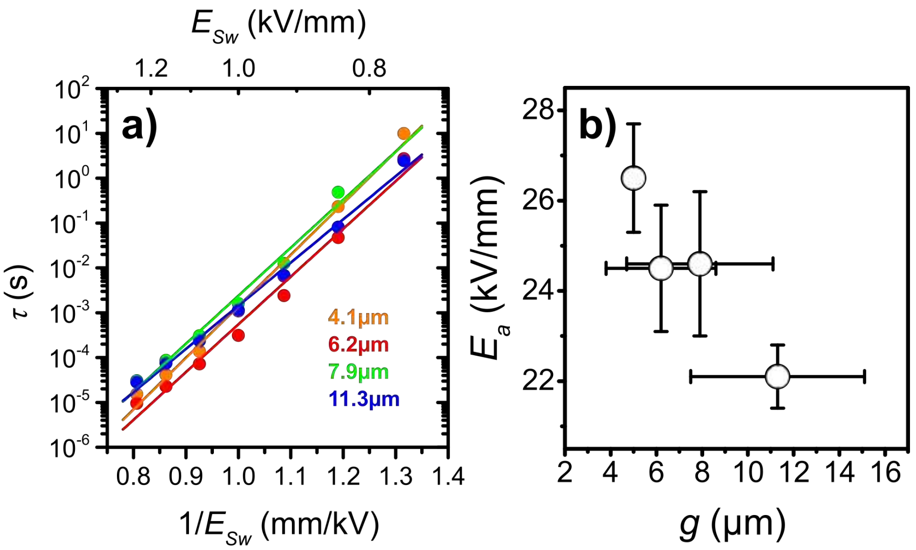

Figure 5.22.: Influence of the average grain size on the activation field for the main switching phase. a) Field-dependent switching times (determined from $\Delta P(t)$ curves (Fig. 5.19); time where 50% of the polarization is reversed) plotted as a function of the inverse applied electric field. The solid lines show fits to the data points according to the Merz law. The determined activation fields are plotted as a function of the grain size in b). The error bars represent the standard deviation obtained by the least square method.

5.2.3 Influence of degree of texture[1]

Microstructural and crystallographic analysis

Polycrystalline samples on the basis of BCT15 were prepared with different degrees of crystallographic texture. The XRD patterns of the samples are provided in Fig. 5.23. No secondary phases can be detected in any of the diffraction patterns and all patterns can be described by a single tetragonal perovskite phase. The samples reveal a (001),(100) crystallographic texture, whereby the (110) reflection group, which usually has the highest intensity in tetragonally-distorted perovskite materials, almost vanishes for the samples with the highest degree of texture.

The degree of crystallographic texture can be described by the Lotgering factor [325], which was determined for the samples according to Eqn. 4.1 and is provided by the numbers in Fig. 5.23b. In the context of the Lotgering factor, a value of 100% represents a perfectly textured sample, while a value of 0% represents a perfectly random sample. For the investigated samples, Lotgering factors in the range of 26–83% were identified.

The MD equation (Eqn. 4.3) [326] can give additional information about the distribution of crystallite orientations. Good fits were obtained for choosing $(h_1k_1l_1)$ to be (100) and $(h_2k_2l_2)$ to be (001) lattice planes (Rietveld refinement results of the XRD diffraction data in Fig. 5.23 are provided in Fig. A.3). In agreement with the structural relationship of the cubic unit cell to the tetragonal perovskite unit cell it was found that the peaks of the (001) and (100) lattice planes have an approximate intensity ratio of 1:2. Therefore, the parameter f was fixed at a value of 66.67%. It was found that good fits could be obtained if $r_1=r_2$, limiting the MD equation to one refinable parameter $r_{1,2}$, which is displayed in Tab. 5.6. The MD parameter $r_{1,2}$ may vary in the range of 0–1, where 0 represents a sample with a perfect crystallographic orientation and 1 represents a perfectly-random sample. As can be concluded from Tab. 5.6, the MD equation and the Lotgering equation give similar qualitative values to describe the degree of crystallographic texture. Therefore, in the

---

[1] Part of this section was published previously in [182; 383].

following discussion, the degree of crystallographic orientation will be described by the Lotgering factor. However, it should be noted that the Lotgering factor represents only an arbitrary texture fraction and is not related to the volume of the textured material. [384]

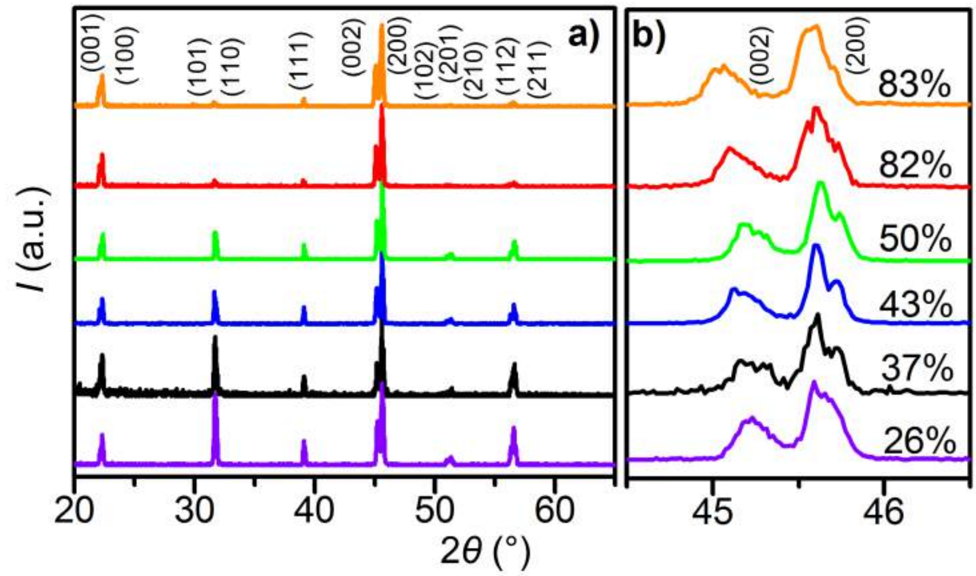

Figure 5.23.: a) Full range XRD patterns and b) (002),(200) reflections of BCT15 samples with different degrees of crystallographic texture. The degree of crystallographic texture is indicated by the Lotgering factor in b).

While all samples were produced by tape casting, only the samples with a high degree of crystallographic texture ($F \geq 82\%$) were manufactured using oriented templated particles, whereas the others ($F < 82\%$) were produced without templates. Interestingly, even samples without templates exhibit an induced preferred crystallographic texture and F values up to 50% could be achieved. Therefore, beyond the platelet-like seed particles other factors influence the degree of crystallographic texture of the samples. One of them is the anisometric shape of the starting powder particles, which get oriented during the doctor blade process.

Table 5.6.: Summary of microstructural parameters and small signal properties for samples with different degrees of crystallographic texture.

F (%)	$r_{1,2}$	ρ (%)	a (Å)	c (Å)	c/a	g (µm)	ϑ_{Cur} (°C)	ϑ_D (°C)
83	0.25	94.3	3.9783(4)	4.0210(5)	1.0107(2)	9.4±0.9	117	116
82	0.26	92.7	3.9763(4)	4.0155(5)	1.0099(2)	9.9±1.0	114	116
50	0.42	97.0	3.9739(5)	4.0097(5)	1.0090(2)	7.1±0.7	104	102
43	0.43	96.0	3.9746(2)	4.0124(5)	1.0095(1)	6.1±1.1	107	107
37	0.50	96.0	3.9749(5)	4.0082(5)	1.0084(2)	5.3±0.5	102	103
26	0.53	96.0	3.9752(4)	4.0081(4)	1.0083(1)	5.7±0.6	92	100

The refined lattice parameters a and c for the tetragonally-distorted unit cell of the samples with the lowest degree of texture (F=26%, a=3.9783(4) and c=4.0210(5), Tab. 5.6) are in good agreement with the values reported in the literature for nontextured polycrystalline materials [385; 386]. As manifested by the larger splitting of the (002)/(200) peaks for samples with a higher degree of texture, demonstrated in Figure 5.23b and quantified by the c/a ratio, presented in Tab. 5.6, the tetragonal distortion increases with increasing the degree of texture. A value of c/a=1.0107(2) and c/a=1.0081(1) was found for the sample with high (F=83%) and the sample with low (F=26%) degree of texture, respectively. This behavior is in agreement with previous reports on textured piezoceramic materials [387; 388] and was often related to a mismatch of lattice parameters between templates and matrix grains, which causes stresses between them. These were quantified by finite element method simulations and stresses up to 8 MPa were found. [389] Interestingly, these stresses are much lower compared to internal stresses in BT ceramics, which are induced by the spontaneous strain upon cooling below T_C and can exceed 70 MPa. [44; 45] In a single-domain crystal with non-constrained surfaces, the spontaneous strain is developed and the crystal remains unstrained. [44] The random crystallographic orientation of the grains in a polycrystalline sample imposes a mechanical constraint and internal residual stresses increase. A decrease of the tetragonality ratio was also observed for BT single crystals, when an external hydrostatic pressure was applied. [390] Crystallographically textured materials can be described as an intermediate state between nontextured polycrystalline materials and single crystals. Crystallographically textured materials show a cooperative development of the spontaneous strain during the phase transformation from the cubic, paraelectric phase to the tetragonal, ferroelectric phase. This cooperative alignment of the tetragonal distortion allows the formation of a tetragonal structure with a c/a ratio that approaches the value of a BCT single crystal. Indeed, the tetragonal distortion of BCT single crystals with 7 mol.% Ca was reported to be 1.012 [391], which is close to the value obtained for the samples with the highest degree of texture in this work (Tab. 5.6).

Microstructures of the samples with a high (F=83%) and a low (F=26%) degree of crystallographic texture are displayed in figure 5.24, while the grain size and density are summarized in Tab. 5.6. The densities of the samples vary between 92% and 97%, while the grain sizes are in the range 5.7–9.4 µm.

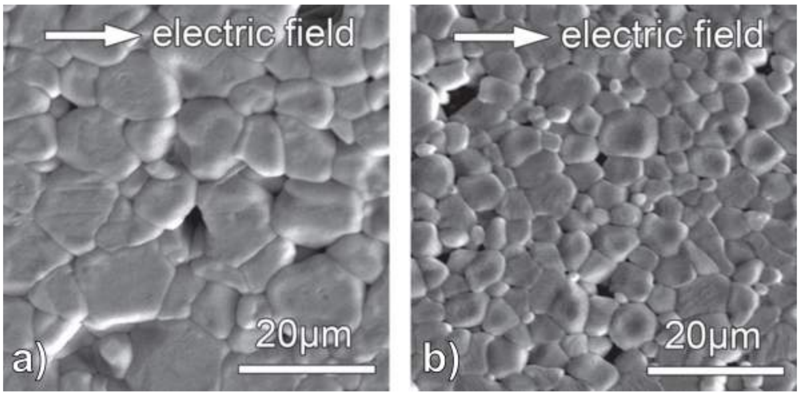

Figure 5.24.: Microstructure of polycrystalline BCT15 samples with a) high (*F*=82%) and b) low (*F*=26%) degree of texture. The direction of the applied external electric field during poling, electromechanical characterization, and switching experiments is indicated by the arrows. The electric field is applied perpendicular to the tape casting direction.

Small signal properties

Temperature-dependent dielectric permittivity and loss factors of the samples with different degrees of texture are displayed in Fig. 5.25a. The inset in Fig. 5.25a highlights the temperature-dependent permittivity at different frequencies for the BCT15 (F=83%) sample. The observed peak of the loss factor curve can be related to the structural phase transition between the ferroelectric tetragonal and the paraelectric cubic phase, which is commonly associated with the Curie temperature. As observed in many other BT-based polycrystalline ceramic material [392], the peak is smeared over a broad temperature range, which indicates a diffuse phase transition. An additional feature in the permittivity curve is the appearance of a second peak for the samples with a high degree of texture (F=82–83%). The peak at higher temperatures might occur due to chemically-inhomogeneous regions with slightly different Curie temperatures. The use of BT and CT templates might induce a Ba/Ca concentration gradient from the interior of the grain to the grain boundary. Similar features in the permittivity curves have been previously observed for core-shell structures and were also related to chemical inhomogeneity. [393] This gradient, however, could not be resolved using energy-dispersive X-ray spectroscopy due to poor resolution of the Ca peak and small variations in the concentration profile.

In addition, the TSDC was measured (Fig. 5.25b). The depolarization temperature (ϑ_D) is determined at the maximum of the current and is related to the ferroelectric-paraelectric phase transition. [394] The inset in Fig. 5.25b depicts temperature-dependent polarization obtained from TSDC measurements by integration of depolarization current density over time. For all samples, the polarization starts to decrease at room temperature, followed by a steep decrease at corresponding ϑ_D, after which, zero polarization value is reached. This behavior is typical for ferroelectric materials. [394]

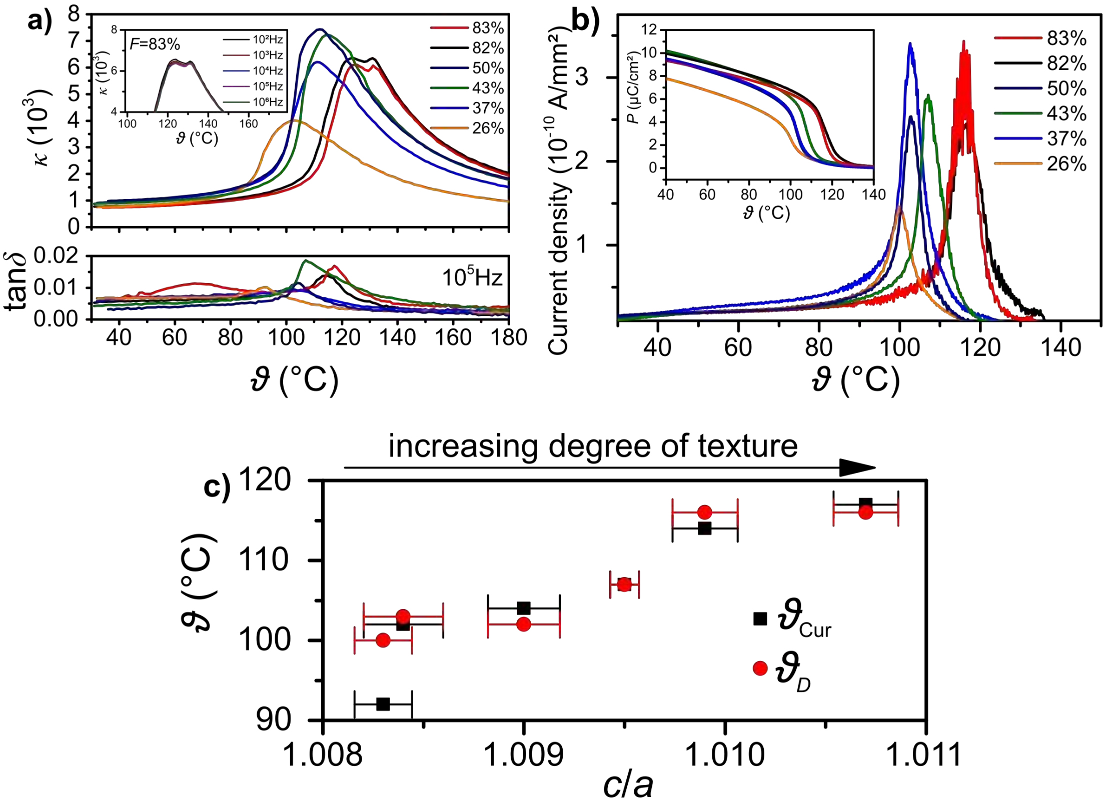

Figure 5.25.: Influence of crystallograpic texture on small signal properties. a) Temperature-dependent permittivity and loss factor. The frequency-dependency of a sample with a high degree of texture (F=83%) is shown in the inset. b) TSDC measurements for samples with different degrees of crystallographic texture. The inset shows the temperature-dependent polarization calculated from TSDC measurements. c) Dependence of the Curie and depolarization temperatures on the tetragonality ratio of the BCT15 samples.

The characteristic temperatures obtained from dielectric and TSDC measurements are summarized in Tab. 5.24. Samples with a high degree of texture depict higher characteristic temperatures (F=82–83%; ϑ_{Cur}=114–117°C; ϑ_D=116°C) than their counterparts with a low degree of texture (F=26–50%; ϑ_{Cur}=92–107 °C; ϑ_{D}=100–102 °C). For comparison, a value of ϑ_{Cur}=121 °C was reported for a single crystal with a similar composition. [395]. This is close to the values found for high degrees of crystallographic orientation. As revealed in previous studies, the Curie and depolarization temperatures of ferroelectric materials are influenced by the chemical composition [387; 396] or mechanical stresses [397; 398], but do not depend on the direction of the crystallographic orientation [399–401].

Gradients in the chemical composition of crystallographically-textured polycrystalline ceramics are often induced by the template particles used for the templated grain growth process. A change in the ϑ_C of about 20 °C was previously observed if templates with a different chemical composition compared to the bulk were used. [387; 396; 402] On the other hand, only minor changes (below 4 °C) were observed for templates with the same chemical composition as the bulk materials [403], for templates with a high chemical stability in the matrix [404; 405], or for textured ceramic which had been prepared by a process without templates [406].

The temperature change observed in this study is therefore partially related to the chemical modification induced by the BT and CT platelet particles, which were used for the templated grain growth process. In addition, the Curie temperature is influenced by the change of mechanical stress states. It is known that hydrostatic and uniaxial pressures can lead to a decrease of the Curie temperature of BT [293; 397], whereas radial pressure results in an increase [407], which is related to the stability of the tetragonal structure [408; 409]. In the case of textured polycrystalline ceramics, it may therefore be assumed that a different internal stress state in ceramics with a high degree of crystallographic texture, compared to random ceramics, results in a more stable tetragonal distortion, thus increasing its tetragonal to cubic phase transition temperature, as outlined in Fig. 5.25c.

Large signal polarization and strain loops for polycrystalline BCT15 samples, measured at 3 kV/mm and 0.1 Hz, are presented in Fig. 5.26a and b. A polarization loop of a [100] oriented BT single crystal is displayed for comparison [271] in Fig. 5.26c. Characteristic parameters are summarized in Tab. 5.7.

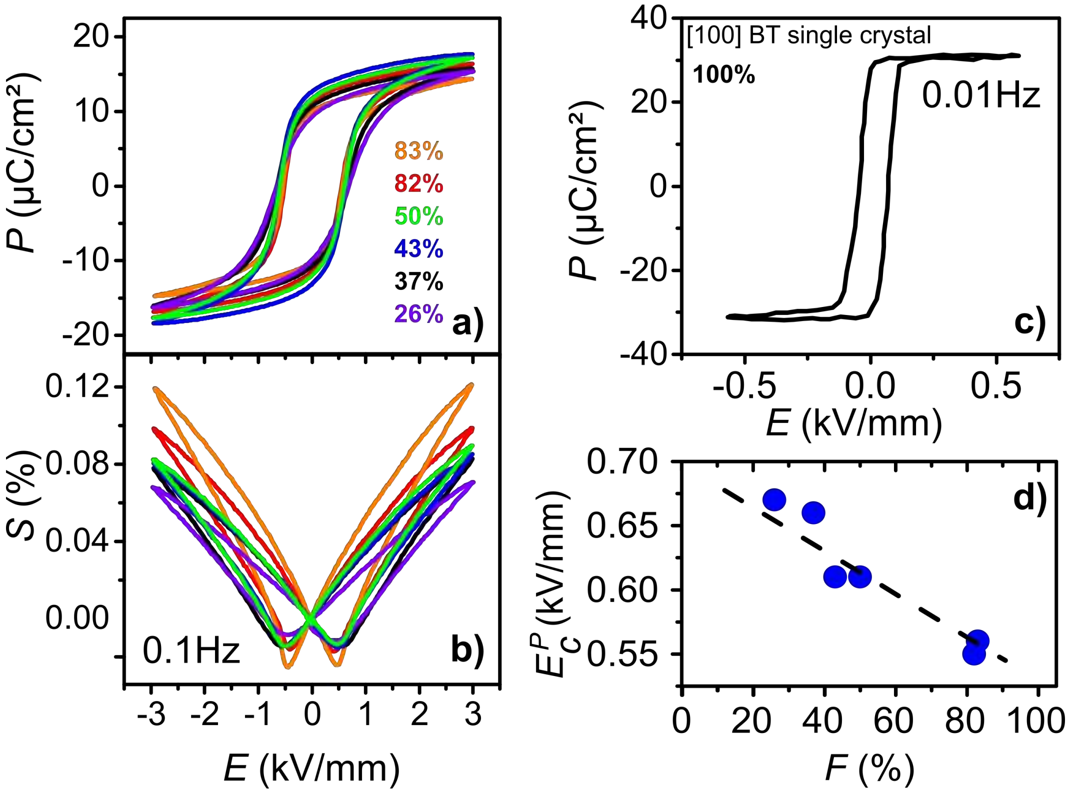

Figure 5.26.: Influence of degree of crystallographic texture on bipolar large signal measurements. Large signal a) polarization, and b) strain loops as a function of the electric field of polycrystalline BCT15 samples with different degrees of crystallographic texture (indicated by the Lotgering factor), measured at 0.1 Hz. The polarization loop of a [100] BT single crystal, measured at a frequency of 0.01 Hz, is plotted for comparison [Redrawn after Ref. [271]]. d) The coercive field plotted as a function of the Lotgering factor.

The dependence of the coercive field on the Lotgering factor is plotted in Fig. 5.26d. The coercive field of highly textured samples (0.55–0.67 kV/mm) decreases by about 18% compared to samples with a lower degree of crystallographic texture (0.60–0.67 kV/mm). For comparison, the coercive field of a [100] BT single crystalline material was found to be 0.05 kV/mm, which is about an order of magnitude lower compared to the coercive field of the polycrystalline counterparts. Interestingly, literature is inconsistent regarding the influence of texture on the coercive field. Some authors report an increase of the coercive field for crystallographically textured samples [403–405], others observe no effect [402], while again in other publications a decrease was reported [224; 410–412]. The effect seems to be strongly dependent on the volume percentage of templates used [402; 413] and was related to interfacial stresses between templated particles and matrix grains [402].

The shape of the *P(E)* loops was characterized by the squareness ratio, according to Eq. 5.2. [201] As revealed in Tab. 5.7, samples with a high degree of crystallographic texture (F=83%) exhibit a value of R_{Sq}=0.93, while lower values of R_{Sq}=0.77 were found for samples with a low degree of crystallographic texture (F=26%). A polarization loop with a higher squareness ratio is a well known feature of textured materials, previously reported for perovskite-layer-structured materials [223], perovskite bulk ceramics [224; 414–416], and perovskite thin films [417; 418]. However, even the sample with the highest degree of crystallographic texture in this study (F=83%), still has a much lower squareness ratio compared to the BT single crystal with R_{Sq}=1.37. This value is lower than the squareness ratio of a perfect, defect free single crystal, which is R_{Sq}=2 [201].

For this series of samples only the polarization was measured due to experimental limitations on the sample thickness. Therefore, only $\Delta P(t)$ measurements are displayed in Fig. 5.27a. The dynamic behavior is compared to a [100] oriented BT single crystalline sample. It can be observed that ceramics with a high degree of crystallographic texture (F=83%) have a 2 to 3 orders of magnitude higher switching speed, as compared to ceramics with a low degree of crystallographic texture (F=26%). While the BT single crystal shows a sharp and fast switching transition, the polycrystalline samples exhibit a slow and dispersive response. Application of the Merz law [13] to dynamic curves measured at different field pulses (not displayed here) allowed to determine activation fields for the main switching phase (regime 2 in Fig. 5.2). These are displayed in Tab. 5.7 and plotted as a function of the Lotgering factor in Fig. 5.27b. While samples with a high degree of crystallographic texture (F=82–83%) exhibit a low activation field of 5.19–7.52 kV/mm, higher activation field values of 8.52–9.68 kV/mm were found for samples, which exhibit a low degree of crystallographic texture (F=26–37%). For a BT single crystal, an activation field of 0.61 kV/mm was determined.

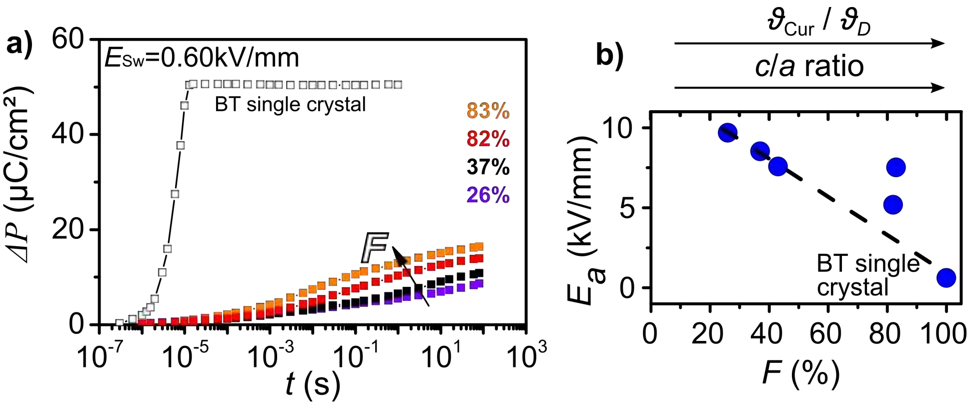

Figure 5.27.: Summary of measurements characterizing the influence of degree of crystallographic texture on polarization reversal. a) Comparison of polarization dynamic curves for polycrystalline BCT15 samples with different degrees of texture, measured under a constant electric field of E_{SW}=0.60 kV/mm. The full squares represent data points of polycrystalline samples with different degrees of crystallographic texture, characterized according to the Lotgering factor, while the empty squares represent data points for a BT single crystal. b) The activation field plotted as a function of the Lotgering factor. The activation field for F=100% represents a single crystalline sample. The dashed line is a guide for the eye and indicates a linear dependence. The arrows in b) indicate the increasing c/a ratio and paraelectric/ferroelectric phase transition temperatures.

Facilitation of the switching behavior with increasing degree of crystallographic texture, as revealed by a decrease of coercive field (Fig. 5.26d), an increase of the squareness parameter (Tab. 5.7) and a decrease of the activation field (Fig. 5.27b), with Lotgering factor, can mainly be related to internal stresses. Samples with a high degree of crystallographic orientation exhibit reduced internal stresses, allowing a cooperative alignment of the polarization vectors during the polarization reversal process and thus facilitated switching. Reduced internal stresses due to the cooperative alignment of the spontaneous strain at the paraelectric-ferroelectric phase transition temperature during cooling, also allows higher c/a ratios in textured materials (Tab. 5.6), approaching the value of a single crystalline material. A facilitated alignment of the spontaneous strain at the phase transition temperature also influences the value of the transition temperature itself. Samples with a high degree of crystallographic texture exhibit a high phase transition temperature, similar to a single crystalline material, while the phase transition temperature (Tab. 5.24) decreases for samples with a reduced degree of crystallographic texture. The correlation between the phase transition temperatures, the c/a ratio, and the Lotgering factor is displayed by arrows in Fig. 5.27b.

It should be mentioned that the switching behavior is in principle also influenced by the grain size of the material, as revealed in Sec. 5.2.2. According to Tab. 5.6 the grain size of the samples varies in the range between 5.7 and 9.4 μm. The dependence of the coercive field, the activation field for the main switching phase and the depolariaztion temperatures, plotted as a function of grain size and Lotgering factor are displayed in Fig. A.4. Since similar tendencies are observed, it cannot be unambiguously concluded that the observed changes are solely a result of the degree of crystallographic texture. However, it should be noted that the effect of the grain size on the properties is expected to be small, because all investigated samples exhibit a grain size larger than a threshold grain size of about 1.5 μm. Above this threshold grain size, properties are not expected to change significantly in BT ceramic materials. [236; 419]

For non-piezoelectric Al_2O_3 polycrystalline ceramics, lower residual stresses and a narrower stress distribution was previously reported for textured materials compared to their random counterparts. [246; 247] While experimental results on the influence of crystallographic texture on the stress state in bulk ferroelectric ceramics are rare, a decrease in elastic energy with increasing degree of crystallographic texture was reported in polycrystalline thin films. [163] It was also suggested that the in-plane component of mechanical stresses, localized at the grain boundaries and triple points, can exceed 10 MPa for BT with a low degree of texture (r=0.8) and vanishes completely if the material is highly textured (r=0) [420]. A direct consequence of this effect is that larger domains are expected in crystallographically textured samples, compared to the random ones [233], and thus the domain wall movement is facilitated [166; 227].

While the degree of domain switching was found to be limited in non-textured materials by microstructural aspects, numerical simulations [420] and experimental results [421] show that the domain switching fraction can be nearly doubled if the microstructure is textured. It was recently also found that crystallographically textured $0.91Na_{0.5}Bi_{0.5}TiO_3$-$0.06BaTiO_3$-$0.03AgNbO_3$ ceramics require a lower poling field for the relaxor-ferroelectric phase transition compared to their randomly oriented counterparts. This was attributed to the reduced misorientation angle between the directions of the polarization and the electric field. [422]

Table 5.7.: Summary of large signal ferroelectric properties (measured at 0.1 Hz and 3 kV/mm) of BCT15 polycrystalline samples with different degrees of crystallographic texture.

F (%)	E_C^P (kV/mm)	P_r (μC/cm^2)	S_{bip} (%)	R_{Sq} (%)	E_a (kV/mm)
83	0.56	10.0	0.146	0.92	7.52
82	0.55	11.4	0.117	0.93	5.19
50	0.61	11.7	0.104	0.90	*n.a.*
43	0.61	12.7	0.100	0.95	7.58
37	0.66	10.7	0.096	0.87	8.52
26	0.67	9.3	0.081	0.77	9.68
BT single crystal	0.05	24.2	*n.a.*	1.37	0.61

The difference in the activation and coercive fields between the polycrystalline ceramic with the highest degree of crystallographic texture (F=83%) and the single crystal is about one order of magnitude. In addition, the gap between the $\Delta P(t)$ response of the BT single crystal and the crystallographically textured BCT15 polycrystalline materials is obvious in Fig. 5.27a. Grain boundaries and grain-to-grain interactions are apparently still dramatically slowing down the switching process in polycrystalline compared to single crystalline materials. Elimination of the effect of grain boundaries parallel to the substrate, for example, results in fast and easy switching and a narrow distribution of switching times for columnar-structured thin films. [417]

6 Conclusion and outlook

In the present work, an improved understanding of the sequence of the mechanisms during the polarization reversal of polyrystalline ferroelectric/ferroelastic ceramic materials could be obtained by a simultaneous measurement of the macroscopic polarization and strain dynamics, combined with the detection of microscopic structural changes and Landau free energy calculations. In particular, it could be revealed that switching consists of a sequence of individual events, separated into three regimes: rapid movement of non-180° domain walls, main switching phase with 180° and non-180° switching events, and creep-like non-180° domain wall movement.

These findings help to improve theoretical models. An example is the recently developed multi-step stochastic mechanism (MSM) model, which describes the field-driven polarization reversal in polycrystalline ferroelectric ceramics and was developed based on the results of this work. In the spirit of the classical KAI approach, it includes two parallel channels of switching: 180°-polarization reversal and sequential two-step 90°-switching events. With the mathematical framework of this models being derived elsewhere [423], the time-dependent variation of switched polarization and strain of a tetragonal PZT sample can be calculated, as displayed in Fig. 6.1. Here, experimental curves are highlighted by red symbols, while calculated contributions from 180° and 90° events are shown by dotted lines. The sum, displayed as the black solid line, describes the experimental observations rather well. An important finding of the model is that the polarization contribution of the 90° events accounts to 34%. [423] In addition, activation barriers for 180° and non-180° events can be determined, which are an important experimental input parameter for micromechanical models.

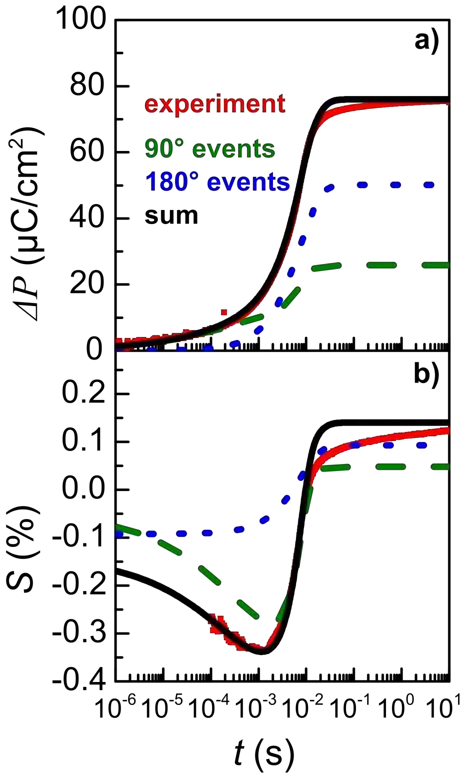

Figure 6.1.: Application of the results obtained in this study to the MSM model for the dynamic polarization reversal in polycrystalline ceramic materials. a) Switched polarization and strain variation as a function of time for a tetragonal PZT sample at a constant applied electric field. Fits to the experimental data according to the MSM model display the contribution of 90° and 180° events [Redrawn after Ref. [423]].

While the recent development of the MSM model represents a more complete physical description of the dynamic polarization reversal responses in polycrystalline ceramic materials, it still neglects many physical characteristics of the switching process. In particular, it does not consider domain walls, their interaction with matter, as well as electric and mechanical grain correlations. As already pointed out in 2000 by Hwang and Arlt, the synergy of different models could be beneficial for a more complete description of the dynamics of the polarzation response in ferroelectric/ferroelastic ceramic materials. Despite their suggestion that future studies need "to focus on bridging the gap of the Landau-Ginzburg-Devonshire model (or a double-well potential model) and the Avrami model (or a nucleation and growth model)" [145], no such research is available today. However, this is desperately needed, because the potential energies are the basis for many finite element models. While those account for mechanical interactions between grains, they fail to describe the dynamics of the polarization and strain response. Avrami models, on the other side, can describe the dynamics of the polarization response well, however, they do not consider any grain coupling.

From an experimental point of view, many questions regarding the polarization reversal dynamic remain unanswered. In particular, macroscopic techniques and statistical diffraction experiments cannot reveal if the polarization in the main switching phase occurs by 180° events or strain-free synchronized non-180° events. In addition, the physical origin of the broad distribution of switching times in polycrystalline ceramic materials cannot be conclusively described. While the broad distribution of switching times is apparently influenced by many microstructural parameters, such as chemical composition by doping, internal stresses, grain-to-grain interaction, and the inhomogeneous distribution of the local electric field, macroscopic techniques fail to identify the dominant contribution.

An improved understanding could be obtained, if the electric field-driven dynamics of individual domain walls inside a grain of a polycrystalline ceramic material could be monitored. This might be realized by advances in high-energy synchrotron diffraction techniques in the near future. Dark-field X-ray microscopy, for example, is a novel innovative way for 3D mapping the lattice strains and orientations in crystalline materials. 3D structures, such as domain walls within individual grains of a polycrystalline ceramic body can be mapped nondestructivly and the response of domain walls to an external electric field can be monitored *in situ*. [424; 425] This is a clear advantage over current time-resolved techniques, such as *in situ* PFM or *in situ* TEM, which usually oversimplify the boundary conditions of grains, since a very thin sample or a free surface, are used. While the time resolution of this new technique is currently in the range of minutes to seconds, future advances in the brightness of synchrotron light will help to improve the feasibility of this technique further. Compared to the radiation used by Röntgen in 1895 for his seminal studies, state of the art synchrotron radiation sources provide light with brightness increased by more than 14 orders of magnitude [426], with the potential of an further increase of 10 orders of magnitude in the near future by 4th generation facilities [427]. While technologies are advancing rapidly the interaction between X-ray light and matter, which might influences the dynamic response of domain walls, is usually overlooked. However, it is well known that ferroelectric materials are suffering from radiation damage. [428–430] An issue, that was also hampering diffraction experiments in this study. While this is usually neglected, there is exigent need to define boundary conditions, such as the interplay between radiation time and electric field amplitude or the influence of different chemical elements on the interactions between ferroelectric materials and high-energy synchrotron radiation.

A Appendix

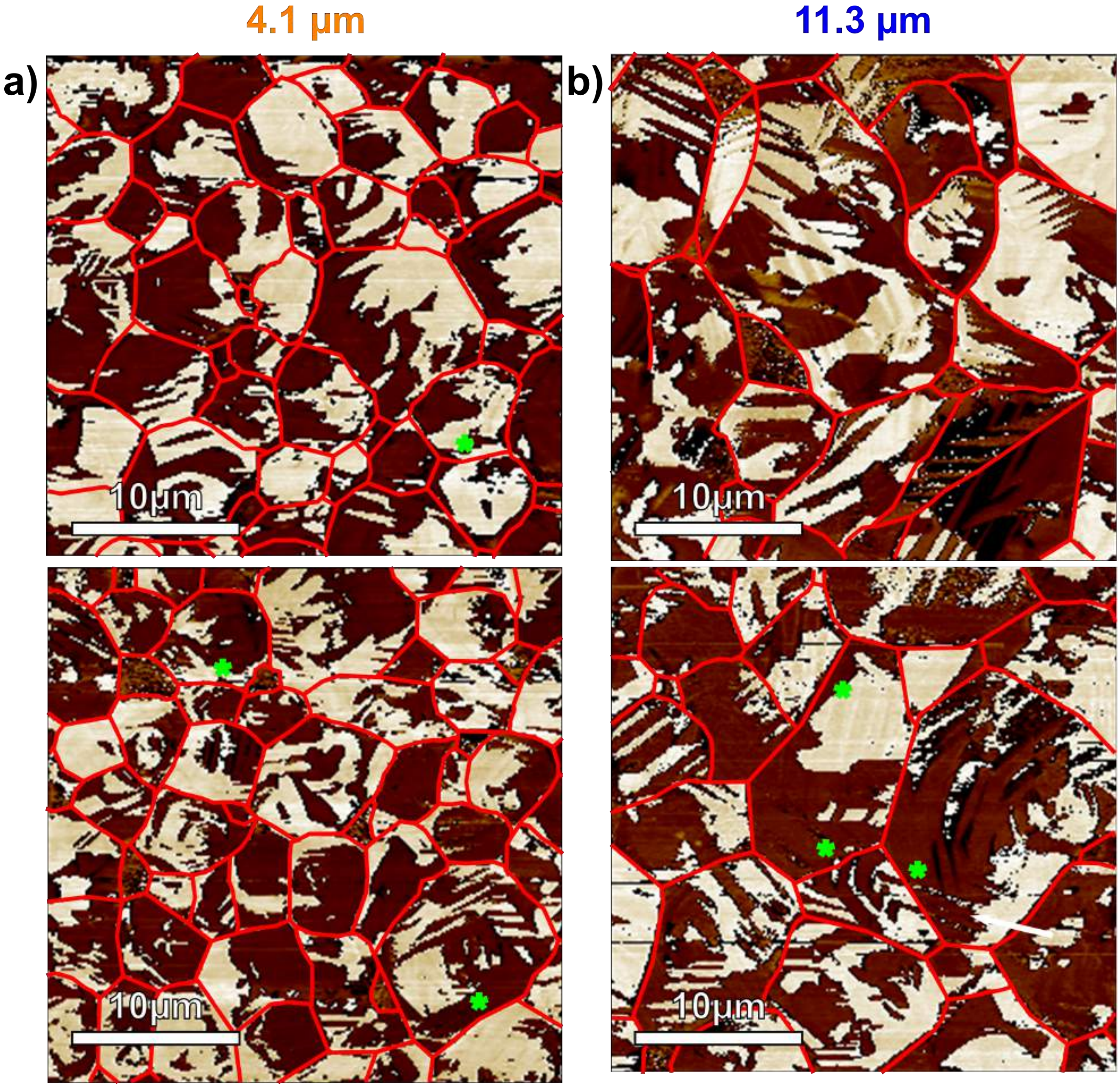

Figure A.1.: Influence of grain size on the size and morphology of domains. PFM phase images of unpoled PZT samples with different grain sizes of a) 4.1 µm and b) 11.3 µm. For each sample representative images at two different positions are displayed. The red lines indicate the position of the grain boundaries according to topography images measured simultaneously. The green asterisks highlight grain boundaries, that exhibit domain wall continuity.

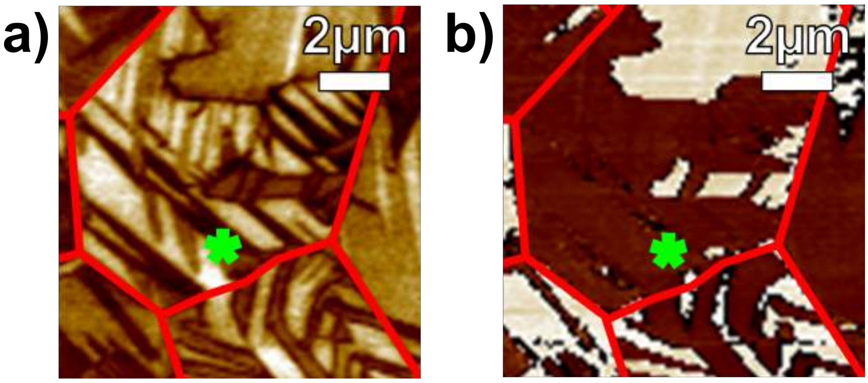

Figure A.2.: Domain wall continuity over grain boundaries. The images show the magnified blue area highlighted in Fig. 5.16. a) Amplitude and b) phase images are displayed. The red lines indicate the position of grain boundaries according to topography images. The green asterisks highlight the grain boundary, that exhibits domain wall continuity. The shape of the domain and the phase is continuous over the grain boundary, as displayed in a) and b), respectively.

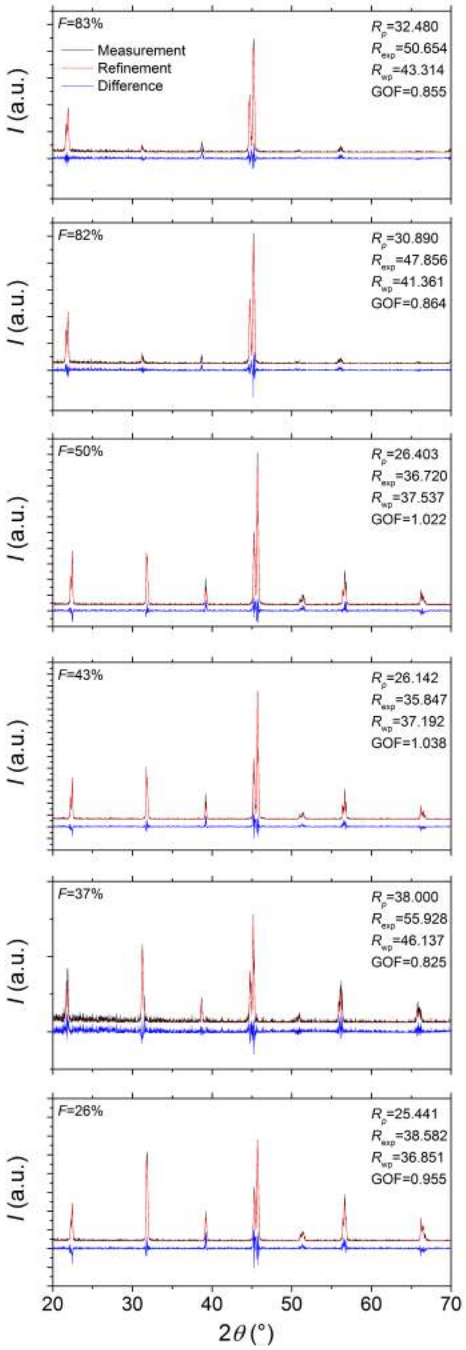

Figure A.3.: Rietveld refinement of XRD data for samples with different degrees of crystallogrpahic texture. The black line represent the measurement data and the red line the calculated intensities. The difference is highlighted by the blue line. The quality of the fit is described by numerical indicators: residual of least-squares refinement R_p, weighted profile R-factor R_{wp}, expected R-factor R_{exp}, and the goodness of fit (GOF) value. A GOF value around 1 is considered as a good fit. [431]

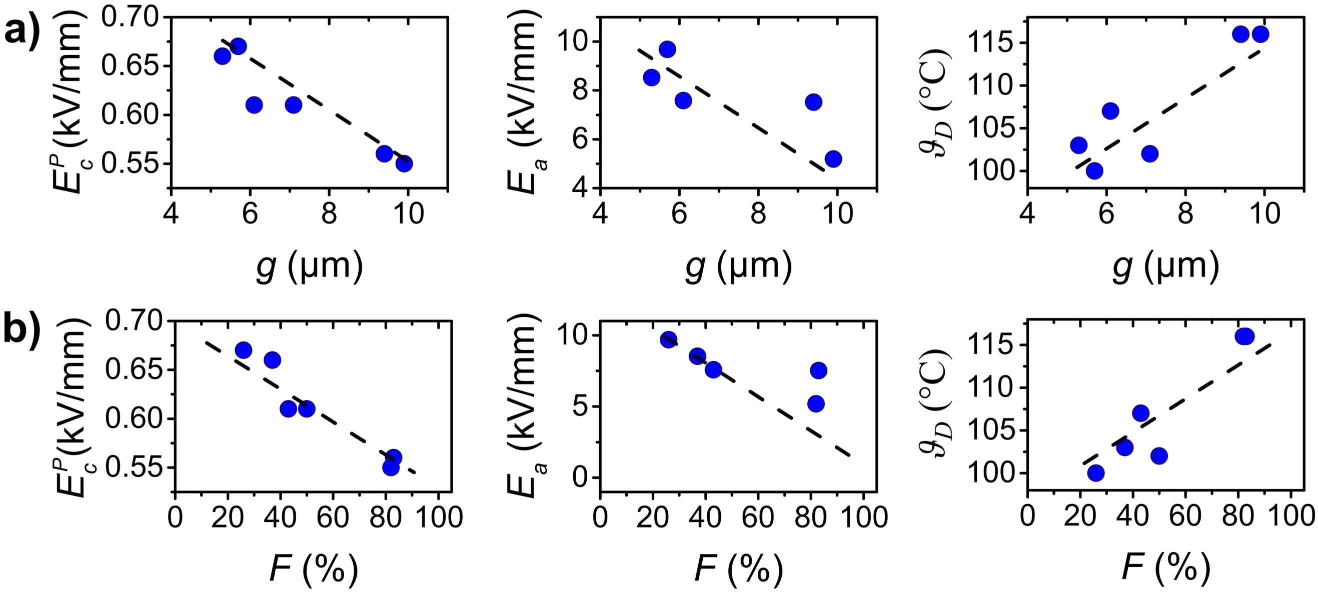

Figure A.4.: The interplay between grain size and degree of crystallographic texture. The coercive field, the activation field, and the depolarization temperature are plotted as a function of the a) grain size and b) Lotgering factor. The dashed lines represent guidelines to the eyes.

Bibliography

[1] K. Uchino, *Ferroelectric Devices Second Edition*. Boca Raton: CRC press, 2009.

[2] B.-E. Park, H. Ishiwara, M. Okuyama, S. Sakai, and S.-M. Yoon, *Ferroelectric-Gate Field Effect Transistor Memories*. Dordrecht: Springer Science+Business Media, 2016.

[3] S. Khanna, M. Jung, M. Zwerg, and S. Bartling, "Ferro-Electric RAM Based Microcontrollers: Ultra-Low Power Intelligence for the Internet of Things," in *Enabling the Internet of Things: From Integrated Circuits to Integrated Systems* (M. Alioto, ed.), pp. 503–520, Cham: Springer International Publishing, 2017.

[4] L. W. Martin and A. M. Rappe, "Thin-film ferroelectric materials and their applications," *Nature Reviews Materials*, vol. 2, no. 2, 2017.

[5] K. T. Butler, J. M. Frost, and A. Walsh, "Ferroelectric materials for solar energy conversion: photoferroics revisited," *Energy & Environmental Science*, vol. 8, no. 3, pp. 838–848, 2015.

[6] S. Priya, H.-C. Song, Y. Zhou, R. Varghese, A. Chopra, S.-G. Kim, I. Kanno, L. Wu, D. S. Ha, and J. Ryu, "A Review on Piezoelectric Energy Harvesting: Materials, Methods, and Circuits," *Energy Harvesting and Systems*, vol. 4, no. 1, pp. 3–39, 2017.

[7] X. Moya, S. Kar-Narayan, and N. D. Mathur, "Caloric materials near ferroic phase transitions," *Nature Materials*, vol. 13, no. 5, pp. 439–450, 2014.

[8] Y. Q. Cao, W. Li, J. Figueroa, T. Wang, D. Torres, C. Wang, Z. L. Wang, and N. Sepulveda, "Impact-activated programming of electro-mechanical resonators through ferroelectret nanogenerator (FENG) and vanadium dioxide," *Nano Energy*, vol. 43, pp. 278–284, 2018.

[9] I. Grinberg, D. V. West, M. Torres, G. Y. Gou, D. M. Stein, L. Y. Wu, G. N. Chen, E. M. Gallo, A. R. Akbashev, P. K. Davies, J. E. Spanier, and A. M. Rappe, "Perovskite oxides for visible-light-absorbing ferroelectric and photovoltaic materials," *Nature*, vol. 503, no. 7477, pp. 509–+, 2013.

[10] M. Gagliardi, "Materials with market value: Global ceramic and glass industry poised to reach $1 trilion," *American Ceramic Society Bulletin*, vol. 96, no. 3, pp. 27–37, 2017.

[11] S. Trolier-McKinstry and C. A. Randall, "Movers, shakers, and storers of charge: The legacy of ferroelectricians L. Eric Cross and Robert E. Newnham," *Journal of the American Ceramic Society*, vol. 100, no. 8, pp. 3346–3359, 2017.

[12] A. K. Bain and P. Chand, *Ferroelectrics: Principles and Applications*. Weinheim: Wiley Online Library, 2017.

[13] W. J. Merz, "Domain Formation and Domain Wall Motions in Ferroelectric $BaTiO_3$ Single Crystals," *Physical Review*, vol. 95, no. 3, pp. 690–698, 1954.

[14] E. A. Little, "Dynamic Behavior of Domain Walls in Barium Titanate," *Physical Review*, vol. 98, no. 4, pp. 1201–1202, 1955.

[15] V. Y. Shur and E. L. Rumyantsev, "Kinetics of Ferroelectric Domain Structure during Switching: Theory and Experiment," *Ferroelectrics*, vol. 151, no. 1, pp. 171–180, 1994.

[16] Y. Ishibashi and Y. Takagi, "Note on Ferroelectric Domain Switching," *Journal of the Physical Society of Japan*, vol. 31, no. 2, pp. 506–510, 1971.

[17] S. C. Hwang, C. S. Lynch, and R. M. McMeeking, "Ferroelectric/Ferroelastic Interactions and a Polarization Switching Model," *Acta Metallurgica et Materialia*, vol. 43, no. 5, pp. 2073–2084, 1995.

[18] G. Arlt, "Switching and dielectric nonlinearity of ferroelectric ceramics," *Ferroelectrics*, vol. 189, pp. 91–101, 1996.

[19] A. K. Tagantsev, I. Stolichnov, N. Setter, J. S. Cross, and M. Tsukada, "Non-Kolmogorov-Avrami switching kinetics in ferroelectric thin films," *Physical Review B*, vol. 66, no. 21, p. 213109, 2002.

[20] J. F. Scott, “Applications of Modern Ferroelectrics,” *Science*, vol. 315, no. 5814, pp. 954–959, 2007.

[21] Y. Fujisaki, “Current Status of Nonvolatile Semiconductor Memory Technology,” *Japanese Journal of Applied Physics*, vol. 49, no. 10, p. 100001, 2010.

[22] O. Lohse, M. Grossmann, U. Boettger, D. Bolten, and R. Waser, “Relaxation mechanism of ferroelectric switching in $Pb(Zr,Ti)O_3$ thin films,” *Journal of Applied Physics*, vol. 89, no. 4, pp. 2332–2336, 2001.

[23] R. J. Xu, S. Liu, I. Grinberg, J. Karthik, A. R. Damodaran, A. M. Rappe, and L. W. Martin, “Ferroelectric polarization reversal via successive ferroelastic transitions,” *Nature Materials*, vol. 14, no. 1, pp. 79–86, 2015.

[24] J. F. Scott, A. Hershkovitz, Y. Ivry, H. Lu, A. Gruverman, and J. M. Gregg, “Superdomain dynamics in ferroelectric-ferroelastic films: Switching, jamming, and relaxation,” *Applied Physics Reviews*, vol. 4, no. 4, 2017.

[25] R. Waser, U. Böttger, and S. Tiedke, *Polar Oxides: Properties, Characterization, and Imaging*. Weinheim: John Wiley & Sons, 2006.

[26] A. J. Moulson and J. M. Herbert, *Electroceramics: Materials, Properties, Applications*. West Sussex: John Wiley & Sons, 2003.

[27] N. Setter and E. Colla, *Ferroelectric Ceramics: Tutorial Reviews, Theory, Processing, and Applications*. Basel: Birkhauser, 1993.

[28] F. E. Neumann and O. E. Meyer, *Vorlesungen über die Theorie der Elasticität der festen Körper und des Lichtäthers: gehalten an der Universität Königsberg*, vol. 4. BG Teubner, 1885.

[29] R. Newnham, *Properties of materials: anisotropy, symmetry, structure*. Oxford: Oxford University Press Oxford, 2005.

[30] M. E. Lines and A. M. Glass, *Principles and Applications of Ferroelectrics and Related Materials*. Oxford: Oxford University Press, 1977.

[31] G. H. Haertling, “Ferroelectric ceramics: History and Technology,” *Journal of the American Ceramic Society*, vol. 82, no. 4, pp. 797–818, 1999.

[32] D. Damjanovic, “Ferroelectric, dielectric and piezoelectric properties of ferroelectric thin films and ceramics,” *Reports on Progress in Physics*, vol. 61, no. 9, pp. 1267–1324, 1998.

[33] C. Steinmetz, “Dielektrische Hysteresis, der Energieverlust in dielektrischen Medien unter dem Einfluß eines wechselnden elektrischen Feldes,” *Elektrotechnische Zeitschrift*, vol. 13, pp. 227–228, 1892.

[34] A. Kleiner, “Ueber die durch dielectrische Polarisation erzeugte Wärme,” *Annalen der Physik*, vol. 286, no. 9, pp. 138–146, 1893.

[35] J. Valasek, “Piezo-Electric and Allied Phenomena in Rochelle Salt,” *Physical Review*, vol. 17, no. 4, p. 475, 1921.

[36] A. Von Hippel, R. Breckenridge, F. Chesley, and L. Tisza, “High dielectric constant ceramics,” *Industrial & Engineering Chemistry*, vol. 38, no. 11, pp. 1097–1109, 1946.

[37] H. Jaffe, “Piezoelectric Ceramics,” *Journal of the American Ceramic Society*, vol. 41, no. 11, pp. 494–498, 1958.

[38] K. Aizu, “Possible Species of "Ferroelastic Crystals" and of Simultaneously Ferroelectric and Ferroelastic Crystals,” *Journal of the Physical Society of Japan*, vol. 27, no. 2, pp. 387–396, 1969.

[39] A. F. Devonshire, “XCVI. Theory of Barium Titanate: Part I,” *The London, Edinburgh, and Dublin Philosophical Magazine and Journal of Science*, vol. 40, no. 309, pp. 1040–1063, 1949.

[40] M. J. Haun, E. Furman, S. J. Jang, and L. E. Cross, “Thermodynamic theory of the lead zirconate-titanate solid-solution system, part I: Phenomenology,” *Ferroelectrics*, vol. 99, pp. 13–25, 1989.

[41] L.-Q. Chen, “Physics of ferroelectrics: a modern perspective,” Heidelberg: Springer Science & Business Media, 2007.

[42] G. Arlt, “Twinning in Ferroelectric and Ferroelastic Ceramics - Stress Relief,” *Journal of Materials Science*, vol. 25, no. 6, pp. 2655–2666, 1990.

[43] J. F. Ihlefeld, D. T. Harris, R. Keech, J. L. Jones, J. P. Maria, and S. Trolier-McKinstry, “Scaling Effects in Perovskite Ferroelectrics: Fundamental Limits and Process-Structure-Property Relations,” *Journal of the American Ceramic Society*, vol. 99, no. 8, pp. 2537–2557, 2016.

[44] W. R. Buessem, L. E. Cross, and A. K. Goswami, “Phenomenological Theory of High Permittivity in Fine-Grained Barium Titanate,” *Journal of the American Ceramic Society*, vol. 49, no. 1, pp. 33–36, 1966.

[45] R. C. Pohanka, R. W. Rice, and B. E. Walker, “Effect of Internal Stress on Strength of $BaTiO_3$,” *Journal of the American Ceramic Society*, vol. 59, no. 1-2, pp. 71–74, 1976.

[46] T. R. Armstrong and R. C. Buchanan, “Influence of Core Shell Grains on the Internal-Stress State and Permittivity Response of Zirconia-Modified Barium-Titanate,” *Journal of the American Ceramic Society*, vol. 73, no. 5, pp. 1268–1273, 1990.

[47] A. K. Tagantsev, L. E. Cross, and J. Fousek, *Domains in Ferroic Crystals and Thin Films*. New York, Dordrecht, Heidelberg, London: Springer, 2010.

[48] W. T. Lee, E. K. H. Salje, L. Goncalves-Ferreira, M. Daraktchiev, and U. Bismayer, “Intrinsic activation energy for twin-wall motion in the ferroelastic perovskite $CaTiO_3$,” *Physical Review B*, vol. 73, no. 21, p. 214110, 2006.

[49] M. Tanaka and G. Honjo, “Electron Optical Studies of Barium Titanate Single Crystal Films,” *Journal of the Physical Society of Japan*, vol. 19, no. 6, pp. 954–970, 1964.

[50] H. Kawata, S. Suzuki, and M. Takagi, “X-Ray Topographic Study on Lattice Strain at 180° Domain-Wall in Ferroelectric $BaTiO_3$,” *Journal of the Physical Society of Japan*, vol. 50, no. 10, pp. 3398–3406, 1981.

[51] X. Zhang, T. Hashimoto, and D. C. Joy, “Electron Holographic Study of Ferroelectric Domain-Walls,” *Applied Physics Letters*, vol. 60, no. 6, pp. 784–786, 1992.

[52] X. Zhang, D. C. Joy, Y. Zhang, T. Hashimoto, L. Allard, and T. A. Nolan, “Electron Holography Techniques for Study of Ferroelectric Domain-Walls,” *Ultramicroscopy*, vol. 51, no. 1-4, pp. 21–30, 1993.

[53] R. C. Rogan, N. Tamura, G. A. Swift, and E. Ustundag, “Direct measurement of triaxial strain fields around ferroelectric domains using X-ray microdiffraction,” *Nature Materials*, vol. 2, no. 6, pp. 379–381, 2003.

[54] T. Hoshina, K. Takizawa, J. Y. Li, T. Kasama, H. Kakemoto, and T. Tsurumi, “Domain Size Effect on Dielectric Properties of Barium Titanate Ceramics,” *Japanese Journal of Applied Physics*, vol. 47, no. 9, pp. 7607–7611, 2008.

[55] Y.-K. Choi, T. Hoshina, H. Takeda, T. Teranishi, and T. Tsurumi, “Effects of oxygen vacancies and grain sizes on the dielectric response of $BaTiO_3$,” *Applied Physics Letters*, vol. 97, no. 21, p. 212907, 2010.

[56] W. N. Lawless, “180° Domain-Wall Energies in $BaTiO_3$,” *Physical Review*, vol. 175, no. 2, pp. 619–624, 1968.

[57] W. Kinase and H. Takahasi, “On the 180°-Type Domain Wall of $BaTiO_3$ Crystal,” *Journal of the Physical Society of Japan*, vol. 12, no. 5, pp. 464–476, 1957.

[58] J. Padilla, W. Zhong, and D. Vanderbilt, “First-principles investigation of 180° domain walls in $BaTiO_3$,” *Physical Review B*, vol. 53, no. 10, pp. R5969–R5973, 1996.

[59] W. Kinase, H. Okayama, A. Yoshikawa, and N. Taguchi, “On the 90°-Type Domain Wall of $BaTiO_3$ Crystal,” *Journal of the Physical Society of Japan*, vol. 28, pp. S383–S385, 1970.

[60] S. Pöykko and D. J. Chadi, “Ab initio study of 180° domain wall energy and structure in $PbTiO_3$,” *Applied Physics Letters*, vol. 75, no. 18, pp. 2830–2832, 1999.

[61] B. Meyer and D. Vanderbilt, “Ab initio study of ferroelectric domain walls in $PbTiO_3$,” *Physical Review B*, vol. 65, no. 10, p. 104111, 2002.

[62] E. V. Burtsev and S. P. Chervonobrodov, “Some Problems of 180°-Switching in Ferroelectrics,” *Ferroelectrics*, vol. 45, no. 1-2, pp. 97–106, 1982.

[63] R. C. Miller and A. Savage, “Velocity of Sidewise 180° Domain-Wall Motion in $BaTiO_3$ as a Function of the Applied Electric Field,” *Physical Review*, vol. 112, no. 3, pp. 755–762, 1958.

[64] R. C. Miller and A. Savage, “Motion of 180° Domain Walls in $BaTiO_3$ under Application of a Train of Voltage Pulses,” *Journal of Applied Physics*, vol. 32, no. 4, pp. 714–721, 1961.

[65] V. Y. Shur, A. L. Gruverman, V. P. Kuminov, and N. A. Tonkachyova, “Dynamics of Plane Domain-Walls in Lead Germanate and Gadolinium Molybdate,” *Ferroelectrics*, vol. 111, pp. 197–206, 1990.

[66] R. C. Miller and A. Savage, “Further Experiments on the Sidewise Motion of 180° Domain Walls in $BaTiO_3$,” *Physical Review*, vol. 115, no. 5, pp. 1176–1180, 1959.

[67] G. W. Taylor, “High Field Polarization Reversals in Liquid Electroded Barium Titanate Crystals,” *Australian Journal of Physics*, vol. 15, no. 4, pp. 549–567, 1962.

[68] H. L. Stadler and P. Zachmand, “Temperature Dependence of 180° Domain Wall Velocity in $BaTiO_3$,” *Journal of Applied Physics*, vol. 35, no. 10, pp. 2895–2899, 1964.

[69] H. L. Stadler and P. J. Zachmanidis, “Nucleation and Growth of Ferroelectric Domains in $BaTiO_3$ at Fields from 2 to 450 kV/cm,” *Journal of Applied Physics*, vol. 34, no. 11, pp. 3255–3260, 1963.

[70] H. L. Stadler, “Forward Velocity of 180° Ferroelectric Domain Walls in $BaTiO_3$,” *Journal of Applied Physics*, vol. 37, no. 5, pp. 1947–1948, 1966.

[71] A. Savage and R. C. Miller, “Temperature Dependence of the Velocity of Sidewise 180° Domain-Wall Motion in $BaTiO_3$,” *Journal of Applied Physics*, vol. 31, no. 9, pp. 1546–1549, 1960.

[72] H. Bittel, *Untersuchungen über ferroelektrische Domänenwände und Nachwirkungserscheinungen*. Wiesbaden: Springer-Verlag, 1955.

[73] E. K. H. Salje, “On the dynamics of ferroelastic domain boundaries under thermal and elastic forcing,” *Phase Transitions*, vol. 83, no. 9, pp. 657–669, 2010.

[74] E. K. H. Salje, “Ferroelastic Materials,” *Annual Review of Materials Research*, vol. 42, pp. 265–283, 2012.

[75] T. Mitsui and J. Furuichi, “Domain Structure of Rochelle Salt and KH_2PO_4,” *Physical Review*, vol. 90, no. 2, pp. 193–202, 1953.

[76] J. Bornarel, “Needle-Shaped Domains in KH_2PO_4 - Correlation between Length and Width,” *Ferroelectrics*, vol. 106, pp. 21–26, 1990.

[77] R. C. Miller and G. Weinreich, “Mechanism for the Sidewise Motion of 180° Domain Walls in Barium Titanate,” *Physical Review*, vol. 117, no. 6, pp. 1460–1466, 1960.

[78] M. E. Drougard, “Detailed Study of Switching Current in Barium Titanate,” *Journal of Applied Physics*, vol. 31, no. 2, pp. 352–355, 1960.

[79] R. Abe, “Theoretical Treatment of the Movement of 180° Domain in $BaTiO_3$ Single Crystal,” *Journal of the Physical Society of Japan*, vol. 14, no. 5, pp. 633–642, 1959.

[80] M. Hayashi, “Kinetics of Domain Wall Motion in Ferroelectric Switching. I. General Formulation,” *Journal of the Physical Society of Japan*, vol. 33, no. 3, pp. 616–628, 1972.

[81] T. Tybell, P. Paruch, T. Giamarchi, and J. M. Triscone, “Domain Wall Creep in Epitaxial Ferroelectric $Pb(Zr_{0.2}Ti_{0.8})O_3$ Thin Films,” *Physical Review Letters*, vol. 89, no. 9, p. 097601, 2002.

[82] Y. H. Shin, I. Grinberg, I. W. Chen, and A. M. Rappe, “Nucleation and growth mechanism of ferroelectric domain-wall motion,” *Nature*, vol. 449, no. 7164, pp. 881–884, 2007.

[83] C. L. Jia, S. B. Mi, K. Urban, I. Vrejoiu, M. Alexe, and D. Hesse, “Atomic-scale study of electric dipoles near charged and uncharged domain walls in ferroelectric films,” *Nature Materials*, vol. 7, no. 1, pp. 57–61, 2008.

[84] Y. X. Jiang, Y. J. Wang, D. Chen, Y. L. Zhu, and X. L. Ma, “First-principles study of charged steps on 180° domain walls in ferroelectric $PbTiO_3$,” *Journal of Applied Physics*, vol. 122, no. 5, p. 054101, 2017.

[85] R. J. Harrison and E. K. H. Salje, “The noise of the needle: Avalanches of a single progressing needle domain in $LaAlO_3$,” *Applied Physics Letters*, vol. 97, no. 2, p. 021907, 2010.

[86] S. Puchberger, V. Soprunyuk, W. Schranz, A. Tröster, K. Roleder, A. Majchrowski, M. A. Carpenter, and E. K. H. Salje, "The noise of many needles: Jerky domain wall propagation in $PbZrO_3$ and $LaAlO_3$," *APL Materials*, vol. 5, no. 4, p. 046102, 2017.

[87] E. K. H. Salje, X. Ding, Z. Zhao, T. Lookman, and A. Saxena, "Thermally activated avalanches: Jamming and the progression of needle domains," *Physical Review B*, vol. 83, no. 10, p. 104109, 2011.

[88] E. K. H. Salje, X. F. Wang, X. D. Ding, and J. F. Scott, "Ultrafast Switching in Avalanche-Driven Ferroelectrics by Supersonic Kink Movements," *Advanced Functional Materials*, vol. 27, no. 21, p. 1700367, 2017.

[89] P. Chauve, T. Giamarchi, and P. Le Doussal, "Creep and depinning in disordered media," *Physical Review B*, vol. 62, no. 10, pp. 6241–6267, 2000.

[90] A. Pramanick, A. D. Prewitt, J. S. Forrester, and J. L. Jones, "Domains, Domain Walls and Defects in Perovskite Ferroelectric Oxides: A Review of Present Understanding and Recent Contributions," *Critical Reviews in Solid State and Materials Sciences*, vol. 37, no. 4, pp. 243–275, 2012.

[91] E. Fatuzzo and W. J. Merz, "Switching Mechanism in Triglycine Sulfate and Other Ferroelectrics," *Physical Review*, vol. 116, no. 1, pp. 61–68, 1959.

[92] J. Y. Jo, S. M. Yang, T. H. Kim, H. N. Lee, J. G. Yoon, S. Park, Y. Jo, M. H. Jung, and T. W. Noh, "Nonlinear Dynamics of Domain-Wall Propagation in Epitaxial Ferroelectric Thin Films," *Physical Review Letters*, vol. 102, no. 4, p. 045701, 2009.

[93] P. Paruch, T. Giamarchi, T. Tybell, and J. M. Triscone, "Nanoscale studies of domain wall motion in epitaxial ferroelectric thin films," *Journal of Applied Physics*, vol. 100, no. 5, p. 051608, 2006.

[94] S. M. Yang, J. Y. Jo, D. J. Kim, H. Sung, T. W. Noh, H. N. Lee, J. G. Yoon, and T. K. Song, "Domain wall motion in epitaxial $Pb(Zr,Ti)O_3$ capacitors investigated by modified piezoresponse force microscopy," *Applied Physics Letters*, vol. 92, no. 25, p. 252901, 2008.

[95] P. Paruch, T. Giamarchi, and J. M. Triscone, "Domain Wall Roughness in Epitaxial Ferroelectric $PbZr_{0.2}Ti_{0.8}O_3$ Thin Films," *Physical Review Letters*, vol. 94, no. 19, p. 197601, 2005.

[96] N. A. Pertsev, A. Petraru, H. Kohlstedt, R. Waser, I. K. Bdikin, D. Kiselev, and A. L. Kholkin, "Dynamics of ferroelectric nanodomains in $BaTiO_3$ epitaxial thin films via piezoresponse force microscopy," *Nanotechnology*, vol. 19, no. 37, p. 375703, 2008.

[97] S. Liu, I. Grinberg, and A. M. Rappe, "Intrinsic ferroelectric switching from first principles," *Nature*, vol. 534, no. 7607, pp. 360–363, 2016.

[98] R. Landauer, "Electrostatic Considerations in $BatiO_3$ Domain Formation during Polarization Reversal," *Journal of Applied Physics*, vol. 28, no. 2, pp. 227–234, 1957.

[99] S. Ducharme, V. M. Fridkin, A. V. Bune, S. P. Palto, L. M. Blinov, N. N. Petukhova, and S. G. Yudin, "Intrinsic Ferroelectric Coercive Field," *Physical Review Letters*, vol. 84, no. 1, pp. 175–178, 2000.

[100] S. Zhukov, Y. A. Genenko, and H. von Seggern, "Experimental and theoretical investigation on polarization reversal in unfatigued lead-zirconate-titanate ceramic," *Journal of Applied Physics*, vol. 108, no. 1, p. 014106, 2010.

[101] E. Fatuzzo and W. J. Merz, *Ferroelectricity*. Amsterdam: North-Holland Publishing Company, 1967.

[102] W. J. Merz, "Switching Time in Ferroelectric $BaTiO_3$ and Its Dependence on Crystal Thickness," *Journal of Applied Physics*, vol. 27, no. 8, pp. 938–943, 1956.

[103] R. C. Miller, "Some Experiments on the Motion of 180° Domain Walls in $BaTiO_3$," *Physical Review*, vol. 111, no. 3, pp. 736–739, 1958.

[104] A. Kumada, "Domain Switching in $Gd_2(Mo0_4)_3$," *Physics Letters A*, vol. A 30, no. 3, pp. 186–187, 1969.

[105] M. Ayoub, H. Futterlieb, J. Imbrock, and C. Denz, "3D Imaging of Ferroelectric Kinetics during Electrically Driven Switching," *Advanced Materials*, vol. 29, no. 5, p. 1603325, 2017.

[106] V. Y. Shur, “Fast polarization reversal process: evolution of ferroelectric domain structure in thin films,” in *Ferroelectric Thin Films: Synthesis and Basic Properties*, Abingdon: Gordon and Breach, 1996.

[107] W. Pan, Q. Zhang, A. S. Bhalla, and L. E. Cross, “Field-Induced Strain in Single-Crystal $BaTiO_3$,” *Journal of the American Ceramic Society*, vol. 71, no. 6, pp. C302–C305, 1988.

[108] B. Jiang, Y. Bai, W. Y. Chu, Y. J. Su, and L. J. Qiao, “Direct observation of two 90° steps of 180° domain switching in $BaTiO_3$ single crystal under an antiparallel electric field,” *Applied Physics Letters*, vol. 93, no. 15, p. 152905, 2008.

[109] J. Yin and W. Cao, “Polarization reversal study using ultrasound,” *Applied Physics Letters*, vol. 79, no. 27, pp. 4556–4558, 2001.

[110] W. W. Cao, “Switching mechanism in single crystal $0.955Pb(Zn_{1/3}Nb_{1/3})O_3$-$0.045PbTiO_3$,” *Ferroelectrics*, vol. 290, pp. 107–114, 2003.

[111] W. Zhu and L. E. Cross, “Direct evidence of ferroelastic participation in 180° polarization switching and fatigue for 111 oriented rhombohedral ferroelectric $0.955Pb(Zn_{1/3}Nb_{2/3})O_3$:$0.045PbTiO_3$ single crystals,” *Applied Physics Letters*, vol. 84, no. 13, pp. 2388–2390, 2004.

[112] Z. H. Zhang, X. Y. Qi, and X. F. Duan, “Two-step evolution mechanism of multi-domains in $BaTiO_3$ single crystal investigated by in situ transmission electron microscopy,” *Scripta Materialia*, vol. 58, no. 6, pp. 441–444, 2008.

[113] J. E. Daniels, T. R. Finlayson, M. Davis, D. Damjanovic, A. J. Studer, M. Hoffman, and J. L. Jones, “Neutron diffraction study of the polarization reversal mechanism in [111] c-oriented $Pb(Zn_{1/3}Nb_{2/3})O_3$- $xPbTiO_3$,” *Journal of Applied Physics*, vol. 101, no. 10, p. 104108, 2007.

[114] Y. W. Li and F. X. Li, “The effect of domain patterns on 180° domain switching in $BaTiO_3$ crystals during antiparallel electric field loading,” *Applied Physics Letters*, vol. 104, no. 4, p. 042908, 2014.

[115] D. Berlincourt and H. H. A. Krueger, “Domain Processes in Lead Titanate Zirconate and Barium Titanate Ceramics,” *Journal of Applied Physics*, vol. 30, no. 11, pp. 1804–1810, 1959.

[116] N. Uchida and T. Ikeda, “Electrostriction in Perovskite-Type Ferroelectric Ceramics,” *Japanese Journal of Applied Physics*, vol. 6, no. 9, p. 1079, 1967.

[117] N. Uchida and T. Ikeda, “Temperature and Bias Characteristics of $Pb(Zr\text{-}Ti)O_3$ Families Ceramics,” *Japanese Journal of Applied Physics*, vol. 4, no. 11, p. 867, 1965.

[118] T. Tsurumi, Y. Kumano, N. Ohashi, T. Takenaka, and O. Fukunaga, “90° domain reorientation and electric-field-induced strain of tetragonal lead zirconate titanate ceramics,” *Japanese Journal of Applied Physics*, vol. 36, no. 9b, pp. 5970–5975, 1997.

[119] A. Achuthan and C.-T. Sun, “Effect of residual stresses on domain switching in ferroelectric ceramic materials,” in *Smart Structures and Materials*, pp. 379–389, International Society for Optics and Photonics, 2004.

[120] S. P. Li, A. S. Bhalla, R. E. Newnham, L. E. Cross, and C. Y. Huang, “90° Domain Reversal in $Pb(Zr_xTi_{1\text{-}x})O_3$ Ceramics,” *Journal of Materials Science*, vol. 29, no. 5, pp. 1290–1294, 1994.

[121] Y. Y. Jing, J. E. Blendell, and K. J. Bowman, “Three dimensional piezoresponse force microscopy polarization difference maps,” *Journal of Applied Physics*, vol. 109, no. 7, p. 074110, 2011.

[122] C. Y. Hsieh, Y. F. Chen, W. Y. Shih, Q. Zhu, and W. H. Shih, “Direct observation of two-step polarization reversal by an opposite field in a substrate-free piezoelectric thin sheet,” *Applied Physics Letters*, vol. 94, no. 13, p. 131101, 2009.

[123] T. M. Kamel and G. de With, “Double-peak switching current in soft ferroelectric lead zirconate titanate,” *Journal of Applied Physics*, vol. 102, no. 4, p. 044118, 2007.

[124] J. E. Daniels, C. Cozzan, S. Ukritnukun, G. Tutuncu, J. Andrieux, J. Glaum, C. Dosch, W. Jo, and J. L. Jones, “Two-step polarization reversal in biased ferroelectrics,” *Journal of Applied Physics*, vol. 115, no. 22, p. 224104, 2014.

[125] C. M. Fancher, S. Brewer, C. C. Chung, S. Röhrig, T. Rojac, G. Esteves, M. Deluca, N. Bassiri-Gharb, and J. L. Jones, "The contribution of 180° domain wall motion to dielectric properties quantified from in situ X-ray diffraction," *Acta Materialia*, vol. 126, pp. 36–43, 2017.

[126] S. Gorfman, H. Simons, T. Iamsasri, S. Prasertpalichat, D. P. Cann, H. Choe, U. Pietsch, Y. Watier, and J. L. Jones, "Simultaneous resonant x-ray diffraction measurement of polarization inversion and lattice strain in polycrystalline ferroelectrics," *Scientific Reports*, vol. 6, p. 20829, 2016.

[127] A. Roelofs, U. Böttger, R. Waser, F. Schlaphof, S. Trogisch, and L. M. Eng, "Differentiating 180° and 90° switching of ferroelectric domains with three-dimensional piezoresponse force microscopy," *Applied Physics Letters*, vol. 77, no. 21, pp. 3444–3446, 2000.

[128] G. Arlt, "A model for switching and hysteresis in ferroelectric ceramics," *Integrated Ferroelectrics*, vol. 16, no. 1-4, pp. 229–236, 1997.

[129] E. T. Keve and K. L. Bye, "Phase Identification and Domain-Structure in PLZT Ceramics," *Journal of Applied Physics*, vol. 46, no. 2, pp. 810–818, 1975.

[130] A. Yamada, Y.-K. Chung, M. Takahashi, and T. Ogawa, "Poling Field Dependence of Ferroelectric Domains in Tetragonal Lead Zirconate Titanate Ceramics," *Japanese Journal of Applied Physics*, vol. 35, no. 9S, p. 5232, 1996.

[131] T. Ogawa and K. Nakamura, "Poling field dependence of ferroelectric properties and crystal orientation in rhombohedral lead zirconate titanate ceramics," *Japanese Journal of Applied Physics*, vol. 37, no. 9S, p. 5241, 1998.

[132] G. Krüger, "Domain-Wall Motion Concept to Describe Ferroelectric Rhombohedral PLZT Ceramics," *Ferroelectrics*, vol. 11, no. 3-4, pp. 417–422, 1976.

[133] N. A. Schmidt, "Coercive Force and 90° Domain-Wall Motion in Ferroelectric PLZT Ceramics with Square Hysteresis Loops," *Ferroelectrics*, vol. 31, no. 3-4, pp. 105–111, 1981.

[134] P. Gerthsen and G. Krüger, "Coercive Field in Fine-Grained PLZT Ceramics," *Ferroelectrics*, vol. 11, no. 3-4, pp. 489–492, 1976.

[135] J. E. Zhou, T. L. Cheng, and Y. U. Wang, "Correlated nucleation and self-accommodating kinetic pathway of ferroelectric phase transformation," *Journal of Applied Physics*, vol. 111, no. 2, p. 024105, 2012.

[136] A. M. Bratkovsky and A. P. Levanyuk, "Easy collective polarization switching in ferroelectrics," *Physical Review Letters*, vol. 85, no. 21, pp. 4614–4617, 2000.

[137] A. Leschhorn, S. Djoumbou, and H. Kliem, "Microscopic model of domain wall motion," *Journal of Applied Physics*, vol. 115, no. 11, p. 114106, 2014.

[138] K. B. Chong, F. Guiu, and M. J. Reece, "Thermal activation of ferroelectric switching," *Journal of Applied Physics*, vol. 103, no. 1, p. 014101, 2008.

[139] A. Leschhorn and H. Kliem, "Influence of thermal vibrations on polarization switching in the model of local fields," *Journal of Applied Physics*, vol. 121, no. 1, p. 014103, 2017.

[140] R. Khachaturyan, J. Wehner, and Y. A. Genenko, "Correlated polarization-switching kinetics in bulk polycrystalline ferroelectrics: A self-consistent mesoscopic switching model," *Physical Review B*, vol. 96, no. 5, p. 054113, 2017.

[141] Y. A. Genenko, J. Wehner, and H. von Seggern, "Self-consistent model of polarization switching kinetics in disordered ferroelectrics," *Journal of Applied Physics*, vol. 114, no. 8, p. 084101, 2013.

[142] Y. A. Genenko, J. Glaum, O. Hirsch, H. Kungl, M. J. Hoffmann, and T. Granzow, "Aging of poled ferroelectric ceramics due to relaxation of random depolarization fields by space-charge accumulation near grain boundaries," *Physical Review B*, vol. 80, no. 22, p. 224109, 2009.

[143] G. Arlt and J. H. Calderwood, "Coercive and switching fields in ferroelectric ceramics," *Applied Physics Letters*, vol. 81, no. 14, pp. 2605–2607, 2002.

[144] G. Arlt, "A Physical Model for Hysteresis Curves of Ferroelectric Ceramics," *Ferroelectrics*, vol. 189, pp. 103–119, 1996.

[145] S. C. Hwang and G. Arlt, “Switching in ferroelectric polycrystals,” *Journal of Applied Physics*, vol. 87, no. 2, pp. 869–875, 2000.

[146] S. C. Hwang and R. Waser, “Study of electrical and mechanical contribution to switching in ferroelectric/ferroelastic polycrystals,” *Acta Materialia*, vol. 48, no. 12, pp. 3271–3282, 2000.

[147] M. Kamlah, A. C. Liskowsky, R. M. McMeeking, and H. Balke, “Finite element simulation of a polycrystalline ferroelectric based on a multidomain single crystal switching model,” *International Journal of Solids and Structures*, vol. 42, no. 9-10, pp. 2949–2964, 2005.

[148] A. Haug, J. E. Huber, P. R. Onck, and E. Van der Giessen, “Multi-grain analysis versus self-consistent estimates of ferroelectric polycrystals,” *Journal of the Mechanics and Physics of Solids*, vol. 55, no. 3, pp. 648–665, 2007.

[149] R. C. Devries and J. E. Burke, “Microstructure of Barium Titanate Ceramics,” *Journal of the American Ceramic Society*, vol. 40, no. 6, pp. 200–206, 1957.

[150] H. Takahashi, Y. Numamoto, J. Tani, and S. Tsurekawa, “Domain properties of high-performance barium titanate ceramics,” *Japanese Journal of Applied Physics*, vol. 46, no. 10b, pp. 7044–7047, 2007.

[151] S. Tsurekawa, K. Ibaraki, K. Kawahara, and T. Watanabe, “The continuity of ferroelectric domains at grain boundaries in lead zirconate titanate,” *Scripta Materialia*, vol. 56, no. 7, pp. 577–580, 2007.

[152] J. W. Jang, H. J. Youn, C. Byun, I. T. Kim, and K. S. Hong, “Ferroelectric domain structures of polycrystalline $PbTiO_3$ thin films prepared by MOCVD,” *Ferroelectrics*, vol. 227, no. 1-4, pp. 15–28, 1999.

[153] A. Gruverman, O. Auciello, and H. Tokumoto, “Nanoscale investigation of fatigue effects in $Pb(Zr,Ti)O_3$ films,” *Applied Physics Letters*, vol. 69, no. 21, pp. 3191–3193, 1996.

[154] S. Mantri, J. Oddershede, D. Damjanovic, and J. E. Daniels, “Ferroelectric domain continuity over grain boundaries,” *Acta Materialia*, vol. 128, pp. 400–405, 2017.

[155] G. Gottstein, *Physical Foundations of Materials Science*. Heidelberg: Springer Science & Business Media, 2013.

[156] F. Ernst, M. L. Mulvihill, O. Kienzle, and M. Rühle, “Preferred grain orientation relationships in sintered perovskite ceramics,” *Journal of the American Ceramic Society*, vol. 84, no. 8, pp. 1885–1890, 2001.

[157] S. Y. Cheng, N. J. Ho, and H. Y. Lu, “Crystallographic Relationships of the $11\bar{1}$ Growth Twins in Tetragonal Barium Titanate Determined by Electron-Backscatter Diffraction,” *Journal of the American Ceramic Society*, vol. 89, no. 11, pp. 3470–3474, 2006.

[158] Y. C. Wu, C. C. Lee, H. Y. Lu, D. E. McCauley, and M. S. H. Chu, “The $1\bar{1}1$ Growth Twins in Tetragonal Barium Titanate,” *Journal of the American Ceramic Society*, vol. 89, no. 5, pp. 1679–1686, 2006.

[159] Y. Ivry, J. F. Scott, E. K. H. Salje, and C. Durkan, “Nucleation, growth, and control of ferroelectric-ferroelastic domains in thin polycrystalline films,” *Physical Review B*, vol. 86, no. 20, p. 205428, 2012.

[160] Y. Ivry, D. P. Chu, J. F. Scott, and C. Durkan, “Domains Beyond the Grain Boundary,” *Advanced Functional Materials*, vol. 21, no. 10, pp. 1827–1832, 2011.

[161] W. W. Cao and C. A. Randall, “Grain size and domain size relations in bulk ceramic ferroelectric materials,” *Journal of Physics and Chemistry of Solids*, vol. 57, no. 10, pp. 1499–1505, 1996.

[162] R. E. Garcia, B. D. Huey, and J. E. Blendell, “Virtual piezoforce microscopy of polycrystalline ferroelectric films,” *Journal of Applied Physics*, vol. 100, no. 6, p. 064105, 2006.

[163] S. Wicks, K. Seal, S. Jesse, V. Anbusathaiah, S. Leach, R. E. Garcia, S. V. Kalinin, and V. Nagarajan, “Collective dynamics in nanostructured polycrystalline ferroelectric thin films using local time-resolved measurements and switching spectroscopy,” *Acta Materialia*, vol. 58, no. 1, pp. 67–75, 2010.

[164] A. Gruverman, A. Kholkin, A. Kingon, and H. Tokumoto, “Asymmetric nanoscale switching in ferroelectric thin films by scanning force microscopy,” *Applied Physics Letters*, vol. 78, no. 18, pp. 2751–2753, 2001.

[165] S. Wicks, V. Anbusathiah, and V. Nagarajan, “Nanoscale domain switching behaviour in polycrystalline ferroelectric thin films,” *Nanotechnology*, vol. 18, no. 46, p. 465502, 2007.

[166] N. A. Pertsev and G. Arlt, “Forced translational vibrations of 90° domain-walls and the dielectric-dispersion in ferroelectric ceramics,” *Journal of Applied Physics*, vol. 74, no. 6, pp. 4105–4112, 1993.

[167] P. Bintachitt, S. Jesse, D. Damjanovic, Y. Han, I. M. Reaney, S. Trolier-McKinstry, and S. V. Kalinin, “Collective dynamics underpins Rayleigh behavior in disordered polycrystalline ferroelectrics,” *Proceedings of the National Academy of Sciences of the United States of America*, vol. 107, no. 16, pp. 7219–7224, 2010.

[168] S. Choudhury, Y. L. Li, C. E. Krill, and L. Q. Chen, “Phase-field simulation of polarization switching and domain evolution in ferroelectric polycrystals,” *Acta Materialia*, vol. 53, no. 20, pp. 5313–5321, 2005.

[169] S. Choudhury, Y. L. Li, C. Krill, and L. Q. Chen, “Effect of grain orientation and grain size on ferroelectric domain switching and evolution: Phase field simulations,” *Acta Materialia*, vol. 55, no. 4, pp. 1415–1426, 2007.

[170] W. Zhang and K. Bhattacharya, “A computational model of ferroelectric domains. Part II: grain boundaries and defect pinning,” *Acta Materialia*, vol. 53, no. 1, pp. 199–209, 2005.

[171] J. D. Eshelby, “The Determination of the Elastic Field of an Ellipsoidal Inclusion, and Related Problems,” *Proceedings of the Royal Society of London Series A*, vol. 241, no. 1226, pp. 376–396, 1957.

[172] D. A. Hall, A. Steuwer, B. Cherdhirunkorn, T. Mori, and P. J. Withers, “A high energy synchrotron x-ray study of crystallographic texture and lattice strain in soft lead zirconate titanate ceramics,” *Journal of Applied Physics*, vol. 96, no. 8, pp. 4245–4252, 2004.

[173] D. Hull and T. W. Clyne, *An Introduction to Composite Materials*. Cambridge: Cambridge University Press, 1996.

[174] J. E. Daniels, M. Majkut, Q. G. Cao, S. Schmidt, J. Wright, W. Jo, and J. Oddershede, “Heterogeneous grain-scale response in ferroic polycrystals under electric field,” *Scientific Reports*, vol. 6, p. 22820, 2016.

[175] M. Majkut, J. E. Daniels, J. P. Wright, S. Schmidt, and J. Oddershede, “Electromechanical Response of Polycrystalline Barium Titanate Resolved at the Grain Scale,” *Journal of the American Ceramic Society*, vol. 100, no. 1, pp. 393–402, 2017.

[176] J. Oddershede, M. Majkut, Q. H. Cao, S. Schmidt, J. P. Wright, P. Kenesei, and J. E. Daniels, “Quantitative grain-scale ferroic domain volume fractions and domain switching strains from three-dimensional X-ray diffraction data,” *Journal of Applied Crystallography*, vol. 48, pp. 882–889, 2015.

[177] D. C. Lupascu, S. Fedosov, C. Verdier, J. Rödel, and H. von Seggern, “Stretched exponential relaxation in perovskite ferroelectrics after cyclic loading,” *Journal of Applied Physics*, vol. 95, no. 3, pp. 1386–1390, 2004.

[178] R. D. Redin, G. W. Marks, and C. E. Antoniak, “Symmetry limitations to polarization of polycrystalline ferroelectrics,” *Journal of Applied Physics*, vol. 34, no. 3, pp. 600–610, 1963.

[179] E. M. Anton, R. E. Garcia, T. S. Key, J. E. Blendell, and K. J. Bowman, “Domain switching mechanisms in polycrystalline ferroelectrics with asymmetric hysteretic behavior,” *Journal of Applied Physics*, vol. 105, no. 2, p. 024107, 2009.

[180] R. Khachaturyan, S. Zhukov, J. Schultheiß, C. Galassi, C. Reimuth, J. Koruza, H. von Seggern, and Y. A. Genenko, “Polarization-switching dynamics in bulk ferroelectrics with isometric and oriented anisometric pores,” *Journal of Physics D: Applied Physics*, vol. 50, no. 4, p. 045303, 2017.

[181] S. Zhukov, H. Kungl, Y. A. Genenko, and H. von Seggern, “Statistical electric field and switching time distributions in PZT 1Nb2Sr ceramics: Crystal- and microstructure effects,” *Journal of Applied Physics*, vol. 115, no. 1, p. 014103, 2014.

[182] S. Zhukov, Y. A. Genenko, J. Koruza, J. Schultheiß, H. von Seggern, W. Sakamoto, H. Ichikawa, T. Murata, K. Hayashi, and T. Yogo, “Effect of texturing on polarization switching dynamics in ferroelectric ceramics,” *Applied Physics Letters*, vol. 108, no. 1, p. 012907, 2016.

[183] X. H. Du, U. Belegundu, and K. Uchino, “Crystal Orientation Dependence of Piezoelectric Properties in Lead Zirconate Titanate: Theoretical Expectation for Thin Films,” *Japanese Journal of Applied Physics*, vol. 36, no. 9a, pp. 5580–5587, 1997.

[184] S. Stemmer, S. K. Streiffer, F. Ernst, and M. Rühle, “Atomistic structure of 90° domain-walls in ferroelectric $PbTiO_3$ thin-films,” *Philosophical Magazine A*, vol. 71, no. 3, pp. 713–724, 1995.

[185] S. I. Hamazaki, F. Shimizu, S. Kojima, and M. Takashige, “AFM Observation of 90° Domains of $BaTiO_3$ Butterfly Crystals,” *Journal of the Physical Society of Japan*, vol. 64, no. 10, pp. 3660–3663, 1995.

[186] M. Takashige, S. I. Hamazaki, N. Fukurai, F. Shimizu, and S. Kojima, “Atomic Force Microscope Observation of Ferroelectrics: Barium Titanate and Rochelle Salt,” *Japanese Journal of Applied Physic*, vol. 35, no. 9b, pp. 5181–5184, 1996.

[187] S. Balakumar, J. B. Xu, J. X. Ma, S. Ganesamoorthy, and I. H. Wilson, “Surface Morphology of ferroelectric domains in $BaTiO_3$ Single Crystals: An Atomic Force Microscope Study,” *Japanese Journal of Applied Physics*, vol. 36, no. 9a, pp. 5566–5569, 1997.

[188] Y. G. Wang, J. Dec, and W. Kleemann, “Study on surface and domain structures of $PbTiO_3$ crystals by atomic force microscopy,” *Journal of Applied Physics*, vol. 84, no. 12, pp. 6795–6799, 1998.

[189] M. Takashige, S. Hamazaki, N. Fukurai, and F. Shimizu, “Surface Morphology of Tetragonal $PbTiO_3$ and $BaTiO_3$ Observed by Atomic Force Microscopy,” *Journal of the Physical Society of Japan*, vol. 66, no. 6, pp. 1848–1849, 1997.

[190] I. MacLaren, L. A. Schmitt, H. Fuess, H. Kungl, and M. J. Hoffmann, “Experimental measurement of stress at a four-domain junction in lead zirconate titanate,” *Journal of Applied Physics*, vol. 97, no. 9, p. 094102, 2005.

[191] G. Arlt and P. Sasko, “Domain configuration and equilibrium size of domains in $BaTiO_3$ ceramics,” *Journal of Applied Physics*, vol. 51, no. 9, pp. 4956–4960, 1980.

[192] G. King and E. K. Goo, “Effect of the c/a Ratio on the Domain-Structure in $(Pb_{1-x}Ca_x)TiO_3$,” *Journal of the American Ceramic Society*, vol. 73, no. 6, pp. 1534–1539, 1990.

[193] T. Leist, T. Granzow, W. Jo, and J. Rödel, “Effect of tetragonal distortion on ferroelectric domain switching: A case study on La-doped $BiFeO_3$-$PbTiO_3$ ceramics,” *Journal of Applied Physics*, vol. 108, no. 1, p. 014103, 2010.

[194] N. A. Pertsev and G. Arlt, “Theory of the banded domain structure in coarse-grained ferroelectric ceramics,” *Ferroelectrics*, vol. 132, no. 1-4, pp. 27–40, 1992.

[195] M. U. Farooq, R. Villaurrutia, I. MacLaren, T. L. Burnett, T. P. Comyn, A. J. Bell, H. Kungl, and M. J. Hoffmann, “Electron backscatter diffraction mapping of herringbone domain structures in tetragonal piezoelectrics,” *Journal of Applied Physics*, vol. 104, no. 2, p. 024111, 2008.

[196] B. Jaffe, *Piezoelectric ceramics*. London and New York: Academic Press, 1971.

[197] Y. H. Seo, D. J. Franzbach, J. Koruza, A. Benčan, B. Malič, M. Kosec, J. L. Jones, and K. G. Webber, “Nonlinear stress-strain behavior and stress-induced phase transitions in soft $Pb(Zr_{1-x}Ti_x)O_3$ at the morphotropic phase boundary,” *Physical Review B*, vol. 87, no. 9, p. 094116, 2013.

[198] P. Gerber, U. Böttger, and R. Waser, “Composition influences on the electrical and electromechanical properties of lead zirconate titanate thin films,” *Journal of Applied Physics*, vol. 100, no. 12, p. 124105, 2006.

[199] X. F. Chen, X. L. Dong, H. L. Zhang, F. Cao, G. S. Wang, Y. Gu, H. L. He, and Y. S. Liu, “Frequency Dependence of Coercive Field in Soft $Pb(Zr_{1-x}Ti_x)O_3$ $(0.20 \leq x \leq 0.60)$ Bulk Ceramics,” *Journal of the American Ceramic Society*, vol. 94, no. 12, pp. 4165–4168, 2011.

[200] H. Kungl and M. J. Hoffmann, “Effects of sintering temperature on microstructure and high field strain of niobium-strontium doped morphotropic lead zirconate titanate,” *Journal of Applied Physics*, vol. 107, no. 5, p. 054111, 2010.

[201] G. Haertling and W. Zimmer, “An analysis of hot pressing parameters for lead zirconate lead titanate ceramics containing two atom percent bismuth,” *American Ceramic Society Bulletin*, vol. 45, no. 12, pp. 1084–1089, 1966.

[202] S. Zhukov, Y. A. Genenko, M. Acosta, H. Humburg, W. Jo, J. Rödel, and H. von Seggern, “Polarization dynamics across the morphotropic phase boundary in $Ba(Zr_{0.2}Ti_{0.8})O_3$-$x(Ba_{0.7}Ca_{0.3})TiO_3$ ferroelectrics,” *Applied Physics Letters*, vol. 103, no. 15, p. 152904, 2013.

[203] S. Zhukov, M. Acosta, Y. A. Genenko, and H. von Seggern, “Polarization dynamics variation across the temperature- and composition-driven phase transitions in the lead-free $Ba(Zr_{0.2}Ti_{0.8})O_3$-$x(Ba_{0.7}Ca_{0.3})TiO_3$ ferroelectrics,” *Journal of Applied Physics*, vol. 118, no. 13, p. 134104, 2015.

[204] N. Wongdamnern, K. Kanchiang, A. Ngamjarurojana, S. Ananta, Y. Laosiritaworn, A. Charoenphakdee, S. Gupta, S. Priya, and R. Yimnirun, “Crystal-structure dependent domain-switching behavior in $BaTiO_3$ ceramic,” *Smart Materials and Structures*, vol. 23, no. 8, p. 085022, 2014.

[205] X. F. Chen, X. L. Dong, F. Cao, J. X. Wang, and G. S. Wang, “Field and Frequency Dependence of the Dynamic Hysteresis in Lead Zirconate Titanate Solid Solutions,” *Journal of the American Ceramic Society*, vol. 97, no. 1, pp. 213–219, 2014.

[206] H. G. Baerwald, “Thermodynamic Theory of Ferroelectric Ceramics,” *Physical Review*, vol. 105, no. 2, pp. 480–486, 1957.

[207] J. Y. Li, R. C. Rogan, E. Üstündag, and K. Bhattacharya, “Domain switching in polycrystalline ferroelectric ceramics,” *Nature Materials*, vol. 4, no. 10, pp. 776–781, 2005.

[208] D. A. Hall, A. Steuwer, B. Cherdhirunkorn, T. Mori, and P. J. Withers, “Analysis of elastic strain and crystallographic texture in poled rhombohedral pzt ceramics,” *Acta Materialia*, vol. 54, no. 11, pp. 3075–3083, 2006.

[209] D. A. Hall, A. Steuwer, B. Cherdhirunkorn, P. J. Withers, and T. Mori, “Micromechanics of residual stress and texture development due to poling in polycrystalline ferroelectric ceramics,” *Journal of the Mechanics and Physics of Solids*, vol. 53, no. 2, pp. 249–260, 2005.

[210] D. A. Hall, A. Steuwer, B. Cherdhirunkorn, P. J. Withers, and T. Mori, “Texture of poled tetragonal PZT detected by synchrotron X-ray diffraction and micromechanics analysis,” *Materials Science and Engineering A*, vol. 409, no. 1-2, pp. 206–210, 2005.

[211] H. Kungl, R. Theissmann, M. Knapp, C. Baehtz, H. Fuess, S. Wagner, T. Fett, and M. J. Hoffmann, “Estimation of strain from piezoelectric effect and domain switching in morphotropic PZT by combined analysis of macroscopic strain measurements and synchrotron X-ray data,” *Acta Materialia*, vol. 55, no. 6, pp. 1849–1861, 2007.

[212] M. Hoffmann, M. Hammer, A. Endriss, and D. Lupascu, “Correlation between microstructure, strain behavior, and acoustic emission of soft PZT ceramics,” *Acta Materialia*, vol. 49, no. 7, pp. 1301–1310, 2001.

[213] M. J. Hoffmann and H. Kungl, “High strain lead-based perovskite ferroelectrics,” *Current Opinion in Solid State and Materials Science*, vol. 8, no. 1, pp. 51–57, 2004.

[214] G. Arlt, “The influence of microstructure on the properties of ferroelectric ceramics,” *Ferroelectrics*, vol. 104, pp. 217–227, 1990.

[215] C. A. Randall, N. Kim, J. P. Kucera, W. W. Cao, and T. R. Shrout, “Intrinsic and Extrinsic Size Effects in Fine-Grained Morphotropic-Phase-Boundary Lead Zirconate Titanate Ceramics,” *Journal of the American Ceramic Society*, vol. 81, no. 3, pp. 677–688, 1998.

[216] T. A. Kamel and G. de With, “Grain size effect on the poling of soft $Pb(Zr,Ti)O_3$ ferroelectric ceramics,” *Journal of the European Ceramic Society*, vol. 28, no. 4, pp. 851–861, 2008.

[217] T. Hungría, M. Algueró, A. B. Hungría, and A. Castro, “Dense, fine-grained $Ba_{1\text{-}x}Sr_xTiO_3$ Ceramics Prepared by the Combination of Mechanosynthesized Nanopowders and Spark Plasma Sintering,” *Chemistry of Materials*, vol. 17, no. 24, pp. 6205–6212, 2005.

[218] H. Amorín, R. Jiménez, J. Ricote, T. Hungría, A. Castro, and M. Algueró, “Apparent vanishing of ferroelectricity in nanostructured $BiScO_3$-$PbTiO_3$,” *Journal of Physics D: Applied Physics*, vol. 43, no. 28, p. 285401, 2010.

[219] M. Algueró, J. Ricote, R. Jiménez, P. Ramos, J. Carreaud, B. Dkhil, J. M. Kiat, J. Holc, and M. Kosec, “Size effect in morphotropic phase boundary $Pb(Mg_{1/3}Nb_{2/3})O_3$-$PbTiO_3$,” *Applied Physics Letters*, vol. 91, no. 11, p. 112905, 2007.

[220] R. Jiménez, H. Amorín, J. Ricote, J. Carreaud, J. M. Kiat, B. Dkhil, J. Holc, M. Kosec, and M. Algueró, “Effect of grain size on the transition between ferroelectric and relaxor states in $0.8Pb(Mg_{1/3}Nb_{2/3})O_3$-$0.2PbTiO_3$ ceramics,” *Physical Review B*, vol. 78, no. 9, p. 094103, 2008.

[221] M. V. G. Babu, B. Bagyalakshmi, L. Venkidu, and B. Sundarakannan, “Grain size effect on structure and electrical properties of lead-free $Na_{0.4}K_{0.1}Bi_{0.5}TiO_3$ ceramics,” *Ceramics International*, vol. 43, no. 15, pp. 12599–12604, 2017.

[222] W. Cai, C. L. Fu, J. C. Gao, and H. Q. Chen, “Effects of grain size on domain structure and ferroelectric properties of barium zirconate titanate ceramics,” *Journal of Alloys and Compounds*, vol. 480, no. 2, pp. 870–873, 2009.

[223] H. Yan, F. Inam, G. Viola, H. Ning, H. Zhang, Q. Jiang, T. Zeng, Z. Gao, and M. J. Reece, “The contribution of electrical conductivity, dielectric permittivity and domain switching in ferroelectric hysteresis loops,” *Journal of Advanced Dielectrics*, vol. 1, no. 1, pp. 107–118, 2011.

[224] W. Meier, K. E. Meyer, D. F. Sava Gallis, M. A. Blea-Kirby, J. Roth, D. Felman, T. Breuer, G. J. Dension, F. J. Zutavern, W. Huebner, and G. L. Brennecka, “Highly Textured $BaTiO_3$ via Templated Grain Growth and Resulting Polarization Reversal Dynamics,” *Journal of the American Ceramic Society*, vol. 99, no. 3, pp. 922–929, 2016.

[225] A. Krell, A. Teresiak, and D. Schläfer, “Grain size dependent residual microstresses in submicron Al_2O_3 and ZrO_2,” *Journal of the European Ceramic Society*, vol. 16, no. 8, pp. 803–811, 1996.

[226] Q. Ma and D. R. Clarke, “Piezospectroscopic Determination of Residual-Stresses in Polycrystalline Alumina,” *Journal of the American Ceramic Society*, vol. 77, no. 2, pp. 298–302, 1994.

[227] G. Arlt and N. A. Pertsev, “Force-constant and effective mass of 90° domain-walls in ferroelectric ceramics,” *Journal of Applied Physics*, vol. 70, no. 4, pp. 2283–2289, 1991.

[228] Q. Y. Jiang, E. C. Subbarao, and L. E. Cross, “Grain size dependence of electric fatigue behavior of hot-pressed PLZT ferroelectric ceramics,” *Acta Metallurgica et Materialia*, vol. 42, no. 11, pp. 3687–3694, 1994.

[229] H. Martiren and J. C. Burfoot, “Grain-size effects on properties of some ferroelectric ceramics,” *Journal of Physics C: Solid State Physics*, vol. 7, no. 17, pp. 3182–3192, 1974.

[230] A. J. Bell, A. J. Moulson, and L. E. Cross, “The effect of grain-size on the permittivity of $BaTiO_3$,” *Ferroelectrics*, vol. 54, no. 1-4, pp. 487–490, 1984.

[231] S. B. Kim, D. Y. Kim, J. J. Kim, and S. H. Cho, “Effect of Grain-Size and Poling on the Fracture Mode of Lead Zirconate Titanate Ceramics,” *Journal of the American Ceramic Society*, vol. 73, no. 1, pp. 161–163, 1990.

[232] D. Ghosh, A. Sakata, J. Carter, P. A. Thomas, H. Han, J. C. Nino, and J. L. Jones, “Domain Wall Displacement is the Origin of Superior Permittivity and Piezoelectricity in $BaTiO_3$ at Intermediate Grain Sizes,” *Advanced Functional Materials*, vol. 24, no. 7, pp. 885–896, 2014.

[233] C. Kittel, “Theory of the Structure of Ferromagnetic Domains in Films and Small Particles,” *Physical Review*, vol. 70, no. 11-1, pp. 965–971, 1946.

[234] L. Néel, “Les lois de l’aimantation et de la subdivision en domaines élémentaires d’un monocristal de fer,” *Journal de Physique et le Radium*, vol. 5, no. 12, pp. 265–276, 1944.

[235] P. Zheng, J. L. Zhang, Y. Q. Tan, and C. L. Wang, “Grain-size effects on dielectric and piezoelectric properties of poled $BaTiO_3$ ceramics,” *Acta Materialia*, vol. 60, no. 13-14, pp. 5022–5030, 2012.

[236] G. Arlt, D. Hennings, and G. Dewith, “Dielectric-properties of fine-grained barium titanate ceramics,” *Journal of Applied Physics*, vol. 58, no. 4, pp. 1619–1625, 1985.

[237] N. Floquet, C. M. Valot, M. T. Mesnier, J. C. Niepce, L. Normand, A. Thorel, and R. Kilaas, “Ferroelectric domain walls in $BaTiO_3$: Fingerprints in XRPD diagrams and quantitative HRTEM image analysis,” *Journal De Physique III*, vol. 7, no. 6, pp. 1105–1128, 1997.

[238] J. E. Daniels, J. L. Jones, and T. R. Finlayson, “Characterization of domain structures from diffraction profiles in tetragonal ferroelastic ceramics,” *Journal of Physics D: Applied Physics*, vol. 39, no. 24, pp. 5294–5299, 2006.

[239] N. Floquet and C. Valot, “Ferroelectric domain walls in $BaTiO_3$: Structural wall model interpreting fingerprints in XRPD diagrams,” *Ferroelectrics*, vol. 234, no. 1-4, pp. 107–122, 1999.

[240] K. W. Wu and W. A. Schulze, “Aging of the Weak-Field Dielectric Response in Fine- and Coarse-Grain Ceramic $BaTiO_3$,” *Journal of the American Ceramic Society*, vol. 75, no. 12, pp. 3390–3395, 1992.

[241] M. Demartin and D. Damjanovic, “Dependence of the direct piezoelectric effect in coarse and fine grain barium titanate ceramics on dynamic and static pressure,” *Applied Physics Letters*, vol. 68, no. 21, pp. 3046–3048, 1996.

[242] E. Fatuzzo, “Theoretical considerations on switching transient in ferroelectrics,” *Physical Review*, vol. 127, no. 6, pp. 1999–2005, 1962.

[243] M. Avrami, “Kinetics of Phase Change. II Transformation-Time Relations for Random Distribution of Nuclei,” *The Journal of Chemical Physics*, vol. 8, no. 2, pp. 212–224, 1940.

[244] H. M. Duiker and P. D. Beale, “Grain-size effects in ferroelectric switching,” *Physical Review B*, vol. 41, no. 1, pp. 490–495, 1990.

[245] H. M. Duiker, P. D. Beale, J. F. Scott, C. A. P. Dearaujo, B. M. Melnick, J. D. Cuchiaro, and L. D. McMillan, “Fatigue and switching in ferroelectric memories: Theory and experiment,” *Journal of Applied Physics*, vol. 68, no. 11, pp. 5783–5791, 1990.

[246] V. R. Vedula, S. J. Glass, D. M. Saylor, G. S. Rohrer, W. C. Carter, S. A. Langer, and E. R. Fuller, “Residual-stress predictions in polycrystalline alumina,” *Journal of the American Ceramic Society*, vol. 84, no. 12, pp. 2947–2954, 2001.

[247] T. Carisey, I. Levin, and D. G. Brandon, “Microstructure and mechanical properties of textured Al_2O_3,” *Journal of the European Ceramic Society*, vol. 15, no. 4, pp. 283–289, 1995.

[248] B. J. Rodriguez, S. Choudhury, Y. H. Chu, A. Bhattacharyya, S. Jesse, K. Seal, A. P. Baddorf, R. Ramesh, L. Q. Chen, and S. V. Kalinin, “Unraveling Deterministic Mesoscopic Polarization Switching Mechanisms: Spatially Resolved Studies of a Tilt Grain Boundary in Bismuth Ferrite,” *Advanced Functional Materials*, vol. 19, no. 13, pp. 2053–2063, 2009.

[249] P. Marton, T. Shimada, T. Kitamura, and C. Elsasser, “First-principles study of the interplay between grain boundaries and domain walls in ferroelectric $PbTiO_3$,” *Physical Review B*, vol. 83, no. 6, p. 064110, 2011.

[250] B. D. Huey, R. N. Premnath, S. Lee, and N. A. Polomoff, “High Speed SPM Applied for Direct Nanoscale Mapping of the Influence of Defects on Ferroelectric Switching Dynamics,” *Journal of the American Ceramic Society*, vol. 95, no. 4, pp. 1147–1162, 2012.

[251] B. J. Rodriguez, Y. H. Chu, R. Ramesh, and S. V. Kalinin, “Ferroelectric domain wall pinning at a bicrystal grain boundary in bismuth ferrite,” *Applied Physics Letters*, vol. 93, no. 14, p. 142901, 2008.

[252] D. M. Marincel, H. R. Zhang, A. Kumar, S. Jesse, S. V. Kalinin, W. M. Rainforth, I. M. Reaney, C. A. Randall, and S. Trolier-McKinstry, “Influence of a Single Grain Boundary on Domain Wall Motion in Ferroelectrics,” *Advanced Functional Materials*, vol. 24, no. 10, pp. 1409–1417, 2014.

[253] D. M. Marincel, H. R. Zhang, J. Britson, A. Belianinov, S. Jesse, S. V. Kalinin, L. Q. Chen, W. M. Rainforth, I. M. Reaney, C. A. Randall, and S. Trolier-McKinstry, “Domain pinning near a single-grain boundary in tetragonal and rhombohedral lead zirconate titanate films,” *Physical Review B*, vol. 91, no. 13, p. 134113, 2015.

[254] D. M. Marincel, H. R. Zhang, S. Jesse, A. Belianinov, M. B. Okatan, S. V. Kalinin, W. M. Rainforth, I. M. Reaney, C. A. Randall, and S. Trolier-McKinstry, “Domain Wall Motion Across Various Grain Boundaries in Ferroelectric Thin Films,” *Journal of the American Ceramic Society*, vol. 98, no. 6, pp. 1848–1857, 2015.

[255] D. Wolf, “Correlation between structure, energy, and ideal cleavage fracture for symmetrical grain-boundaries in fcc metals,” *Journal of Materials Research*, vol. 5, no. 8, pp. 1708–1730, 1990.

[256] N. Liu, Y. Su, and G. J. Weng, “A phase-field study on the hysteresis behaviors and domain patterns of nanocrystalline ferroelectric polycrystals,” *Journal of Applied Physics*, vol. 113, no. 20, p. 204106, 2013.

[257] W. L. Shu, J. Wang, and T. Y. Zhang, “Effect of grain boundary on the electromechanical response of ferroelectric polycrystals,” *Journal of Applied Physics*, vol. 112, no. 6, p. 064108, 2012.

[258] S. J. Kim, “Polarization switching of ferroelectric ceramics with grain boundary effect: A simple continuum model,” *Journal of Applied Physics*, vol. 92, no. 5, pp. 2668–2673, 2002.

[259] C. A. Randall, D. J. Barber, and R. W. Whatmore, “Ferroelectric domain configurations in a modified-PZT ceramic,” *Journal of Materials Science*, vol. 22, no. 3, pp. 925–931, 1987.

[260] W. Li and M. Alexe, “Investigation on switching kinetics in epitaxial $Pb(Zr_{0.2}Ti_{0.8})O_3$ ferroelectric thin films: Role of the 90° domain walls,” *Applied Physics Letters*, vol. 91, no. 26, p. 262903, 2007.

[261] W. L. Zhu, I. Fujii, W. Ren, and S. Trolier-McKinstry, “Domain Wall Motion in A and B Site Donor-Doped $Pb(Zr_{0.52}Ti_{0.48})O_3$ Films,” *Journal of the American Ceramic Society*, vol. 95, no. 9, pp. 2906–2913, 2012.

[262] Q. M. Zhang, J. Z. Zhao, K. Uchino, and J. H. Zheng, “Change of the weak-field properties of $Pb(ZrTi)O_3$ piezoceramics with compressive uniaxial stresses and its links to the effect of dopants on the stability of the polarizations in the materials,” *Journal of Materials Research*, vol. 12, no. 1, pp. 226–234, 1997.

[263] R. A. Eichel, E. Erunal, P. Jakes, S. Korbel, C. Elsasser, H. Kungl, J. Acker, and M. J. Hoffmann, “Interactions of defect complexes and domain walls in CuO-doped ferroelectric $(K,Na)NbO_3$,” *Applied Physics Letters*, vol. 102, no. 24, p. 242908, 2013.

[264] D. Schrade, R. Mueller, D. Gross, T. Utschig, V. Y. Shur, and D. C. Lupascu, “Interaction of domain walls with defects in ferroelectric materials,” *Mechanics of Materials*, vol. 39, no. 2, pp. 161–174, 2007.

[265] D. C. Lupascu, V. Y. Shur, and A. G. Shur, “Dynamics of a single-planar domain wall in ferroelectric-ferroelastic $Gd_2(MoO_4)O_3$,” *Applied Physics Letters*, vol. 80, no. 13, pp. 2359–2361, 2002.

[266] L. KV, L. M. Riemer, J. Koruza, and J. Rödel, “Hardening of electromechanical properties in piezoceramics using a composite approach,” *Applied Physics Letters*, vol. 111, no. 2, p. 022905, 2017.

[267] L. M. Riemer, K. Lalitha, X. Jiang, N. Liu, C. Dietz, R. W. Stark, P. B. Groszewicz, G. Buntkowsky, J. Chen, S.-T. Zhang, J. Rödel, and J. Koruza, “Stress-induced phase transition in lead-free relaxor ferroelectric composites,” *Acta Materialia*, vol. 136, pp. 271 – 280, 2017.

[268] R. C. Bradt and G. S. Ansell, “Dislocations and 90° domains in barium titanate,” *Journal of Applied Physics*, vol. 38, no. 13, pp. 5407–5408, 1967.

[269] W. Johnson and R. Mehl, “Reaction kinetics in processes of reaction and growth,” *Transactions of the Metallurgical Society of AIME*, vol. 135, pp. 42–58, 1939.

[270] A. N. Kolmogorov, “On the statistical theory of the crystallization of metals,” *Bulletin of the Russian Academy of Sciences: Mathematics*, vol. 1, pp. 355–359, 1937.

[271] A. H. Hubmann, S. Y. Li, S. Zhukov, H. von Seggern, and A. Klein, “Polarisation dependence of Schottky barrier heights at ferroelectric $BaTiO_3/RuO_2$ interfaces: influence of substrate orientation and quality,” *Journal of Physics D: Applied Physics*, vol. 49, no. 29, p. 295304, 2016.

[272] K. Matyjasek, “Analysis of switching process in $(CH_3NH_3)_5Bi_2Br_{11}$ single crystals based on the Avrami model,” *Journal of Physics D: Applied Physics*, vol. 33, no. 20, pp. 2553–2559, 2000.

[273] R. Z. Rogowski, K. Matyjasek, and R. Jakubas, “Polarization switching in $(CH_3NH_3)_5Bi_2Cl_{11}$ ferroelectric crystals,” *Crystal Research and Technology*, vol. 41, no. 6, pp. 557–561, 2006.

[274] K. Matyjasek, “Analysis of the switching process in triglycine sulphate crystals based on the Avrami model,” *Journal of Physics D: Applied Physics*, vol. 34, no. 14, pp. 2211–2219, 2001.

[275] S. Hashimoto, H. Orihara, and Y. Ishibashi, “Study of D-E Hysteresis Loop of TGS Based on the Avrami-Type Model,” *Journal of the Physical Society of Japan*, vol. 63, no. 4, pp. 1601–1610, 1994.

[276] T. D. Usher, C. P. Poole, and H. A. Farach, “Ferroelectric Polarization Reversal in Potassium Dihydrogen Phosphate as Monitored by Switching Current,” *Ferroelectrics*, vol. 110, pp. 67–75, 1990.

[277] A. Gruverman, B. J. Rodriguez, C. Dehoff, J. D. Waldrep, A. I. Kingon, R. J. Nemanich, and J. S. Cross, “Direct studies of domain switching dynamics in thin film ferroelectric capacitors,” *Applied Physics Letters*, vol. 87, no. 8, p. 082902, 2005.

[278] Y. Ishibashi and H. Orihara, “Size Effect in Ferroelectric Switching,” *Journal of the Physical Society of Japan*, vol. 61, no. 12, pp. 4650–4656, 1992.

[279] H. Orihara and Y. Ishibashi, “A Statistical Theory of Nucleation and Growth in Finite Systems,” *Journal of the Physical Society of Japan*, vol. 61, no. 6, pp. 1919–1925, 1992.

[280] V. Shur, E. Rumyantsev, and S. Makarov, “Kinetics of phase transformations in real finite systems: Application to switching in ferroelectrics,” *Journal of Applied Physics*, vol. 84, no. 1, pp. 445–451, 1998.

[281] T. Furukawa, M. Date, M. Ohuchi, and A. Chiba, “Ferroelectric switching characteristics in a copolymer of vinylidene fluoride and trifluorethylene,” *Journal of Applied Physics*, vol. 56, no. 5, pp. 1481–1486, 1984.

[282] K. Dimmler, M. Parris, D. Butler, S. Eaton, B. Pouligny, J. F. Scott, and Y. Ishibashi, “Switching Kinetics in KNO_3 Ferroelectric Thin-Film Memories,” *Journal of Applied Physics*, vol. 61, no. 12, pp. 5467–5470, 1987.

[283] A. Seike, K. Amanuma, S. Kobayashi, T. Tatsumi, H. Koike, and H. Hada, “Polarization reversal kinetics of a lead zirconate titanate thin-film capacitor for nonvolatile memory,” *Journal of Applied Physics*, vol. 88, no. 6, pp. 3445–3447, 2000.

[284] J. F. Scott, L. Kammerdiner, M. Parris, S. Traynor, V. Ottenbacher, A. Shawabkeh, and W. F. Oliver, “Switching kinetics of lead zirconate titanate sub-micron thin-film memories,” *Journal of Applied Physics*, vol. 64, no. 2, pp. 787–792, 1988.

[285] D. Wu, I. Vrejoiu, M. Alexe, and A. Gruverman, “Anisotropy of domain growth in epitaxial ferroelectric capacitors,” *Applied Physics Letters*, vol. 96, no. 11, 2010.

[286] E. J. Guo, K. Dorr, and A. Herklotz, “Strain controlled ferroelectric switching time of $BiFeO_3$ capacitors,” *Applied Physics Letters*, vol. 101, no. 24, 2012.

[287] I. Stolichnov, L. Malin, E. Colla, A. K. Tagantsev, and N. Setter, “Microscopic aspects of the region-by-region polarization reversal kinetics of polycrystalline ferroelectric $Pb(Zr,Ti)O_3$ films,” *Applied Physics Letters*, vol. 86, no. 1, pp. 787–792, 2005.

[288] A. Nautiyal, K. C. Sekhar, N. P. Pathak, N. Dabra, J. S. Hundal, and R. Nath, “Polarization switching properties of spray deposited $CsNO_3$: PVA composite films,” *Applied Physics A*, vol. 99, no. 4, pp. 941–946, 2010.

[289] N. Dabra, J. S. Hundal, A. Nautiyal, K. C. Sekhar, and R. Nath, “Analysis of ferroelectric polarization switching in $(NH_4)_{0.39}K_{0.61}NO_3$ films using nucleation limited switching model,” *Journal of Applied Physics*, vol. 108, no. 2, p. 024108, 2010.

[290] Y. A. Genenko, S. Zhukov, S. V. Yampolskii, J. Schütrumpf, R. Dittmer, W. Jo, H. Kungl, M. J. Hoffmann, and H. von Seggern, “Universal polarization switching behavior of disordered ferroelectrics,” *Advanced Functional Materials*, vol. 22, no. 10, pp. 2058–2066, 2012.

[291] S. Zhukov, J. Glaum, H. Kungl, E. Sapper, R. Dittmer, Y. A. Genenko, and H. von Seggern, “Fatigue effect on polarization switching dynamics in polycrystalline bulk ferroelectrics,” *Journal of Applied Physics*, vol. 120, no. 6, p. 064103, 2016.

[292] J. Lee, A. J. J. M. van Breemen, V. Khikhlovskyi, M. Kemerink, R. A. J. Janssen, and G. H. Gelinck, “Pulse-modulated multilevel data storage in an organic ferroelectric resistive memory diode,” *Scientific Reports*, vol. 6, p. 24407, 2016.

[293] J. Schütrumpf, S. Zhukov, Y. A. Genenko, and H. von Seggern, “Polarization switching dynamics by inhomogeneous field mechanism in ferroelectric polymers,” *Journal of Physics D: Applied Physics*, vol. 45, no. 16, p. 165301, 2012.

[294] M. Kamlah, “Ferroelectric and ferroelastic piezoceramics - modeling of electromechanical hysteresis phenomena,” *Continuum Mechanics and Thermodynamics*, vol. 13, no. 4, pp. 219–268, 2001.

[295] J. E. Huber, “Micromechanical modelling of ferroelectrics,” *Current Opinion in Solid State and Materials Science*, vol. 9, no. 3, pp. 100–106, 2005.

[296] C. M. Landis, “Non-linear constitutive modeling of ferroelectrics,” *Current Opinion in Solid State and Materials Science*, vol. 8, no. 1, pp. 59–69, 2004.

[297] S. Stark, *Hybride Materialmodellierung für ferroelektroelastische Keramiken*. Dresden: Technische Universität Dresden, 2016.

[298] K. H. Chan and N. W. Hagood, “Modeling of nonlinear piezoceramics for structural actuation,” in *Smart Structures and Materials 1994: Smart Structures and Intelligent Systems*, vol. 2190, pp. 194–206, International Society for Optics and Photonics, 1994.

[299] W. Lu, D. N. Fang, C. Q. Li, and K. C. Hwang, “Nonlinear electric-mechanical behavior and micromechanics modelling of ferroelectric domain evolution,” *Acta Materialia*, vol. 47, no. 10, pp. 2913–2926, 1999.

[300] H. Kessler and H. Balke, “On the local and average energy release in polarization switching phenomena,” *Journal of the Mechanics and Physics of Solids*, vol. 49, no. 5, pp. 953–978, 2001.

[301] J. E. Huber, N. A. Fleck, C. M. Landis, and R. M. McMeeking, “A constitutive model for ferroelectric polycrystals,” *Journal of the Mechanics and Physics of Solids*, vol. 47, no. 8, pp. 1663–1697, 1999.

[302] S. C. Hwang, J. E. Huber, R. M. McMeeking, and N. A. Fleck, “The simulation of switching in polycrystalline ferroelectric ceramics,” *Journal of Applied Physics*, vol. 84, no. 3, pp. 1530–1540, 1998.

[303] W. Chen and C. S. Lynch, “A micro-electro-mechanical model for polarization switching of ferroelectric materials,” *Acta Materialia*, vol. 46, no. 15, pp. 5303–5311, 1998.

[304] S. C. Hwang and R. M. McMeeking, “Finite element model of ferroelectric/ferroelastic polycrystals,” in *Smart Structures and Materials 2000: Active Materials: Behavior and Mechanics*, vol. 3992, pp. 404–418, International Society for Optics and Photonics, 2000.

[305] J. Li and G. J. Weng, “A theory of domain switch for the nonlinear behaviour of ferroelectrics,” *Proceedings of the Royal Society A*, vol. 455, no. 1989, pp. 3493–3511, 1999.

[306] J. Y. Li and D. Liu, “On ferroelectric crystals with engineered domain configurations,” *Journal of the Mechanics and Physics of Solids*, vol. 52, no. 8, pp. 1719–1742, 2004.

[307] A. Pathak and R. M. McMeeking, “Three-dimensional finite element simulations of ferroelectric polycrystals under electrical and mechanical loading,” *Journal of the Mechanics and Physics of Solids*, vol. 56, no. 2, pp. 663–683, 2008.

[308] P. Neumeister and H. Balke, “Micromechanical modelling of remanent properties of morphotropic PZT,” *Journal of the Mechanics and Physics of Solids*, vol. 59, no. 9, pp. 1794–1807, 2011.

[309] P. Haupt, “On the mathematical-modeling of material behavior in continuum-mechanics,” *Acta Mechanica*, vol. 100, no. 3-4, pp. 129–154, 1993.

[310] P. J. Chen and S. T. Montgomery, “A macroscopic theory for the existence of the hysteresis and butterfly loops in ferroelectricity,” *Ferroelectrics*, vol. 23, no. 3-4, pp. 199–207, 1980.

[311] P. J. Chen and T. J. Tucker, “One Dimensional Polar Mechanical and Dielectric Responses of the Ferroelectric Ceramic PZT 65/35 due to domain switching,” *International Journal of Engineering Science*, vol. 19, no. 1, pp. 147–158, 1981.

[312] E. Bassiouny, A. F. Ghaleb, and G. A. Maugin, “Thermodynamical formulation for coupled electromechanical hysteresis effects–I. Basic equations,” *International Journal of Engineering Science*, vol. 26, no. 12, pp. 1279–1295, 1988.

[313] E. Bassiouny, A. F. Ghaleb, and G. A. Maugin, “Thermodynamical formulation for coupled electromechanical hysteresis effects–II. Poling of ceramics,” *International Journal of Engineering Science*, vol. 26, no. 12, pp. 1297–1306, 1988.

[314] A. C. F. Cocks and R. M. McMeeking, “A phenomenological constitutive law for the behaviour of ferroelectric ceramics,” *Ferroelectrics*, vol. 228, no. 1-4, pp. 219–228, 1999.

[315] C. M. Landis, “Fully coupled, multi-axial, symmetric constitutive laws for polycrystalline ferroelectric ceramics,” *Journal of the Mechanics and Physics of Solids*, vol. 50, no. 1, pp. 127–152, 2002.

[316] M. Kamlah and Z. G. Wang, “A thermodynamically and microscopically motivated constitutive model for piezoceramics,” *Computational Materials Science*, vol. 28, no. 3-4, pp. 409–418, 2003.

[317] V. Mehling, C. Tsakmakis, and D. Gross, “Phenomenological model for the macroscopical material behavior of ferroelectric ceramics,” *Journal of the Mechanics and Physics of Solids*, vol. 55, no. 10, pp. 2106–2141, 2007.

[318] R. C. Smith, S. Seelecke, Z. Ounaies, and J. Smith, “A Free Energy Model for Hysteresis in Ferroelectric Materials,” *Journal of Intelligent Material Systems and Structures*, vol. 14, no. 11, pp. 719–739, 2003.

[319] R. C. Smith and Z. Z. Hu, “Homogenized energy model for characterizing polarization and strains in hysteretic ferroelectric materials: Material properties and uniaxial model development,” *Journal of Intelligent Material Systems and Structures*, vol. 23, no. 16, pp. 1833–1867, 2012.

[320] R. C. Smith, A. G. Hatch, B. Mukherjee, and S. F. Liu, “A Homogenized Energy Model for Hysteresis in Ferroelectric Materials: General Density Formulation,” *Journal of Intelligent Material Systems and Structures*, vol. 16, no. 9, pp. 713–732, 2005.

[321] B. L. Ball, R. C. Smith, S. J. Kim, and S. Seelecke, “A Stress-dependent Hysteresis Model for Ferroelectric Materials,” *Journal of Intelligent Material Systems and Structures*, vol. 18, no. 1, pp. 69–88, 2007.

[322] S. Seelecke, S. J. Kim, B. L. Ball, and R. C. Smith, “A rate-dependent two-dimensional free energy model for ferroelectric single crystals,” *Continuum Mechanics and Thermodynamics*, vol. 17, no. 4, pp. 337–350, 2005.

[323] M. Hammer and M. J. Hoffmann, “Sintering Model for Mixed-Oxide-Derived Lead Zirconate Titanate Ceramics,” *Journal of the American Ceramic Society*, vol. 81, no. 12, pp. 3277–3284, 1998.

[324] H. Ichikawa, W. Sakamoto, Y. Akiyama, H. Maiwa, M. Moriya, and T. Yogo, “Fabrication and Characterization of (100),(001)-Oriented Reduction-Resistant Lead-Free Piezoelectric (Ba,Ca)TiO_3 Ceramics Using Platelike Seed Crystals,” *Japanese Journal of Applied Physics*, vol. 52, no. 9, p. 09KD08, 2013.

[325] F. K. Lotgering, “Topotactical reactions with ferrimagnetic oxides having hexagonal crystal structures–I,” *Journal of Inorganic & Nuclear Chemistry*, vol. 9, no. 2, pp. 113–123, 1959.

[326] W. A. Dollase, “Correction of intensities for preferred orientation in powder diffractometry: application of the March model,” *Journal of Applied Crystallography*, vol. 19, pp. 267–272, 1986.

[327] V. Tiwari, D. Pandey, P. Krishna, R. Chakravarthy, and B. Dasannacharya, “Neutron diffraction study of ferroelectric $Ba_{0.88}Ca_{0.12}TiO_3$,” *Physica B: Condensed Matter*, vol. 174, no. 1-4, pp. 112–116, 1991.

[328] H. von Seggern and S. Fedosov, “A novel displacement component in PVDF and its role in ferroelectric switching,” *IEEE Transactions on Dielectrics and Electrical Insulation*, vol. 7, no. 4, pp. 543–550, 2000.

[329] Meder Electronic, “H Serie, Hochspannungs-Reedrelais,” tech. rep., 2015.

[330] Behlke Power Electronics GmbH, “Fast High Voltage Transistor Switches,” tech. rep., 2017.

[331] C. B. Sawyer and C. Tower, “Rochelle Salt as a Dielectric,” *Physical Review*, vol. 35, no. 3, pp. 269–273, 1930.

[332] Philtec Inc., “Fiber Optic Displacement Sensors with Analog Output,” tech. rep., 2004.

[333] J. E. Daniels, A. Pramanick, and J. L. Jones, “Time-Resolved Characterization of Ferroelectrics Using High-Energy X-Ray Diffraction,” *IEEE Transactions on Ultrasonics Ferroelectrics and Frequency Control*, vol. 56, no. 8, pp. 1539–1545, 2009.

[334] J. E. Daniels, “Determination of directionally dependent structural and microstructural information using high-energy X-ray diffraction,” *Journal of Applied Crystallography*, vol. 41, pp. 1109–1114, 2008.

[335] A. Pramanick, D. Damjanovic, J. E. Daniels, J. C. Nino, and J. L. Jones, “Origins of Electro-Mechanical Coupling in Polycrystalline Ferroelectrics During Subcoercive Electrical Loading,” *Journal of the American Ceramic Society*, vol. 94, no. 2, pp. 293–309, 2011.

[336] B. D. Cullity, “Elements of X-ray Diffraction,” 1978.

[337] E. Soergel, “Piezoresponse force microscopy (PFM),” *Journal of Physics D: Applied Physics*, vol. 44, no. 46, p. 464003, 2011.

[338] D. Damjanovic, “Contributions to the piezoelectric effect in ferroelectric single crystals and ceramics,” *Journal of the American Ceramic Society*, vol. 88, no. 10, pp. 2663–2676, 2005.

[339] J. Schultheiß, L. Liu, H. Kungl, M. Weber, L. K. Venkataraman, S. Checchia, D. Damjanovic, J. E. Daniels, and J. Koruza, “Revealing the sequence of switching mechanisms in polycrystalline ferroelectric/ferroelastic materials,” *Acta Materialia*, vol. 157, pp. 355–363, 2018.

[340] K. L. Kim and J. E. Huber, “Mapping of ferroelectric domain structure using angle-resolved piezoresponse force microscopy,” *Review of Scientific Instruments*, vol. 86, no. 1, p. 013705, 2015.

[341] B. Hardiman, R. Zeyfang, and C. Reeves, “Direct observation of ferroelectric domains in modified PZT ceramics by transmission electron microscopy,” *Journal of Applied Physics*, vol. 44, no. 12, pp. 5266–5267, 1973.

[342] P. G. Lucuta, V. Teodorescu, and F. Vasiliu, "SEM, SAED, and TEM investigation of domain structure in PZT ceramics at morphotropic phase boundary," *Applied Physics A*, vol. 37, no. 4, pp. 237–242, 1985.

[343] Z. Y. Wang, J. E. Blendell, G. S. White, and Q. Jiang, "Atomic force microscope observations of domains in fine-grained bulk lead zirconate titanate ceramics," *Smart Materials and Structures*, vol. 12, no. 2, pp. 217–222, 2003.

[344] X. H. Zhu, J. M. Zhu, S. H. Zhou, Q. Li, Z. Y. Meng, and N. B. Ming, "Configurations of ferroelectric domains in bismuth- and Zinc-modified $Pb(Ni_{1/3}Nb_{2/3})O_3$-$PbTiO_3$-$PbZrO_3$ ceramics," *Journal of Materials Science*, vol. 34, no. 7, pp. 1533–1541, 1999.

[345] V. V. Shvartsman, A. L. Kholkin, C. Verdier, Z. Yong, and D. C. Lupascu, "Investigation of fatigue mechanism in ferroelectric ceramic via piezoresponse force microscopy," *Journal of the European Ceramic Society*, vol. 25, no. 12, pp. 2559–2561, 2005.

[346] R. F. Brown, "Effect of two-dimensional mechanical stress on the dielectric properties of poled ceramic barium titanate and lead zirconate titanate," *Canadian Journal of Physics*, vol. 39, no. 5, pp. 741–753, 1961.

[347] M. McQuarrie and W. Buessem, "The aging effect in barium titanate," *American Ceramic Society Bulletin*, vol. 34, no. 12, pp. 402–406, 1955.

[348] J. Muñoz Saldana, G. Schneider, and L. Eng, "Stress induced movement of ferroelastic domain walls in $BaTiO_3$ single crystals evaluated by scanning force microscopy," *Surface science*, vol. 480, no. 1, pp. L402–L410, 2001.

[349] R. J. Harrison and S. A. Redfern, "The influence of transformation twins on the seismic-frequency elastic and anelastic properties of perovskite: dynamical mechanical analysis of single crystal $LaAlO_3$," *Physics of the Earth and Planetary Interiors*, vol. 134, no. 3-4, pp. 253–272, 2002.

[350] C. Kwamen, M. Rössle, M. Reinhardt, W. Leitenberger, F. Zamponi, M. Alexe, and M. Bargheer, "Simultaneous dynamic characterization of charge and structural motion during ferroelectric switching," *Physical Review B*, vol. 96, no. 13, p. 134105, 2017.

[351] W. Wersing, "Hystereseeigenschaften ferroelektrischer Keramiken," *Berichte der Deutschen Keramischen Gesellschaft*, vol. 51, pp. 318–323, 1974.

[352] F. Kubel and H. Schmid, "Structure of a Ferroelectric and Ferroelastic Monodomain Crystal of the Perovskite $BiFeO_3$," *Acta Crystallographica Section B*, vol. 46, pp. 698–702, 1990.

[353] Y. S. Ng and A. D. McDonald, "X-ray diffraction studies of domain alignments in modified PZT," *Ferroelectrics*, vol. 62, no. 3-4, pp. 167–178, 1985.

[354] E. B. Tadmor, U. V. Waghmare, G. S. Smith, and E. Kaxiras, "Polarization switching in $PbTiO_3$: an ab initio finite element simulation," *Acta Materialia*, vol. 50, no. 11, pp. 2989–3002, 2002.

[355] Q. D. Liu and J. E. Huber, "Creep in ferroelectrics due to unipolar electrical loading," *Journal of the European Ceramic Society*, vol. 26, no. 13, pp. 2799–2806, 2006.

[356] D. Y. Zhou and M. Kamlah, "Determination of room-temperature creep of soft lead zirconate titanate piezoceramics under static electric fields," *Journal of Applied Physics*, vol. 98, no. 10, p. 104107, 2005.

[357] G. Viola, K. Boon Chong, F. Guiu, and M. John Reece, "Role of internal field and exhaustion in ferroelectric switching," *Journal of Applied Physics*, vol. 115, no. 3, p. 034106, 2014.

[358] S. Zhukov, S. Fedosov, J. Glaum, T. Granzow, Y. A. Genenko, and H. von Seggern, "Effect of bipolar electric fatigue on polarization switching in lead-zirconate-titanate ceramics," *Journal of Applied Physics*, vol. 108, no. 1, p. 014105, 2010.

[359] J. Glaum and M. Hoffman, "Electric Fatigue of Lead-Free Piezoelectric Materials," *Journal of the American Ceramic Society*, vol. 97, no. 3, pp. 665–680, 2014.

[360] W. W. Cao, "Ferroelectrics: The strain limits on switching," *Nature Materials*, vol. 4, no. 10, pp. 727–728, 2005.

[361] S. Wan and K. Bowman, "Modeling of electric field induced texture in lead zirconate titanate ceramics," *Journal of Materials Research*, vol. 16, no. 8, pp. 2306–2313, 2001.

[362] M. Hinterstein, K. A. Schoenau, J. Kling, H. Fuess, M. Knapp, H. Kungl, and M. J. Hoffmann, "Influence of lanthanum doping on the morphotropic phase boundary of lead zirconate titanate," *Journal of Applied Physics*, vol. 108, no. 2, p. 024110, 2010.

[363] K. A. Schönau, M. Knapp, H. Kungl, M. J. Hoffmann, and H. Fuess, "*In situ* synchrotron diffraction investigation of morphotropic $Pb[Zr_{1-x}Ti_x]O_3$ under an applied electric field," *Physical Review B*, vol. 76, no. 14, p. 144112, 2007.

[364] V. Isupov, "Properties of $Pb(Ti,Zr)O_3$ piezoelectric ceramics and nature of their orientational dielectric polarization," *Soviet Physics-Solid State*, vol. 10, no. 4, pp. 989–991, 1968.

[365] A. Arockiarajan, A. Menzel, B. Delibas, and W. Seemann, "Computational modeling of rate-dependent domain switching in piezoelectric materials," *European Journal of Mechanics a/Solids*, vol. 25, no. 6, pp. 950–964, 2006.

[366] D. Zhou, M. Kamlah, and D. Munz, "Rate dependence of soft PZT ceramics under electric field loading," in *Smart Structures and Materials 2001: Active Materials: Behavior and Mechanics*, vol. 4333, pp. 64–71, International Society for Optics and Photonics, 2001.

[367] N. Lee and S. J. Kim, "Effects of loading rate and temperature on domain switching and evolutions of reference remnant state variables during polarization reversal in a PZT wafer," *Ceramics International*, vol. 38, no. 2, pp. 1115–1126, 2012.

[368] M. Vopsaroiu, J. Blackburn, M. G. Cain, and P. M. Weaver, "Thermally activated switching kinetics in second-order phase transition ferroelectrics," *Physical Review B*, vol. 82, no. 2, p. 024109, 2010.

[369] M. M. Vopson, P. M. Weaver, M. G. Cain, M. J. Reece, and K. B. Chong, "Polarization dynamics and non-equilibrium switching processes in ferroelectrics," *IEEE Transactions on Ultrasonics Ferroelectrics and Frequency Control*, vol. 58, no. 9, pp. 1867–1873, 2011.

[370] H. Orihara, S. Hashimoto, and Y. Ishibashi, "A theory of D-E Hysteresis Loop Based on the Avrami Model," *Journal of the Physical Society of Japan*, vol. 63, no. 3, pp. 1031–1035, 1994.

[371] X. Du and I. W. Chen, "Frequency Spectra of Fatigue of PZT and other Ferroelectric Thin Films," *MRS Proceedings*, vol. 493, p. 311, 1998.

[372] P. Duran and C. Moure, "Sintering at near theoretical density and properties of PZT ceramics chemically prepared," *Journal of Materials Science*, vol. 20, no. 3, pp. 827–833, 1985.

[373] J. Ricote, R. W. Whatmore, and D. J. Barber, "Studies of the ferroelectric domain configuration and polarization of rhombohedral PZT ceramics," *Journal of Physics: Condensed Matter*, vol. 12, no. 3, pp. 323–337, 2000.

[374] E. G. Fesenko, O. I. Prokopalo, I. P. Raevskii, L. A. Resnitchenko, and A. E. Panich, "Some specific features of hot-pressed ferroelectric piezoelectric ceramics," *Ferroelectrics*, vol. 41, no. 1-4, pp. 267–270, 1982.

[375] G. H. Haertling, "Hot-Pressed Lead Zirconate-Lead Titanate Ceramics Containing Bismuth," *American Ceramic Society Bulletin*, vol. 43, pp. 875–879, 1964.

[376] A. Webster and T. Weston, "The grain-size dependence of the electromechanical properties in lead zirconate-titanate ceramics," *Journal of the Canadian Ceramic Society*, vol. 47, pp. 51–54, 1968.

[377] K. Okazaki and K. Nagata, "Effects of Grain-Size and Porosity on Electrical and Optical Properties of PLZT Ceramics," *Journal of the American Ceramic Society*, vol. 56, no. 2, pp. 82–86, 1973.

[378] T. Yamamoto, "Optimum Preparation Methods for Piezoelectric Ceramics and Their Evaluation," *American Ceramic Society Bulletin*, vol. 71, no. 6, pp. 978–985, 1992.

[379] C. Sakaki, B. L. Newalkar, S. Komarneni, and K. Uchino, "Grain Size Dependence of High Power Piezoelectric Characteristics in Nb Doped Lead Zirconate Titanate Oxide Ceramics," *Japanese Journal of Applied Physics*, vol. 40, no. 12, pp. 6907–6910, 2001.

[380] M. Laurent, U. Schreiner, P. A. Langjahr, A. E. Glazounov, and M. J. Hoffmann, "Microstructural and electrical characterization of La-doped PZT ceramics prepared by a precursor route," *Journal of the European Ceramic Society*, vol. 21, no. 10-11, pp. 1495–1498, 2001.

[381] K. V. Lalitha, A. K. Kalyani, and R. Ranjan, “Analogous stress and electric field driven structural transformation and decrease in polarization coherence on poling around the morphotropic phase boundary in $BiScO_3$-$PbTiO_3$,” *Physical Review B*, vol. 90, no. 22, p. 224107, 2014.

[382] D. K. Khatua, T. Mehrotra, A. Mishra, B. Majumdar, A. Senyshyn, and R. Ranjan, “Anomalous influence of grain size on the global structure, ferroelectric and piezoelectric response of $Na_{0.5}Bi_{0.5}TiO_3$,” *Acta Materialia*, vol. 134, pp. 177–187, 2017.

[383] J. Schultheiß, O. Clemens, S. Zhukov, H. Seggern, W. Sakamoto, and J. Koruza, “Effect of degree of crystallographic texture on ferro- and piezoelectric properties of $Ba_{0.85}Ca_{0.15}TiO_3$ piezoceramics,” *Journal of the American Ceramic Society*, vol. 100, no. 5, pp. 2098–2107, 2017.

[384] J. L. Jones, E. B. Slamovich, and K. J. Bowman, “Critical evaluation of the Lotgering degree of orientation texture indicator,” *Journal of Materials Research*, vol. 19, no. 11, pp. 3414–3422, 2004.

[385] T. Mitsui and W. B. Westphal, “Dielectric and X-Ray Studies of $Ca_xBa_{1-x}TiO_3$ and $Ca_xSr_{1-x}TiO_3$,” *Physical Review*, vol. 124, no. 5, pp. 1354–1359, 1961.

[386] F. Desheng, I. Mitsuru, and K. Shin-ya, “Invariant lattice strain and polarization in $BaTiO_3$–$CaTiO_3$ ferroelectric alloys,” *Journal of Physics: Condensed Matter*, vol. 22, no. 5, p. 052204, 2010.

[387] S. K. Ye, J. Y. H. Fuh, and L. Lu, “Structure and electrical properties of <001> textured $(Ba_{0.85}Ca_{0.15})(Ti_{0.9}Zr_{0.1})O_3$ lead-free piezoelectric ceramics,” *Applied Physics Letters*, vol. 100, no. 25, p. 252906, 2012.

[388] W. Bai, J. Xi, J. Zhang, B. Shen, J. Zhai, and H. Yan, “Effect of different templates on structure evolution and large strain response under a low electric field in <0 0 l>-textured lead-free BNT-based piezoelectric ceramics,” *Journal of the European Ceramic Society*, vol. 35, no. 9, pp. 2489–2499, 2015.

[389] G. L. Messing, S. Trolier-McKinstry, E. M. Sabolsky, C. Duran, S. Kwon, B. Brahmaroutu, P. Park, H. Yilmaz, P. W. Rehrig, K. B. Eitel, E. Suvaci, M. Seabaugh, and K. S. Oh, “Templated grain growth of textured piezoelectric ceramics,” *Critical Reviews in Solid State and Materials Sciences*, vol. 29, no. 2, pp. 45–96, 2004.

[390] M. Malinowski, K. Lukaszewicz, and S. Asbrink, “The influence of high hydrostatic pressure on lattice parameters of a single crystal of $BaTiO_3$,” *Journal of Applied Crystallography*, vol. 19, pp. 7–9, 1986.

[391] R. Imura, Y. Kitanaka, T. Oguchi, Y. Noguchi, and M. Miyayama, “Polarization properties and crystal structures of ferroelectric $(Ba,Ca)TiO_3$ single crystals,” *Journal of Advanced Dielectrics*, vol. 04, no. 01, p. 1450003, 2014.

[392] D. Hennings, A. Schnell, and G. Simon, “Diffuse Ferroelectric Phase-Transitions in $Ba(Ti_{1-y}Zr_y)O_3$ Ceramics,” *Journal of the American Ceramic Society*, vol. 65, no. 11, pp. 539–544, 1982.

[393] Y. Park and H. G. Kim, “Dielectric Temperature Characteristics of Cerium-Modified Barium Titanate Based Ceramics with Core-Shell Grain Structure,” *Journal of the American Ceramic Society*, vol. 80, no. 1, pp. 106–112, 1997.

[394] E. M. Anton, W. Jo, D. Damjanovic, and J. Rödel, “Determination of depolarization temperature of $(Bi_{1/2}Na_{1/2})TiO_3$-based lead-free piezoceramics,” *Journal of Applied Physics*, vol. 110, no. 9, 2011.

[395] D. S. Fu, M. Itoh, S. Y. Koshihara, T. Kosugi, and S. Tsuneyuki, “Anomalous phase diagram of ferroelectric $(Ba,Ca)TiO_3$ single crystals with giant electromechanical response,” *Physical Review Letters*, vol. 100, no. 22, p. 227601, 2008.

[396] T. Richter, S. Denneler, C. Schuh, E. Suvaci, and R. Moos, “Textured PMN-PT and PMN-PZT,” *Journal of the American Ceramic Society*, vol. 91, no. 3, pp. 929–933, 2008.

[397] W. J. Merz, “The Effect of Hydrostatic Pressure on the Curie Point of Barium Titanate Single Crystals,” *Physical Review*, vol. 78, no. 1, pp. 52–54, 1950.

[398] F. H. Schader, E. Aulbach, K. G. Webber, and G. A. Rossetti, “Influence of uniaxial stress on the ferroelectric-to-paraelectric phase change in barium titanate,” *Journal of Applied Physics*, vol. 113, no. 17, p. 174103, 2013.

[399] J. Narvaez, S. Saremi, J. W. Hong, M. Stengel, and G. Catalan, “Large Flexoelectric Anisotropy in Paraelectric Barium Titanate,” *Physical Review Letters*, vol. 115, no. 3, p. 037601, 2015.

[400] Z. Yu, R. Y. Guo, and A. S. Bhalla, “Orientation dependence of the ferroelectric and piezoelectric behavior of $Ba(Ti_{1-x}Zr_x)O_3$ single crystals,” *Applied Physics Letters*, vol. 77, no. 10, pp. 1535–1537, 2000.

[401] H. R. Liu, J. Koruza, P. Veber, D. Rytz, M. Maglione, and J. Rödel, “Orientation-dependent electromechanical properties of Mn-doped $(Li,Na,K)(Nb,Ta)O_3$ single crystals,” *Applied Physics Letters*, vol. 109, no. 15, p. 152902, 2016.

[402] Y. Chang, J. Wu, Y. Sun, S. Zhang, X. Wang, B. Yang, G. L. Messing, and W. Cao, “Enhanced electromechanical properties and phase transition temperatures in [001] textured $Pb(In_{1/2}Nb_{1/2})O_3$-$Pb(Mg_{1/3}Nb_{2/3})O_3$-$PbTiO_3$ ternary ceramics,” *Applied Physics Letters*, vol. 107, no. 8, p. 082902, 2015.

[403] D. Vriami, D. Damjanovic, J. Vleugels, and O. Van der Biest, “Textured $BaTiO_3$ by templated grain growth and electrophoretic deposition,” *Journal of Materials Science*, vol. 50, no. 24, pp. 7896–7907, 2015.

[404] Y. Yan, L. Yang, Y. Zhou, K. H. Cho, J. S. Heo, and S. Priya, “Enhanced temperature stability in <111> textured tetragonal $Pb(Mg_{1/3}Nb_{2/3})O_3$-$PbTiO_3$ piezoelectric ceramics,” *Journal of Applied Physics*, vol. 118, no. 10, p. 104101, 2015.

[405] E. M. Sabolsky, L. Maldonado, M. M. Seabaugh, and S. L. Swartz, “Textured-$Ba(Zr,Ti)O_3$ piezoelectric ceramics fabricated by templated grain growth (TGG),” *Journal of Electroceramics*, vol. 25, no. 1, pp. 77–84, 2010.

[406] H. Yan, M. J. Reece, J. Liu, Z. Shen, Y. Kan, and P. Wang, “Effect of texture on dielectric properties and thermal depoling of $Bi_4Ti_3O_{12}$ ferroelectric ceramics,” *Journal of Applied Physics*, vol. 100, no. 7, p. 076103, 2006.

[407] P. W. Forsbergh, “Effect of a Two-Dimensional Pressure on the Curie Point of Barium Titanate,” *Physical Review*, vol. 93, no. 4, pp. 686–692, 1954.

[408] J. Q. Qi, W. P. Chen, Y. Wang, H. L. W. Chan, and L. T. Li, “Dielectric properties of barium titanate ceramics doped by B_2O_3 vapor,” *Journal of Applied Physics*, vol. 96, no. 11, pp. 6937–6939, 2004.

[409] Z. Zhao, V. Buscaglia, M. Viviani, M. T. Buscaglia, L. Mitoseriu, A. Testino, M. Nygren, M. Johnsson, and P. Nanni, “Grain-size effects on the ferroelectric behavior of dense nanocrystalline $BaTiO_3$ ceramics,” *Physical Review B*, vol. 70, no. 2, p. 024107, 2004.

[410] W. F. Bai, D. Q. Chen, P. Li, B. Shen, J. W. Zhai, and Z. G. Ji, “Enhanced electromechanical properties in <00l>-textured $(Ba_{0.85}Ca_{0.15})(Zr_{0.1}Ti_{0.9})O_3$ lead-free piezoceramics,” *Ceramics International*, vol. 42, no. 2, pp. 3429–3436, 2016.

[411] W. F. Bai, J. G. Hao, B. Shen, F. Fu, and J. W. Zhai, “Processing optimization and piezoelectric properties of textured $Ba(Zr,Ti)O_3$ ceramics,” *Journal of Alloys and Compounds*, vol. 536, pp. 189–197, 2012.

[412] W. Zhao, J. Ya, Y. Xin, L. E, D. Zhao, and H. P. Zhou, “Fabrication of $Na_{0.5}Bi_{0.5}TiO_3$-$BaTiO_3$-Textured Ceramics Templated by Plate-Like $Na_{0.5}Bi_{0.5}TiO_3$ Particles,” *Journal of the American Ceramic Society*, vol. 92, no. 7, pp. 1607–1609, 2009.

[413] Y. Yan, Y. Zhou, S. Gupta, and S. Priya, “Fatigue mechanism of textured $Pb(Mg_{1/3}Nb_{2/3})O_3$-$PbTiO_3$ ceramics,” *Applied Physics Letters*, vol. 103, no. 8, p. 082906, 2013.

[414] Y. Chang, Z. Yang, X. Chao, Z. Liu, and Z. Wang, “Synthesis and morphology of anisotropic $NaNbO_3$ seed crystals,” *Materials Chemistry and Physics*, vol. 111, no. 2-3, pp. 195–200, 2008.

[415] A. B. Haugen, M. I. Morozov, J. L. Jones, and M. A. Einarsrud, “Rayleigh analysis of dielectric properties in textured $K_{0.5}Na_{0.5}NbO_3$ ceramics,” *Journal of Applied Physics*, vol. 116, no. 21, p. 214101, 2014.

[416] W. Bai, H. Li, J. Xi, J. Zhang, B. Shen, and J. Zhai, “Effect of different templates and texture on structure evolution and strain behavior of <001>-textured lead-free piezoelectric BNT-based ceramics,” *Journal of Alloys and Compounds*, vol. 656, pp. 13–23, 2016.

[417] P. K. Larsen, G. L. M. Kampschoer, M. B. v. d. Mark, and M. Klee, “Ultrafast polarization switching of lead zirconate titanate thin films,” *Proceedings of 1992 IEEE International Symposium on Applications of Ferroelectrics*, pp. 217–224, 1992.

[418] K. R. Bellur, H. Al-Shareef, S. Rou, K. Gifford, O. Auciello, and A. Kingon, “Electrical characterization of sol-gel derived PZT thin films,” *Proceedings of 1992 IEEE International Symposium on Applications of Ferroelectrics*, pp. 448–451, 1992.

[419] Y. Huan, X. H. Wang, J. Fang, and L. T. Li, “Grain size effect on piezoelectric and ferroelectric properties of $BaTiO_3$ ceramics,” *Journal of the European Ceramic Society*, vol. 34, no. 5, pp. 1445–1448, 2014.

[420] R. E. García, W. Craig Carter, and S. A. Langer, “The Effect of Texture and Microstructure on the Macroscopic Properties of Polycrystalline Piezoelectrics: Application to Barium Titanate and PZN–PT,” *Journal of the American Ceramic Society*, vol. 88, no. 3, pp. 750–757, 2005.

[421] J. L. Jones, E. B. Slamovich, K. J. Bowman, and D. C. Lupascu, “Domain switching anisotropy in textured bismuth titanate ceramics,” *Journal of Applied Physics*, vol. 98, no. 10, p. 104102, 2005.

[422] H. B. Zhang, P. W. Xu, E. Patterson, J. D. Zang, S. L. Jiang, and J. Rödel, “Preparation and enhanced electrical properties of grain-oriented $(Bi_{1/2}Na_{1/2})TiO_3$-based lead-free incipient piezoceramics,” *Journal of the European Ceramic Society*, vol. 35, no. 9, pp. 2501–2512, 2015.

[423] Y. A. Genenko, R. Khachaturyan, J. Schultheiß, A. Ossipov, J. E. Daniels, and J. Koruza, “Stochastic multistep polarization switching in ferroelectrics,” *Physical Review B*, vol. 97, no. 14, p. 144101, 2018.

[424] H. Simons, A. King, W. Ludwig, C. Detlefs, W. Pantleon, S. Schmidt, I. Snigireva, A. Snigirev, and H. F. Poulsen, “Dark-field X-ray microscopy for multiscale structural characterization,” *Nature Communications*, vol. 6, p. 6098, 2015.

[425] H. Simons, A. C. Jakobsen, S. R. Ahl, C. Detlefs, and H. F. Poulsen, “Multiscale 3D characterization with dark-field x-ray microscopy,” *MRS Bulletin*, vol. 41, no. 6, pp. 454–459, 2016.

[426] H. Winick, “Synchrotron Radiation Sources - Present Capabilities and Future Directions,” *Journal of Synchrotron Radiation*, vol. 5, pp. 168–175, 1998.

[427] S. Mobilio, F. Boscherini, and C. Meneghini, *Synchrotron Radiation*. Heidelberg: Springer, 2016.

[428] A. G. Chynoweth, “Radiation Damage Effects in Ferroelectric Triglycine Sulfate,” *Physical Review*, vol. 113, no. 1, pp. 159–166, 1959.

[429] S. Vanishri, J. N. B. Reddy, and H. L. Bhat, “Irradiation effects on domain dynamics in ferroelectric glycine phosphite,” *Journal of Applied Physics*, vol. 101, no. 5, 2007.

[430] S. R. Fletcher, E. T. Keve, and A. C. Skapski, “Crystal-Structure of Triglycine Sulfate at Low X-Ray Dosage and after Irradiation-Field Treatment,” *Ferroelectrics*, vol. 8, no. 1-2, pp. 479–482, 1974.

[431] B. H. Toby, “R factors in Rietveld analysis: how good is good enough?,” *Powder diffraction*, vol. 21, no. 1, pp. 67–70, 2006.

Curriculum Vitae

Personal data

Name	Jan Schultheiß
Date of birth	September 3rd, 1988
Place of birth	Coburg
Nationality	German

Education

02/2015–present	Technical University of Darmstadt
09/2017–10/2017	Ural Federal University
10/2011–10/2014	Friedrich Alexander University of Erlangen-Nuremberg (Master of Science)
08/2014–10/2014	National Cheng Kung Unviversity
01/2013–08/2013	The Pennsylvania State University
10/2008–10/2011	Friedrich Alexander University of Erlangen-Nuremberg (Bachelor of Science)
02/2011–07/2011	Swiss Federal Institute of Technology in Zurich, ETH Zurich
09/2000–04/2008	Gynmasium Ernestinum Coburg (High school dipolma)

Publications

J. Schultheiß, L. Liu, H. Kungl, M. Weber, K.V. Lalitha, S. Checchia, D. Damjanovic, J. E. Daniels, J. Koruza; Revealing the switching mechanisms in polycrystalline ferroelectric/ferroelastic materials; Acta Mater. 157, 335 (2018)

Y.A. Genenko, R. Khachaturyan, **J. Schultheiß**, A. Ossipov, J.E. Daniels, J. Koruza; Stochastic multi-step polarization switching in ferroelectrics; Phys. Rev. B, 97, 144101 (2018)

M. Acosta, R. Detsch, A. Grünewald, V. Rojas, **J. Schultheiß**, W. Aleksandra, R. Stark, N. Suman, S. Maciej, J. Koruza, A. Boccacini; Cytotoxicity, chemical stability, and surface properties of ferroelectric ceramics for biomaterials; J. Am. Ceram. Soc., 101[1], 440-449 (2018)

J. Schultheiß, O. Clemens, S. Zhukov, H. von Seggern, W. Sakamoto, J. Koruza; Effect of degree of crystallographic texture on dielectric, ferroelectric, and piezoelectric properties of $Ba_{0.85}Ca_{0.15}TiO_3$ piezoceramics; J. Am. Ceram. Soc., 100[5], 2098-2107 (2017)

H. Han, J. Koruza, E. A. Patterson, **J. Schultheiß**, E. Erdem, W. Jo, J. Lee, J. Rödel; Hardening behavior and highly enhanced mechanical quality factor in $(K_{0.5}Na_{0.5})NbO_3$-based ceramics; J. Eur. Ceram. Soc., 37[5], 2083-89 (2017)

R. Khachaturyan, S. Zhukov, **J. Schultheiß**, C. Galassi, C. Reimuth, J. Koruza, H. von Seggern and Y. A. Genenko; Polarization-switching dynamics in bulk ferroelectric with isometric and oriented anisometric pores; J. Phys. D: Appl. Phys., 50 045303 (2017)

S. Zhukov, Y. A. Genenko, J. Koruza, **J. Schultheiß**, H. von Seggern, W. Sakamoto, H. Ichikawa, T. Murata, K. Hayashi, and T. Yogo; Effect of texturing on polarization switching dynamics in ferroelectric ceramics; Appl. Phys. Lett., 108[1] 012907

(2016).

J. Schultheiß, B. Dermeik, I. Filbert-Demut, N. Hock, X. Yin, P. Greil, N. Travitzky; Processing and Characterization of paper-derived Ti_3SiC_2 based ceramic; Ceram. Int., 41[10A] 12595-03 (2015)

Conference contributions

J. Schultheiß, L. Liu, J.E. Daniels, D. Damjanovic, J. Koruza; The polarization switching mechanism in polycrystalline ferroelectric/ferroelastic materials; Electroceramics XVI; Hasselt, Belgium; 07/2018; poster

J. Schultheiß, H. Uršič, B. Malič, J. Koruza; Broad Switching Behavior in Polycrystalline Ferroelectric/Ferroelastic Ceramic Materials; 27th IEEE International Symposium on the Application of Ferroelectrics; Hiroshima, Japan; 05/2018; oral presentation

Y.A. Genenko, R. Khachaturyan, **J. Schultheiß**, A. Ossipov, J.E. Daniels, J. Koruza; Sequential Polarization Switching in Ferroelectrics: Statistical Description of Experiment; 27th IEEE International Symposium on the Application of Ferroelectrics; Hiroshima, Japan; 05/2018; oral presentation

J. Schultheiß, M. Weber, L. Liu, J.E. Daniels, J. Koruza; Switching Mechanisms in Polycrystalline Ferroelectric Materials; 27th IEEE International Symposium on the Application of Ferroelectrics; Hiroshima, Japan; 05/2018; invited talk

J. Schultheiß, Y.A. Genenko, R. Khachaturyan, L. Liu, J.E. Daniels, J. Koruza; Polarization and strain dynamics in polycrystalline ferroelectric/ferroelastic materials: An experimental approach and mechanistic description; Conference on Electronic and Advanced Materials; 01/2018; Orlando, USA, oral presentation

J. Schultheiß, S. Zhukov, R. Khachaturyan, Y.A. Genenko, J. Koruza; Experimental approach for investigating polarization and strain switching dynamics in ferroelectric/ferroelastic materials; International conference scanning probe microscopy; Yekaterinburg, Russia; 08/2017; oral presentation

J. Schultheiß, Y.A. Genenko, S. Zhukov, R. Khachaturyan, L. Liu, J.E. Daniels, J. Koruza; Simultaneous Time-Resolved Measurements of Polariaztion and Strain Dynamics to Explore Switching in Ferroelectric/Ferroelastic Materials; 26th IEEE International Symposium on the Application of Ferroelectrics; 05/2017; Atlanta, GA, USA; oral presentation

J. Schultheiß, Y.A. Genenko, S. Zhukov, R. Khachaturyan, L. Liu, J.E. Daniels, J. Koruza; Simultaneous Time-Resolved Measurements of Polariaztion and Strain Dynamics to Explore Switching in Ferroelectric/Ferroelastic Materials; 26th IEEE International Symposium on the Application of Ferroelectrics; 05/2017; Atlanta, GA, USA; poster

J. Schultheiß, S. Zhukov, H. von Seggern, W. Sakamoto, Y. Genenko, J. Koruza; Effect of texturing on the polarization switching dynamics in ferroelectric ceramics; 25th IEEE International Symposium on the Application of Ferroelectrics; 08/2016; Darmstadt, Germany; oral presentation

J. Schultheiß, S. Zhukov, H. von Seggern, W. Sakamoto, Y. Genenko, J. Koruza; Effect of texturing on the polarization switching dynamics in ferroelectric ceramics; 25th IEEE International Symposium on the Application of Ferroelectrics; 08/2016; Darmstadt, Germany; poster

R. Khachaturyan, S. Zhukov, **J. Schultheiß**, C. Galassi, C. Reimuth, J. Koruza, H. von Seggern and Y. A. Genenko, Polarization-switching dynamics in bulk ferroelectric with isometric and oriented anisometric pores; 25th IEEE International Symposium on the Application of Ferroelectrics; 08/2016; Darmstadt, Germany; oral presentation

R. Khachaturyan, S. Zhukov, **J. Schultheiß**, C. Galassi, C. Reimuth, J. Koruza, H. von Seggern and Y. A. Genenko, Polarization-switching dynamics in bulk ferroelectric with isometric and oriented anisometric pores; 25th IEEE International Symposium on the Application of Ferroelectrics; 08/2016; Darmstadt, Germany; poster

J. Schultheiß, N. Travitzky; Processing and Characterization of Paper-derived MAX Phase Ceramics, 90th DKG Annual conference & Symposium on High-Performance Ceramics; 03/2015; Bayreuth, Germany; oral presentation